Nanostructures of Gallium Oxide and its Hybrid for Photocatalytic and Field Emission Applications

By

Brahami Das

Thin Film and Nanoscience Laboratory,
Department of Physics,
Jadavpur University, Kolkata-700032, India
**September 2022**

CERTIFICATE FROM THE SUPERVISORS

This is to certify that the thesis entitled "**Nanostructures of Gallium Oxide and its Hybrid for Photocatalytic and Field-Emission Applications**" submitted by **Smt. Brahami Das**, who got her name registered on **16/03/2018** for the award of **Ph.D. (Science) degree** of **Jadavpur University**, is absolutely based upon her own work under the supervision of **Dr. Subrata Sarkar and Prof. (Dr.) Kalyan Kumar Chattopadhyay** and that neither this thesis nor any part of it has been submitted for any degree/diploma or any other academic award anywhere before.

Subrata Sarkar
19/09/22

(Dr. Subrata Sarkar)

Signature of the Supervisor
and Date with Office Seal

Dr. Subrata Sarkar
Associate Professor
Department of Physics
Jadavpur University
Kolkata-700 032
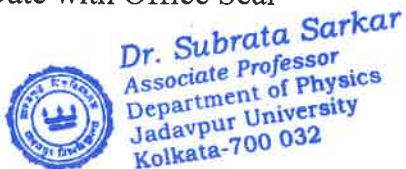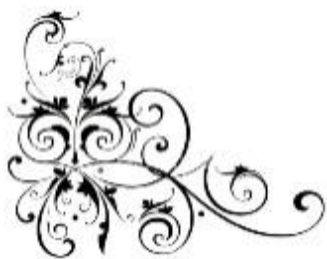
19.9.22

(Dr. Kalyan Kumar Chattopadhyay)

Signature of the Supervisor
and Date with Office Seal

Prof. Kalyan Kr. Chattopadhyay
Professor and Head
Department of Physics
Jadavpur University
Kolkata – 700 032

Special Dedication of This Grateful Feeling to My
Beloved Parents.....

Acknowledgement

This Ph.D. thesis is based on some extended work on the synthesis of gallium oxide and its hybrid nanostructures, their characterizations, properties and applications. This thesis includes a number of articles that we have already published in international journals and presented in various national or international conferences. Throughout my years at the Jadavpur University, I have had the opportunity to meet some wonderful people. I have learned great things not only about science and academics, but also about life, the truth, and faith. It was quite a difficult lesson especially in the beginning, but I admit that I have truly enjoyed every moment of my learning and I am grateful for these various experiences in my life. Today with the submission of my Ph.D. thesis, brings to the end of a wonderful period. During my journey to complete this thesis I have experienced many joyous moments as well as hurdles. I believe this is possible only because of all the people who have given me valuable advice, help, motivation and support. It is pleasure to convey my gratitude to everybody in my humble acknowledgment.

Firstly I would like to express my gratitude to Prof. (Dr). Kalyan Kumar Chattopadhyay, HOD, Department of Physics, Jadavpur University for selection of research-problems, valuable guidance, constant supervision, encouragement, suggestions and painstaking efforts throughout the period of research and preparation of this thesis; without whose active help, ample support and apt guidance, it wouldn't have been possible for me to achieve this work. Dr. Chattopadhyay was there at all times supporting me. I feel contented to have him for his constructive and priceless suggestions, active teamwork and unvarying back-up all the way through the exploration.

My sincere gratitude goes out to another supervisor Dr. Subrata Sarkar, Assistant Professor of Department of Physics, Jadavpur University for his continuous support and valuable suggestions during the completion of this work. My research work was completed efficiently because he gave me enough freedom. It would have been impossible to get so far without your support and understanding. Thank you very much from my heart.

I am indebted to Prof. (Dr.) Sukhen Das, Ex-HOD of the Physics Department, Jadavpur University, and all other authorities for their support during my work, for providing me necessary instrumental, laboratory and library facilities. I am also thankful to all the faculty members and staffs of the Department of Physics, and also The School of Materials Science and Nanotechnology for their wholehearted support. The Officers and Staffs of the Ph.D. and Research Sections of Jadavpur University absolutely deserved my sincere thanks and regards for their cordial support.

I convey my heartiest greetings to the Director and faculty members of the School of Materials Science and Nanotechnology, Jadavpur University, Dr. Sourav Sarkar and Dr. Chandan Kumar Ghosh of for their support, sharing good ideas and encouragements. And special thanks to Dr. Sarkar for being my RAC's member.

Being a member of Prof. Chattopadhyay's research group, I was truly fortunate to work with so many wonderful people. I am grateful to my senior Dr. B. Das ('Biswajit Da') for his unconditional support throughout this entire process. He has continuously motivated me (to this day) for good work. Through this entire journey, his unique insightful discussions,

representation skill, ideas and suggestions have helped me feel confident that I can overcome any obstacle I face.

I wish to thank personally to another senior Dr. N. S. Das ('Nirmalya da') for treating me like your own sister rather than lab colleague. The dedication he has towards research and the welcoming nature of his personality has not only helped me to become a motivated researcher, but also a decent human being. Through this entire journey, his extensive knowledge, manuscript writing skill, ideas and suggestions helped me a lot. Also, his fantastic art work and great skill in using Photoshop inspired me to be more creative with graphics in my manuscripts.

In this connection, I should mention with pleasure the names of all my former and present senior lab mates; Karamjyoti da, Soumen da, Samrat da, Supratim da, Dipayan da, Biplab da, Partha da, Saikat da, Bikam da, Tufan da, Nripen da, Shubhashis da, Kausik da (Chanda), Madhupriya di, Moumita di, Shrabani di, Dimitra Di, Pramita di, Sayantani di, Missisipi di, Rituparna di, Rimpa di. Thank you to this entire team for their help and support throughout my journey.

I would also like to thank all my junior lab collogues; Anibrata, Arnab, Antika, Bikram, Nabanita, Nabamita, Moumita, Pulok, Souvik, Shubhankar (Podder). I am thankful to my colleagues; Dipanwita, Dipayan, Kausik (Sardar), Shubhankar (Mondal) for their continuous encouragement and support. Their presence made the atmosphere very conducive in helping me to complete my research. I must especially mention the names of Ratna and Suvra Di who have always stood beside me and helped in every field. Without them the time taken to complete my Ph.D. would have been much less enjoyable and productive.

I would like to take this opportunity to thank the all the graduate (M.Sc. and M.Tech) students in Prof. Chattopadhyay's Lab, who helped during this period.

I am grateful to the Council of Scientific & Industrial Research (CSIR), Government of India, for rewarding CSIR-SRF [File No of BD: 09/096(0896)/2017-EMR-I] during the execution of Ph. D works. Additionally, I would like to thank the University with Potential for Excellence scheme (UPE-II), Department of Science and Technology (DST) and TEQIP programme for funding various projects during my Ph. D days. Furthermore, I would wish to thanks the Department of Physics, Jadavpur University for giving me this opportunity and allowing me to utilize the valuable resources and instruments throughout my Ph. D journey.

I would like to thank my well-wishers, teachers, friends, and collogues whom I shall always keep in mind and remember them throughout my life.

I have been extremely fortunate to have the most precious people in my life, my parents, who have shown me unconditional love and support. I am truly blessed for their affection and care. Without their support and sacrifice it was very difficult to reach the goal.

Finally, I would like to dedicate this thesis to my family especially my fiancé, without his constant inspiration, support, and encouragement it was not possible, he was there from the very beginning of my journey and it is one of the main reasons why I have been able to complete this dissertation.

21st September 2022
Department of Physics, Jadavpur University
Kolkata -32, India

(Brahami Das)

Contents

5. Novel Ag_2O-Ga_2O_3 type II p-n heterojunction as an efficient water cleanser for green cleaning technology   **131**

Abstract   **133**

Contents

---

6.   Morphology Tuned Ga₂O₃ Nanostructures for Visible Light assisted Dye Sensitized Photocatalytic Water Remediation   163

Abstract   165

7.   Enhanced field emission properties of rGO wrapped Ga₂O₃ micro/nanobricks: Experimental investigation with theoretical validation   185

Contents

Thesis Title:

Nanostructures of Gallium Oxide and its Hybrid for Photocatalytic and Field-Emission Applications

Abstract

Index No: 120/18/Phys./26

Nanostructured gallium oxide (Ga_2O_3) has drawn much attention during the last few decades due to its extraordinary optical and electrical properties. They also include various facilities of tunable structural properties. Ga_2O_3 is a UV-transparent material exhibiting a wide band gap (~4.9 eV) and a higher room temperature mobility (~150-184 cm^2/V.s) which results a good charge separation between the photo-generated electron-hole pairs assisting it to become a potential photocatalytic agent for the degradation of different organic and inorganic hazardous pollutants. Also, Ga_2O_3 has its uses in display industry for making different types of field emission display units, flexible displays, and many other electronic devices due to its suitable work function, electron affinity, crystal structures and variety of morphologies. Although a huge volume of literature exists on the work done on gallium oxide nanostructure, still there are a number of problems regarding the controlled growth of novel nanostructures, understanding its electrical, optical and structural properties and many other aspects. This thesis entitled — "**Nanostructures of gallium oxide and its hybrid for photocatalytic and field-emission applications**" aimed to investigate the synthesis processes, properties and applications of different gallium oxide nanostructures. Another major goal of this thesis is to synthesize new types of gallium oxide based hybrid nanostructures and exploiting their properties for further enhancement of multipurpose performances.

Aiming to this, firstly, porous brick-like low dimensional Ga_2O_3 nanostructures were synthesized through a low-cost chemical route followed by calcination at different temperatures. The pore-density was varied by varying synthesis temperatures and the materials were exhibited a transformation from α-hexagonal to β-monoclinic phase. With traditional structural and morphological characterizations, detailed contaminant removal properties were investigated for the as-prepared samples. The green cleaning efficiency was recognized to be influenced by crystal structure, surface morphology and surface charge type of the catalyst. All of the synthesized material showed promising performance in degradation of traditional organic hazardous dyes like rhodamine B (RhB), methyl orange (MO) and apparently invisible harmful water soluble chemical like phenol. An interesting feature, i.e., obtaining dye specific adsorbent out of the same materials and the mechanism for the ion-selective dye degradation process have been presented in this work. High degradation rate constants of 0.072, 0.051 and 0.18 min^{-1} were obtained for RhB, MO and mixed dyes respectively with almost complete removal of the dyes. The role of •OH, •O_2^- and h^+ radicals was correlated with catalytic performances depending upon modification of band positions of the dyes. The mesoporous Ga_2O_3 structures are hence inferred as potential candidates for future water safety issues.

Encouraged by the fruitful application of mesoporous nanocrystalline Ga_2O_3 in green water disinfection technology, introduction of junctions in the Ga_2O_3 system was attempted aiming an enhancement of its photocatalytic efficiency. For this, Ag_2O-Ga_2O_3 based type II p-n nanoheterojunctions were designed using ex-situ chemical reduction technique with different densities of Ag_2O attachment on Ga_2O_3 surface. A systematic optimization was carried out to establish best performing junction; targeting the photodegradation of noxious organic dye methyl orange (MO). Thorough theoretical and experimental studies were performed to determine relative band positions and ensure charge transfer between the counterparts. Favorable alignment of the electronic bands of Ag_2O and Ga_2O_3 was identified as a key factor for prompt separation of photogenerated e^-/h^+ pair leading to faster decomposition of water contaminant dyes. The optimized nanoheterojunction sample also performed remarkably fast in degrading carcinogenic hazardous phenol and other dyes like RhB, aniline blue (AB), eosin B (EB) and mixtures of dyes with different ionic identities. Additional advantages of these junction-based catalysts were also reflected in retainment of catalytic efficiency over multiple water disinfection cycles and its appreciable performance in active media of different pH values. With high degradation rate constants of 0.4158, 0.3306,
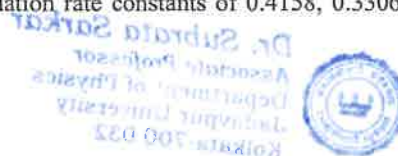
0.2436 and 0.207 min^{-1} for RhB, AB, MO, EB respectively, and multidimensional performance as green cleaning agent, this newly explored Ag$_2$O$_3$-Ga$_2$O$_3$ nanoheterojunctions are identified as a strong candidate for future water cleaning technology.

After the successful junction triggered catalytic activity, photocatalytic applications of Ga$_2$O$_3$ in visible region was further attempted. To achieve this goal, low dimensional Ga$_2$O$_3$ was synthesized via a facile chemical route aiming at easy morphological tuning. Different gallia-precursors as starting materials for hydrothermal synthesis eventually led to spherical nanoparticles and fractured nanobricks as the end product. In addition to the regular characterization of phase, morphology, chemical bond, and surface-related investigations; both the samples were subjected to visible-light-induced photocatalytic degradation of toxic organic pollutants. Despite its wide band gap, the samples showed an efficient dye degradation ability under visible excitation which was explained as originating due to sensitization of the dyes. In the thorough investigation of RhB dye-degradation, the nitrate-salt originated nanobricks appeared to be more efficient than the nanospheres fabricated using chloride-salt with degradation rate constants of 0.0394 min^{-1} and 0.0057 min^{-1} respectively. The performances of the samples differed due to their electronic band position. Also, morphological features like higher specific surface area, porosity, and aspect ratio enabled faster degradation of RhB for nanobricks. However, lower surface area, as reflected from BET studies and inherent agglomeration, caused comparatively weaker degradation performance of the nanospheres. This remediation technology can provide a lead for the optimization of similar future catalyst systems to be fabricated using the hydrothermal-synthesis route for the purpose of wastewater treatment.

Successful application of Ga$_2$O$_3$ in different aspects of waste water treatment encouraged us to find out whether the material can be used in a true multipurpose way. For this, gallium oxide had to response in some novel electrical application. Among different novel electrical applications, cold electron emission was identified as an important emerging sector.

Aiming for efficient cold cathode applications in low dimension, pure and rGO wrapped gallium oxide micro/nanobricks were synthesized via cost-effective solid-state and hydrothermal routes. The synthesized samples were characterized using X-ray diffractometry, field emission scanning electron microscopy, high-resolution transmission electron microscopy, and Raman spectroscopy for phase, morphology, composition, and structure-related investigations. In addition, all samples were thoroughly investigated, and as a result, experimental modifications were adapted accordingly for improving the field emission properties. Remarkable enhancement of field-emission performances with a high emission current-density of 1.08 mA/cm^2 and enhancement factor of 7400 has been observed as an effect of rGO wrapping. The results have been correlated with the increase in the availability of emission sites and proper charge carrier transport between the components in the hybrid structure. Furthermore, the probability of charge carrier transport across Ga$_2$O$_3$ /rGO junction was validated using theoretical analysis via DFT calculations. Moreover, the improvement of field emission properties due to rGO wrapping was also predicted from ANSYS simulations. Hence, 3.5 times increment of current density and 2.5 times lowering of turn-on field, the Ga$_2$O$_3$/rGO hybrid system emerged as one of the most functional future cold cathodes. This work opens up new applications for Ga$_2$O$_3$-based composites beyond the sensing and catalysis sectors.

Signature of the Candidate: *Brahami Das.*

Date: 21/09/2022

Subrata Sarkar
19/09/22
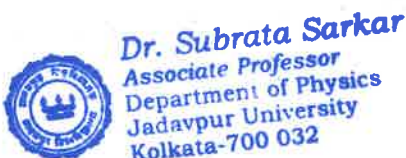
(Dr. Subrata Sarkar)
Signature of the Supervisor
and Date with Office Seal

Dr. Subrata Sarkar
Associate Professor
Department of Physics
Jadavpur University
Kolkata-700 032

K. Chattopadhyay
19.9.22

(Dr. Kalyan Kumar Chattopadhyay)
Signature of the Supervisor
and Date with Office Seal

Prof. Kalyan Kr. Chattopadhyay
Professor and Head
Department of Physics
Jadavpur University
Kolkata – 700 032

2/2

List of Publications

This thesis is based on the following publications/communicated articles (1-4)

1. **Tailored mesoporous nanocrystalline Ga_2O_3 for dye-selective photocatalytic degradation**
   Brahami Das, Biswajit Das, Nirmalya Sankar Das, Subrata Sarkar, Kalyan Kumar Chattopadhyay
   (Microporous and Mesoporous Materials, 288 (2019) 109600)

2. **Novel Ag_2O-Ga_2O_3 type II p-n heterojunction as an efficient water cleanser for green cleaning technology**
   Brahami Das, Biswajit Das, Suvra Pal, Nirmalya Sankar Das, Bikram Kumar Das, Subrata Sarkar, Kalyan Kumar Chattopadhyay
   (Applied Surface Science, 515 (2020) 145958)

3. **Enhanced field emission properties of rGO wrapped Ga_2O_3 micro/nanobricks: Experimental investigation with theoretical validation**
   Brahami Das, Biswajit Das, Nirmayla Sankar Das, Suvra Pal, Bikram Kumar Das, Ratna Sarkar, Rimpa Khan, Subrata Sarkar and Kalyan Kumar Chattopadhyay **(Journal of Alloys and Compounds; 902 (2022) 163726)**

4. **Morphology tuned Ga_2O_3 nanostructures for visible light assisted dye sensitized photocatalytic water remediation**
   Brahami Das, Nirmalya Sankar Das, Biswajit Das, Ratna Sarkar, Subrata Sarkar, Kalyan Kumar Chattopadhyay
   (Communicated, in 2021)

Additional list of publications:

5. **V doped $BaSnO_3$ nanocubes as a field emitting material: Experimental and theoretical investigation**
   Suvra Pal, Nirmalya Sankar Das, **Brahami Das**, Bikram Kumar Das, Subhadipta Mukhopadhyay, Kalyan Kumar Chattopadhyay
   (Applied Surface Science, 530 (2020) 147102)

6. **Hierarchical nickel sulphide microstructures for controlled water disinfection and cold cathode emission**

Rimpa Khan, Nirmalya Sankar Das, Biswajit Das, **Brahami Das**, Kalyan Kumar Chattopadhyay

(Journal of Photochemistry and Photobiology A: Chemistry, 412 (2021) 113212)

7. **Calcination temperature dependent dielectric properties of nanocrystalline BaSnO$_3$**

   Suvra Pal, Nirmalya Sankar Das, **Brahami Das**, Subhadipta Mukhapadhyay, Kalyan Kumar Chattopadhyay

   (ECS Journal of solid state science and technology, 10(7) (2021) 071018)

8. **Hydrothermal synthesis of GO wrapped BiOCl nanosheet to Visible light assisted catalytic photodegradation for Rhodamine B dye**

   Ratna Sarkar, Dimitra Das, Kausik Chanda, **Brahami Das**, Subrata Sarkar and Kalyan K. Chattopadhyay

   (Materials Chemistry and Physics; 279 (2022) 125796)

9. **Chalcogenide beyond photovoltaics: Field Emission from morphology tailored nanostructured molybdenum sulphide**

   Rimpa Khan, Nirmalya Sankar Das, **Brahami Das** and Kalyan Kumar Chattopadhyay

   (Communicated in 2022)

10. **Morphology tuned electrochemical properties of CuBO$_2$ nanostructures**

    Pulok Das, Nirmalya Sankar Das, Kausik Sardar, **Brahami Das**, Ashadul Adalder and Kalyan Kumar Chattopadhyay

    (Communicated in 2022)

Publications in conference proceedings:

1. **Facile Preparation of Porous Ga$_2$O$_3$ Nano/microbars for Highly Efficient Photocatalytic Degradation**

   Brahami Das, Biswajit Das, Suvra Pal, Ratna Sarkar, Nirmalya Sankar Das, Subrata Sarkar and Kalyan Kumar Chattopadhyay

   (AIP Conference Proceedings 2220 (2020) 020013)

2. **Efficient Photocatalytic Activity of Bismuth Oxyhalides with preferentially oriented (210) facets under Visible light**

   Ratna Sarkar, Dimitra Das, **Brahami Das**, Subrata Sarkarand Kalyan K. Chattopadhyay

   (AIP Conference Proceedings 2220 (2020) 020030)

3. **BaSnO$_3$ nanoparticles as blue emitting phosphor and efficient photocatalyst**

   Suvra Pal, Nirmalya Sankar Das, **Brahami Das**, Biswajit Das, Subhadipta Mukhopadhyay and Kalyan Kumar Chattopadhyay

   (AIP Conference Proceedings 2220 (2020) 020014)

Publications in book chapter:

1. **Morphological tuning of low dimensional β-Ga₂O₃ for enhanced photocatalytic performance**

Brahami Das, Nirmalya Sankar Das, Biswajit Das, Ratna Sarkar, Suvra Pal, Subrata Sarkar and Kalyan Kumar Chattopadhyay

Basic and Applied Sciences into next frontiers; New Delhi Publishers;

ISBN: 978-81-948993-0-3

2. **Structural Tuning of BiOCl nano-crystals: PVP modulated visible light stimulated photocatalytic dye degradation**

Ratna Sarkar, Dimitra Das, **Brahami Das**, Subrata Sarkar and Kalyan Kumar Chattopadhyay

Emarging Trends and New Horizons in Applied Sciences; New Delhi Publishers; ISBN: 978-81-940943-5-7

Paper presented in national and international conferences:

1. National Conference on 'Recent Trends in Condensed Matter Physics' **(RTCMP 2017).** Venue: Organized by Bose Institute, Kolkata (October 31-November 3, 2017) Presentation mode– **Poster (Prediction of Enhanced Cold Emission Properties of Ga₂O₃ Nanostructures By Tuning Their Porosity)**

2. International Conference on Nanotechnology: Ideas, Innovations & Initiatives- 2017 **(ICN:3I 2017).** Venue: Organized by Department of Mechanical & Industrial Engineering and Centre of Nanotechnology, IIT Roorkee, India (December 6-8, 2017) Presentation mode–**Oral (Ga₂O₃ nanostructures for wastewater treatment: Morphology induced degradation of methyl orange)**

3. National Seminar on 'Recent Trend in Frontier Research in Physics' **(RTFRP-2018).** Venue: Organized by Department of Physics, Jadavpur University, Kolkata, West   Bengal (March 6, 2018)

   Presentation Mode- **Poster (Facile Morphology tuning of porous Ga₂O₃ Cold Cathodes)**

4. National Conference on 'Recent Developments in Nanoscience & Nanotechnology' (**NCRDNN-2019**). Venue: Organized by School of Materials Science and Nanotechnology, Jadavpur University, Kolkata, West   Bengal (January 29-31, 2019)   Presentation Mode- **Participation**

5. National Seminar on 'Physics at Surfaces and Interfaces of Soft Materials' (**PSISM- 2019**). Venue: Organized by Department of Physics, Jadavpur University, Kolkata, West Bengal. (September 26-27, 2019)

Presentation Mode- **Poster (Morphology Tuned Ga$_2$O$_3$ nanostructures: Ultrafast removal of Eosin B)**

6. International Conference on Condensed Matter & Applied Physics (**ICC-2019**). Venue: Govt. Engineering College, Bikaner, Rajasthan. (October 14-15, 2019) Presentation Mode- **Poster (Facile Preparation of Porous Ga$_2$O$_3$ Nano/microbars for Highly Efficient Photocatalytic Degradation)**

ISBN: 978-93-89008-10-4 (Abstract book of 3rd International Conference on Condensed Matter & Applied Physics)

7. Workshop on 'Writing Quality Research Article for Publication'

Venue: Organized by Faculty of Engineering and Technology, Jadavpur University, Kolkata, West Bengal (January 13-14, 2020)

Presentation Mode- **Participation**

8. National Conference on 'Frontiers of Material Science and Photonics: Issues and Developments (**NCFMSP-2020**). Venue: Organized by Department of Physics, Sidhu-Kanho-Birsha University, Purulia, West Bengal (March 5-6, 2020)

Presentation Mode- **Oral (Impact of morphological variation on enhancement of photocatalytic activity of Ga$_2$O$_3$ based system)**

ISBN: 978-81-936317-4-4 (Proceedings of National Conference on Frontiers of Material Science and Photonics: Issues and Developments)

9. Online Course on 'An Introduction to Materials Characterization Techniques'. Organized by Department of Physics, K. J. Somaiya College of Science and Commerce, Mumbai, India. (22nd -28th June, 2020)

10. Certificate Course in 'Organic Optoelectronics & Spintronics: Fabrication, Modelling and Experimental Techniques' Organized by Kazi Nazrul University, Kalla (C.H.), Asansol, Paschim Barddhaman, West Bengal, India. (July – September, 2020)

11. International Conference on Recent Trends in Basic and Applied Sciences (**VirtCon2020).** Organized by Department of Physics, Bhairab Ganguly College and Dam Dam Motijheel College (6th -7th July, 2020)

Presentation Mode- **Oral (Morphological Tuning of Low Dimensional β-Ga₂O₃ for Enhanced Photocatalytic performance)**
ISBN: 978-81-948993-0-3 (Basic and Applied Sciences into Next Frontiers**)**

12. International Web Conference on Recent Advances in Nanoscience & Nanotechnology for High-end Applications (**IWCRANHA-2020**). Organized by Department of Applied Science and Humanities, Assam University Silchar (25ᵗʰ -26ᵗʰ July, 2020)
Presentation Mode- **Oral (Type II Heterojunction Involving Ag₂O/Ga₂O₃: A Strong Alternative to Combat Water Contamination)**

13. National Conference on Materials and Devices (**NCMD-2020**). Organized by Department of Physics, Faculty of Engineering and Computing Sciences, Teerthanker Mahaveer University, Moradabad (18ᵗʰ -19ᵗʰ December, 2020)
Presentation Mode**- Oral**

14. 6ᵗʰ International Conference on Nanoscience and Nanotechnology (Virtual Conference) (**ICONN 2021**). Organized by SRM Institute of Science and Technology, India, (1ˢᵗ – 3ʳᵈ February, 2021)
Presentation Mode- **Oral (Morphology Tuned Ga₂O₃ Nanostructures for Visible Light Assisted Dye-Sensitized Photocatalytic Water Disinfection)**

Chapter 1

Introduction

1.1. Nanoscience and nanotechnology

Feynman's revolutionary concept of nanotechnology, which depends on the fabrication of nanostructured materials through a precise and controlled route, has already proved its immense potential in every aspect of science and emerging technology fields. Such unconventional prediction formed nanotechnology as a banner and urged to do a nanotechnology race in the contemporary era. In the 1980s, the term "nanotechnology" was specified for the first time to characterize the technical aspects of the materials with at least one of their dimensions in the nano regime (10^{-9} m). This technology is designated to include all aspects of production, development and the use of materials and devices at the nanoscale with superior functionality. By focusing our naked eyes, we can visualize down to a scale of ~75 microns. For reference, recall that the diameter of a human hair strand exhibits ~ 60,000 to 120,000 nm thickness, whereas diameter of a red blood cell is approximately 2,500 nm, and that of a DNA is about 2–12 nm. Researchers have been paid enormous efforts to develop new instruments that support to investigate different properties of nanomaterials with a resolution next to the atomic level. As introduced earlier, the famous physicist Richard Feynman first mentioned the concepts of nanotechnology in a talk "There's Plenty of Room at the Bottom" in 'California Institute of Technology' (Caltech) during American Physical Society meeting on 29th December, 1959. In 1986, basic notion of nanoscience and nanotechnology was further investigated thoroughly by Dr K. Eric Drexler. In early 1980s, through the company of two prime evolutions; (a) the formation of cluster science (b) discovery of scanning tunnelling microscope, the blossoming of nanoscience and nanotechnology was ignited. That evolution assisted towards the invention of fullerenes and carbon nanotubes in 1985 & 1991, respectively[1, 2]. Also, in 1986 the scientists Gerd Binnig & Heinrich Rohrer achieved Nobel Prize for developing a scanning tunnelling microscope. After that, a tremendous advancement in scientific investigations in the nanoscience and technology field is achieved worldwide. Successive research has been accomplished on lower-dimensional materials such as semiconductors, metals, oxides, ceramics, polymers and their composites in search of novel advanced properties. In the case of nano-dimensional materials, many exclusive phenomena (physical, chemical and/or biological) can be discovered that may be distinctive from their bulk form. Specifically, thermal conductivity, electronic transport properties, magnetic characteristics and various mechanical properties can be altered remarkably in the nanomaterials. These nanomaterials exhibit high surface energy, spatial confinement, reduced imperfections and an enhanced surface-to-volume proportion, that is the presence of a huge

fraction of surface atoms with respect to their bulk counterpart. This behaviour imposes an impressive development in surface-dependent phenomena of the materials such as catalysis, field emission etc. This promising potential for novel applications encouraged researchers to manipulate the substances at the nanometric scale with control at the atomic level. **Figure 1.1** represents various materials of different scales, from bulk range to micro, nano and angstrom. However, the nanomaterials can be synthesized following two main approaches, i.e. 'top down' as well as 'bottom up' techniques. In the 'top-down' method, nanostructures can be produced from a large piece of material. In contrast, in the case of the 'bottom-up' technique, nanomaterials can be fabricated by self-assembly of the atom by atom or molecules.
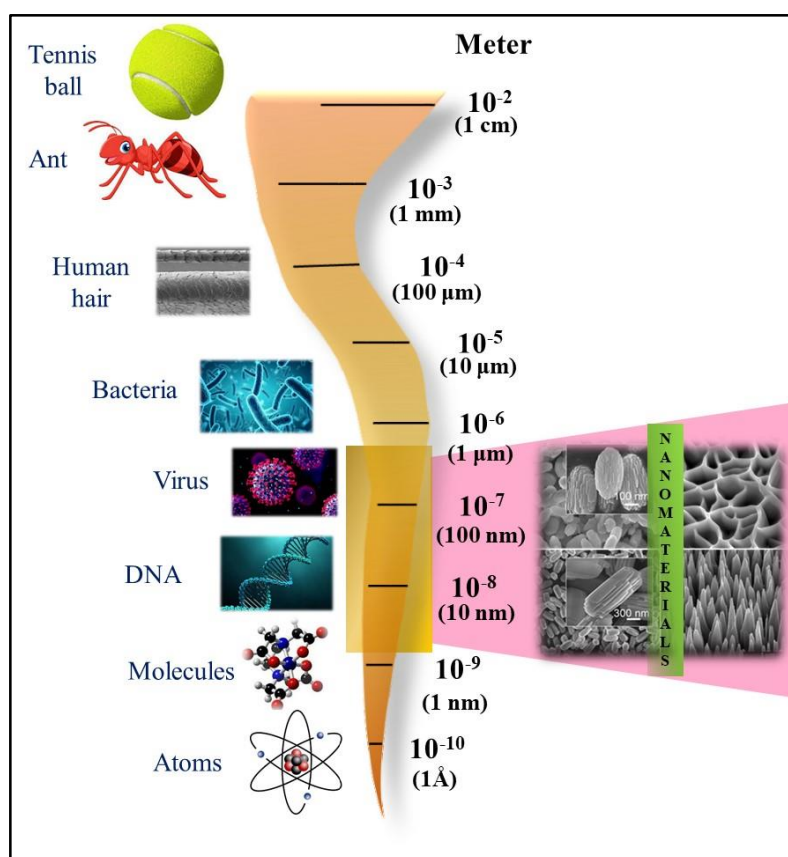
Figure 1. 1 Comparison of different sizes of materials with nanoscale dimension

Based on the dimensional point of view, the nanomaterials are divided into four categories:

1. Zero dimensional (0D), broadly called nanoparticle or quantum dot in which the motion of the charge carriers (electrons, holes) is constricted in entire three directions (X, Y, Z).

2. One dimensional (1D) nanomaterial where the movement of the same is allowed in one direction only (Example: nanorods, nanotubes, nanowires, nanobelts, nanopins, nanoneedles etc.).

3. Two-dimensional (2D) in which the motion of the charge carriers (electrons, holes) is restricted in one direction, and that dimension of the material is very small as compared to the other two (Example: nanosheets, nanoflake, a nanoplate, nanofoil etc.).

4. Three-dimensional (3D) nanomaterials in which the charge carriers can be moved freely in all three directions can be considered as the accumulation of one-dimensional (1D) nanorods, nanotubes, nanowires etc.
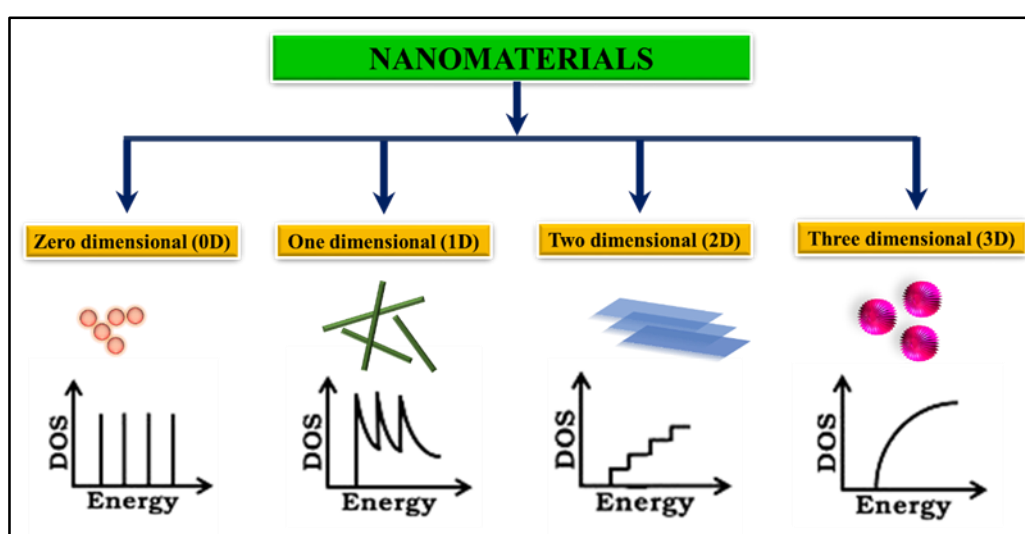
Figure 1. 2 Schematic presentation of structural dimensionality of materials with density of states

The electronic band-structure of any low-dimensional material is easily found by shrinking its dimensions one by one down to a nanometre scale. The bulk materials exhibit continuous absorption and electronic spectra. In contrast, quantum confinement occurs in the nano regime after reaching the physical length scale equivalent to or less than exciton Bohr radius, resulting in the appearance of discrete and more atomic-like optical and electronic spectra. When the de Broglie wavelength associated with an interacting material particle is comparable with the size of the material, a free carrier restricted in that structure acts like a particle in a potential box. However, electronic structure of any material changes with dimensionality. For three-dimensional (3D) material, it can be observed that the density of states D_{3D} (E) varies with $\sqrt{E}$ i.e. the square root of energy, and the possible electronic states become quasi-continuous. For two-dimensional materials (2D), the density of states D_{2D} (E) is not an energy dependent function but appears as a quasi-continuous step-function. For example, for one-dimensional

materials (1D), the density of states D_{1D} (E) is equivalent to $E^{-1/2}$, producing singularities near band edges. Finally, for a zero-dimensional solid (0D), density of states D_{0D} (E) becomes comparable to E^{-1}, which represents a delta function. **Figure 1.2** presents the dimension-dependent variation of density of states with energy.

1.2.   Transparent metal oxide (TMO)

In the present age, transparent metal oxides (TMO) have become scientifically enthralling and technologically fascinating materials due to their wide variety of electronic and chemical properties. They are found to be both chemically and thermally stable, also often exhibit relatively high conductivity and are transparent in visible and UV spectral range as a consequence of wide band gap[3]. There exists a huge variety of binary oxides, like ZnO, TiO_2, Ga_2O_3, In_2O_3 and SnO_2, which cover large-scale optical and electrical properties as well as the applications in optical coatings to catalysis, sensing technology to field emission devices, solar cells etc[4-6]. The unique feature of transparent conducting oxides combines transparency in the visible to UV range and high reflectivity in infrared, making them applicable for high-power electronics and optoelectronic devices operating in the former spectral region. Furthermore, polymorphic transparent conducting oxides seek attention because of their structure-dependent properties, encouraging researchers to perform investigations on phase transition behaviours to further enlarge their functionality[7-9].

Generally, in the visible spectral range, transparent conducting oxides with thickness ~0.1– 1.0 micron show high average transparency ($\geq 80\%$) due to their band gap which is higher than 3 eV and consume huge carrier concentration (10^{18}– 10^{21} cm^{-3})[10]. Usually, the n-type conductivity in TCOs originated as a consequence of available oxygen vacancies or low cation-interstitial formation energy. Also, the dopant incorporation may lead to the enhancement of electrical conductivity. Whereas, few dopants, for example transition metals, have a notable absorption in the visible range. Also, higher carrier mobility plays a vital role in fabricating an excellent transparent conductor. Surprisingly, a few carriers with high mobility may contribute momentous conductivity through diminishing optical-absorption. Conduction bands consisting of s orbitals produce the highly mobile carriers, unlike d orbitals. So, the oxide materials whose conduction bands are formed with 4s, 5s, or 6s orbitals may recognize as suitable TMO candidates. It is observed that energy gap is usually lower when conduction band is comprised of 6s orbitals, and greater visible light transparency is not attainable. Also, it is reported that

both the compounds PbO_2 and Tl_2O_3 are of black coloured. On the other hand, the CBs of gallium oxide (Ga_2O_3) and tin oxide (SnO_2) are comprised of 4s and 5s orbitals, respectively, and demonstrate good TMO behavior[11, 12].

1.3. Gallium oxide (Ga_2O_3)

In the past few decades, Gallium oxide has triggered tremendous motivation among researchers through interesting physical and chemical properties as well as its plausible usage potential in diverse fields. Depending upon preparation conditions, there exist five different polymorphisms of Ga_2O_3 named α, β, δ, γ, κ and ε (presented in **Table. 1.1**), each of them possessing similar close-packing of oxygen layers, with different filling of tetrahedral and octahedral gallium site, schematically shown in **Figure 1.3**. Out of those phases, monoclinic β-Ga_2O_3 is most stable both thermally and chemically, whereas the other phases exist in metastable state. Furthermore a transformation into β-phase occures at sufficiently high temperatures (> 600 °C). Hence, it is challenging to obtain a good-quality single crystal for those phases. These facts are highly responsible for input limitations in characterizing them. As a consequence, numerous fundamental properties are yet unrevealed, or a matter of debate, and sometimes even the existence of the polymorph itself is criticised.
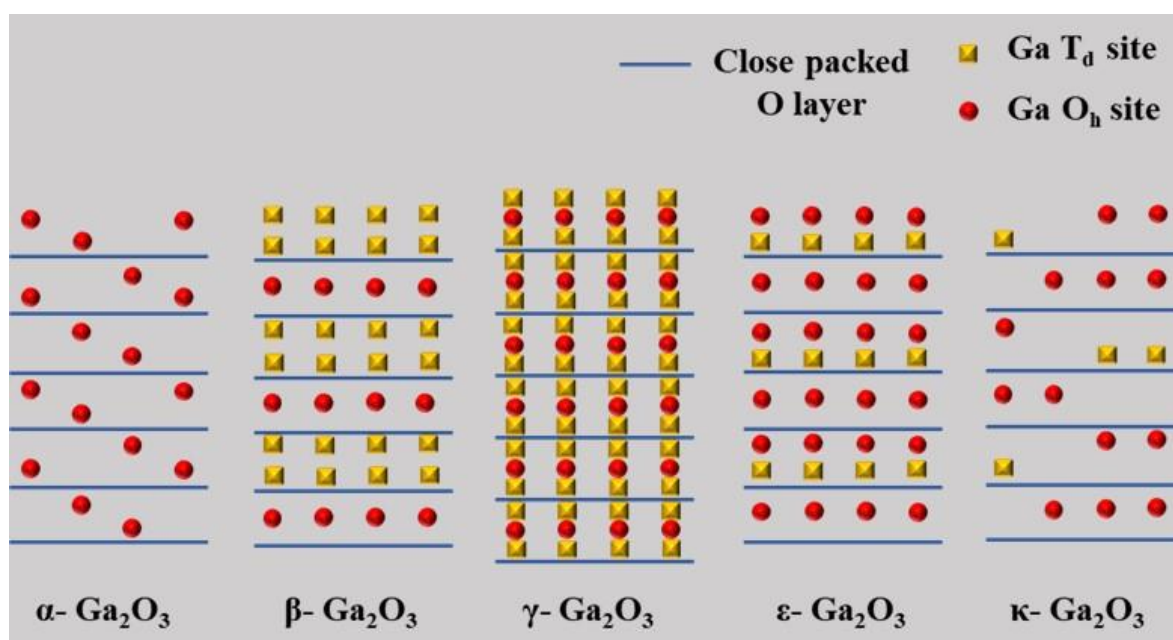
Figure 1. 3 Simplified stacking sequence of different phases of Ga_2O_3. β and γ phase Ga_2O_3 are formulated on a FCC- oxygen lattice, while others are relied on hcp- oxygen lattice. The oxygen layers may actually be distorted from[13]

Table 1.1: Gallium oxide polymorphs

Phase	Symmetry	Space group	Lattice constants	Data type
α	Rhombohedral	$R\bar{3}C$	a = 4.9825 Å c = 13.433 Å a = 5.059 Å c = 13.618 Å	Experimental[14] Calculated[15]
β	Monoclinic	$C\,2/m$	a = 12.214 Å b = 3.0371 Å c = 5.7981 Å β = 103.83° a = 12.27 Å b = 3.04 Å c = 5.80 Å β = 103.7°	Experimental[16] Calculated[17]
γ	Cubic (Spinal)	$Fd\bar{3}m$	a = 8.23760 Å	Experimental[13]
δ	Cubic (bixbyite)	$Ia\bar{3}$	a = 10.00 Å a = 9.401 Å	Experimental[18] Calculated[15]
ε	Hexagonal	$P6_3mc$	a = 2.9036 Å c = 9.2554 Å	Experimental[13]
	Orthorhombic	$Pna2_1$	a = 5.120 Å b = 8.792 Å c = 9.410 Å	Calculated[15]
κ	Orthorhombic (Transient)	$Pna2_1$	a = 5.0557 Å b = 8.68842 Å c = 9.27585 Å	Experimental[13]

1.3.1. The stable β phase:

As expected, β phase gallium oxide is the most studied Ga_2O_3 -polymorph, as it is the only one that retains its stability up to melting point. This high thermal-stability enables the production of high quality bulk-single-crystals and epitaxial films to be characterised extensively. The reported values of the primary physical properties are summarized in **Table 1.2**. However, even if this β-phase has been well studied concerning its metastable forms, the literature data exhibit several contradictions.

Table 1.2: Physical properties of β-Ga$_2$O$_3$

Property	Value	Reference
Crystal system	Monoclinic	[16], [19]
Space group	$C\,2/m$	[16], [19]
Molar mass	187.444 g/mol	[19]
Lattice parameters		
a	12.214(3) Å	[16]
b	3.0371(9) Å	[16]
c	5.7981(9) Å	[16]
β	103.83(2)°	[16]
Density	5.95 g/cm^3	[20]
Melting point	1740 ∘C	[18]
	1795 ∘C	[21]
	1820±20 ∘C	[22]
Dielectric constant	9.9−10.2	[23]
	13.9	[24]
Specific heat	0.56 J/g K	[25]
	0.49 J/g K	[20]
Band gap	4.85±0.1 eV	[25]
	4.7 eV	[26]
	4.9 eV	[27]
	4.4 eV	[23]
Electronic mobility	110–130 cm^2/V.s	[25]
Electronic effective mass	0.28 m$_e$	[25]

1.3.1.1. Crystal structure:

The most stable monoclinic β-Ga$_2$O$_3$ presents C 2⁄m symmetry having four adequate numbers of atoms present per unit crystallographic cell. The structure is characterised according to 4 lattice parameters, such as a, b, c, and β, first reported by Kohn et al.[28], while Geller[19] solved the structures. Initially, Wolten et al. reported that the material exhibited $P1$ space group[29]. Later a depth study with X-ray diffraction symmetry along with systematic extinctions, it was confirmed that β-gallium oxide belongs to the C-centred monoclinic lattice with $C2/m$ space group. Specifically, a more recent study by Åhman et al.[16] is repeatedly cited by other publications due to its superior precision, ten times better than respect to previous works. **Figure 1.4** represents unit cell of the β-gallium oxide lattice. Three inequivalent O-sites and two crystallographically inequivalent Ga-sites are the building blocks of the unit cell. For this

most stable crystalline form of gallium oxide, half of Ga^{3+} ions take up distorted tetrahedral, & another half occupy the octahedral sites. Whereas, the oxide ions are localized at $4i$ $(x, 0, z)$ positions and ordered in distorted cubic closed-packed array with gallium-oxygen bond lengths of 1.83 and 2.00 Å. So, this crystal structure is sketched in respect of GaO_6 octahedra and GaO_4 tetrahedra, occupied in proportion similarly to θ-Al_2O_3. Zigzag double chains of edge-sharing GaO_6 octahedra are linked by single chains of vertex-sharing GaO_4 tetrahedra along the **b** axis.
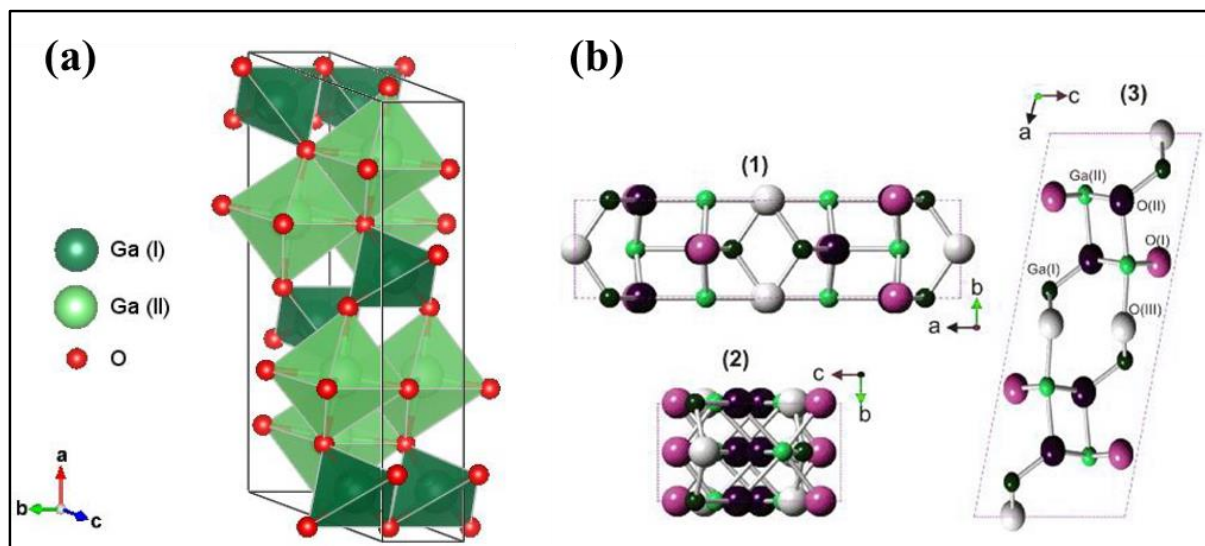
Figure 1. 4 (a) crystallographic unit cell of β-Ga₂O₃, highlighted several gallium coordination; (b) Projection along (1) c- (2) a- and (3) b-axis. Inequivalent gallium and oxygen sites are marked with different colours (from Janowitz et al.[25])

1.3.1.2. Electronic structure:

Numerous theoretical investigations have been performed to establish electronic structural framework of gallium oxide. The theoretical approaches are established on Density-functional-theory (DFT) with Local-density-approximation (LDA). Although this technique underestimates the absolute values (especially the band gap), it provides an excellent qualitative description[30, 31]. Besides, the hybrid functionals may give a more accurate picture associating a better agreement between theoretical and experimental results[17, 32, 33]. It is reported that β-Ga_2O_3 possess direct band gap ~4.87 eV (although the indirect energy gap shows a slightly smaller value ~4.83 eV). The delocalized Ga 4s derived states are the fundamental components to construct the conduction band (CB) contributing smaller electron-effective mass. In contrast, the filled up O $2p^6$ states exhibiting a little hybridization with Ga 3d, 4p, 4s orbitals[34] is responsible for valence band (VB) creation.

In case of β-phase gallium oxide, conduction-band-minima (CBM) is positioned at Γ-point of Brillouin Zone (BZ). But that does not maintain for the position of valence band maximum (VBM), indicating the indirect nature of corresponding energy band gap. Valence band is nearly flat and exhibits a minor dispersion. So, it is hard to obtain the actual position of absolute valance band maximum. He and team[17] reported the position of VBM is near about M point, which is almost degenerate with the one at Γ-point. From there, the computed band-gap for M-Γ indirect was 4.66 eV, and the same for Γ direct was 4.69 eV. Also, Varley et al.[33] identified the same type of quasi-degeneracy, resulting from only a little higher values of band gaps (4.83 eV for indirect & 4.87 eV for direct transitions) with valance band maximum just off the M-point. Besides, Peelaers et al.[32] found VBM on the line joining I and L points, that is on face of the Brillouin zone and calculated their band gap values, which were surprisingly similar to those obtained by Varley et al.[33], such as 4.84 eV (indirect transition) and 4.88 eV (direct transition), respectively.

However, experimentally the VBM issue was resolved by Janowitz et al.[25]. They used Angular Resolved Photoemission Spectroscopy (ARPES) to determine the fundamental gaps & electronic structures together with high-symmetry directions of Brillouin Zone. **Figure 1.5b** represents the detailed experimental band-structure plot which agrees well with the theoretical analysis. The indirect characteristics of the band gap was observed in this study, with a magnitude of 4.85 ± 0.1 eV, and also the VBM was positioned in the vicinity of the M point. Whereas, at the centre of Brillouin Zone, the direct band gap value ~ (4.9 ± 0.1) eV was found.

Further dipole-matrix element analysis predicted that the indirect transitions are weaker than the direct ones[33]. There is only a small difference in energy connecting direct and indirect band gap. It may lead to defining β-Ga_2O_3 as an "almost" direct-gap material, and Varley et al.[33] used the high optical gap (~ 4.9 eV)[27] value while evaluating absorption onsets (presented in **Figure 1.5a**). This interpretation, though relevant, does not consider the other effects, for example, absorption anisotropy, as will be elaborated in "optical properties" unit of β-Ga_2O_3.

Like the other band-related properties, the effective electron mass was calculated to be 0.27–0.28 m_e[32, 33]. Further, this small value and almost isotropic nature were confirmed experimentally[25]. Moreover, because of the flatness of valence band, whole effective-mass is expected to be larger and highly anisotropic. A large value of 40 m_e was roughly estimated

along the Γ–Z direction, while a significantly smaller hole effective mass of 0.40 m_e was obtained along the Γ–A direction[33].
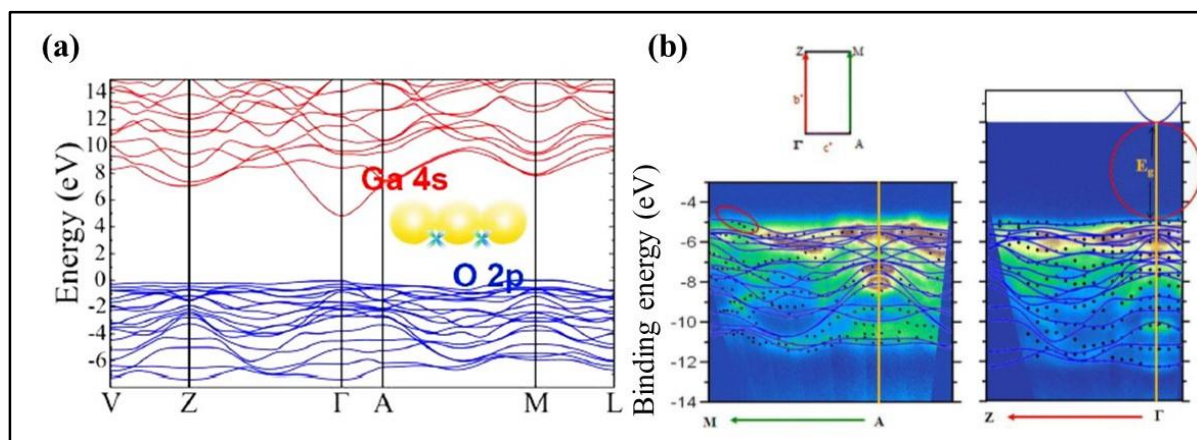
Figure 1. 5 (a) β-Ga₂O₃ band structure as computed by Varley et al.[33] The CBM is situated at Γ-point, while the VBM is near M-point. (The inset represents Ga 4s and O 2p orbital hybridization), (b) Experimental electronic band structure of β-Ga₂O₃ by Janowitz et al.[25]

1.3.1.3. Thermal Properties:

The thermal conductivity of β-Ga₂O₃ shows poor value; it is only half of the thermal conductivity value of aluminium oxide and one order of magnitude less than gallium nitride. Because of its structural anisotropy, the highest thermal conductivity is observed ahead [010] direction, whereas the lowest is along the [100] direction. Laser-flash methods[36, 37] or time domain thermoreflectance[35] can be employed to estimate thermal conductivity (k), and slightly different results were obtained due to additional analysis. A simple equation can fit the temperature (T) dependency of thermal conductivity (k) in the form:

$$k(T) = AT^{-m} \tag{1.3.1}$$

Where, exponent $m \approx 3.5$; in the range $80\,K \leq T \leq 200\,K$

And, ≈ 1.2 ; in the range $200\,K \leq T \leq 495\,K$

Further, at a low temperature, the phonon scattering and free electron scattering present a crucial factor in heat conduction process, leading to the deviation of thermal conductivity from typical $T^{-3/2}$ dependence. Víllora and team[36] studied the thermal expansion coefficient of the lattice constants of β-Ga₂O₃ within temperature range between 5–293 K. It can be observed that thermal expansion coefficients are almost equivalent for *b* and *c*, approximately twice that of *a*. Also, Ricerca et al. studied the nature of the thermal expansion coefficients at higher temperatures (300–700 K).

1.3.1.4. Optical properties:

Pure β-Ga$_2$O$_3$ crystals are colourless because of their large band gap (~ 4.8 eV) as well as display huge transparency through the ultraviolet region of electromagnetic spectrum. However, defects or incorporation of impurities may cause crystals colouration, which successively provides a first indication of the material conductivity[37, 38]. The variation of transmittance spectra of β-Ga$_2$O$_3$ crystals for different carrier concentrations is presented in **Figure 1.6.** Insulating β-Ga$_2$O$_3$ becomes colourless because of their steep absorption edge, nearly around 255–260 nm and sometimes appears light-yellowish due to a little absorption at blue region of visible-frequency band. However, the n-type semiconducting crystals exhibit an increased free-carrier absorption in red and near infrared regions of the electromagnetic spectrum, resulting in a bluish colouration. Also, a greyish colouration can be visualized in presence of carbon impurities in the final product.
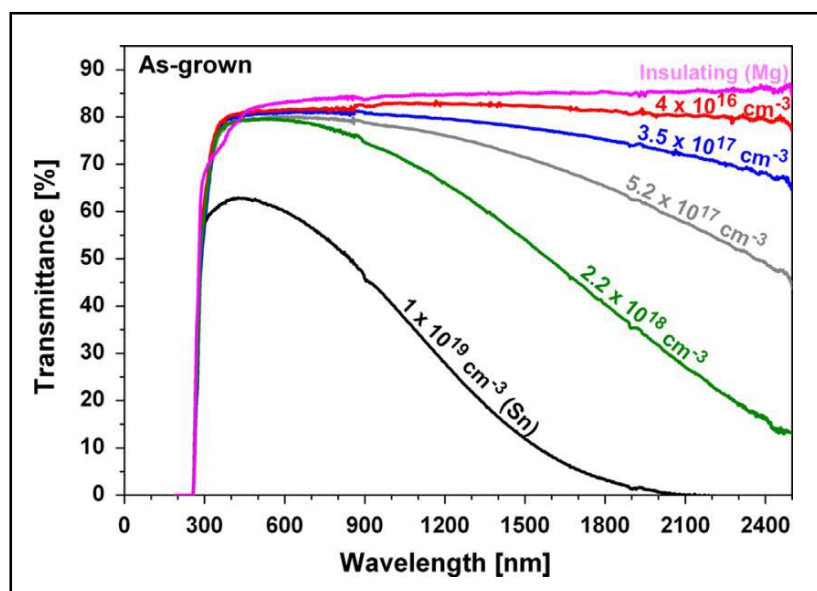
Figure 1. 6 Transmittance spectra of β-Ga$_2$O$_3$ single crystals with various free electron concentrations. (From Galazka et al.[38])

Wide band gap nature of β-Ga$_2$O$_3$ supports it to become a potential candidate for UV photonic applications. Also, it shows superior conduction properties because of a shallow donor band associated with oxygen vacancies. Also, at ambient temperature, its appreciable exciton-binding energy (~270 meV) drives it favourable for high emission. In case of β-Ga$_2$O$_3$, room temperature exciton-binding energy becomes higher than thermal energy. Therefore, it can readily constitute a stable electron-hole pair, becoming a potential luminescent material. Photoluminescence spectroscopy is non-destructive and contactless methodology that not only

probes the electronic structure of material but also depicts the usage possibility of that material in optoelectronic devices. Room temperature photoluminescence spectra of β-Ga$_2$O$_3$ comprise a broadband emission in ultra-violet and visible (covers blue and green regions) range of the electromagnetic spectrum[39-41]. That broad emission band can be categorised at least into two emission bands: one is near 3.2-3.6 eV (near-UV region), and the other is near 2.8-3.0 eV (blue region) [42-44]. The familiar UV emission does not depend on sample preparation or impurity incorporation and can be assigned as radiative recombination between free electrons and self-trapped holes[41, 44]. So, acceptors and donors are probably associated in this blue emission process[40, 44]. A possible mechanism would be a rate-determining transfer by tunnel effect of an electron from a donor cluster to a hole trapped at an acceptor site. Consecutively, in acceptor site faster recombination of electron-hole pair takes place involving a strong electron-phonon coupling, which produces a blue emission[44]. An additional green emission band is observed in doped β-Ga$_2$O$_3$ crystals and is probably associated with self-trapped or bound excitons. Typical impurities giving green luminescence are Be, Ge, Sn, and Li, while Fe and Cu act as killers for the blue emission[41].

To visualize the vibrational properties of β-Ga$_2$O$_3$, using group theory at $k = 0$ a total 30 number of normal modes can be predicted while considering space group $C2/m$ and 10 atoms per unit cell:

$$\Gamma_{vib} = 10A_g + 5B_g + 5A_u + 10B_u \qquad (1.3.2)$$

Among them the number of optically active Raman modes (A_g and B_g) are 15 and infrared modes (A_u and B_u) are 12 whereas there are 3 acoustic modes ($1A_u + 2B_u$) [45-47]. In addition, a detailed investigation of the vibrational characteristics of β-Ga$_2$O$_3$ was conducted by Dohy and team[45], which resulted in a complete assignment of the wavenumbers for all modes based on their symmetry for the first time (**Table 1.3**).

Specifically, depending on the individual polarisation of incident and analysed light, two types of Raman modes can be obtained, from where it may be confirmed that β-Ga$_2$O$_3$ belongs to $C2/m$ space group[45]. The modes, lower than 200 cm^{-1}, can be assigned to "liberation and translation of the doubly linked straight chains of GaO$_6$ edge-shared octahedra running along the b-axis of the crystal". Also, the modes within the range 318–415 cm^{-1}, can be considered to the GaO$_6$ octahedral deformation. Further, the Raman modes found higher than 600 cm^{-1} would depict the bending mode and stretching mode of GaO$_4$ tetrahedra.

Table 1.3: Optical vibrational modes of β-Ga₂O₃ (From Dohy *et al.*[45])

Raman		Infrared	
Mode	**Wavenumber (cm⁻¹)**	**Mode**	**Wavenumber (cm⁻¹)**
A_g	763	B_u	770
A_g	657	B_u	720
B_g	651	A_u	668
A_g	628	B_u	640
A_g	475	B_u	525
B_g	475	A_u	455
A_g	415	B_u	375
B_g	353	A_u	352
A_g	346	B_u	310
A_g	318	B_u	290
A_g	199	A_u	250
A_g	169	B_u	155
B_g	147		
B_g	114		
A_g	111		

1.3.1.5. Electrical properties:

Intrinsically, gallium oxide can be treated as an insulating material because of its wide band gap. However, Ga_2O_3 generally shows n-type conductivity even when it is not intentionally doped. The occurrence of oxygen vacancies may be the prime cause of this n-type semiconducting behaviour, where the former could be easily ionised to form active donors. Also, an active interaction exists within the high conductivity of beta gallium oxide and the oxygen partial pressure in growth environment. For example, simply by lowering the amount of oxygen in growth atmosphere during the floating zone process, the conductivity values in the range of 10^{-9}–38 $\Omega^{-1}cm^{-1}$ were found[26]. A similar trend was displayed in Czochralski growth under a CO_2 atmosphere, whose partial pressure was used to control the conductivity of the grown material[37]. Once again, the latter decreased when CO_2 partial pressure was increased, while the colour of the ingots deviated from blue, associated with free carrier absorption, to transparent.

However, few recent theoretical studies on various types of impurities in β-Ga$_2$O$_3$ recommend that the oxygen vacancies possess very high activation energy which significantly affect the carrier concentration, thus acting as deep donors and not contributing to electrical conductivity[33, 48]. Indeed, some reports attribute the n-type behaviour of unintentionally doped gallium oxide samples to the presence of hydrogen[33]. Moreover, it was recently demonstrated that commercially available gallium oxide powders could be effectively considered Si-doped[36]. This would be an additional possible cause of the often-observed high electrical conductivity, thus further proving that oxygen vacancies would have no sizeable effect on the phenomenon.

As for electron mobility μ_e, it is usually reported to fluctuate around 100 cm^2/Vs at room temperature, with a decreasing trend when free carrier concentration increases. Therefore, within n = 10^{15}–10^{16} cm^{-3}, it is the usual range exploited for drift-layer of vertical-power-devices, a value of $\mu_e \sim$ 300 cm^2/V.s was extrapolated[49].

1.3.2. Metastable α Phase

In 1928, Zachariasen et al.[50] were the first who reports α phase Ga$_2$O$_3$. It may be considered the first metastable polymorph explicitly characterised from the structural point of view[14]. It possess rhombohedral crystal symmetry with $R\overline{3}c$ space group, and this classic corundum structure becomes analogous to α-Al$_2$O$_3$. α-Ga$_2$O$_3$ possess 2 individual lattice-parameters, a and c, and two internal coordinate-variables, z_{Ga} and x_O. Six Ga$_2$O$_3$ formula units are required to compose its crystallographic cell (**Figure 1.7a**). The structure is constructed as the hexagonal close-packing of oxygen ions, where Ga-ions take up two-third of the octahedral places. Each Ga-octahedron, moderately distorted, collaborates one face and three edges with three other octahedra.

This polymorph is to be prepared by calcining gallium oxide hydroxide GaO(OH) in open air within temperature range 450 °C to 550 °C, while it converts into beta phase upon annealing at 650 °C, at atmospheric pressure[13, 18]. However, in high pressure beta may be converted to alpha because of the higher density of alpha (6.273 g/cm^3)[17]. To study β to α phase transition of crystalline gallium oxide powder sample under pressure, Raman spectroscopic analysis was recently employed. From the result seven Raman active modes were found ($\Gamma_{Raman} = 2A_{1g} + 5E_g$) reported by Machon et al.[46]

Along with the confirmation of experimental crystal structure, theoretical modeling can also be employed to examine some additional physical properties[17]. In search of the electronic

structure, a wide indirect energy gap ~5.03 eV & comparatively lower effective mass ~0.276 m_e were found. Moreover, superior symmetry of electronic band structure may forces to display high-level valance band degeneracy, which has been reflected in **Figure 1.7b**.
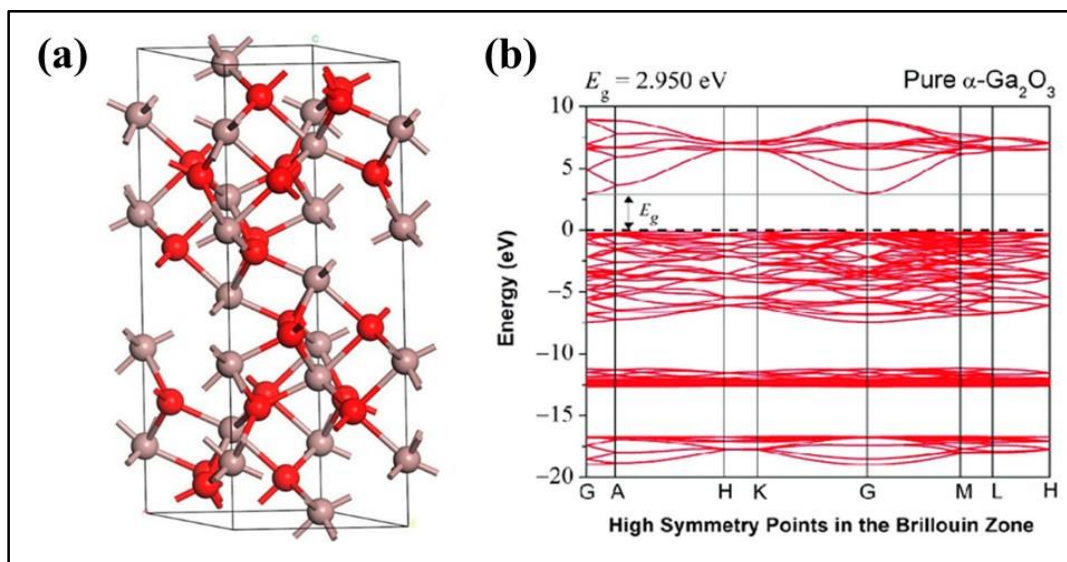
Figure 1. 7 Unit cell (a) and energy band structure diagram (b) of α-Ga₂O₃ (Mondal et al.)[50]

As for optical properties, dielectric constant values of 3.07 in basal-plane and 2.97 along the *c*-axis were extrapolated from the calculated dielectric function. Despite the anisotropy become more pronounced than β-gallium oxide, no anisotropy in optical absorption edge was observed. Hence, the first-principal calculations suggest α-Ga₂O₃ to have a larger bulk modulus, refractive index, Debye temperature and reflectance of β-Ga₂O₃.

1.4.   Applications for environmental remedy:

In the past centuries, the industrial revolution conducted a massive change in human life which became the prime cause of the development of the world. However, these developments have intercalated industrial pollution and, for this developed world, pollution is the most significant environmental challenge nowadays. The growing countries are becoming more advanced with better technology and commercial enrichment. Still, on contrary, the world is becoming more contaminated and losing its natural resources, which results in ill health, death, disabilities and off-course a potential impact of climate change. So, scientists, world leaders, and environmentalists are very concerned and working rigorously to keep the earth green and sustainable by following safe, harmless procedures with green technologies[51, 52].

For living bodies' environmental remediation is one of the most desired requirements. With the rapidly rising equipment-based advancement in industrial areas, human life faces an enhancing threat of toxic, hazardous infection by means of consumable water. Many dyes are regularly produced and utilized in several industries like textile, leather, paper, cosmetic, pharmaceutical, nutrition etc. For example, more than 100,000 textile dyes and textile-colourless disinfection agents, like phenol, can cause severe health hazards in both water-dissolved, solid and vapour form[53, 54]. Removal of such wastes from the water was long ago recognized as an alarming challenge as the drawbacks of some conventional methods like activated carbon adsorption, solvent extraction and common chemical oxidation were revealed in the form of high cost or generation of hazardous by-products[55]. Therefore, the search for cleaner, safer and environment-friendly water purification technologies continues. However, significant advancement has been achieved with the development of metal oxide nanoparticles as adsorbents and photocatalysts (such as TiO_2, ZnO, and WO_3) under appropriate (UV or visible) irradiation[56, 57]. Adsorption and catalysis methods are very attractive as it is cost-effective, highly efficient, reusable and eco-friendly process which leads to the complete degradation of hazardous pollutants.

1.4.1. Effect of textile dyes on health and environment:

Dye is commonly employed to impart colour on textiles, papers, leathers, and other different materials. The resulted colour of that materials is not easily affected by the exposure of light, heat, washing, or any other factors. The differences between dyes and pigments are: (i) Dyes are usually organic compounds, on-the-other-hand pigments are inorganic or organic by nature. (ii) Dyes are soluble in the host material- typically water but the pigments form a dispersion of finely crushed solids in host liquid, for example paint or ink, or blended with other materials. (iii) Dyes cannot scatter light and look transparent, whereas pigments can scatter light and thus, generally give brighter colours. Different dyes, including synthetic dye, azo dye, acid dye, mordant dye, pigment dye etc. are extensively applied in textiles[58]. **Figure 1.8** represents the impact of dyes on water.

Dyes can originate countless problems in environment. Some of them are given below:

(a) The colours of textile dyes not only generates the aesthetic damage to the water bodies but also encounters the penetration of sunlight into the water by absorption and reflection, which results in the decrement of photosynthesis rate as well as dissolved oxygen level. Due to this, the entire aquatic biotas get affected.

(b)   Dyes are toxic, carcinogenic and mutagenic agents. Based on their exposure time and concentration, they may seriously damage the food chain, and also it may affects severely the exposed organisms. Exposure to azo dyes (example: Methyl orange) is very harmful to soil microbial communities and the growth of plants.

(c) A little amount of dyes in water (< 1 ppm) are highly visible because of their radiance.

(d)   In environment, dyes can retain for a longer time because of high photo and thermal stability. Such as, at 25 °C the dye hydrolysed-reactive-blue 19 possess its half-life approximately equal to 46 years with pH ~7.

(e) The reported primary cancers including dye workers' kidneys, liver and urinary bladder. Also, dyes can cause different kinds of respiratory diseases, skin irritation, allergic reactions in eyes, and irritation to the upper respiratory tract and mucous membrane.
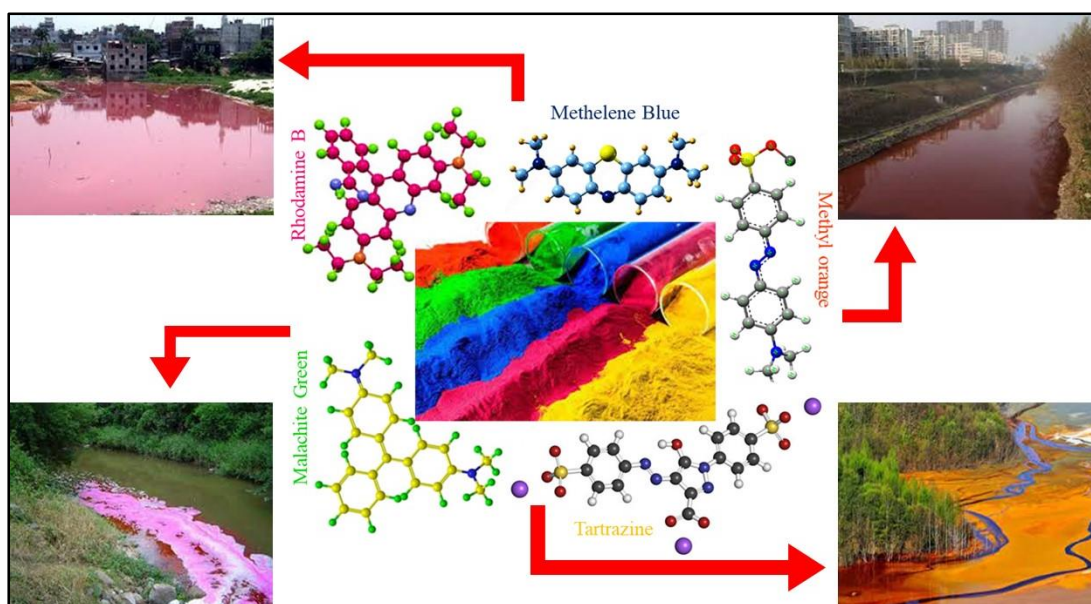
Figure 1. 8 Different kinds of dyes and their impact on water

1.4.2. Different dye removal techniques: Photocatalysis

There are different famous technologies involved in the removal of dyes from wastewater. The methods are filtration, coagulation, adsorption, catalysis etc. Three different types of filtration methods, such as nanofiltration, ultrafiltration, reverse osmosis etc.[59, 60] can be employed to eliminate the chemical contaminants from wastewater. This process is applied to filter and recycle the pigmented industrial wastewater and mercerize and bleach it. Different filtration methods can be carried out depending on specific pollutants and temperature of the wastewater.

Among them, the membrane technology is efficient for dye removal[61, 62]. However, a lot of limitations are there to utilizing this method, such as its expenses, requirement of frequent membrane fouling, the necessity of various pre-treatments based on the type of polluted water, and also the construction of focused dye-bath undergoes a suitable remedy before its safe disposal to the environment[63, 64].

The coagulation process is widely used worldwide to disinfect waste water[65, 66]. This method follows three more steps such as flocculation, sedimentation and disinfection. There are several kinds of a coagulant, such as synthetic polymer, inorganic coagulant, and biological coagulant[66, 67]. Although it is a low-cost process, the sludge-generation and ineffective-decolonization of several soluble dyes are its major limitations[68].

The dye-affinity of the adsorbents is the key factor in the dye-removal adsorption process, followed by decolonization. In addition, various physical as well as chemical aspects like interactions between dye & adsorbent, surface area and particle size of the adsorbents, contact time, pH, temperature etc., play a vital role in this method[69]. For adsorption purpose, activated carbon method is the most effective and most used process[70]. Limitations of this technology are the high maintenance costs, environmental-friendly ejection of used adsorbents, and wastewater pre-treatment to reduce the suspended solids.

The working principle of a catalyst is to participate in a reaction and then lower the reaction's activation energy and regenerate at the end of the reaction. A photocatalyst has all of these properties in the presence of light which can be of different frequencies (mainly the visible and UV lights are of interest). Therefore, the photocatalytic reaction mechanisms are widely studied. During the photocatalytic process, the system is excited by appropriate irradiation, which promotes the production of a lot of photo-induced electron-hole pairs (e^-/h^+), and they are separated for a longer time when a wide-band-gap semiconductor is considered as a photocatalyst.

These electron-hole pairs (e^-/h^+) may react with the chemical species like H_2O, hydroxyl ions (OH^-), and surface-adsorbed O_2 to produce superoxide-radicals ($\bullet O_2^-$), hydroxide radicals ($\bullet OH$) and H_2O_2 which efficiently decompose the organic pollutants adsorbed at the catalyst-surface. If the valence band (h^+) potential of catalyst molecule is positive enough with respect to the reduction potential of ($OH/\bullet OH$) and ($H_2O/\bullet OH$) then it may promote oxidation response of H_2O/OH to $\bullet OH$ by supplying photo-generated holes. Similarly, if conduction band (e^-) potential becomes less positive than redox potential of (O_2/H_2O_2) and ($O_2/\bullet O_2^-$),

then the electron rich conduction band can trigger the formation of hydrogen per oxide and superoxide radicals from molecular oxygen as shown in the following equations,

$$Photoexcitation: \ Photocatalyst \ (such \ as: Ga_2O_3) \rightarrow h^+ + e^-$$

$$O_2 + \ e^- \rightarrow \bullet O_2^-$$

$$H_2O + h^+ \rightarrow H^+ + \bullet \ OH$$

$$\bullet \ O_2^- + 2H^+ + e^- \rightarrow H_2O_2$$

$$H_2O_2 + e^- \rightarrow \bullet \ OH + OH^-$$

$$OH^- + h^+ \rightarrow \bullet \ OH$$

$$Reactive \ species \ (\bullet \ OH, \bullet \ O_2^-, h^+) + Organic \ pollutants (RhB, MO)$$

$$\rightarrow Degraded \ products$$
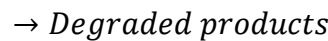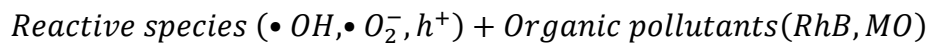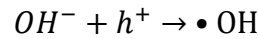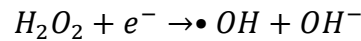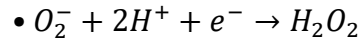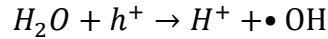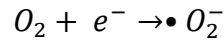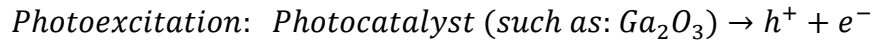
Both the reduction and oxidation may encounter at the nanostructured catalyst surface (**Figure 1.9**). The surface adsorbed oxygen helps to scavenge the electrons to form superoxide-radicals, which boosts the formation of hydroperoxyl radical followed by hydrogen peroxide and this process slows down the recombination between electrons and holes.

➢ **Degradation kinetics**:

The degradation rate constant, r, con be determined by Langmuir– Hinshelwood (L–H) model[53]

$$r = -\frac{dC}{dt} = \frac{k_r k_a C}{1 + k_a C + k_w C_w + \sum_{i=1}^{n} k_i C_i} \tag{1.4.1}$$

Where, r is the degradation rate of the reaction, k_r is the specific rate constant for the oxidation of the dye-molecule, k_a is the adsorption constant of the dye in equilibrium, C represents the dye concentration, k_w is the solvent adsorption constant in equilibrium, C_w is the solvent concentration, k_i is the equilibrium adsorption constant of product, C_i is the concentration of the product. As the sole contribution of the actual catalysis process should consider after achieving the adsorption-desorption equilibrium, we can write,

$\sum_{i=1}^{n} k_i C_i = 0 \ and \ k_w C_w = 0$. Now the above equation can be modified as,

$$\frac{1}{r} = \frac{1}{k_r} + \frac{1}{k_r k_a C} \tag{1.4.2}$$

By integrating eq. (1.1), we get

$$t = \frac{C_0 - C}{k_r} + [\ln(C_0/C)] \left[\frac{1 + k_a C + k_w C_w + \sum_{i=1}^{n} k_i C_i}{k_r k_a} \right] \tag{1.4.3}$$

Now applying $\sum_{i=1}^{n} k_i C_i = 0 \ and \ k_w C_w = 0$ in the above equation, we get

$$t = \frac{C_0 - C}{k_r} + [\ln (C_0/C)] \left[\frac{1 + k_a C}{k_r k_a}\right]$$

$$\text{Or, } \ln\frac{C_0}{C} + k_a(C_0 - C) = k_a k_r t \qquad (1.4.4)$$

When, the dye concentration is low i.e. C_0 is small ($k_a C \ll 1$), it represents first-order reaction having a constant coefficient rate,

$$\ln (C_0/C) = k_a k_r t = k_{app} t$$

$$\text{Or, } \ln(C_0 - C) = k_{app} t \qquad (1.4.5)$$
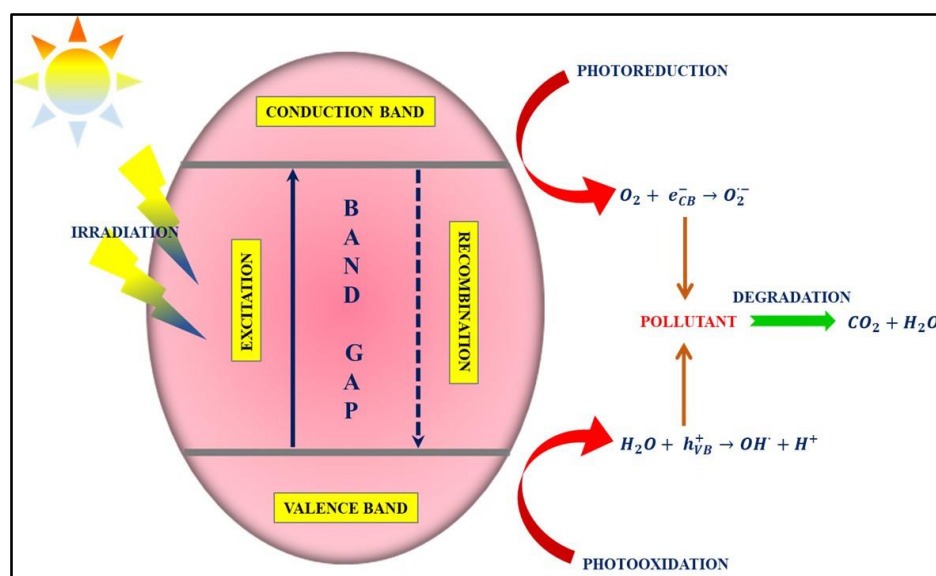
Figure 1. 9 Schematic representation of photocatalytic degradation mechanism

➢ Advantage of nanostructured Ga₂O₃ as photocatalyst:

Nowadays, it is evident that the materials in the nano regime are the prime focus of the researchers as compared to the bulk. Several remarkable advantages of these nanomaterials are their high surface area-to-volume proportion, enriched physical properties such as melting point or hardness, and alterable electronic properties. The pronounced surface area of these nanomaterials can provide many active sites either for storage or reaction. Also, the formation of nanostructure hinders the further bending of the particles, resulting in an enhanced hardness of the nanoparticles compared to that of bulk. Additionally, some other physical properties, such as malleability, brittleness, ductility, toughness etc., of the materials can be modified with an incremental hardness variation. Occasionally, the further decrement of particle dimension (less than 10 nm) may result in quantum-confinement effect, increasing the band gap of that materials, thereby enhancing the charge separation between the valance and conduction band.

Moreover, nanomaterials with different morphologies like tubes, rods, sheets, flakes, flowers, spheres, and many more can be efficiently synthesized by only changing the synthesis-conditions, and the characteristics of that particular morphology may vary accordingly. At room temperature, the wide band gap of gallium oxide (~4.9 eV) makes it a promising candidate for photocatalytic applications due to superior charge-separation ability for a longer time and high mobility of the photogenerated electrons. Also, the metal oxides exhibiting d^{10} configurations (In^{3+}, Ge^{4+}, Ga^{3+}, Sb^{5+}, Sn^{4+}) draw attention as the hybridization between s and p orbital of metals in the conduction band helps to increase the photogenerated electron's mobility, which in turn produces superior photocatalytic performance. On the other hand, being an n-type semiconductor, β-Ga_2O_3 carries shallow donor negative oxygen vacancies with ionization energy ~30–40 meV. Those oxygen vacancies are highly accountable for conduction, luminescence, and photocatalytic properties in the β-Ga_2O_3. The photocatalytic property of gallium oxide is utilized to transform solar energy into chemical energy by oxidation/reduction processes to remove bacteria and/or pollutants on wall surfaces in air or water and sometimes to get useful materials, like hydrogen and hydrocarbons.

1.5. Field emission Applications

Nanoscale field emission (or electron field emission) dependent electron sources have now became a prime target of attention because of their implementations in dynamic CT (computerized tomography) scanners, flat panel displays, vacuum microelectronic devices, X-ray sources, high-intensity luminescent tubes, infrared imaging devices etc.[70-75]. CNTs (Carbon nanotubes) have already convinced their excellence as a promising field-emitter for their little tip radius-curvature and capability to generate substantial emission current-density at comparatively smaller operating voltage. However, CNTs suffer considerable challenges which hampers their practical uses. Such as, CNTs are highly affected by residual oxygen present in the vacuum-chamber which basically oxidize and degrade them very fast. Whereas the natural oxides like ZnO, TiO_2, CuO, Ga_2O_3 etc. are not influenced by oxygen. Additionally good chemical and thermal stabilities along with low electron affinity plays a crucial role to produce large emission current at low applied field. In contrast, issues like field-emission current-density & field-enhancement depend on various factors including the radii and length of the nano-emitters, density, inter-tip distance, the tip-cone angle, and geometry of the nanostructure, etc[76-77].

The Ga_2O_3 nanostructure has already presented its immense promise as a field emitter among its numerous application windows. Field emission is an electrical property of a material that can be treated as electric field-assisted electron emission on which the present study is focused. Thus it is very much essential to understand the basic field emission mechanism. Furthermore, an in-depth discussion on work function and various electronic emission processes from the metal surfaces is reasonably necessary to reinforce a conceptual foundation on this subject.

The minimal energy needed to free an electron from a solid surface into an immediate outside-point is known as the material's work function. Also it is considered as the amount of energy required to tear out an electron into vacuum from Fermi-level. It is not the property of bulk material but a surface characteristic of the materials. Generally, it is measured in electron volts. So, to escape from the metal, the electron has to defeat the potential-energy barrier at material surface. Various external energy sources like heat, light, electricity etc., may help overcome the energy accumulation barrier. Based on the nature of the external energy, electron emission, i.e. discharge of the loosely bound electrons from the surface of a material, can be divided into four categories: (a) secondary electron emission, (b) thermionic emission, (c) photovoltaic emission and (d) field emission[78-79].

(a) Secondary electron emission:

Secondary electron emission is a phenomenon where fast-moving primary electrons with sufficient energy may collide on a surface or pass through some material resulting in the emission of secondary electrons.

(b) Thermionic emission:

Whereas in thermionic emission, heat helps the electron gain additional kinetic energy, resulting in electrons escaping from the metal surface. The necessity of heating elements is the obvious disadvantage of thermionic devices. Additionally, excessive heating of the material limits its lifetime.

(c) Photovoltaic emission:

The Photovoltaic emission takes place when a material is started to interact with photons i.e. a beam of light. Also this emission is highly dependent on the intensity of light source.

(d) Field emission:

The phenomenon of E- field-aided electron emission from the condensed phase (usually metal or semiconductor) surface into other phase (vacuum) is commonly known as field emission (FE). It has certain benefits over other emission processes, like being comparatively inconsiderate to temperature variations, ionizing radiation etc. In addition, a very high electron

emission-efficiency association relative to others has made this emission procedure very significant for current device applications. Before the discussion on field emission, realizing Schottky emission is essential, as it will help to understand the field emission mechanism. Schottky emission is a field-induced thermionic emission in which, besides sweeping the accumulated electrons, the applied field also reduces the barrier height. Electrons residing at 'x' distance outside the conducting surface due to polarization experience an electrostatic force. The distance 'x' is chosen in such a way that the surface of the conductor can be considered to be smooth. Using the method of image potential, this force can be expressed as[80]:

$$F_{image} = -\frac{e^2}{4x^2} \qquad (1.4.6)$$

And the corresponding potential energy can be expressed as:

$$V_{image} = -\frac{e^2}{4x} \qquad (1.4.7)$$

This potential is appeared to diverge at $x = 0$. However at $x = 0$ the assumption of a perfectly smooth surface does not hold. In Schottky emission we assume a constant potential which actually spreads over a very small distance of few angstroms. Now, under the application of E-field of strength ξ, the electron felt a potential of $-e\xi x$. So the total potential within which the electron is moved will be[80]:

$$V_{total} = -\frac{e^2}{4x} + e\xi x \qquad (1.4.8)$$

Considering the distance of x_m at which the value of total potential will be highest we can write:

$$x_m = \frac{1}{2}\left(\frac{e}{\xi}\right)^{1/2} \qquad (1.4.9)$$

Where
$$V_m = -e(e\xi)^{1/2} \qquad (1.4.10)$$

So the modified value of work function will be:

$$\phi_{red} = \phi - e(e\xi)^{1/2} \qquad (1.4.11)$$

Now if an electron can reach to x_m, it can escape from the surface barrier and contribute to emission current which can be given as:

$$J = AT^2 \exp\left[-\left(\frac{\phi - e(e\xi)^{1/2}}{K_B T}\right)\right] \qquad (1.4.12)$$

Equation (1.10) is known as Schottky equation[81].

The entire state of affairs is depicted in **Figure 1.10**. It should be mentioned that though the force does not influence barrier height determination, the step potential is rounded at the surface, which signifies the initiation of the Schottky lowering effect. For the electric field value lower than~10^8 V/m, the equation (1.4.12) is fairly accurate; however, for higher field strength (greater than 10^8 V/m), Fowler-Nordheim (F-N) tunnelling becomes the main source of electron emission, which is entirely different from Schottky emission. Schottky emission involves barrier crossing over of the electron where the cold emission occurs due to the barrier tunnelling of electrons. Going beyond the necessity of any thermal heating, with reduced barrier height, the electron owing to their wave nature can easily tunnel through where the tunnelling process is commonly dubbed as field emission and sometimes as cold cathode emission. The applied electric field reduces the barrier height by distorting the potential energy barrier between emitter and vacuum, further promoting quantum mechanical electron tunnelling. R. W. Wood first reported this barrier deformation phenomenon in 1897[82]. If an E-field of strength 'E' is implied to an electron of charge 'e', then the potential energy of the electron will be $-eEx$. For visualization, a schematic of cold emission is presented in **Figure 1.10**, where the line AB denotes the potential. In the figure, the value of d should be less than 10 Å so that electrons at the close vicinity of the Fermi-level may tunnel across the barrier. More electrons tunnel through the barrier for higher field strength & generate emission current. Several research groups have paid a considerable amount of effort to the development of a formula that can relate emitted current and the applied field; however, the most accepted form was given by Fowler and Nordheim[83-86] which can be written as:

$$I = CV^k \exp\left(-\frac{B}{V}\right) \qquad (1.4.13)$$

Where, B, C and k are constants. Considering k=0 as suggested by Millikan and Lauritsen, and then the plot between $\ln I$ and $1/V$ becomes a straight line[83]. Abbott and Hendersen proposed the value of k=4 which provides the best straight-line nature of current versus voltage plot in a log scale[87].

However Fowler and Nordheim have suggested the value of K=2 which is mostly accepted. Fowler and Nordheim first proposed the quantum mechanical tunnelling model for field-emission from a metallic surface in 1928. The Fowler- Nordheim theory is based on the following assumptions:

(i) Metal possess free-electron band structure

(ii) Temperature is taken as 0K

(iii) Electrons are fermions and they follow the Fermi-Dirac statistics

(iv)The surface from where emission takes place is assumed to be planar where irregularities of atomic dimensions are neglected

(v) Classical image potential is taken into account

(vi)The value of work-function is constant throughout the sample
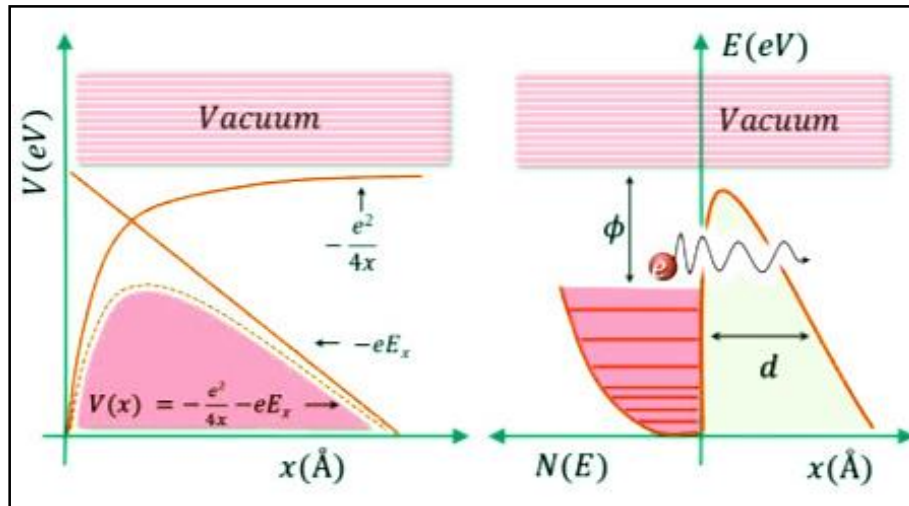
Figure 1.10 Potential bending because of the application of external electric field; (b) Schematic of field electron emission

Under this consideration current density can be written as:

$$J = e \int_0^\infty n E_x D(E_x, F) dE_x \qquad (1.4.14)$$

Where e is an electronic-charge, $n(E_x)$ is the number of electrons/second with energy between E_x and $E_x + dE_x$ incident on unit area of the barrier surface from inside. D is the tunnelling probability of electrons. D is also known as barrier transparency and can be written as:

$$D(E_x, F) = \exp\left[-\frac{8\pi(2m)^{1/2}}{3eh}\right] \frac{E_x^{3/2}}{F} V(y) \qquad (1.4.15)$$

In equation (1.4.15) the term $V(y)$ is known as Nordheim function.

After proper approximation and calculation the final expression of Fowler Nordheim (F-N) equation is obtained as

$$I = \frac{A\alpha F^2}{\phi} \exp\left(\frac{-b\phi^{3/2}}{f}\right) \qquad (1.4.16)$$

Where a=1.54 x 10^{-6} A eVV^{-2} and b = 6.83 x 10^7 eV$^{-3/2}$ Vcm^{-1} are Fowler-Nordheim constants. A represents the emission area. Sommerfield and Bethe[88] have developed an extension of F-N equation to include the effect of local electric field, which is different from macroscopic field. Thus they include the field enhancement factor. According to this consideration current-density (J) is written down as follows:

$$J = \frac{A\beta^2 E^2}{\phi} \exp\left(\frac{-b\phi^{3/2}}{\beta E}\right) \qquad (1.4.17)$$

Here E represents the electric-field & ϕ becomes the work-function of the material. For Ga$_2$O$_3$, ϕ= 4.9 eV. β represents the field-enhancement factor. It measures the capability of the emitting sites to amplify the E-field. 'A' and 'B' are the same values with the **a** and **b** in the equation 1.4.17. The value of field-enhancement factor is obtained from the slope of ln (J/E^2) vs. 1/E curve. Field-enhancement factor depends on various parameters including morphological geometry, conductivity, work function etc.

1.6. Aims and objectives

Nowadays, nanoscience and nanotechnology have been identified as one key technology. There has been a faster growth in research and advancement of nanoscience and nanotechnology worldwide during recent years. The development of suitable materials with accurate control over their growth and morphology is the key to exploiting the huge potential of this technology.

Gallium oxide (Ga$_2$O$_3$) is a very important group III metal-oxide-semiconductor with unique optical, electrical, physical and chemical properties and has been extensively studied. This material also has applications in several key areas like sensors, catalysts, lithium-ion batteries, photovoltaic cells, dye-sensitized solar cells, etc. There are ample scopes for developing and understanding this technologically important material, particularly its low-dimensional form.

Specifically, the objectives of the thesis are the following:

❖ Synthesis of novel kind of Ga$_2$O$_3$ nanostructures through some suitable, cost-effective, environmental-friendly route for some specific applications. Optimization and understanding of the growth process for obtaining porosity-tailored Ga$_2$O$_3$ nanostructures. Also, synthesis of some Ga$_2$O$_3$-based composite materials, which may be two-dimensional growths above the host material or hybridization with any other oxide materials.

❖ Detail structural, morphological, optical and electrical characterizations of synthesized nanostructures through a number of advanced characterization techniques.

❖ Ga_2O_3 is well-known wide band gap UV-transparent photocatalyst material and has been utilised for the same for decades. In this thesis, we have explored the adsorption capability and the dye selective photocatalytic degradation property of Ga_2O_3, which can be varied just by altering some synthesis parameters like calcination temperature, precursor material etc.

❖ It is one of the aims of the thesis to enhance the photocatalysis performance of the Ga_2O_3 nanostructures, and it was possible by incorporating some novel ideas like the fabrication of type II p-n heterojunction with other oxide materials. The built–in the electric field caused due to junction formation helps to separate photogenerated electron-hole pairs for a longer time. Hindrance of electron-hole pair recombination boosts the photocatalytic performance of the as-synthesized material.

Also, we would like to investigate the photocatalytic removal of the pollutants via visible excitation with Ga_2O_3 as a catalyst in alternative ways. Exciting the pollutant via visible irradiation may be a remarkable idea. An entire new field of dye-sensitized photocatalysis has flourished based on this idea.

❖ Purpose-built synthesis of Ga_2O_3 nanostructures for some exotic application like field electron emission. Understanding and optimisation of the electron emission process for such nanostructures. Investigation of the enhanced field emission performance of 2D rGO wrapped Ga_2O_3 nanostructures is also an important goal of the thesis.

❖ Speculate the correlations between the properties and different characterization results of the Ga_2O_3 nanostructures for different applications.

1.7. Outlines of the thesis

➢ Chapter 1: Introduction

The thesis contains eight chapters. Chapter 1 provides a basic introduction to "nanostructures and nanotechnology". The general discussion of crystal structures, electronic structures and different kinds of properties of gallium oxide is delivered. Fundamental explanations of the applications: photocatalysis and field emission are given. Furthermore, the main achievements of this thesis are summarized, and it provides an outline of the thesis, where a short explanation of every chapter is mentioned.

➢ **Chapter 2: Review of past works**

Chapter 2 contains a comprehensive literature review of the present status of research, different synthesis procedures, and applications of Ga_2O_3 nanomaterials.

➢ **Chapter 3: Instruments and apparatus**

Chapter 3 reflects the general introduction of the major experimental apparatus, characterization tools and the description of the instruments used in the basic application part.

➢ **Chapter 4: Work #1**

Chapter 4 explores the dye selective photocatalytic degradation properties of tailored mesoporous nanocrystalline Ga_2O_3. This chapter is on the basis of the publication '*Microporous and Mesoporous Materials 288 (2019) 109600*'.

➢ **Chapter 5: Work #2**

Chapter 5 focuses on the fabrication of novel Ag_2O/Ga_2O_3 type II p-n heterojunction that can perform greater removal efficiency of different kinds of organic and inorganic pollutants from industrial waste water. This chapter is on the basis of the publication '*Applied Surface Science 515 (2020) 145958*'.

➢ **Chapter 6: Work #3**

Chapter 6 describes the synthesis of gallium oxide nanostructures with different Gallia-precursors and focuses on visible light assisted dye sensitized photocatalytic water remediation. This work is communicated for future publication.

➢ **Chapter 7: Work #4**

Chapter 7 describes synthesis, characterization and field emission properties of pure and rGO wrapped Ga_2O_3 nanostructures. Experimental investigation as well as theoretical validation is reported. This chapter is on the basis of the publication '*Journal of Alloys and Compounds 902 (2022) 163726*'.

➢ **Chapter 8: Conclusion and future outlook**

Finally, Chapter 9 draws the conclusions of the thesis which is based on the summary of the main achievements and also provides a discussion on the possible future outlooks.

1.8. References

1. H.W. Kroto, J.R. Heath, S.C. O'Brien, R.F. Curl, R.E. Smalley, Nature, 318 (1985) 162.

2. S. Iijima, Nature, 354 (1991) 56.

3. S. S. Farvid, T. Wang and P. V.Radovanovic, J. Am. Chem. Soc., 133 (2011) 6711–6719.

4. M. K. Gish, A. M. Lapides, M. K. Brennaman, J. L. Templeton, T. J. Meyer and J. M. Papanikolas, J. Phys. Chem. Lett., 7 (2016) 5297–5301.

5. M. Alonso-Orts, A. M. Sánchez, S. A. Hindmarsh, I. López, E. Nogales, J. Piqueras and B. Méndez, Nano Lett., 17 (2017) 515–522.

6. X. Zhao, Z. Wu, W. Cui, Y. Zhi, D. Guo, L. Li and W. Tang, ACS Appl. Mater. Interfaces, 9 (2017) 983–988.

7. L. N. Hutfluss and P. V. Radovanovic, J. Am. Chem. Soc., 137(2015) 1101–1108.

8. S. S. Farvid and P. V Radovanovic, J. Am. Chem. Soc., 134(2012) 7015–7024.

9. T. Wang and P. V. Radovanovic, J. Phys. Chem. C, 115 (2011) 18473–18478.

10. K. L. Chopra, S. Major and D. K. Pandya, Thin Solid Films, 102(1983) 1–46.

11. D. S. Ginley, H. Hosono and D. C. Paine, Eds., Handbook of Transparent Conductors, Springer, New York, (2011).

12. A. Klein, J. Am. Ceram. Soc., 96 (2013) 331–345.

13. H. Y. Playford, A. C. Hannon, E. R. Barney, R. I. Walton, Chem. - A Eur. J., 19(2013) 2803–2813.

14. M. Marezio, J. P. Remeika, J. Chem. Phys., 46(1967) 1862.

15. S. Yoshioka, H. Hayashi, A. Kuwabara, F. Oba, K. Matsunaga, I. Tanaka, J. Phys. Condens. Matter, 19(2007) 346211–11.

16. J. Åhman, G. Svensson, J. Albertsson, ActaCrystallogr., 52(1996) 1336–1338.

17. H. He, R. Orlando, M. Blanco, R. Pandey, E. Amzallag, I. Baraille, M. Rérat, Phys. Rev., 74(2006) 195123.

18. R. Roy, V. G. Hill, E. F. Osborn, J. Am. Chem. Soc., 74(1952) 719.

19. S. Geller, J. Chem. Phys., 33(1960) 676.

20. Tamura Corporation, "Single-Crystal Gallium Oxide Substrates Specifications," can be found under http://www.tamura-ss.co.jp/en/gao/, 2016.

21. E. G. Víllora, K. Shimamura, Y. Yoshikawa, T. Ujiie, K. Aoki, Appl. Phys. Lett., 92(2008) 202120.

22. Z. Galazka, R. Uecker, K. Irmscher, M. Albrecht, D. Klimm, M. Pietsch, M. Brützam, R. Bertram, S. Ganschow, R. Fornari, Cryst. Res. Technol., 45(2010) 1229–1236.

23. M. Passlack, E. F. Schubert, W. S. Hobson, M. Hong, N. Moriya, S. N. G. Chu, K. Konstadinidis, J. P. Mannaerts, M. L. Schnoes, G. J. Zydzik, J. Appl. Phys.,77 (1995) 686.

24. S.-A. Lee, J.-Y. Hwang, J.-P. Kim, S.-Y. Jeong, C.-R. Cho, Appl. Phys. Lett., 89(2006) 182906.

25. C. Janowitz, V. Scherer, M. Mohamed, A. Krapf, H. Dwelk, R. Manzke, Z. Galazka, R. Uecker, K. Irmscher, R. Fornari, et al., New J. Phys., 13(2011) 85014.

26. N. Ueda, H. Hosono, R. Waseda, H. Kawazoe, Appl. Phys. Lett,.71(1997) 933.

27. M. Orita, H. Ohta, M. Hirano, H. Hosono, Appl. Phys. Lett., 77 (2000) 4166.

28. J. A. Kohn, G. Katz, J. D. Broder, Am. Miner., 42 (1957) 5–6.

29. G. M. Wolten, A. B. Chase, J. Solid State Chem.,16 (1976) 377–383.

30. K. Yamaguchi, Solid State Commun., 131 (2004) 739–744.

31. L. Zhang, J. Yan, Y. Zhang, T. Li, X. Ding, Sci. China Physics, Mech. Astron.,55 (2012)19–24.

32. H. Peelaers, C. G. Van de Walle, Phys. status solidi, 252 (2015) 828–832.

33. J. B. Varley, J. R. Weber, A. Janotti, C. G. Van de Walle, Appl. Phys. Lett.,97 (2010) 142106.

34. J. Zhang, J. Shi, D-C Qi, L. Chen, K. H. L. Zhang, APL Mater., 8 (2020) 020906.

35. Z. Guo, A. Verma, X. Wu, F. Sun, A. Hickman, T. Masui, A. Kuramata, M. Higashiwaki, D. Jena, T. Luo, Appl. Phys. Lett., 106 (2015) 111909.

36. E. G. Víllora, K. Shimamura, T. Ujiie, K. Aoki, Appl. Phys. Lett., 92(2008) 202118.

37. Z. Galazka, K. Irmscher, R. Uecker, R. Bertram, M. Pietsch, A. Kwasniewski, M. Naumann, T. Schulz, R. Schewski, D. Klimm, et al., J. Cryst. Growth, 404 (2014) 184–191.

38. Z. Galazka, R. Uecker, K. Irmscher, M. Albrecht, D. Klimm, M. Pietsch, M. Brützam, R. Bertram, S. Ganschow, R. Fornari, Cryst. Res. Technol., 45(2010) 1229–1236.

39. T. Harwig, F. Kellendonk, S. Slappendel, J. Phys. Chem. Solids, 39 (1978) 675–680.

40. G. Blasse, A. Bril, Solid State Commun., 7(1969) iii–iv.

41. T. Harwig, F. Kellendonk, J. Solid State Chem., 24 (1978) 255–263.

42. J. B. Varley, A. Janotti, C. Franchini, C. G. Van de Walle, Phys. Rev. B,85 (2012) 81109.

43. T. Onuma, S. Fujioka, T. Yamaguchi, M. Higashiwaki, K. Sasaki, T. Masui, T. Honda, Appl. Phys. Lett., 103(2013) 41910.

44. L. Binet, D. Gourier, J. Phys. Chem. Solids, 59 (1998) 1241–1249.

45. D. Dohy, L. Lucazeau, A. Revcolevschi, J. Solid State Chem., 45(1982) 180–192.

46. D. Machon, P. McMillan, B. Xu, J. Dong, Phys. Rev., 73 (2006) 94125.

47. T. Onuma, S. Fujioka, T. Yamaguchi, Y. Itoh, M. Higashiwaki, K. Sasaki, T. Masui, T. Honda, J. Cryst. Growth, 401(2014) 330–333.

48. T. C. Lovejoy, R. Chen, X. Zheng, E. G. Víllora, K. Shimamura, H. Yoshikawa, Y. Yamashita, S. Ueda, K. Kobayashi, S. T. Dunham, et al., Appl. Phys. Lett.,100 (2012) 181602.

49. K. Sasaki, A. Kuramata, T. Masui, E. G. Víllora, K. Shimamura, S. Yamakoshi, Appl. Phys. Express,5 (2012) 35502.

50. A.K. Mondal, M. A. Mohamed, L. K. Ping, M. F. MohamadTaib, M. H. Samat, M. Aniq, Materials, 14 (2021) 604.

51. P. Bradu, A. Biswas, C. Nair, S. Sreevalsakumar, M. Patil, S. Kannampuzha, A.G. Mukherjee, U. R. Wanjari, K.Renu, B. Vellingiri, and A. V. Gopalakrishnan, Environmental Science and Pollution Research, (2022)1-32.

52. S. Vachon, Int. J. Prod. Res, 45(18-19) (2007) 4357-4379.

53. M.-h Wu, L. Lia, Y.-c Xue, G. Xu, L. Tang, N. Liu, W.-y Huang, Appl. Catal. B: Environ, 228 (2018) 103-112.

54. K.M. Zhang, Z.G. Wen, J. Environ. Manage. 88 (2008) 1249–1261.

55. A. Bhatnagar, A.K. Minocha, Indian. J. Chem. Technol. 13 (2006) 203-217.

56. K. Intarasuwan, P. Amornpitoksuk, S. Suwanboon, P. Graidist, Sep. Purif. Technol., 177 (2017) 304–312.

57. V. Iliev, D. Tomova, L. Bilyarska, J. Photochem. Photobiol. A: Chem., 351 (2018) 69–77.

58. Z. Carmen, and S. Daniela, Textile organic dyes-characteristics, polluting effects and separation/elimination procedures from industrial effluents-a critical overview, 3 (2012) 55-86. Rijeka: IntechOpen.

59. C. Fersi, and M. Dhahbi, Desalination, 222 (2008) 263-271.

60. N. Zaghbani, A.Hafiane, and M.Dhahbi, Sep. Purif. Technol, 55 (2007) 17-124.

61. G. Mitra, N.Simmin, R. Mohammad, M. Alireza, Water Qual. Res. J. Canada, 38 (2) (2003) 379–39.

62. Y. Kiso, Y. Sugiura, T. Kitao, and K. Nishimura, K., Journal of Membrane Science, 192(1-2) (2001) 1-10.

63. S. Buetehorn, P. Le-Clech, M. Brannock, D. Volmering, G. Leslie, K. Vossenkaul, T. Melin, Sep. Purif. Technol., 95 (2012) 202-215.

64. C. M. Kao, R.Y. Surampalli, B. M. Yang, C. Z. Tian, ASCE, Chapter-17, 2013.

65. Y. Zhu, X. Ma, and Y. Liu, Journal of atomic and molecular sciences, 6(2) (2015)137-144.

66. M. Latifa Chowdhury, Hybridization of gallium oxide with magnetic graphene oxide toward a low cost and reusable photocatalyst (2018).

67. S. Sadri Moghaddam, M. R.AlaviMoghaddam, & M. Arami, J. Haz. Mat, 175(2010) 651-657.

68. S. L. Chai, R. John, F. C. Mei, Process. Saf. Environ, 92(2014) 489-508.

69. G. M. Walker, and L. R. Weatherly, Water Research, 31 (1997) 2093-2101.

70. S. Babel, T. A. Kurniawan, J. Haz. Mat, 97 (2003) 219-243.

71. Q. H. Wang, M. Yan, and R. P. H. Chang, Applied Physics Letters, 78(9) (2001) 1294-1296.

72. D. Sarkar, C. K. Ghosh, and K. K. Chattopadhyay, Cryst Eng Comm, 14(8) (2012) 2683-2690.

73. X. M. Henry Huang, C. A. Zorman, M. Mehregany, and M. L. Roukes, Nature, 421(6922) (2003) 496-496.

74. G. Cao, Y. Z. Lee, R. Peng, Z. Liu, R. Rajaram, X. Calderon-Colon, L. An, P. Wang, T. Phan, S. Sultana, and D. S. Lalush, Physics in Medicine & Biology, 54(8) (2009) 2323.

75. H. Sugie, M. Tanemura, V. Filip, K. Iwata, K. Takahashi, and F. Okuyama, Appl. Phys. Lett, 78(17) (2001) 2578-2580.

76. T. Serin, A. Yildiz, S. H. Şahin, and N. Serin, Physica B: Condensed Matter, 406(3) (2011) 575-578.

77. T. Serin, A. Yildiz, S. H. Şahin, and N. Serin, Physica B: Condensed Matter, 406(19) (2011) 3551-3555.

78. M.T.S. Nair, L. Guerrero, O. L. Arenas, and P. K. Nair, Applied Surface Science, 150(1-4) (1999) 143-151.

79. X. Fang, Y. Bando, U. K. Gautam, C. Ye, and D. Golberg, Journal of materials chemistry, 18(5) (2008) 509-522.

80. Carbon Based Nanostructures for Field Emission Applications by D. Banerjee.

81. W. Schottky, Zeitschrift für Physik, 14(1) (1923) 63-106.

82. R. H. Good, and E. W. Müller, Field emission. In Electron-Emission Gas Discharges I/Elektronen-Emission Gasentladungen, Springer, Berlin, Heidelberg (1956) 176-231.

83. R. A. Millikan, and C. C. Lauritsen, Proceedings of the National Academy of Sciences, 14(1) (1928) 45-49.

84. T. E. Stern, R.H. Fowler, B.S. Gossling, Proc. R. Soc. London, Ser. A, 124 (1929) 699.

85. F. R. Abbott et al. Phys. Rev. 56 (1939) 113.

86. R. H. Fowler, and L. Nordheim, Electron emission in intense electric fields. Proceedings of the Royal Society of London. Series A, Containing Papers of a Mathematical and Physical Character, 119(781) (1928) 173-181.

87. F. R. Abbott et al. Physical Review, 56 (1939) 113.

88. Sommerfeld & H. Bethe, Handbuch der Physik, 24 (1933) 441.

Chapter 2

Literature Review of Past Works

In 1875, French chemist Paul-Emile discovered gallium (Symbol Ga)[1]. The position of gallium in the periodic table is at group 13 and it has a similarity with the other metals of this group like aluminium, indium etc. However, Ga is an unstable metal and doesn't occur freely in nature i.e. a rare element. Whereas gallium (III) in compound form, such as gallium oxide (Ga_2O_3), is chemically and thermally sustainable as well as easily available. In most of the acids and alkali media, Ga_2O_3 is soluble but in water media it is not. Also, gallium oxide shows different polymorphism like α, β, γ, ε, δ- phase etc. Among which β-phase is very much interesting and stable one. In 1960s, researchers started investigating the various crystal structures of gallium oxide[2]. After that from the early age of 21st century, the focus shifted towards the morphological alteration of gallium oxide by some crucial techniques like the fabrication of monoclinic- Ga_2O_3 nanowires using arc discharge method[3], pulse laser deposition[4] etc. However, Ga_2O_3 is an ultra-wide band gap (~4.9 eV) semiconducting material which possess excellent conduction and luminescence behaviour[5]. The higher electrical conductivity of Ga_2O_3 can be related with the point-defects present in the structure of the same[6]. Whereas sufficient oxygen vacancy available in the interstitial sites helps gallium oxide to become an eligible gas sensor material[7]. Also due to higher band gap it can acquire a varied wavelengths across a deeper ultraviolet range; therefore efficient utilization of more solar energy happens and Ga_2O_3 may be used a potential candidate in solar cell, photocatalysis and photovoltaic applications[8-10].

Being an emerging semiconductor, gallium oxide has drawn a great attention among the scientists and researchers due to its unique optical, electrical, and morphological properties. Furthermore, those characteristics of Ga_2O_3 may be manipulated by synthesizing nanostructures of the material. So, it is an important task to choose the correct, efficient as well as cost-effective techniques for the synthesis of gallium oxide nanostructures as the structures of the as-prepared materials are highly dependent on the synthesis parameters and techniques. Hence to fabricate different gallium oxide nanostructures, a huge variety of synthesis methods have been published by researchers till today. Those synthesis routes of Ga_2O_3 are usually high energy-consuming but provide low yields and sometimes generate impurities[11-12]. In this review chapter, the main fabrication techniques for gallium oxide nanostructures along with both contemporary and plausible future applications of the same will be described in detail.

2.1. Gallium oxide: previous work on synthesis

Since the 1950s, for the growth of β-Ga_2O_3 in bulk form an enormous effort has been employed by the researchers. Several techniques are reported for that purpose such as the floating zone

method (FZ) [13-14], the Czochralski method (CZ) [15-16], the Verneuil method [17, 18], the edge-defined film-fed growth method (EDFG) [19-20], and the vertical Bridgman method [21, 22]. Over time those methods were eligible for the successful synthesis of bulk β-Ga_2O_3 in single crystal form along different crystallographic directions: (100), (010) and (001). The produced bulk crystals are in the form of cylinder, slab or sometimes depend on the furnace-shape; with crystal size in between 9×25 mm to 150×150 mm based on different synthesis techniques. To contain the melt, iridium (Ir) and platinum-rhodium (Pt-Rh) crucible were used in both the CZ and EDFG methods, and VB method respectively. Whereas Verneuil and floating zone methods are crucible-free techniques. Among them only the EDFG method has been able to make large bulk crystal with highest growth rate and perform n-type doping easier. However to achieve unique optical, electrical and surface properties, the surface-to-volume ratio of the as-prepared materials were enhanced only by producing their nanostructures. Crystalline Ga_2O_3 films and nanostructures can be prepared using different techniques, including sol-gel[25-30], sputtering[33-39], laser ablation[40-45], chemical vapour deposition[68-73], etc. Literature review of different synthesis processes are discussed below.

2.1.1. Sol-Gel method

Fabrication of nanostructures by sol-gel route is one of the most convenient synthesis techniques due to its simplicity and flexibility. Also this technique is suitable for the materials with low curing temperatures[23] and does not involve an expensive and complicated setup. The fundamental mechanism of sol-gel route is firstly to prepare a solution (or sol). Then the solution can be used to make deposition over the substrate or the deposition may be done by spin coating or dip coating to prepare thin film. A polymer solution is used in dip coating method to coat both side of the wafers and for this purpose Nafion be the top performing material as it carries strongest Lewis acidity[24]. The next step is to dry that with the application of heat. Up to the middle of 21st century, many research groups carried out this method to synthesize gallium oxide.

In 2000, T. Miyata et al.[25] reported sol-gel synthesis of manganese-activated gallium oxide (Ga_2O_3: Mn) thin-films for electroluminescent device applications. To prepare required solution a mixture of trimethoxy gallium and manganese chloride was dissolved into appropriate amount of methanol with constant room temperature magnetic stirring in nitrogen atmosphere for one hour. Simultaneously barium titanate sheets were immersed into the solution and a proper amount of deionized water and hydrochloric acid were combined. After

that, the sheets were dried by providing heat and annealing was also done at higher temperature up to 1000 °C. Highest luminance (~1000 cd/m^2) was found for the Ga$_2$O$_3$: Mn thin films annealed at the higher temperature. This work demonstrates that the annealing temperature became a major factor to alter the optical and electrical behaviours of the as-prepared films. Also, the authors made a comparison between the thin films fabricated via sol-gel route and sputtering technique; resulted better performance of sol-gel films for electro-luminescent devices which can be accounted for better crystallization. So, heat-treatment became pre-dominant for achieving a good crystalline film.

In 2002, Aldinger et al.[26] reported the synthesis of rhombohedral and monoclinic Ga$_2$O$_3$ by open air annealing of crystalline Ga(OOH) at temperatures greater than 500 °C. The later was prepared in aqueous media following two distinct precipitation routes: homogeneous-decomposition of urea and forced-hydrolysis in pure water. For both the methods 6.7 mL aliquot (i.e., 2.5 mmol of Ga(NO$_3$)$_3$×0.4H$_2$O) of the gallium nitrate stock solution was used and precipitation formation pH and temperature were maintained as 2.05 and 85 °C. Zeppelin and rod-like Ga$_2$O$_3$ nanostructures were formed following this synthesis method shown in **Figure. 2.1 (a-f)**.

In 2006, employing the sol-gel technique Sinha et al.[27] developed Ga$_2$O$_3$ quantum dots having particular sizes (2–5 nm) over silica gel matrix. To start the synthesis process two different solutions were prepared. First one was the mixture of metallic gallium and HNO$_3$ sustaining its pH value from 1-2. And another one was the combination of the source of SiO$_2$, i.e. tetraethyl orthosilicate, water, ethanol and an appropriate amount of HCl which was used for hydrolysis. After that the sol was stirred for one hour. Then both the solutions were mixed and magnetically stirred for few hours. During this process the pre-mentioned pH value was retained and a constant heat (~70 °C) was supplied to speed up the hydrolysis and condensation process. Then to obtain a clear gel the final mixture was dried for 4 hours with temperature 200 °C. Then the as-synthesized white coloured, highly porous moisture-less gel pieces were annealed within a horizontal-tube furnace at different high temperatures (400 °C, 500 °C, 900 °C) up to 11 hour to obtain Ga$_2$O$_3$:SiO$_2$ nanocomposites.

There are some previous reports[28-29] which reflect that only α-Ga$_2$O$_3$ could be synthesized below 500 ˚C temperature. But the study of Sinha et al. confirms the formation of monoclinic β-Ga$_2$O$_3$ at annealing temperature 400 °C. It may be accounted for the capping effect of silica, that restricts Ga$_2$O$_3$ particles to tiny size (approx. ~2–5 nm) [27].

In 2018, R. Gopal et al.[30] showed the production of Ga$_2$O$_3$ nanorods was done by sol-gel transformation of gallium (III) isopropoxide. In this method, to make a transparent solution, 2

g of compound, Ga(OPri)$_3$ was dissolved in anhydrous isopropanol (~ 20 mL). Then the solution was stirred with addition of few drop of water–isopropanol mixture until the sol formation started. To confirm the complete hydrolysis some water was added to it, with continuous stirring. After that resultant yellow coloured gel was formed and it was washed multiple times using acetone & DI water, then dried at 100 °C and sintered at 600 °C for 6 hours to get final product. FESEM images and EDX spectra of as-synthesized β-Ga$_2$O$_3$ samples are shown in **Figure. 2.1 (g, h)**.
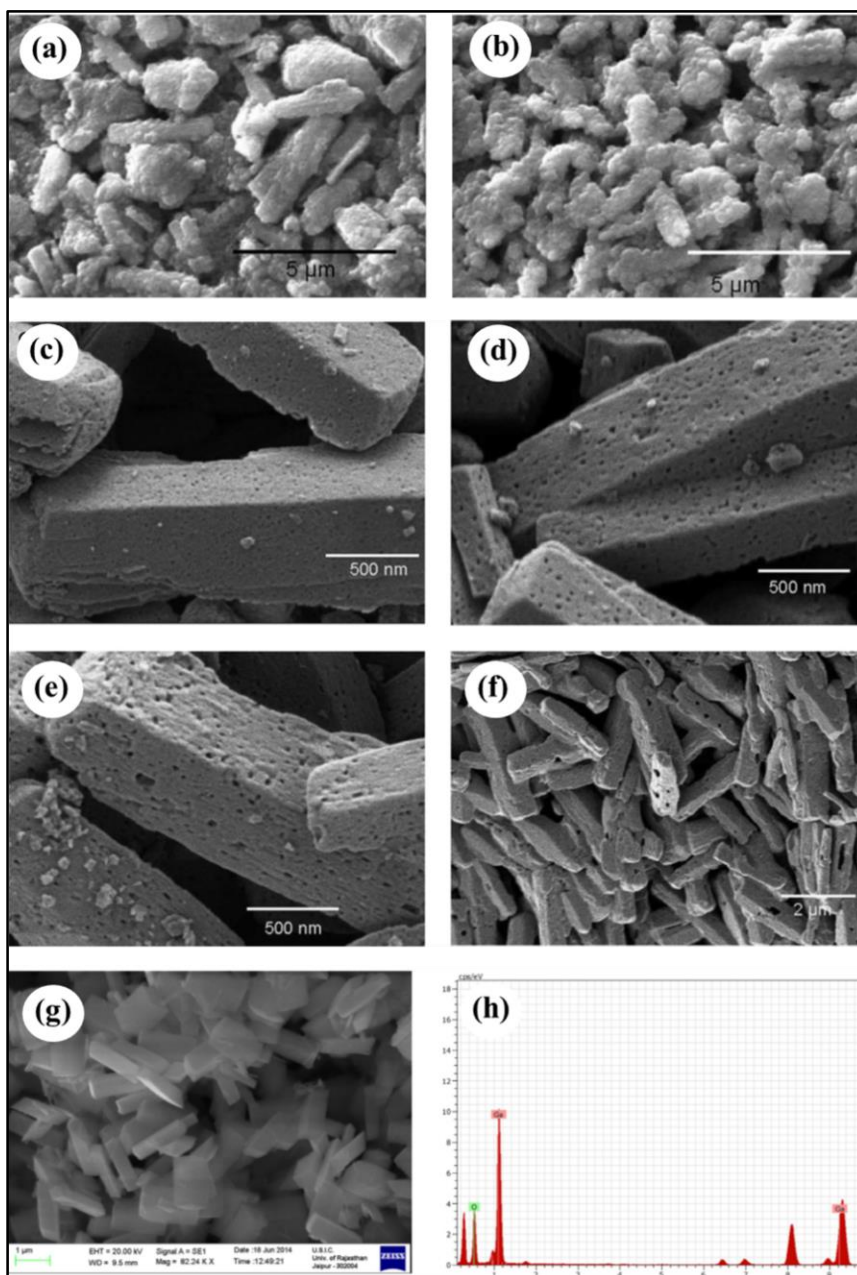

Figure 2. 1 SEM micrograph of samples prepared using urea-containing solutions and calcined at 750 °C (a) and at 1000 °C (b); FESEM images of the samples after calcining at (c) 500 °C, (d) 750 °C, (e) 1000 °C, and (f) 1200 °C for 6 h in air by Aldinger et al.[26] ; (g) SEM image and (h) EDX spectra of β-Ga₂O₃ by R. Gopal et al [30]

2.1.2. Sputtering technique

Radio frequency magnetron sputtering is very familiar and famous process for the fabrication of gallium oxide nanostructures. A chamber and a proper environment is needed to carry out this synthesis which would promote the formation of gallium oxide. Generally due to the bombardment of noble gas ions on target material ejection of particle from the later takes place which may be deposited over the substrate. In this process the electric potential can be easily varied by altering the radio frequency, resulted better cleaning of the target and facilitates more deposition[31, 32].

In 2001, M. Ogita et al.[33] suggested the fabrication of gallium oxide thin-film over silicon substrate using radio frequency magnetron sputtering. In this process, they used sintered gallium oxide powder as target material. Preparation of thin film with 1μm thickness was done in argon environment with radio frequency power 50 W. Different Ga_2O_3 thin film samples were fabricated by varying a few parameters like sputtering pressure, the argon to oxygen ratio within chamber, temperature etc. Then the samples were annealed at 1000 °C in open air. Resistivity of Ga_2O_3 thin film depends on the O_2 content of the thin-film which solely depends on the sputtering conditions. This work reported Ga_2O_3 thin film as an efficient oxygen sensor at high temperatures.

In 2011, J. Wang et al.[34] prepared one-dimensional β-Ga_2O_3 nanostructures on Si (111) substrates by calcining the sputtered-Ga_2O_3/Mo films in a quartz tube with ammonia environment. The whole synthesis was performed in two steps. Firstly, using RF magnetron sputtering system Ga_2O_3/Mo film was deposited on silicon substrate, previously washed with isopropyl alcohol, acetone, and deionized water respectively. Then the sputtering chamber pressure was lowered down to 7.8×10^{-4} Pa. During synthesis process argon (Ar) gas (99.999%) was injected into the chamber, stabilized the pressure down to 2 Pa and set RF power to 150 W. Sputtering was continued for 5 and 90 minutes for Mo and Ga_2O_3, respectively maintaining room temperature. In the second step, as-synthesized samples were calcined in tube furnace under ammonia atmosphere with a flow-rate of 500 ml/min for 15 min at different high temperatures 850 °C, 900 °C, 950 °C and 1000 °C, respectively to produce nanostructured β-Ga_2O_3. The authors suggested there the Mo middle layer became very important for the growth of β-Ga_2O_3 nanostructures. However, the synthesis resulted morphology variation of the samples with the increment of annealing temperature. Initially the formation of β-Ga_2O_3 occurred in nanowire-shape, and after high temperature calcination nanowires transformed to

nanorods. Morphological features along with the XRD pattern of the β-Ga$_2$O$_3$ nanorods are presented in **Figure. 2.2A.**

In 2015, H. C. Kang et al.[35] used radio-frequency powder sputtering to produce β-Ga$_2$O$_3$ nanowires (NWs) deposited on amorphous SiN/Si (001), SiO$_x$/Si (001), and glass substrates. Following synthesis was performed in a pure Ar (99.999%) environment with 20 sccm flow rate and 5×10^{-3} Torr chamber pressure. The distance between the substrate and the target was maintained 4 cm and the power was adjusted to 100 W. The nanostructure formation characteristics were examined on SiN/Si (001) substrates at various growth-temperatures from room temperature to 625 °C. Also, the thickness variation of the samples (between 1.6 to 4.5 µm) was performed by varying deposition time. The sample synthesized up to 320 °C was non-crystalline in nature, whereas the crystal fabrication was observed with annealing temperatures 450 °C, 550 °C and 650 °C shown in **Figure. 2.2B**.
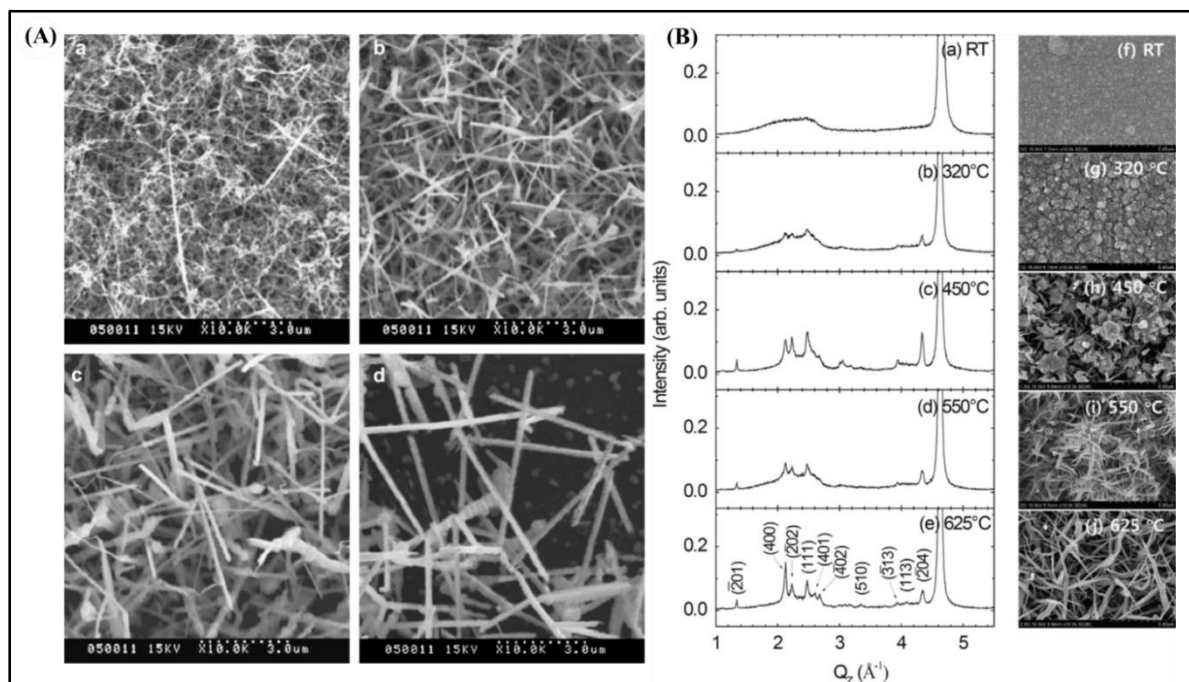
Figure 2. 2 (A) SEM images of the products annealed for 15 minutes at various temperatures: (a) 850 °C, (b) 900 °C, (c) 950 °C, (d) 1000 °C by Wang et al [34]; (B) XRD profiles (a)–(e) and (f)–(j) top-view SEM images of the samples grown at room temperature, 320 °C, 450 °C, 550 °C, 625 °C respectively by Kang et al[35]

Further in 2021, A.K. Singh et al.[36] studied the contribution of annealing-temperature on β-Ga$_2$O$_3$ thin-films deposited by radio frequency sputtering technique. At room temperature sputtering involved β-Ga$_2$O$_3$ wafer as target exhibiting 2-inch diameter and; quartz or n-type Si (100) as the substrate materials respectively. The target to substrate distance was kept as 7 cm. After initial evacuation the sputtering-chamber pressure was lowered down to 10^{-6} Torr and the power was adjusted to 50 W. Then the Ar & O$_2$ gas mixture (having a flow rate of 50

sccm and 2 sccm respectively) was used as gaseous environment of the chamber and due to this the working pressure was increased to 5×10^{-3} Torr. After 90 minutes of deposition, β-Ga_2O_3 thin films were produced with approximate thickness ~89.9 nm–103 nm. Then it was annealed in air for 120 minutes at 600 °C, 800 °C, 950 °C, and 1000 °C. This study concluded that the highly crystalline thin films were obtained only after high temperature annealing (1000 °C). Some other studies in 2021[37-39] also confirms the amorphous gallium oxide formation tendency at low annealing temperature.

2.1.3. Pulsed Laser Deposition technique

Pulsed laser deposition is an easy & convenient technique for the production of nanomaterials. The deposition takes place on the substrate materials after the ablation of the target with the laser source. The laser ablation process usually executed in a chamber, where the target and substrate materials are kept apart from each other and the system is filled with various gasses maintaining constant pressure. This technique is highly compelling for the preparation of Ga_2O_3 nanostructures.

In 2004, Lam et al.[40] first used pulsed laser ablation technique to synthesize β-Ga_2O_3 nanoparticles. Authors used gallium nitrate (GaN) powder with purity 99.99%, as target material and 99.9995% ultra-pure nitrogen as surrounding gas at room temperature. To ablate the GaN target, A krypton fluoride (KrF) excimer laser (Lextra 50, LAMBDA PHYSIK) with characteristic wavelength 248 nm, duration of the pulse 23 ns, and pulse energy range between 100 mJ to 200 mJ per pulse was utilized. Also the area of the laser beam on the target was 0.04 cm^2. At the beginning chamber pressure was lowered down to 3.8×10^{-5} Torr and then during laser ablation to maintain the chamber pressure 1 to 100 Torr, purified nitrogen gas was flowed into the chamber. To operate at different pressure region, the target-substrate distance could be varied as 1-3 cm. A p-type (100) silicon wafer was considered as substrate and it was washed using acetone and IPA before use. Finally, it can be observed that monoclinic β-Ga_2O_3 nanoparticles with diameter ranging between 10 nm to 500 nm were deposited on Si-substrates in enormous quantities. In this synthesis the chamber pressure played a vital role to control the surface morphologies, shape, size, and the amount of aggregation of the nanoparticles.

In 2012, S. L. Ou et al.[41] suggested the fabrication of Ga_2O_3 films on sapphire (0 0 1) following pulsed-laser-deposition technique at several substrate-temperatures from 400 °C to 1000 °C without any catalyst where a KrF excimer-laser was used as laser source. Authors used 99.99% pure gallium oxide powder target which was 50 mm away from the substrate. Initially the base

pressure was kept down to 5×10^{-8} Torr, then after introduction of 99.999% pure oxygen into the chamber the deposition-pressure became 5×10^{-2} Torr. A transformation from amorphous to polycrystalline β phase Ga_2O_3 was obtained with the increment of substrate temperature. AFM analysis of the samples are presented in **Figure. 2.3 (a-d)**. In same year H. Yamahara et al.[42] used catalyst gold particle to prepare Ga_2O_3 nanowires using pulsed laser deposition. To prepare required catalyst (0.25 mm^2 ultrathin gold layer deposited on an Al_2O_3 substrate), radio frequency magnetron sputtering was employed. Instead of powder gallium oxide, a sintered β-Ga_2O_3 (99.99%) pellet was considered as target and the target to substrate distance was maintained 2.0 cm. Pulsed lased deposition was continued using ArF excimer laser (wavelength 193 nm, pulse repetition frequency 10 Hz and 60 mJ laser energy). During the nanowire growth the surrounding oxygen pressure and the substrate temperature were kept as 0.1 Pa and varied between 700 °C – 850 °C, respectively (presented in **Figure. 2.3 (e-h)**).

Further in 2015, Q. Feng et al.[43] suggested the application of PLD techniques for the deposition of Ga_2O_3-films on $MgAl_6O_{10}$ (1 0 0) substrates using KrF excimer laser. The authors prepared different film samples at temperature 600 °C in an oxygen atmosphere with varying pressure such as 0.13 mbar, 0.01 mbar, 0.0015 mbar etc. The as-synthesized film becomes homogeneous and an increased grain size observed with the decrement of O_2 pressure.

In 2016, Garten et al.[44] produced high quality β-gallium oxide thin films on sapphire (0001) and Ga_2O_3 ($\bar{2}01$) single crystals using PLD method. Authors explored the dependence of the stability, growth, and dopability of those films with respect to oxygen partial pressure and temperature. This work confirmed the morphology, phase, and electronic properties of as-synthesized β-Ga_2O_3 films had a strong temperature dependence while varying the chamber temperature within 350 to 550 °C.

A recent study in 2020 by Hameed et al.[45] reported the production of gallium oxide (Ga_2O_3) nanoparticles using the Nd: YAG laser deposition method with a characteristic-wavelength of 1064 nm. By varying the deposition parameters, like gas pressure, growth temperature, pulse period, laser energy, etc. synthesis was performed. The dimension of the as-prepared nanomaterials were within 60 to 85 nm. Also, the sample's optical properties such as, optical transmittance, reflectance and absorbance; displayed the crystallite size dependency.
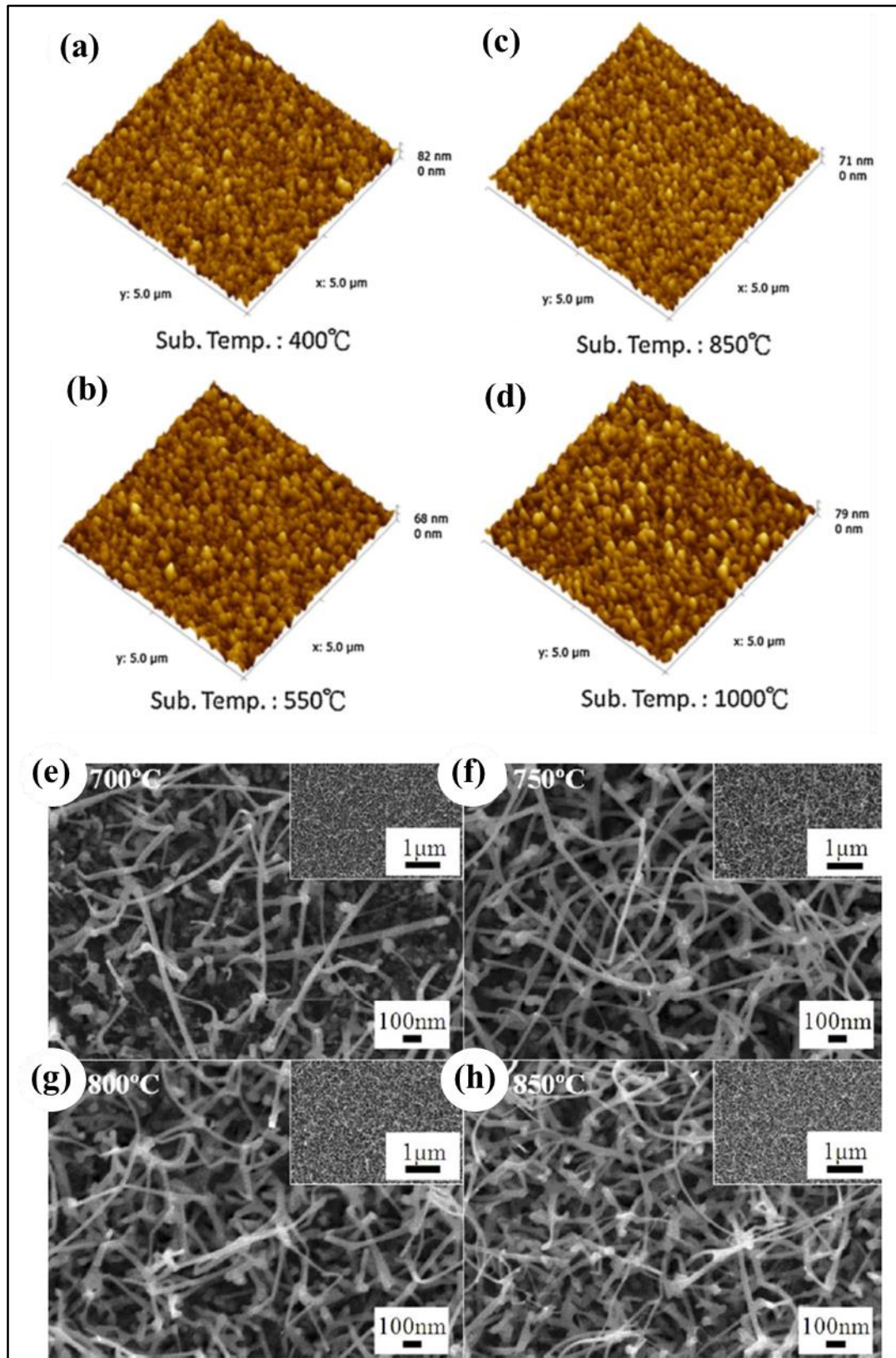
Figure 2. 3 AFM images of Ga₂O₃ thin films with substrate temperature (a) 400 °C, (b) 550 °C, (c) 850 °C, and (d) 1000 °C by S.-L. Ou et al [41]; FESEM images of Ga₂O₃ nanowires on 1 nm thick gold-catalyst at growth temperatures of (e) 700 °C, (f) 750 °C, (g) 800 °C and (h) 850 ˚C. The inset shows FESEM images scanned in wide range by Yamahara et al.[42]

2.1.4. Chemical Vapour Deposition method

Chemical vapour deposition (CVD) is basically an atomic layer deposition process where the nanomaterial deposition takes place on the substrate within a vacuum chamber during a specific deposition time[46-49]. Depending upon the synthesis conditions of the materials, different types of chemical vapour deposition are there; such as atomic pressure CVD[50,51], low-pressure CVD[52,53], and ultra-high vacuum CVD[54] etc. Chemical vapour deposition may be categorized depending on the parameters, such as whether a hot wall or a cold wall is used for the heating process of the substrate. Most of the time metallo-organic chemical vapour deposition (MOCVD) technique was exploited by the researchers for the preparation of gallium oxide[55-57]. This modern improved CVD technique offers a large control over the specific growth parameters of the nanostructures[58]. It is analogous to low-pressure CVD where the gases contain the metallic part and the substrate, where decomposition occurs, is heated[59]. There is another type of CVD, called Aerosol Assisted Chemical Vapor Deposition (AACVD), which involves aerosol instead of vacuum chamber[60-62]. Deposition rate for this method is higher as it is performed in normal atmospheric pressure[63]. Also, Mist-CVD is another employed technique, which is low-scale technique and operated in atmospheric conditions, often reported to synthesize α-Ga_2O_3 nanostructure[64-65] as well as β-Ga_2O_3 nanostructure[66-67]. The operating temperature for Mist-CVD is smaller compare normal CVD.

Ga_2O_3 NS/NWs can be easily synthesized following CVD technique. In experimental set-up, the metallic gallium is placed inside the furnace & after evaporation the Ga-vapours are transmitted over the substrate through some carrier gas. Ga_2O_3 nanowires were synthesized by Li et al.[68], Chang and Wu[69] and Dai et al.[70] following that technique. These synthesis process confirmed that the reaction between gallium vapour and H_2O occurred within 700°C to 950 °C on silicon[68, 70] or alumina[69] substrates. The reaction is presented below:

$$2Ga + 3H_2O = Ga_2O_3 + 3H_2$$
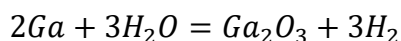
This whole process was performed in a quartz tube introduced into a tubular-furnace. In Ref. 69, authors were able to reduce the diameter as well as enhance the length of the β-Ga_2O_3 NWs remarkably. To avoid the oxidation of the Ga-metal, the team employed a modified Ga vapor supply maintaining a separation between the Ga-vapor and H_2O before reaching the substrate. In 2004 Kim et al.[71] used metalorganic chemical vapor deposition technique to produce amorphous Ga_2O_3 nanowire arrays on sapphire substrates (α-Al_2O_3) with (0 0 0 1) orientation without using any catalyst. The reaction between the mixture of trimethylgallium (TMGa) and oxygen (O_2) was done at 600 °C with 5 minutes deposition time to obtain the required sample.

The carrier gas, argon, was flowed with 30 sccm flow rate through the TMGa bubbler maintaining −5 °C. Also, the flow rate of O_2 was set to 6 sccm. Cross-section wise the as-prepared Ga_2O_3 nanowires were of circular-shaped having diameter ranging between 40–110 nm as confirmed by SEM and TEM analysis presented in **Figure. 2.4 (a-d).**

After two years, in 2006[72], the same group reported structural properties and the growth of amorphous Ga_2O_3 nanowire synthesized using MOCVD. That time they used Si (100) substrates instead of sapphire substrates and examined the growth mechanism as well as structural morphologies for various deposition times in the range of 3–5 min. Other synthesis parameters were kept identical with the previous one. Authors observed the thickness and surface coverage ratio of the thin films of nanowires increased with deposition time. The as-prepared dense and continuous gallium oxide nanowires exhibited diameter within range of 50 to 250 nm with no nanoparticles at their tips.

In 2019, T. Rajesh et al.[73] suggested plasma Chemical vapor deposition to fabricate β-Ga_2O_3 nanostructures on sapphire substrate using metallic gallium vapor in presence of nickel catalyst at 900 °C. Authors observed that the crystallinity of β-Ga_2O_3 nanostructures enhanced with increment of deposition time & the samples exhibited different kinds of morphologies like nanosheets, nanoribbons and nanowires presented in **Figure. 2.4 (e-j).**
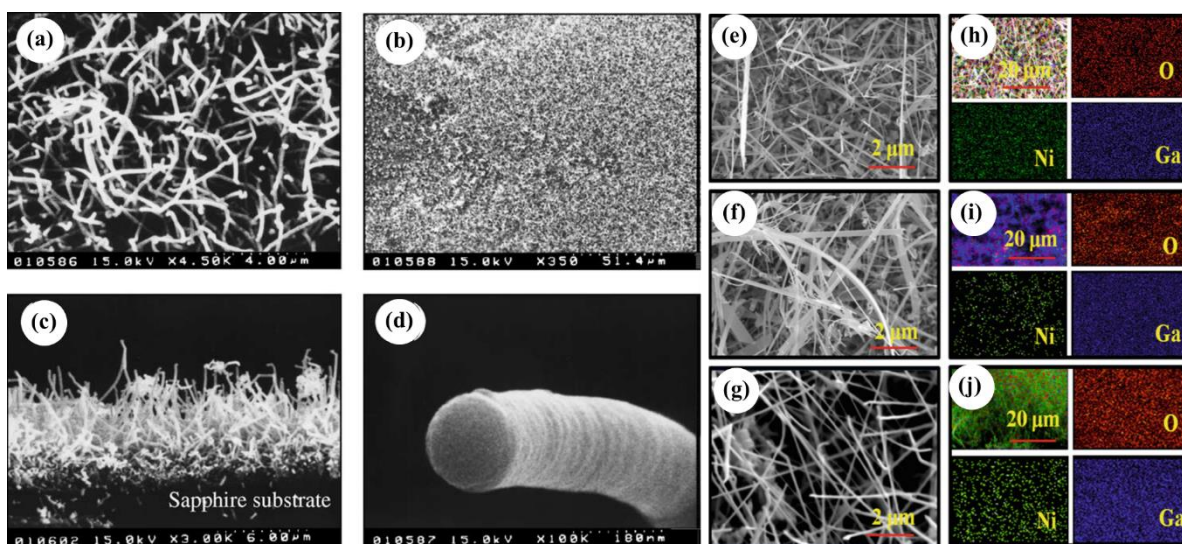
Figure 2. 4 SEM images of Ga_2O_3 nanowires. (a) High magnification Plan-view image. (b) low-magnification plan-view image presenting the uniform nanowire distribution over a large area. (c) Side-view image. (d) Higher-magnification image of single nanowire by Kim et al.[70]; (e-g) SEM images and (h-j) Elemental mapping of the samples synthesized at different deposition time of 30, 60 and 90 minutes by T. Rajesh et al.[72]

In addition, various types of Ga_2O_3 NS including nanorods, nanowires, nanoribbons, and nanocones have also been fabricated employing this method[74-76]. Auer et al.[76] utilized metallic gallium and O_2 as sources. It was mentioned that nanoribbons and nanorods were synthesized

using a vapour-solid mechanism, while the nanowires were fabricated via vapour-liquid-solid mechanism. The superior epitaxial-growth was obtained for nanowire growth on sapphire-substrates that mapped the hexagonal symmetry of (0001) sapphire.

2.1.5. Molecular Beam Epitaxy

Molecular Beam Epitaxy (MBE) is other widely used procedure for the purpose of nanomaterial synthesis[77, 78]. This method can produce high quality thin films. However a high vacuum chamber, exhibits a complex component structure, is essential for this synthesis. Also, an effusion cell is needed and throughout this process the metals are heated and deposited on the substrate. The orientation of the as-produced thin films can be easily changed as a motor is placed there which can rotate the substrate. Whereas the surface morphology of as-synthesized material may be investigated employing a RHEED (Reflection High Energy Electron Diffraction) gun[79]. But this technique is one of the most expensive and complex methods.

In 2010, a group of researcher prepared thin films of Ga_2O_3 applying plasma-assisted molecular-beam-epitaxy technique[80]. Sapphire and gallium oxide itself were used as substrate for the growth of crystalline structure. Oxygen pressure inside the chamber kept unaltered while the plasma beam pressure was varied. The growth characteristics was examined using RHEED gun and during deposition the material was heated up to 700 °C. Here plasma-beam pressure executed a vital role in the growth-rate of the nanostructures. Higher growth rate was observed at lower pressure, and vice versa.

In 2016, Ghose et al.[81] prepared epitaxial β-Ga_2O_3 on sapphire (c-plane) by plasma assisted molecular beam epitaxy technique. Authors used two different techniques; first one was based on a Ga_2O_3 compound source with O_2 plasma and next one involved elemental-gallium source with O_2 plasma. For both sources pure phase β-Ga_2O_3 single crystal thin films with $(\bar{2}01)$ orientation were produced with various substrate temperatures.

Further in 2019, formation and characteristics of Ga_2O_3 films grown with nitrogen employing plasma assisted molecular-beam-epitaxy were performed by T.S. Ngo et al.[82]. C-plane sapphire was used as substrate which was properly cleaned before use. Through one plasma source, there was a simultaneous supply of nitrogen and oxygen gases which played a key role for the growth of monoclinic structured β-Ga_2O_3 gallium oxide films whose surface roughness increased with increasing nitrogen supply. Also, the authors tuned the band gap energies of β-Ga_2O_3 films simply by enhancing nitrogen supply during growth without any post-annealing process under nitrogen condition.

2.1.6. Hydrothermal treatment

Hydrothermal treatment has become a widely used technique to synthesize Ga_2O_3 nanostructures for the unique advantages of this synthesis. It is not only a simple and less expensive reaction apparatus but also its production yield is high. Also various kinds of morphologies such as nanorod, nanowire, nanobrick, nanoneedle, nanosheaf, nanoblock etc. can be easily synthesized employing this techniques just by varying the synthesis parameters. For a typical hydrothermal reaction an autoclave is used. An autoclave is a specially designed pressurized reactors to heat aqueous solutions or organic solvents above their boiling point at a pressure higher than normal atmospheric pressure. It basically consists of two different parts: Teflon-lined inner part and an outer stainless steel case. The inner part can easily fit into the outer part which can resist high pressure during a reaction. A cylindrical Teflon tube with a Teflon cap, which serves as the inert reaction chamber, was fitted inside the iron chamber with an iron screw cap.

In 2007, X. Liu et al[83] reported the production of α-Ga_2O_3 and β-Ga_2O_3 1D nanorods after calcining as-synthesized gallium oxide hydroxide nanorods for 5 hours at 500 °C and 750 °C temperature, respectively in O_2 atmosphere. Whereas the single crystalline α-GaOOH nanorods were successfully prepared in high yield following hydrothermal-treatment using sodium azide as alkaline agent, hydrazine hydrate as complexing reagent and Ga_2O_3 as the Ga-source. The resulted gallium oxide samples were porous-nanorod structured with diameter between 40-200 nm. In the same year Zhao and co-workers[84] reported low temperature hydrothermal synthesis of nano- to microsized Ga_2O_3 with and without surfactant. Rod like gallium oxide hydroxide crystals with ~2.5 μm in length and ~1.5 μm in width were produced with starting molar-ratio of Ga to OH was 1:3. After that, the as-prepared samples were converted to β-Ga_2O_3 after calcining at 900 °C which retain its initial morphology. Also, tube like γ- Ga_2O_3 nanostructures with length ~65 nm, inner and outer diameters ~0.8 and 3 nm, respectively were easily synthesized following hydrothermal route (with or without surfactants) maintaining 100 °C temperature and the starting molar ratio of Ga to OH was 1:5.

In 2010, Y. Quan et al[85] reported the synthesis of crystalline 1D nanowires of α and β phase Ga_2O_3 by thermal decomposition (600 – 900 °C for 5 hours) of gallium oxide hydroxide nanowires. The authors produced GaOOH nanowires in huge amounts following hydrothermal synthesis process for 10 hours at 140 °C; taking gallium nitrate as the source of gallium and sodium dodecyl benzene sulfonate (SDBS) or sodium acetate (SA), as the surfactant. Morphological features of as-prepared samples are presented in figure below.

In 2013, Girija et al.[86] proposed organic-additives-assisted hydrothermal synthesis of mesoporous nanostructured β-Ga$_2$O$_3$. Authors used gallium nitrate (0.01 mol L^{-3}) as starting material and continued hydrothermal treatment at 120 °C for 12 hours employing 40 ml Teflon-lined stainless-steel autoclave and finally produced some fascinating morphologies such as spindles, blocks, and rods applying cationic (CTAB), anionic (SDS) and non-ionic (PEG) surfactants during synthesis. W. Zheng[87] prepared mesoporous α-Ga$_2$O$_3$ hierarchical structures following hydrothermal synthesis maintaining 180 °C temperature for 24 hours additionally adding DMF as surfactant. In the same year Shao et al. synthesized needle-like[88] and sheaf-like[89] β-Ga$_2$O$_3$ nanostructures using polyvinyl alcohol (PVA) assisted hydrothermal route following heat treatment. The samples exhibited large specific-surface-area (25.95 and 36.1 m^2/g respectively) and huge number of nanopores (4–25 nm and 2–4 nm respectively).

In 2014, X. Xu et al[90] attempted hydrothermal treatment (for 8 hours at 150 °C) of gallium acetylacetonate which is a single-source organometallic ingredient and the resulted product was further calcined at 800 °C for 2 h in air to prepare porous beta-gallium oxide nanowires. That year Girija and team[91] fabricated β-Ga$_2$O$_3$ microspheres constituted of nanospheres using surfactant assisted hydrothermal process. Authors used Ga(NO$_3$)$_3$ (0.01 mol / L) as precursor & F127 as surfactant and continued hydrothermal process at 180 °C for 12 hours.

Further in 2015, Reddy and team[92] again suggested the hydrothermal synthesis of β-Ga$_2$O$_3$ nanorods. Firstly they formed gallium oxide hydroxide (GaOOH) nanorods using the aqueous solution of hydrated gallium nitrate and NH$_4$OH with growth temperature 95 °C. Then they calcined the as-prepared GaOOH nanorods at 500 °C and 1000 °C for 3 hours to produce single crystalline α and β phase Ga$_2$O$_3$.

In 2016, A. Dulda[93] studied the consequence of alkali types and their addition rate on the growth and morphology of Ga$_2$O$_3$ samples. The author used GaCl$_3$ as the source of gallium and urea, NH$_4$OH or NaOH as reducing agent to achieve interesting morphologies. Further Ga$_2$O$_3$ thin films were synthesized by another research group on the glass substrate following chemical-bath-deposition with various post annealing treatments[94]. The chemical reactions are summarized below:

$$(CH_2)_6N_4 + 6H_2O \rightarrow 4NH_3 + 6HCHO$$
$$NH_3 + H_2O \rightarrow NH_4^+ + OH$$
$$3OH^- + Ga^{3+} \rightarrow Ga(OH)_3$$
$$Ga(OH)_3 \rightarrow GaOOH + H_2O$$
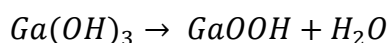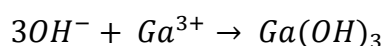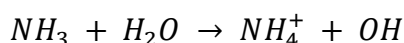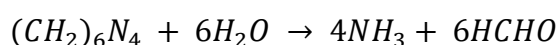
After that H. J. Bae and co-workers[95] produced β-Ga$_2$O$_3$ nanorods with high aspect ratio consisting of prism-like crystals involving gallium oxyhydroxide and ammonia hydroxide via a hydrothermal synthesis (140 °C for 10 hours) without as surfactants; accompanied by the subsequent calcination process at 1000 °C for 5 h. Also the authors continued the study for different aging temperatures and different aging times. In 2019, C. R. Michel and team[96] synthesized α-Ga$_2$O$_3$ by a novel synthesis method from metallic gallium. They proposed the following reactions:

$$Ga^{\circ} + 6\,HNO_3 \rightarrow Ga + 3(NO_3)_3 + 3\,H_2O + 3\,NO_2$$

$$3OH^- + Ga^{3+} \rightarrow Ga(OH)_3$$

$$Ga(OH)_3 \rightarrow GaOOH + H_2O$$

$$2\,GaOOH \rightarrow Ga_2O_3 + H_2O$$
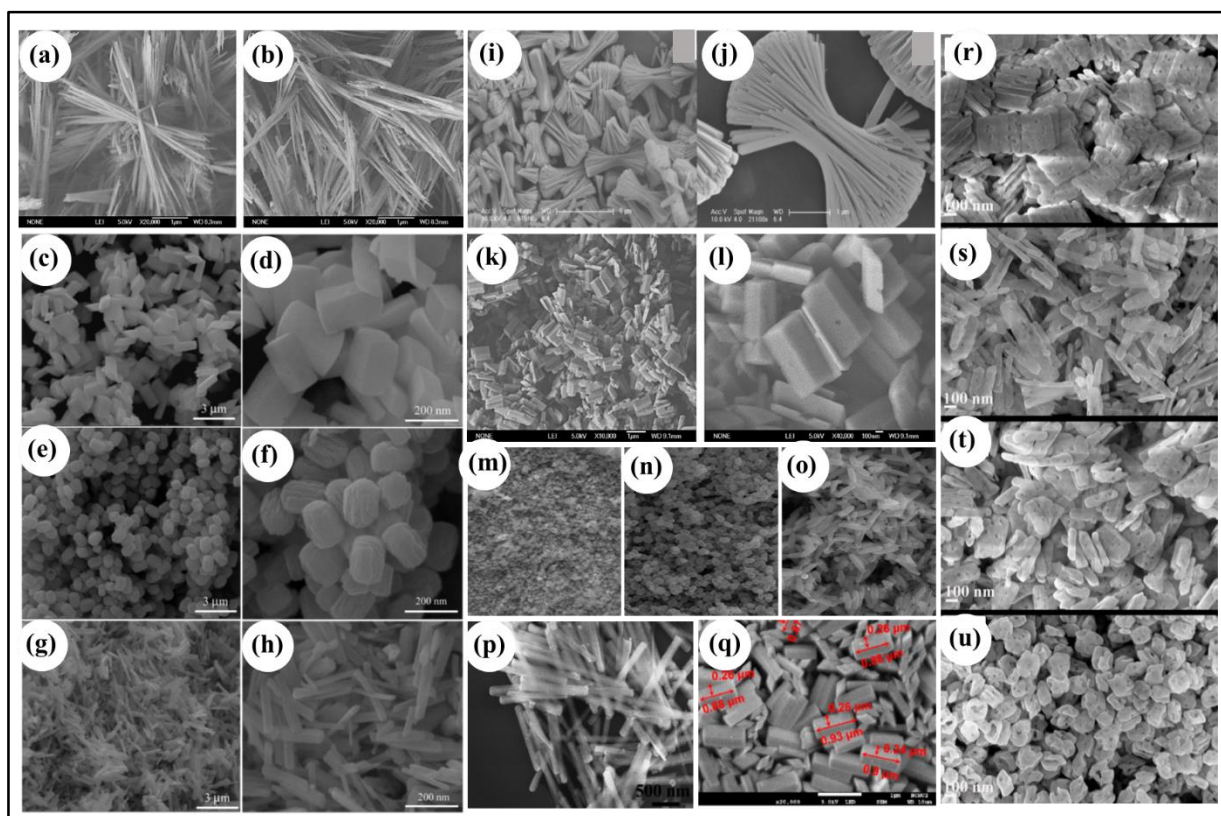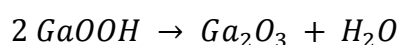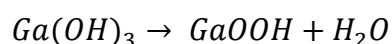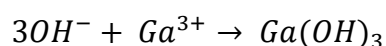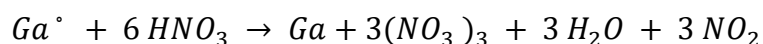
Figure 2. 5 FESEM images of different gallium oxide nanostructures synthesized by hydrothermal treatment: (a-b) X. Liu et al.[83], (c-h) K. Girija et al.[86], (i-j) T. Shao et al.[89],(k-l) Y. Quan et al.[85] (m-o) A. Dulda et al.[93], (p) X. Xu et al.[90], (q) Sam Zhang et al.[94] (r-u) Z. Wang et al.[125]

However there are several another synthesis techniques for the production of gallium oxide nanostructures such as spray pyrolysis[97-98], microwave synthesis[99], electron beam evaporation[100-102], carbo-thermal reduction[103-105], arc discharge[106-108], reflux condensation[109-110] etc.

2.2. Gallium oxide nanostructures: previous work on applications

2.2.1. Photocatalysis

Gallium oxide has become a widely used material for its catalytic activity; involved different chemical reactions like CO oxidation, catalytic combustion, NO_x's selective reduction etc. The fantastic catalytic activity of gallium oxide can be associated with distinctive structural-characteristics of co-ordinatively unsaturated surface Ga^{3+} cations; as it becomes a vital factor for the activation of hydrocarbons in CO_2 atmosphere. Also, the polymorphism property of gallium oxide may influence its catalytic performance. Among the other phases β-Ga_2O_3 exhibits the greatest catalytic activity for the dehydrogenation of propane to propene[111], oxidation of hydrocarbons[112] etc. The polymorph-reactivity can be interconnected with the surface-acidity, so the surface-acid-site-density may attributes a vital role in catalysis[111]. In case of β-Ga_2O_3 there exists tetrahedral Ga^{3+} ions which can be considered as the source of the Lewis acidity. Whereas for α-Ga_2O_3, the abundance of octahedral Ga^{3+} ions may hinders the Lewis acid formation on its sites. So, due to highest surface acid site density β-Ga_2O_3 becomes the most active catalyst amongst the other polymorphs.

Ga_2O_3 can be considered as highly efficient and environmental-friendly photocatalyst. The aim of research in the area of catalysis is to search the efficient materials for photocatalytic decomposition of different pollutants and to remove persistent organic compounds or inorganic pollutants and microorganisms in water[113]. For photocatalysis, firstly, the electron-hole pair generation takes place due to the illumination of the catalyst material with appropriate wavelength. Then the electron-hole pair may react with water molecules and produce superoxide radicals ($\bullet\, O_2^-$) and hydroxide radicals ($\bullet\, OH$) respectively. After that, depending upon the reaction conditions, electron-hole pairs, $\bullet\, OH$ radicals, $\bullet\, O_2^-$ radicals, H_2O_2, and O_2 can take part into the photocatalytic degradation mechanism. Photocatalysis is a less-expensive, efficient, and environmentally friendly process and can be carried out at room temperature. Ga_2O_3 has much wider band gap with respect to the other conventional photocatalysts such as TiO_2; which retains the electron-hole pair separation for a longer time therefore enhances their reductive capacity. Also, the conduction and valence band-edge potentials are observed to be at 1.1 V higher and 2.5 V lower than the redox potentials[114] of H^+/H_2 and O_2/H_2O, respectively. This comparatively high over-potentials makes gallium oxide a potential candidate for water photoelectrolysis[115, 116] and then oxidation as well as mineralization of organic compounds i.e. pollutants.

Scientific studies on photocatalytic activity of Ga_2O_3 have been reported since the early part of the 21th century. In 2006, Fu and team[117] reported the photocatalytic efficiency of porous β-Ga_2O_3 for benzene decomposition in air with UV-light irradiation. That result was also correlated with the performance of commercial TiO_2 (Degussa P25) and Pt/P25. The as-produced sample not only mineralized benzene but also its derivatives such as toluene and ethylbenzene; and the CO_2 was the final product under ambient conditions. The authors suggested that strong oxidative capacity and high specific-surface-area of β-Ga_2O_3 may be the reason of higher activity and longer stability in comparison with P25. After one year, Yoshida et al.[118] proposed the photocatalytic reformation of methane and CO_2 to produce both CO and H_2 at ambient temperatures with Ga_2O_3 as the photocatalyst. In 2009, Yang et al.[119] adopted the photocatalytic activities of single-crystalline hexagonal disk-like β-Ga_2O_3 nanostructures. The as-prepared samples were able to degrade an organic pollutant, Methyl orange into CO_2 and H_2O under UV light irradiation and at room temperature. In 2011, Tien et al.[120] proposed the correlation between defect-states and photocatalytic performance of β-Ga_2O_3 nanobelts. The authors studied the photocatalytic degradation of two distinct dyes: rhodamine B (RhB) and methyl blue (MB); and observed that the removal efficiency was enhanced with the increment of the acceptor sites connected with gallium-defects. Therefore, the sample with largest number of defect-states showed highest photocatalytic performance. One year after K. Girija et al.[109] reported improved photocatalytic activity of novel self-assembled monoclinic phased gallium oxide floral nanorods. The authors observed that the synthesized sample exhibits 40.8 m^2/g specific surface area and the energy band gap of 4.59 eV; which played an important role to degrade RhB dye. In same year the same group[86] reported the photocatalytic dye degradation performance of mesoporous β-Ga_2O_3 nanostructures synthesized assisting organic additives. The authors synthesized different morphologies like nanoblocks, nanospindles and nanorods and used RhB as target dye. They addressed the enhanced photocatalytic behaviour of β-Ga_2O_3 nanostructures was due to high surface area, uniform porosity distribution and suitable optical characteristics. Then Shao et al.[88, 89] suggested the photocatalytic degradation of perfluorooctanoic acid (PFA) in pure water and municipal wastewater by needle-like and sheaf-like nanostructured gallium oxide. The authors also compared the photocatalylic performance of the as-synthesized samples with commercial Ga_2O_3 and TiO_2 (P25) under vacuum-UV (VUV) irradiation and identified large specific surface area (25.95 m^2/g) with a lot of nanopores (4–25 nm) as the cause of efficient photocatalytic performance. In 2014, Girija and co-workers[91] reported the photocatalytic decomposition of organic hazards by β-Ga_2O_3 microspheres comprised of nanospheres for

environmental remedy. The authors observed that the synthesized β-Ga$_2$O$_3$ microspheres acquired attractive morphology, suitable particle size (80 nm), high bandgap energy (4.6 eV) and high surface area (82 m^2/g) and those factors were favourable for the effective photocatalytic degradation of RhB and MB (degradation efficiency of 90.45 and 92.65% respectively). Also, they examined the role of different reactive species such as ($\bullet\, O_2^-$), $\bullet\, OH$ and H$^+$ contribute to the photocatalytic degradation. Thereafter in 2015, X. Xu et al.[90] suggested the enhancement of photocatalytic activity by synthesizing porous β-Ga$_2$O$_3$ NWs-rGO hybrids. They used methylene blue (MB) as target dye and proposed that the notable photocatalytic-performance of hybrid samples can be correlated with the enhanced optical absorption band after the incorporation of rGO, inhibiting the recombination of photogenerated e$^-$/h$^+$ pairs induced by the charge transfer between the rGO nanosheets and the porous β-Ga$_2$O$_3$ NWs. In the same year Reddy et al.[92] reported and compared the photocatalytic degradation performance of α-Ga$_2$O$_3$ and β-Ga$_2$O$_3$ nanorods with 180 minutes of UV illumination. In 2016, A. Dulda[93] investigated the importance of alkali type and their addition rate on the particle growth as well as their final size, i.e. morphology and finally the photocatalytic property of as-produced Ga$_2$O$_3$ samples. Further Bagheri and co-worker reported the synthesis of ferric oxide–gallia nanostructures[121] and their photocatalytic performance to degrade an azo dye, Congo red. They performed the reusability test of the catalysts for the photodecoloration of CR with UV light illumination. In 2017, N. Syed and team[122] reported sonication-assisted synthesis and photocatalytic performance of hexagonal α-Ga$_2$O$_3$ nanoflakes using congo red as organic model dye. Authors observed superior photocatalytic performance under solar-light-illumination which may be related with the reduction of energy band gap, as the trap states are located at $\approx$1.65 eV under the conduction band minimum. After that in 2018, Rania E. Morsi[123] prepared stable gallium oxide@ silica/polyvinyl pyrrolidone hybrid nanofluids and investigated its photocatalytic efficiency toward the decomposition of malachite green dye under UV irradiation. Then V. Devthade[124] reported light-driven dinitrogen fixation i.e. the photoreduction of nitrogen to ammonia and dye-degradation ability of graphitic carbon nitride-γ-gallium oxide (GCN-γ-Ga$_2$O$_3$) nano-hybrid photocatalyst under solar light. The authors proposed a suitable photogradation mechanism. In the same year Z. Wang and team[125] examined the effect of pH on β-Ga$_2$O$_3$ microstructures for photocatalytic-antibiotic-degradation. They correlated the results mainly with the morphology and oxygen vacancy of the samples synthesized at different pH values. In 2019, H. J. Bae and team[126] adopted boosted photocatalytic removal of 2-butanone using Ga$_2$O$_3$-rGO hybrid nanostructures under UV-C radiation. The authors observed that the degradation capability of Ga$_2$O$_3$-rGO hybrid sample

was greater compared to Ga_2O_3 and TiO_2-P25 because of the enhanced specific surface area of the former. Further Amdeha et al.[127] reported the formation of Ga_2O_3–TiO_2 nanostructured composites and their photocatalytic dye degradation capacity using RhB as target dye. They investigated the role of hydroxyl radicals (•OH), superoxide radicals (•O_2^-), and hole (h+) in the decomposition of RhB dye; using tertiary-butanol, 1, 4-benzoquinone, and ammonium oxalate, respectively, as scavengers. Also, they performed reproducibility test of the catalysts for RhB photodegradation up to four-cycle experiments maintaining identical concentration of dye (10 ppm), pH (8), and irradiation time (240 min). Also, in the same year C-Y Yeh and team[128] suggested fabrication and photocatalytic activities of α-gallium oxide films using chemical bath deposition taking methylene blue as toxic pollutant. And Carlos R. Michel and co-workers[129] reported the photocatalyst degradation of malachite green dye with α-Ga_2O_3 as catalyst material. In 2020, F. Du et al.[130] suggested the fabrication of Zn-doped Ga_2O_3 nanofibers with different concentrations and observed 5% Zn dopped Ga_2O_3 nanofibers was the best performing samples for the photocatalytic removal of rhodamine B (RhB) dye among the others. After that in 2021, E. S. Ignat'eva et al.[131] reported defect assisted photocatalytic performance of glass-embedded Ga_2O_3 nanocrystals. Then Carlos R. Michel and co-worker[132] reported the photocatalytic ability of β-Ga_2O_3 microcubes for the effective removal of malachite green under violet light (λ = 405 nm), at room temperature. Authors identified that high crystallinity and electron mobility played a crucial role in photocatalytic degradation experiment. In 2022, Orozco et al.[133] reported the photocatalytic decomposition of RhB as model dye using Fe-doped Ga_2O_3 as photocatalyst in presence of two different light sources i.e. visible and UV light; and with three different reaction pH such as 3, 5 and 9. Analysis of the photocatalytic performance of reported works of gallium oxide are presented in **Table 2.1**.

Table 2.1: Comparison between the photocatalysis performances of different gallium oxides reported previously

Material	Average Width/ diameter	Pollutant Concentration	Photocatalyst Concentration (mg/L)	Target Pollutant	Illumination Source	Pollutant degradation with time	Kinetic rate constant K(min^{-1})	Ref.
porous β-Ga$_2$O$_3$	Pore size 7.3 nm	450 ppm	3000	Benzene	four 4 W UV-lamps	~42%	--	[117]
β-Ga$_2$O$_3$ hexagonal nanodisks	Diagonals~ 4.5-5.0 μm and a thickness~ 300 nm	5.0×10^{-5} mol/L	--	Methyl orange	300 W Hg lamp	80% after 12 h	0.145	[119]
β-Ga$_2$O$_3$ nanobelts	Diameter~ 50–90 nm and length~10– 40 mm	10^{-5} M	2600	RhB MB	UV lamp	Almost degraded within 120 min	0.0087 0.0142	[120]
Floral β-Ga$_2$O$_3$ nanorods	1 μm	2×10^{-5} M	1000	RhB	150 W xenon lamp	39% in 1h	--	[109]
α-Ga$_2$O$_3$ nanorods	50-100 nm	0.84×10^{-5} M	1000	RhB	UV lamp	62% in 1h	--	[87]
β-Ga$_2$O$_3$ nanorods	50 nm	2×10^{-5} M	1000	RhB	150 W Xenon lamp	34% in 1h	0.015	[86]
needle-like β-Ga$_2$O$_3$	Length ~3– 6 μm and Width~ 100–200 nm	500 μg/L	5000	PFOA	2 low pressure mercury lamps; 14 W	92% in 3h	0.067	[88]
sheaf-like β-Ga$_2$O$_3$	Length~ 2– 3 μm, diameter~ 0.5-1 μm	500 μg/L	5000	PFOA	2 low pressure mercury lamps; 14 W	100% in 3h	0.0715	[89]
β-Ga$_2$O$_3$ micro spheres	1-3 μm	2×10^{-5} M	1000	RhB	150 W Xenon lamp	60%	--	[91]
(β-Ga$_2$O$_3$ NWs)- (rGO) hybrids	80-90 nm	10^{-5} M	200	MB	mercury lamp 500W	74%	0.0164	[90]
α-Ga$_2$O$_3$ nanorods	300-400 nm	2×10^{-4} M	1000	RhB	100 W UV lamp	35%	--	[92]
β-Ga$_2$O$_3$ nanorods	300-400 nm	2×10^{-4} M	1000	RhB	100 W UV lamp	40%	--	[92]
β-Ga$_2$O$_3$ sheet	--	2.15×10^{-5} M	500	CR	30 W UV lamp	33%	0.005	[134]
Ga$_2$O$_3$ nano particles	400-900 nm	6mg/L	500	RhB	8 W UV lamp	90%	--	[93]
α-Ga$_2$O$_3$ nano plates	(25–250) nm	0.45×10^{-5} M	90	Congo red	AM1.5 1000 W m^{-2} solar simulator	70%	0.016	[122]
α-Ga$_2$O$_3$ nano plates	(25–250) nm	0.45×10^{-5} M	90	RhB	AM1.5 1000 W m^{-2} solar simulator	53%	0.014	[122]

Material	Size	Dose		Dye	Light source	Degradation	Rate constant	Ref
β-Ga₂O₃ /SNF fliuds	~500 nm	25 mg/L	250	MG	8W UV-Vilberlourmat T-8C lamp	--	0.0176	[123]
β-Ga₂O₃	~200 nm in length	20 mg/L 25 mg/L	400	MNZ TC	30 W UV lamp	99.8% in 40 min 99.6% in 100 min	-- --	[125]
Ga₂O₃– TiO₂ Nano-composites	~284 nm²	100 ml of 10 mg/L	1000	RhB	8W UV-Vilber Lourmat T-8C lamp	96%	0.0052	[127]
Gallium oxide thin film	Length~ 1.25 μm, width~ 0.25 μm	0.075 M	--	MB	8 W UV lamp	90% in 5h	--	[128]
α-Ga₂O₃	Length~ 1 μm,	5 x10⁻⁵ M	1000	MG	light emitting diode (LED) with irradiance 80 mW/cm²	50% in 6h	--	[129]
Zn doped Ga₂O₃ nanofibres	Diameter 150-550 nm	10 mg/L	1000	RhB	300 W Xe lamp	92% in 60 mins	0.039	[130]
β-Ga₂O₃ micro-cubes	Side~ 1 μm	5 x10⁻⁵ M	--	MG	light emitting diode (LED) with irradiance 10 mW/cm²	78% in 20 mins	--	[132]

2.2.2. Gas sensors

A lot of research works on Ga_2O_3-based gas sensors have been reported till date. Oxygen partial pressure in the surrounding ambient becomes inversely proportional to the n-type β-Ga_2O_3 polycrystalline films which is crucially used for oxygen sensing purpose. Oxygen deficiency in beta phase-gallium oxide crystal lattice is observed at high temperatures and there exists a dynamic-equilibrium with the surrounded atmospheric-oxygen. Sometimes the variations of the ionized oxygen vacancy concentration may lead to the variations in the conductivity of the sensor. So, whenever an increment of the density of reducing-gases or a decrement of oxygen occur in atmosphere where the sensor is positioned; the conductivity of the material increases due to an enhancement of number of conducting electrons[135]. The linear relation within the conductivity of the sensor material and the oxygen content is valid when the partial pressure becomes greater than 10^{-10} Pa. For low partial pressures the conductivity diminishes rapidly by several orders of magnitude. Fleischer and team[135] proposed that a phase transformation of β-Ga_2O_3 may happens at lower oxygen pressures, but they were not successful to identify any new phase. Although above the temperature 600 °C, oxygen-sensitivity of polycrystalline-Ga_2O_3 remarkably decreases, the films can instead be utilized to detect reducing gases such as hydrogen. Researchers[136] suggested that in ambient atmosphere in the temperature range 400

°C to 600 °C, the following relation holds between film conductance and hydrogen partial pressure:

$$\sigma = \sqrt[3]{P_{H_2}}$$

The authors concluded that the H_2-induced changes in the electrical conductance of β-Ga_2O_3 result from reversible chemisorption of the hydrogen on the whole surface of grains of the polycrystalline Ga_2O_3 with subsequent electron transfer from the adsorbed hydrogen to the Ga_2O_3. Trinchi et al.[137] suggested the synthesis of Ga_2O_3 Schottky diode for efficient hydrogen sensing. They synthesizes Pt/ Ga_2O_3 Schottky junction. They observed that the Schottky barrier height was reduced at Pt/ Ga_2O_3 interface due to the introduction of hydrogen gas and a shift in I-V characteristics was found. It was observed that the relationship between the Schottky barrier height shift and the hydrogen concentration was nearly linear. Also it offers higher relative shift and faster response in sensor output. After that Nakagomi et al.[138] fabricated large response hydrogen sensors based on Pt/Ga_2O_3/SiC structures on p-type and n-type silicon carbide substrates. Under appropriate bias conditions, the sensors can detect up to 40 ppm of hydrogen for certain under 20% O_2/N_2 at 500 °C. Besides the response of Ga_2O_3 for ethanol or propane sensing even at high temperature of 800 °C is also reported[139]. Whereas, the cross-sensitivity to reducing counterparts may be defeated using supplementary catalytic or filter layers. Such as, at high temperatures gallium oxide sensors shield with nickel oxide do not have any response to methane. However polycrystalline gallium oxide gas sensor films are proactive only at higher temperatures as the O_2-vacancies become deactivated/frozen at low temperatures within the material and only the reactions at oxygen defect sites exist at the material surface. Arnold et al.[140] overcame that limitation by demonstrating gas sensors based on Ga_2O_3 nanowires by which the accessible surface area for sensor/analyte interaction was dramatically increased. The sensors had a reversible and rapid responses at room temperature to methanol and acetone, and some limited response to few hydrocarbons like toluene. A more detail review on gas sensors relied on different oxide materials including gallium oxide is published by Moos et al.[139] and Fleischer[141].

2.2.3. Phosphors and luminescent devices

Nowadays gallium oxide has achieved a considerable attention for being a potential phosphor host material used in emissive luminescent devices such as light emitters, fluorescent lamps

etc. There are a lot of disadvantages of traditional sulphide based phosphors including insufficient emissions of primary colours and less chemical stability, particularly in moisture environment. On the other hand, gallium oxide has considerable thermal and chemical stability. Also, sufficient higher electric fields can be employed to the Ga_2O_3 electroluminescent devices due to high electric strength of the same. It can be observed that after activating gallium oxide with transition metals, rare-earths, or other elements; steady luminescence-emissions at several wavelengths take place. To achieve primary colours in full-colour displays, J. H. Kim et al.[142] fabricated manganese doped gallium oxide; and Stodilka et al.[143] and Wellenius et al.[144] synthesized europium doped gallium oxide which in turn produced green and red emissions respectively. A wide emission-peak, centred near 500 nm, was obtained due to Mn doping[145, 146]. In 2000, T. Miyata et al.[146] designed multicolor-emitting phosphors considering gallium oxide as host material for the purpose of thin-film-electroluminescent (TFEL) devices. They activated gallium oxide with a series of rare-earth elements like Eu, Sm, Nd, Ce, Dy, Ho, Er, Tb, Pr, or Tm, a transition metal like Mn, Co or Cr, or other metals like Sn or Bi to obtain multicolor-emitting phosphors. Co, Nd, Cr, Sm, or Eu-activated Ga_2O_3 phosphors provided red colour and Mn, Tb or Ho activated Ga_2O_3 phosphors exhibited green colour emissions were respectively. Activation of Ga_2O_3 phosphors with Ce, Tm or Sn and Dy were responsible for yellow and blue coloured emission, respectively. Moreover, white emission was obtained in Pr-activated Ga_2O_3 TFEL device. To fabricate electroluminescent devices using Ga_2O_3, usually trivalent rare-earth ions are doped as isovalent impurities. Wager and team[147] proposed, whatever be the luminescent impurity, a donor or an acceptor, it highly disturbs the space charge neutrality, resulting wide-band-gap phosphor to introduce new electronic-states into the band gap. Because of this, an electroluminescent device provides a non-ideal characteristics. The especial luminescent properties of trivalent-rare-earth dopants are better manifested in the host materials with a group III cation such as Ga_2O_3. Terbium doped Gallium oxide produced green phosphor with emission line at 543 nm[148]. Also, many research groups fabricated bright red phosphor using europium doping on gallium oxide[149-150]. It is reported that white light emission from gallium oxide nanoparticles may takes place after doping with Eu^{3+} and Tb^{3+} together[151-152] as the host material (Ga_2O_3) itself provide a bright blue emission; and red and green emissions are produced due to Eu^{3+} and Tb^{3+} respectively. The combination of these emission lines is recognized as white light with chromaticity coordinates (0.33, 0.33)[151] or (0.32, 0.36)[152] which matches well in the white region of the CIE chromaticity.

2.2.4. Field-emission properties

Field emission, based on quantum-mechanical tunneling effect, is a popular source of highly-luminous electrons with low energy spread. Those electrons can easily overcome the potential energy barrier and can jump from the Fermi level to vacuum when a sufficient high electric field is employed. A good filed-emission material should possess very low threshold-emission fields and a high emission current density with greater degree of stability. Also, a high field-enhancement factor and a low work function promote to a low threshold electron-emission-field. However, work-function is an intrinsic property of a material, the field-enhancement factor (FEF) primarily depends on the emitter-geometry. For the production of field-emission tips with descending small radius expensive and monotonous top-down approach was performed[153, 154] though most of the emitter exhibit limited lifetime and their performance may be degraded after a short period.

In 2004, Zhan et al[155], investigated the field-emission characteristics of Ga_2O_3-C nanocables for the first time with a turn on field of 7.73 V/μm. The samples had average core diameter ~40 nm and wall thickness ~6 nm. The authors observed that the emission current density was sharply increased near the threshold-field and reached to a maximum value ~722.5 mA/cm^2 with applied electric field of 10 V/μm. Then in 2008, Cao and team[156] suggested the field-emission performances of cactus-like Ga_2O_3 nanostructures comprised of a hollow microsphere and a lot of β-Ga_2O_3 nanowires developed from the surface. The authors found that the turn on fields and the threshold-fields were 12.6 V/μm and 23.2 V/μm respectively. In the same year Bayam and team[157] investigated the field emission properties of rod like Ga_2O_3 nanstructures with ultra-sharp tips. Those special structures exhibited a turn on electric field of ~2.1 V/μm and the threshold-electric field of 5.6 V/μm. Then in 2009, Huang et al.[158] investigated the field-emission behaviors of quasi-aligned gallium oxide nanowires developed on brass wire meshes. The authors highlighted the enhanced field-emission performance of Ga_2O_3 nanowire/brass wire hybrids. Also, they measured the emission-current-density was 10 μA/cm^2 with a turn on field of ~6.2 V/μm and the fluctuation of emission current was within ±13% at a mean field-emission-current-density of ~0.56 μA/cm^2. Further they calculated the field-enhancement factor was about 880 when the distance between cathode to anode was set as 100 μm. That year G Sinha et al.[159] fabricated Ga_2O_3 nanowire arrays on Ga_2O_3 thin films with control growth and investigated their field emission performances. They found the turn on field was to be 1.88 V/μm and the emission-current became stable over 2 h at the pre-set current value of 1μA with the applied field of ~2.2 V/μm. Further in 2012, I. Lo´ pez and team.[160]

studied field emission performances of Sn doped gallium oxide nanostructures. They obtained threshold-field below 1 V/μm and the field-enhancement factor over 4000. Then in 2013, Hsueh et al.[161] studied the electron-field-emission characteristics of gallium compound by ammonification of gallium oxide nanowires. They observed that the threshold field of Ga_2O_3 nanowires was 5.65 V/μm and it became 3.82, 3.03 and 2.12 V/μm after ammonification under 750, 800 and 900 °C respectively. Also they calculated enhancement factor of Ga_2O_3 NWs was around 1700. After few years, in 2019, Grillo and co-workers[162] reported the field emission from gallium oxide nanopillars, etched by Ne^+ ion milling on β-polymorph (100) single crystals. They achieved very high field-emission current density almost 100 A/cm^2 and a turn on field of ~ 30 V/μm. The field enhancement-factor was calculated to be 200 with the cathode-anode distance 1 micron. This literature review demonstrates that the material gallium oxide becomes competitive or sometimes better than other well-known field emitters.

2.3. References

1. M. E. Weeks, Journal of Chemical Education, 9(9) (1932) 1605.

2. J. Åhman, G. Svensson, and J. Albertsson, Acta Crystallographica Section C: Crystal Structure Communications, 52(6) (1996) 1336-1338.

3. G.-S. Park, W. Choi, J.-M. Kim, Y. C. Choi, Y. H. Lee, C. B. Lim, J. Cryst. Growth, 220 (2000) 494–500.

4. H. J. Chun, Y. S. Choi, S. Y. Bae, H. W. Seo, A. S. J. Hong, J. Park, H. J. Yang, Phys. Chem. B, 107 (2003) 9042–9046.

5. E. Chikoidze, C. Sartel, H. Mohamed, I. Madaci, T. Tchelidze, M. Modreanu, P. Vales-Castro, C. Rubio, C. Arnold, V. Sallet, and Y. Dumont, Journal of Materials Chemistry C, 7(33) (2019) 10231-10239.

6. Z. Hajnal, J. Miró, G. Kiss, F. Réti, P. Deák, R. C. Herndon, and J. M. Kuperberg, Journal of applied physics, 86(7) (1999) 3792-3796.

7. M. N. Padvi, A.V. Moholkar, S. R. Prasad, and N. R Prasad, Engineered Science, 15 (2021) 20-37.

8. A. K. Battu, S. Manandhar, V. Shutthanandan, and C. V. Ramana, Chemical Physics Letters, 684 (2017) 363-367.

9. M. G. Ju, X. Wang, W. Liang, Y. Zhao, and C. Li, Journal of Materials Chemistry A, 2(40) (2014) 17005-17014.

10. S. Mitra, Y. Pak, B. Xin, D. R. Almalawi, N. Wehbe, and I. S. Roqan, ACS applied materials & interfaces, 11(42) (2019) 38921-38928.

11. M. Niederberger, G. Garnweitner, Chem. A Eur. J. 12 (2006) 7282–7302.

12. X. Chen, F. Ren, S. Gu, J. Ye, Photonics Res. 7 (2019) 381–415.

13. A. S. Pratiyush, U. U. Muazzam, S. Kumar, P. Vijayakumar, S. Ganesamoorthy, N. Subramanian, D. N. Nath, IEEE Photonics Technol. Lett. 31 (2019) 923–926.

14. V. Nikolaev, V. Maslov, S. Stepanov, A. Pechnikov, V. Krymov, I. Nikitina, L. Guzilova, V. Bougrov, A. Romanov, J. Cryst. Growth, 457 (2017) 132–136.

15. D. Bauman, A. Borodkin, A. Petrenko, D. Panov, A. Kremleva, V. Spiridonov, D. Zakgeim, M. Silnikov, M. Odnoblyudov, A. Romanov, Acta Astronaut. 180 (2020) 125–129.

16. Z. Galazka, Czochralski Method. In Gallium Oxide; Springer: Berlin/Heidelberg, Germany, 2020; pp. 15–36.

17. X. Tao, J. Semicond. 40 (2019) 010401.

18. B. Bayraktaroglu, Assessment of Gallium Oxide Technology; Air Force Research Laboratory, Sensors Directorate WPAFB United States: Wright-Patterson AFB, OH, USA, 2017.

19. M. Higashiwaki, S. Fujita, S. Gallium Oxide: Materials Properties, Crystal Growth, and Devices; Springer Nature: Berlin, Germany, 2020.

20. J. Blevins, D. Thomson, K. Stevens, G. Foundos, In Proceedings of the CSMANTECH, Indian wells, CA, USA, 22–25 May 2017.

21. J. Park, S.-M. Hong, ECS J. Solid State Sci. Technol. 8 (2019) Q3116–Q3121.

22. H. Mohamed, C. Xia, Q. Sai, H. Cui, M. Pan, H. Qi, J. Semicond. 40 (2019) 011801.

23. H. Dislich, J. Non-Cryst. Solids. 80 (1986) 115–121.

24. W. Ji, Y. Zhao, H.M. Fahad, J. Bullock, T. Allen, D.-H. Lien, S. De Wolf, A. Javey, ACS Nano 13 (2019) 3723–3729.

25. T. Miyata, T. Nakatani, T. Minami, Thin Solid Film. 373 (2000) 145–149.

26. A.C. Tas, P.J. Majewski, F. Aldinger, J. Am. Ceram. Soc. 85 (2002) 1421–1429.

27. G. Sinha, D. Ganguli, S. Chaudhuri, S. J. Phys. Condens. Matter 18 (2006) 11167–11176.

28. X. Liu, G. Qiu, Y. Zhao, N. Zhang, R. Yi, J. Alloys Compd. 439 (2007) 275–278.

29. Y. Quan, D. Fang, X. Zhang, S. Liu, K. Huang, Mater. Chem. Phys. 121 (2010) 142–146.

30. R. Gopal, A. Goyal, A. Saini, M. Nagar, N. Sharma, D. K. Gupta, V. Dhayal, Ceram. Int. 44 (2018) 19099–19105.

31. A. K. Saikumar, S. Sundaresh, S. D. Nehate, K. B. Sundaram, ECS J. Solid State Sci. Technol. 11 (2022) 023005.

32. T. Takeuchi, H. Ishikawa, N. Takeuchi, Y. Horikoshi, Thin Solid Films 516 (2008) 4593–4597.

33. M. Ogita, K. Higo, Y. Nakanishi, Y. Hatanaka, Appl. Surf. Sci. 175 (2001) 721–725.

34. J. Wang, H. Zhuang, X. Zhang, S. Zhang, J. Li, Vacuum 85 (2011) 802–805.

35. S. Lee, H. Kang, J. Cryst. Growth 412 (2015) 25–30.

36. A.K. Singh, M. Gupta, V. Sathe, Y. Katharria, Superlattices Microstruct. 156 (2021) 106976.

37. P.H.M.A. Hedei, Z. Hassan, H. J. Quah, Appl. Surf. Sci. 550 (2021) 149340.

38. S.H. Lee, S. Lee, S. C. Jang, N. On, H.-S. Kim, J. K. Jeong, J. Alloys Compd. 862 (2020) 158009.

39. G. Gutierrez, E. M. Sundin, P. G. Nalam, V. Zade, R. Romero, A. N. Nair, S. Sreenivasan, D. Das, C. Li, C. V. Ramana, J. Phys. Chem. C 125 (2021) 20468–20481.

40. H. Lam, M. Hong, S. Yuan, T. Chong, Appl. Phys. A 79 (2004) 2099–2102.

41. S.-L. Ou, D.-S. Wuu, Y.-C. Fu, S.-P. Liu, R.-H. Horng, L. Liu, Z.-C. Feng, Mater. Chem. Phys. 133 (2012) 700–705.

42. H. Yamahara, M. Seki, H. Tabata, J. Cryst. Process Technol. 2 (2012) 125–129.

43. Q. Feng, F. Li, B. Dai, Z. Jia, W. Xie, T. Xu, X. Lu, X. Tao, J. Zhang, Y. Hao, Appl. Surf. Sci. 359 (2015) 847–852.

44. L. M. Garten, A. Zakutayev, J. D. Perkins, B. Gorman, P. F. Ndione, D. S. Ginley, MRS Commun. 6 (2016) 348–353.

45. M. M. Hameed, A.-M. E. Al-Samarai, K. A. Aadim, Iraqi J. Sci. 61 (2020) 2582–2589.

46. P. Jubu, F. Yam, O. Obaseki, Y. Yusof, Mater. Sci. Semicond. Process. 121 (2020) 105361.

47. E. Rubio, T. Mates, S. Manandhar, M. Nandasiri, V. Shutthanandan, C. Ramana, J. Phys. Chem. C 120 (2016) 26720–26735.

48. S. Kumar, C. Tessarek, G. Sarau, S. Christiansen, R. Singh, Adv. Eng. Mater. 17 (2015) 709–715.

49. M.-I. Chen, A. Singh, J.-L. Chiang, R.-H. Horng, D.-S. Wuu, Nanomaterials 10 (2020) 2208.

50. T. Terasako, H. Ichinotani, M. Yagi, Phys. Status Solidi (C) 12 (2015) 985–988.

51. R. Binions, C. Carmalt, I. Parkin, A. K. F. E. Pratt, G. A. Shaw, Chem. Mater. 16 (2004) 2489–2493.

52. M. Valet, D. M. Hoffman, Chem. Mater. 13 (2001) 2135–2143.

53. L. Mîinea, S. Suh, S. G. Bott, J. R. Liu, W. K. Chu, D. M. J. Hoffman, Mater. Chem. 9 (1999) 929–935.

54. I. Zardo, L. Yu, S. Conesa-Boj, S. Estradé, P. J. Alet, J. Rössler, M. Frimmer, P. R. Cabarrocas, F. Peiró, J. Arbiol, Nanotechnology, 20 (2009) 155602.

55. M. Hellwig, K. Xu, D. Barreca, A. Gasparotto, B. Niermann, J. Winter, H.- W. Becker, D. Rogalla, R. Fischer, A. Devi, ECS Trans. 25 (2009) 617.

56. H. W. Kim, N. H. Kim, MOCVD Growth and Annealing of Gallium Oxide Thin Film and Its Structural Characterization. In Materials Science Forum; Trans Tech Publications: Zurich, Switzerland, 475 (2005) 3377–3380.

57. J. -H. Park, R. McClintock, M. Razeghi, Semicond. Sci. Technol. 34 (2019) 08LT01.

58. F. Yang, Modern Metal-Organic Chemical Vapor Deposition (Mocvd) Reactors and Growing Nitride-Based Materials. In Nitride Semiconductor Light-Emitting Diodes (LEDs); Elsevier: Amsterdam, The Netherlands, (2014) 27–65.

59. A. Sarangan, Nanofabrication: Principles to Laboratory Practice; CRC Press: Boca Raton, FL, USA, 2016.

60. C. E. Knapp, G. Hyett, I. P. Parkin, C. J. Carmalt, Chem. Mater. 23 (2011) 1719–1726.

61. X. Hou, K. -L. Choy, Chem. Vap. Depos. 12 (2006) 583–596.

62. C.E. Knapp, I.D. Prassides, S. Sathasivam, I. P. Parkin, C. J. Carmalt, Chem Plus Chem 79 (2013) 122–127.

63. F. E. Annanouch, S. Vallejos, T. Stoycheva, C. Blackman, E. Llobet, Thin Solid Film. 548 (2013) 703–709.

64. D. Yang, B. Kim, T. H. Lee, J. Oh, S. Lee, W. Sohn, E. Yoon, Y. Park, H. W. Jang, ACS Appl. Electron. Mater. 3 (2021) 4328–4336.

65. D. Yang, B. Kim, J. Oh, T. H. Lee, J. Ryu, S. Park, S. Kim, E. Yoon, Y. Park, H. W. Jang, ACS Appl. Mater. Interfaces, 14 (2022) 5598–5607.

66. S.-D. Lee, K. Kaneko, S. Fujita, J. Appl. Phys. 55 (2016) 1202B8.

67. K. Kaneko, H. Ito, S. Lee, S. Fujita, Phys. Status Solidi (C) 10 (2013) 1596–1599.

68. J. Y. Li, X. L. Chen, Z. Y. Qiao, M. He, and H. Li, J. Phys: Condens. Mater. 13 (2001) L937–L941.

69. K. W. Chang and J. J. Wu, Appl. Phys. A 76 (2003) 629–631.

70. L. Dai, X. L. Chen, X. N. Zhang, A. Z. Jin, T. Zhou, B. Q. Hu, and Z. Zhang, J. Appl. Phys. 92 (2002) 1062–1064.

71. N.H. Kim, H.W. Kim, C. Seoul, C. Lee, Mater. Sci. Eng. B 111 (2004) 131–134.

72. H.W. Kim, N. H. Kim, Adv. Appl. Ceram. 105 (2006) 84–87.

73. T. Rajesh, G. Sasikala, S. Sumathi, S. Suguna, Springer: Berlin/Heidelberg, Germany, (2017) 1217–1222.

74. Z. R. Dai, Z. W. Pan, and Z. L. Wang, J. Phys. Chem. B 106 (2002) 902–904.

75. J. H. Zhan, Y. Bando, J. Q. Hu, F. F. Xu, and D. Golberg, Small 1 (2005) 883–888.

76. E. Auer, A. Lugstein, S. Loffler, Y. J. Hyun, W. Brezna, E. Bertagnolli, and P. Pongratz, Nanotechnology 20 (2009) 434017.

77. T. S. Ngo, D. D. Le, J. -H. Song, S. -K. Hong, Thin Solid Film. 682 (2019) 93–98.
78. P. Mukhopadhyay, W. V. Schoenfeld, Appl. Opt. 58 (2019) D22–D27.

79. W. Nunn, T. K. Truttmann, B. Jalan, J. Mater. Res. 36 (2021) 4846–4864.

80. M.-Y.Tsai, O. Bierwagen, M. E. White, J. S. Speck, J. Vac. Sci. Technol. A, 28 (2010) 354–359.

81. S. Ghose, M. S. Rahman, J. S. Rojas-Ramirez, M. Caro, R. Droopad, A. Arias, N. Nedev, J. Vac. Sci. Technol. B Nanotechnol. 34 (2016) 02L109.

82. T. S. Ngo, D. D. Le, J. -H. Song, S. -K. Hong, Thin Solid Film. 682 (2019) 93–98.

83. Y. Zhao, R. L. Frost, and W. N. Martens, J. Phys. Chem. C 111 (2007) 16290-16299.

84. Y. Zhao, R. L. Frost, and W. N. Martens, J. Phys. Chem. C, 111(44) (2007) 16290-16299.

85. Y. Quan, D. Fang, X. Zhang, S. Liu, K. Huang, Mater. Chem. Phys. 121 (2010) 142–146.

86. K Girija, S Thirumalairajan, A.stam K Patra, D Mangalaraj, N Ponpandian, and C Viswanathan, Semicond. Sci. Technol. 28 (2013) 035015.

87. D. Li, X. Duan, Q. qin, H. Fan and W. Zheng, J. Mater. Chem. A, 1 (2013) 12417–12421.

88. T. Shao, P. Zhang, Z. Li, L. Jin, Chinese J. of Catal. 34 (2013) 1551–1559.

89. T. Shao, P. Zhang, L. Jin, Z. Li, Appl. Catal. B: Environ 142–143 (2013) 654–661.

90. X. Xu, M. Lei, K. Huang, C. Liang, J.C. Xu, Z.C. Shangguan, Q.X. Yuan, L.H. Ma, Y.X. Du, D.Y. Fan, H.J. Yang, Y.G. Wan, W.H. Tang, J. Alloys Compd. 623 (2015) 24–28.

91. K. Girija, S. Thirumalairajan, Valmor R. Mastelaro and D. Mangalaraj, J. Mater. Chem. A (2014) DOI: 10.1039/C4TA05295A.

92. L. S. Reddy, Y. H. Ko and J. S. Yu, Nanoscale Res. Lett. 10 (2015) 364.

93. A. Dulda, Adv. Mater. Sci. Eng. 2016, Article ID 3905625, 9 pages.

94. C.-Y. Yeh, Y.-M. Zhao, H. Li, F.-P. Yu, S. Zhang, and D.-S. Wuu, Crystals, 9 (2019) 564.

95. H. J. Bae, T. H. Yoo, Y. Yoon, I. G. Lee, J. P. Kim, B. Jin Cho and W. S. Hwang, Nanomaterials, 8 (2018) 594.

96. C. I. M. Rodríguez, M. Á. L. Álvarez, J. de J. F. Rivera, G. G. C. Arízaga, and C. R. Michel, ECS J. Solid State Sci. Technol. 8 (7) (2019) 3180-3186.

97. A. Ortiz, J. C. Alonso, E. Andrade, and C. Urbiola, 148(2) (2001) 26.

98. T. Ogi, Y. Kaihatsu, F. Iskandar, E. Tanabe, and K. Okuyama, Advanced Powder Technology, 20(1) (2009) 29-34.

99. C. A. Deshmane, J. B. Jasinski, M. A. Carreon, Micro. Meso. Mater. 130 (2010) 97–102.

100. M. F. Al-Kuhaili, S. M. A. Durrani, and E. E. Khawaja, Appl. Phys. Lett. 83(22) (2003) 4533-4535.

101. M. Passlack, N.E.J. Hunt, E.F. Schubert, G.J. Zydzik, M. Hong, J. P. Mannaerts, R. L. Opila, and R. J. Fischer, Appl. Phys. Lett. 64(20) (1994) 2715-2717.

102. A. H. A. Makinudin, T. M. Bawazeer, N. Alsenany, M. S. Alsoufi, and A. Supangat, Mater. Lett. 194 (2017) 53-57.

103. X. C. Wu, W. H. Song, W. D. Huang, M. H. Pu, B. Zhao, Y. P. Sun, and J. J. Du, Chem. Phys. Lett. 328(1-2) (2000) 5-9.

104. G. Domènech-Gil, I. P. Riera, E. López-Aymerich, P. Pellegrino, S. Barth, I. Gràcia, C. Cané, J. D. Prades, M. Moreno-Sereno, and A. Romano-Rodriguez, Multidisciplinary Digital Publishing Institute Proceedings, 1(4) (2017) 468.

105. S. Sharma, and M. K. Sunkara, J. Am. Chem. Soc. 124(41) (2002) 12288-12293.

106. G. S. Park, W. B. Choi, J. M. Kim, Y. C. Choi, Y. H. Lee, and C.B. Lim, Journal of crystal growth, 220(4) (2000) 494-500.

107. Y. C. Choi, W. S. Kim, Y. S. Park, S. M. Lee, D. J. Bae, Y. H. Lee, G. S. Park, W. B. Choi, N. S. Lee, and J. M. Kim, Adv. Mater. 12(10) (2000) 746-750.

108. K. M. Al-Khamis, R. M. Mahfouz, A. A. Al-Warthan, and M. R. H. Siddiqui, Arab. J. Chem. 2(2) (2009) 73-77.

109. K. Girija, S. Thirumalairajan, A. K. Patra, D. Mangalaraj, N. Ponpandian, C. Viswanathan, Curr. Appl. Phys. 13 (2013) 652-658.

110. J. J. Shan, C. H. Li, J. M. Wu, J. A. Liu, and Y. S. Shi, Ceram. Int. 43(8) (2017) 6430-6436.

111. B. Zheng, W. Hua, Y. Yue, and Z. Gao, Journal of Catalysis, 232(1) (2005) 143-151.

112. K. Sasaki, M. Higashiwaki, A. Kuramata, T. Masui, and S. Yamakoshi, Applied Physics Express, 6(8) (2013) 086502.

113. Y. Hou, L. Wu, X. Wang, Z. Ding, Z. Li, and X. Fu, Journal of Catalysis, 250(1) (2007) 12-18.

114. T. Oshima, K. Kaminaga, H. Mashiko, A. Mukai, K. Sasaki, T. Masui, A. Kuramata, S. Yamakoshi, and A. Ohtomo, Japanese journal of applied physics, 52(11R) (2013) 111102.

115. S.-J. Chang, Y.-L. Wu, W.-Y. Weng, Y.-H. Lin, W.-K. Hsieh, J.-K. Sheu and C.-L. Hsu, J. Electrochem. Soc. 161 (2014) H508.

116. N. K. Shrestha, K. Lee, R. Kirchgeorg, R. Hahn and P. Schmuki, Electrochem. commun. 35 (2013) 112.

117. Y. Hou, X. Wang, L. Wu, Z. Ding, And X. Fu, Environ. Sci. Technol. 40 (2006) 5799-5803.

118. L. Yuliati, H. Itoh, and H. Yoshida, Chemical Physics Letters, 452(1-3) (2008) 178-182.

119. H. Yang, R. Shi, J. Yu, R. Liu, R. Zhang, H. Zhao, L. Zhang, and H. Zheng, The Journal of Physical Chemistry C, 113(52) (2009) 21548-21554.

120. L.-C. Tien, W.-T. Chen, and C.-H. Ho, J. Am. Ceram. Soc., 94 [9] (2011) 3117–3122.

121. M. Bagheri, and A. R. Mahjoub, RSC Adv 6 (90) (2016) 87555–87563.

122. N. Syed et al. Adv. Funct. Mater. 2017, 1702295.

123. R. E. Morsi, and R. A. El-Salamony, Journal of Molecular Liquids, 297 (2020) 111848.

124. V. Devthade, A. Gupta, and S. S. Umare, ACS Applied Nano Materials, 1(10) (2018) 5581-5588.

125. J. Liu, W. Lu, Q. Zhong, H. Wu, Y. Li, L. Li, and Z. Wang, 519 (2018) 255-262.

126. H. J. Bae, T. H. Yoo, S. Kim, W. Choi, Y. S. Song, D.-K. Kwon, B. J. Cho, and W. S. Hwang, Catalysts, 9 (2019) 449.

127. E. Amdeha, R. A. El-Salamony, A. M. Al-Sabagh, (2019) DOI: 10.1002/aoc.5336.

128. C-Y Yeh, Y.-M. Zhao, H. Li, F.-P. Yu, S. Zhang, and D.-S. Wuu, Crystals, 9 (2019) 564.

129. C. I. M. Rodríguez, M. Á. L. Álvarez, J. de J. F Rivera, G. G. C. Arízaga, and C. R. Michel, ECS J. Solid State Sci. Technol. 8 (7) (2019) Q3180-Q3186.

130. F. Du, D. Yang, Y. Sun, Y. Jiao, F. Teng, H. Fan, Ceramics International 47 (2021) 4963–4971.

131. R. Lorenzi, N. V. Golubev, E. S. Ignat'eva, V. N. Sigaev, C. F. Maurizio Acciarri, G. M. Vanacore, A. Paleari, Journal of Colloid and Interface Science 608 (2022) 2830–2838.

132. C. R. Michel, A. H. Martínez-Preciado, Ceramics International 48 (2022) 9746–9752.

133. S. Orozco, M. Rivero, E. Montiel and J. Espino Valencia, Frontiers in Environmental Science, 10 (2022) 884758. DOI: 10.3389/fenvs.2022.884758.

134. M. Bagheri et al. RSC Adv. 6 (2016) 87555.

135. M. Fleischer et al. Am. Cerain.Soc. 80 (1997) 2121.

136. M. Fleischer J. Giber, and H. Meixner, Applied Physics A, 54(6) (1992) 560-566.

137. A. Trinchi, W. Wlodarski, and Y. X. Li, Sensors and Actuators B: Chemical, 100(1-2) (2004) 94-98.

138. S. Nakagomi, K. Yokoyama and Y. Kokubun, Journal of Sensors and Sensor Systems, 3(2) (2014) 231-239.

139. R. Moons, N. Izu, F. Rettig, S. Reiß, W. Shin and I. Matsubara, Sensors, 11(4) (2011) 3439-3465.

140. S. P. Arnold, S. M. Prokes, F. K. Perkins, and M. E. Zaghloul, Applied Physics Letters, 95(10) (2009) 103102.

141. M. Fleischer, Measurement Science and Technology, 19(4) (2008) 042001.

142. Y. J. Oh, Y. M. Lee, J. H. Kim, H. S. Ahn, J. W. Kim, H. R. Park, J. S. Seo, K. W. Kim, O. R. Kwon, H. K. Park, and E. J. Lee, Korean Journal of Community Nutrition, 13(4) (2008) 499-509..

143. D. Stodilka, A. H. Kitai, Z. Huang, and K. Cook, (2000) In SID Symposium Digest of Technical Papers (Vol. 31, No. 1, pp. 11-13). Oxford, UK: Blackwell Publishing Ltd.

144. G. Wei, K. T. Shiu, N. C. Giebink, and S. R. Forrest, Appl. Phys. Lett. 92, 066101 (2008).

145. T. Minami, T. Shirai, T. Nakatani, and T. Miyata, Japanese Journal of Applied Physics, 39(6A) (2000) L524.

146. T. Miyata, T. Nakatani, and T. Minami, Journal of Luminescence, 87 (2000) 1183-1185.

147. J. F. Wager, J. C. Hitt, B. A. Baukol, J. P. Bender, and D. A. Keszler, Journal of luminescence, 97(1) (2002) 68-81.

148. Y. Tokida, and S. Adachi, ECS Journal of Solid State Science and Technology, 3(6) (2014) R100.

149. J. S. Kim, H. E. Kim, H. L. Park, and G. C. Kim, Solid state communications, 132(7) (2004) 459-463.

150. P. Wellenius, A. Suresh, J. V. Foreman, H.O. Everitt and J.F. Muth, Materials Science and Engineering: B, 146(1-3) (2008) 252-255.

151. P. Patil, J. Park, S.Y. Lee, J. Park and S. Cho, Appl. Sci. Conv. Technol. 23 (2014) 296.

152. G. Sinha and A. Patra, Chemical Physics Letters, 473(1-3) (2009) 151-154.

153. I. Brodie, and C. A. Spindt, (1992) Vacuum microelectronics. In Advances in electronics and electron physics (Vol. 83, pp. 1-106). Academic Press.

154. C.A. Spindt, et al. IEEE Transactions on Electron Devices, vol. 38(10) (1991) 2355-2363.

155. J. Zhan, Y. Bando, J. Hu, Y. Li, and D. Golberg, Chemistry of materials, 16(24) (2004) 5158-5161.

156. C. Cao, Z. Chen, X. An, and H. Zhu, The Journal of Physical Chemistry C, 112(1) (2008) 95-98.

157. Y. Bayam, L. VJ1, A. M. Katzenmeyer, R. J. Chacon, M. C. Wong, C. E. Hunt, and M. Saif Islam, (2008)

158. Y. Huang, Z. Wang, Q. Wang, C. Gu, C. Tang, Y. Bando, and D. Golberg, The Journal of Physical Chemistry C, 113(5) (2009) 1980-1983.

159. G. Sinha, A. Datta, S. K. Panda, P. G. Chavan, M. A. More, D. S. Joag, and A. Patra, Journal of Physics D: Applied Physics, 42(18) (2009) 185409.

160. I. López, E. Nogales, P. Hidalgo, B. Méndez, and J. Piqueras, Physica status solidi (a), 209(1) (2012) 113-117.

161.   Han-Ting Hsueh et al. IEEE transactions on nanotechnology, 12(5) (2013) 692-695.

162.   Alessandro Grillo et al. Appl. Phys. Lett. 114 (2019) 193101.

Chapter 3

Instruments and Apparatus

In the recent times production of nanostructured materials has acquired significant attention of the scientific community by virtue of their novel properties and numerous applications. This chapter covers three major sections; first part is the general description of main synthesis apparatus, second part is the major characterizing accessories and the third part is the illustration of the crucial application apparatus. Preparation of nanomaterials is being advanced by simple chemical route. Instead of using heavy and costly physical techniques, chemical synthesis process was chosen to fabricate the nanostructures. Stirrer with oil-bath heating, autoclave, furnace, and oven were mainly used to synthesize different mesoporous Ga_2O_3 and its heterostructures.

Along with this, a brief description of various characterization tools is given which were utilized to investigate different properties of the as-synthesized nanomaterials. X-ray diffractometer (XRD), X-ray Photo-electron Spectroscopy (XPS) and Energy Dispersive X-ray Spectroscopy (EDX) were used to examine structural and compositional properties of the samples. Whereas, Field Emission Scanning Electron Microscope (FESEM) and High Resolution Transmission Electron Microscope (HRTEM) were utilized to investigate morphological characterization. Specific surface-area as well as porosity distribution features of the prepared samples were examined using Brunauer-Emmett-Teller (BET) surface analyser. Further the structural, bond related information and band-gap values of the samples were analysed employing Raman spectroscopy, FTIR spectroscopy and UV-Vis spectrophotometer respectively. Also the Mott-Schottky studies were performed in PGSTAT302 N AUTOLAB electrochemical workstation in a three-electrode system to obtain flat band potentials of the samples.

Further, a discussion about the apparatus for photocatalytic decomposition of organic dyes and inorganic pollutants from waste water is mentioned here. Also, the description of the laboratory-made ultra-high vacuum field emission measurement setup for analysing the cold-cathode emission properties of the pristine and composite samples is included in this chapter.

3.1. Synthesis techniques of nanomaterials

3.1.1. Magnetic stirrer with oil bath set-up

A magnetic stirrer can be used to prepare a uniform suspension in a glass-beaker with magnetic bead. The required solution was placed on the stirrer with an oil bath set-up as depicted in **Figure 3.1**. The temperature and the revolutions per minute (r.p.m.) of the magnetic stirrer can be easily controlled. Also the oil bath can produce a uniform heating

over the whole solution and a thermometer may be used to measure the temperature of the solution. The targeted nanomaterials can be easily achieved by this simple and cost-effective route. Brick-like gallium oxide hydroxide were prepared by a simple oil bath heating method with magnetic stirring. The solution temperature was maintained 105 °C.

3.1.2. Furnace and Oven

A simple muffle furnace was employed to achieve solid state reactions or annealing of the samples in open air. The furnace was front-loading type and its temperature range

Figure 3.1 Magnetic stirrer with hot-oil bath set-up

was up to 1100 °C. The heating rate of the furnace can be controlled with a precision of ± 0.2 °C by an electronic temperature controller and the samples were generally loaded with the help of alumina boat or crucible.

For hydrothermal or wet chemical reaction, where the reaction temperature was below 250 °C, simple hot air oven were used. Thermostat attached with these ovens controlled the temperature. Apart from synthesis purpose the ovens were used for drying the sample also. The photograph of a furnace and oven has been shown in **Figure 3.2**.

3.1.3. Autoclave

Hydrothermal method has become a commonly used synthesis techniques for the production of metal oxide nanostructures because of their unique advantages in the synthesis. For a typical hydrothermal reaction an autoclave is used. Synthesis of gallium oxide nanostructures and its graphene hybrid,

Figure 3.2 Digital photograph of box furnace and Oven

following the reduction of GO to rGO, were achieved using autoclave apparatus as shown in **Figure 3.3**. An autoclave is a specially designed pressurized reactors to heat aqueous

solutions or organic solvents above their boiling point at a pressure higher than normal atmospheric pressure. It basically consists of two different parts: Teflon-lined inner part and an outer stainless steel case. The inner part can easily fit into the outer part which can resist high pressure during a reaction. A cylindrical Teflon tube with a Teflon cap, which serves as the inert reaction chamber, was fitted inside the iron chamber with an iron screw cap.

Figure 3.3 Photographs of autoclave arrangement (a) and Teflon tube inside the autoclave (b)

3.2. Characterization techniques of nanomaterials

3.2.1. X-Ray diffractometer (XRD)

In 1895, W.C. Röntgen discovered X-rays. The X-ray Diffraction (XRD) techniques, involving the elastic scattering of X- rays from crystalline specimen, were developed to investigate the structural properties of materials. These techniques demonstrate single-crystal X-ray diffraction (SCD) and powder X-ray diffraction (PXRD). Single-crystal X-ray diffraction method may be utilized to resolve the structure of already known or new materials. As a consequence, it is very important appliance in the field of chemical research from pharmaceutical products to mineralogy, or from catalysts to macromolecules[1, 2]. However SCD is cumbersome and time-taking process and also it prescribes a high degree of homogeneity to the crystal which is under observation. So, to

Figure 3.4 Photograph of X-ray diffractometer

defeat analogues difficulties, PXRD was put forward to investigate the crystal structure, crystallite size, stress and strain measurement, the study of phase equilibrium and the distribution of crystalline planes in polycrystal or powdered crystalline materials[3, 4]. A Bruker X-ray diffractometer (XRD, BRUKER D8 ADVANCE) was employed to characterize as-synthesized samples. **Figure 3.4** indicates the digital photograph of that instrument. **Figure 3.5** illustrates the basic working mechanism of XRD device. X-ray diffractmeter consists of three basic components: (a) an X-ray tube; the source of X-ray, (b) a sample holder to hold the analysing samples, and (c) an X-ray detector. The diffraction traces were noted in intensity vs. 2θ mode. Germanium monocromator, exhibiting (022) plane, was employed for Cu Kα (1.5406 Å) radiation from an ultra-stabilized Bruker X-ray generator (K 780). Lattice spacing can be derived from the diffraction applying Bragg's equation for first order diffraction[5]:

$$2d \sin \theta = n\lambda \qquad (3.2.1)$$

Where d represents spacing amidst consecutive parallel planes, θ be the glancing angle, n represents the diffraction order and λ is the wavelength of the X-rays. The standard powder diffraction files, published by JCPDS, can be efficiently used to correlate the experimentally observed diffraction patterns of the samples. The average crystallite size of the samples was obtained applying the Scherrer's formula[6],

$$d = \frac{0.9\lambda}{\beta \cos \theta} \qquad (3.2.2)$$

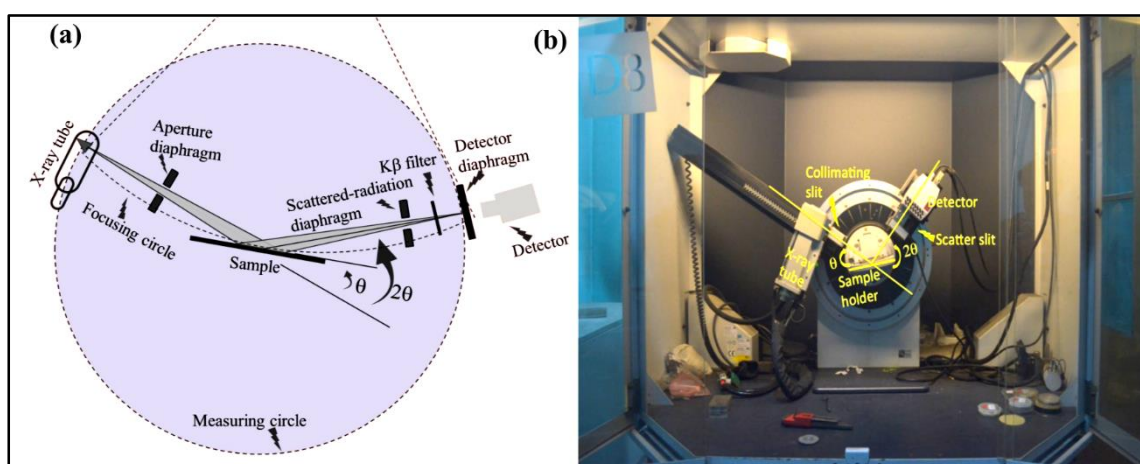Where λ represents X-ray wavelengths and β be the full width at half maximum intensity expressed in radians.

Figure 3.5 (a) Schematic illustration and (b) digital photograph of X-ray diffractometer

3.2.2. X-ray photoelectron spectrometer (XPS)

Chemical Composition of the nanomaterials, charge state or valency of the elements of any composite nanostructures, and purity of sample were investigated by X-ray photoelectron spectroscopy (XPS, Specs, Germany). Basic principle of X-ray photoelectron spectroscopy embraces illuminating the sample using a known energy X-ray beam which helps to emit the photoelectrons from the sample. The mechanism of photoelectron emission is schematically presented in **Figure 3.6a.** The relationship connecting the kinetic energy (E_k) of ejected photo-electrons and their binding energy (E_B) is mentioned below,

$$E_B = h\nu - E_k \qquad (3.2.3)$$

Where, $h\nu$ represents the energy of X-ray photon and the number of emitted electrons can be determined as a function of that energy.
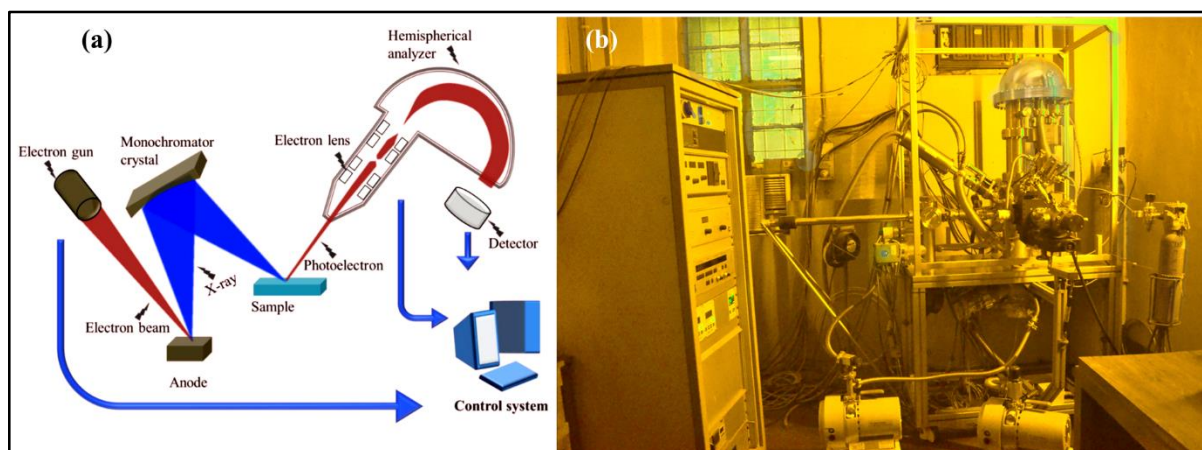

Figure 3.6 (a) Schematic layout of working principle of photoelectron emission and (b) the digital photograph of XPS instrument

As a particular element has a specific set of binding energies, XPS can be the most reliable technique to recognize the surface elements. Additionally, area under the curve at minimal binding energies can be exploited to estimate elemental concentration in the sample. One can easily get the details about the chemical states as well as short-range chemistry of any sample analysing chemical shifts i.e. the slight shifts in those binding energies. Sample scanning was executed on the SPECS with hemispherical energy analyser (HAS 3500) and the photoelectron excitation was achieved by the monochromatic Mg K_α X-ray (1253.6 eV) or Al K_α X-ray (eV) source worked at 10 kV and 17 mA anode current. The residual pressure of the system was almost 10^{-9} mbar. In spectroscopy mode, electrons are dispersed between the inner and outer hemispheres. A 165 mm radius and an eight-channel detector ensure high spectral resolution and excellent sensitivity. Thus, the total count of released photoelectrons

as a function of their kinetic energies i.e. the ejected photo-electron's K.E. distribution can be determined and the resulted spectrum can be recorded. The photograph of the X-ray photoelectron spectroscopy is shown **Figure 3.6b.**

3.2.3. Electron microscope

Electron microscopy is highly efficient and frequently applied technique for the characterization of nanostructured materials. In 1939 German scientist Ernst Abbe discovered optical microscopes. The main drawback of the optical microscope is the limited imaging resolution which relies on the wavelength of participating sources i.e. visible light. To overcome that difficulties transmission electron microscope was developed where visible light source was replaced by the source of electrons. In 1927, French physicist Louis de Broglie[7] predicted the wave-particle duality hypothesis for material particles such as electron, proton etc. After that two different research groups, Davisson & Germer[8] and Thomson & Reid, independently accomplished the electron diffraction experiment that proved the wave nature of electrons[9] experimentally. Two main criterions are there to promote the electron microscopes instead of the optical microscopes (OM). Firstly, the electromagnetic lenses inside the microscope column can easily and efficiently manipulate the electrons. Secondly, the electrons possess very small wavelengths which can provide an improved resolution as compared to that of OM. So, the wavelength of the source plays a critical role to deliver a better resolution of the microscopes. From de Broglie hypothesis it can be written,

$$\lambda = \frac{h}{p} \tag{3.2.4}$$

Where h is the Planck's constant (6.624×10^{-34} J-S), λ is the wavelength associated with a beam of electrons of momentum p.

Considering the K. E. of the electrons emitted from electron gun with an accelerating potential difference (V), the wavelength of the relativistic electron is to be expressed as,

$$\lambda = \frac{h}{\left[2m_0 eV + \left(1 + \frac{eV}{2m_0 c^2}\right)\right]^{1/2}} \tag{3.2.5}$$

In non-relativistic case the wavelength of the electron becomes, $\lambda = \frac{h}{\sqrt{2m_0 eV}}$

Also, the relativistic effects must be considered when energies become greater than 100 KeV as in that case the electron's velocity may nearly equal to the speed of light. For energy= 100

KeV, the value of $\lambda \sim 10^{-12}$ m, which is of the order of atomic separation and this is the basic reason behind the high resolution imaging capability of the electron microscopes.

3.2.3.1. Field emission scanning electron microscope (FESEM)

Manfred von Ardenne was the pioneer of scanning electron microscope and in 1939 he constructed the universal electron microscope. Field emission scanning electron microscope (FESEM) is a high resolution imaging technique which is operated under high vacuum and a field emission source involves to generate the required electrons accelerated in a field gradient. Within the high vacuum column electromagnetic lenses were placed to focus and deflect the erected primary electrons for the construction of a perfect narrow scan beam. The electron beam collides on the sample surface and due to that interaction both electrons and photons are emitted from the sample. The exchange in energy through the sample and electron beam results the secondary electron emission by inelastic scattering, emission of electromagnetic radiation and reflection of high energy electrons by elastic scattering. These can be collected by specific detectors and have been converted into signals which contain the particulars about sample's surface topography, morphology, composition etc. The electrons are emitted from the field emission gun with an energy varying from few hundred to 30 KeV. For conventional imaging in the FESEM, sample under investigation must be electrically conductive as it prevents the assemblage of electronic charge-carriers at the surface. For nonconductive specimens, ultrathin coating of gold/platinum is deposited over the sample using sputtering or evaporation techniques before the process of imaging[10].

> ➢ **Interaction of electrons with matter**

There are various kinds of interactions between electrons and matter; and different energy transfer mechanisms are involved as a consequence of that interactions (**Figure 3.7a**). They can be categorised into two classes, (i) elastic and (ii) inelastic interactions.

In case of elastic interactions, no exchange of energy takes place between electron and the sample. For this, the electron emitting from the sample can retain its original energy. Elastic scattering occurs due to the deflection of electron's route by Coulomb interaction with the positive potential inside the electron cloud.

Further the secondary electrons are produced by the inelastic interaction between the incident electrons and the outer electrons of the atoms which are not strongly bound. When the energy

81

of the atoms become lower than 50 eV, ejection of those outer electrons happens. Whenever the "secondary" electrons are generated near the surface, and their energy becomes greater than the surface-energy (~6 eV) then, they can reach the detector by escaping into the vacuum[11]. Also, while traveling through the atom's electron cloud, an electron can transfer a portion of its energy to the former, and it may occurs that transferred energy is adequate to eject an electron from the localised atom to vacuum. After that these vacancies are easily filled when any electron from the higher level drops down to achieve the energetically favourable ground state. Following this process, the atom may release the excess energy in the form of a characteristic X-ray. However, sometimes an outer shell electron may absorbs the released photon and immediately ejected out from the atom, therefore an Auger electron generates.

When an electron get decelerated due to the Coulomb force of the nucleus while passing through atom's electron cloud. This inelastic interaction produces continuous X-rays which accommodate any amount of energy up to that of the incident beam. The resulted X-rays are named as Bremsstrahlung X-rays. In the spectroscopic purpose, the characteristic X-rays are employed both in a TEM and a SEM to obtain the energy dispersive X-ray (EDX) chemical mapping.
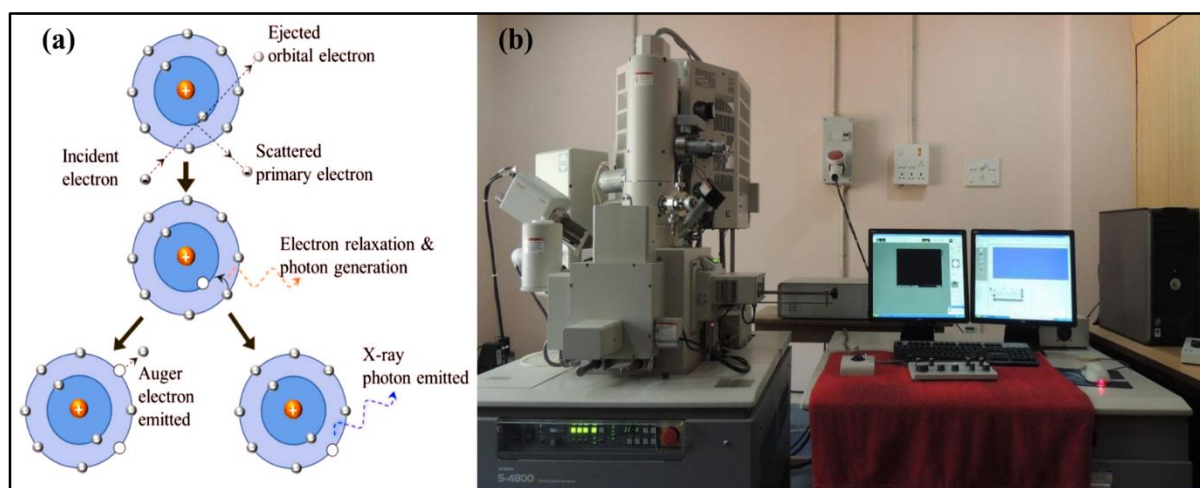

Figure 3.7 (a) Schematic depiction of different interaction between electron and matter and (b) the photograph of FESEM instrument (S-4800, Hitachi)

Detail morphological studies of the gallium oxide and its hybrids' nanostructures were conducted using a FESEM (FESEM, S-4800, Hitachi) instrument. The resolution of the instrument was 2 nm (Accelerating voltage 1 kV) and 1 nm (Accelerating voltage 15 kV). The accelerating voltage lay in the range 0.5 to 30 kV (in 100 V steps). The magnification can be regulated from 30 X to 3,000 X (low magnification mode) and 100 X to 800,000 X

(high magnification mode). The photograph of the FESEM instrument is shown in **Figure 3.7b**. The sample can be easily prepared by coating with a few nm layer of conductive material, such as gold, or platinum, from a sputtering machine.

3.2.3.2. Energy dispersive X-ray spectroscopy (EDS)

Energy Dispersive X-Ray Spectroscopy (EDS), also known as EDX or EDAX, is a chemical microanalysis approach employed in combination with field emission scanning electron microscopy (FESEM) or transmission electron microscopy (TEM). In this technique a focused beam of electrons is bombarded to the sample to generate X-ray photons which is used to achieve a localized chemical analysis. The elements with atomic number 4(Be) to 92(U) can be identified using this method. Therefore, the EDS method encounters the characteristic X-rays emitted from the target material in the time of bombardment by an electron beam and facilitates to find out the elemental composition of that sample which may be as small as 1 micron or less.

An electron from any higher energy level may jump in to any lower energy level if already a vacancy exists there which may be generated by any means such as bombardment of incident electron beam etc. Then the surplus energy releases in the form of characteristic X-ray electromagnetic radiation presented in **Figure 3.8**. Firstly, the incident electron supplies a sufficient amount
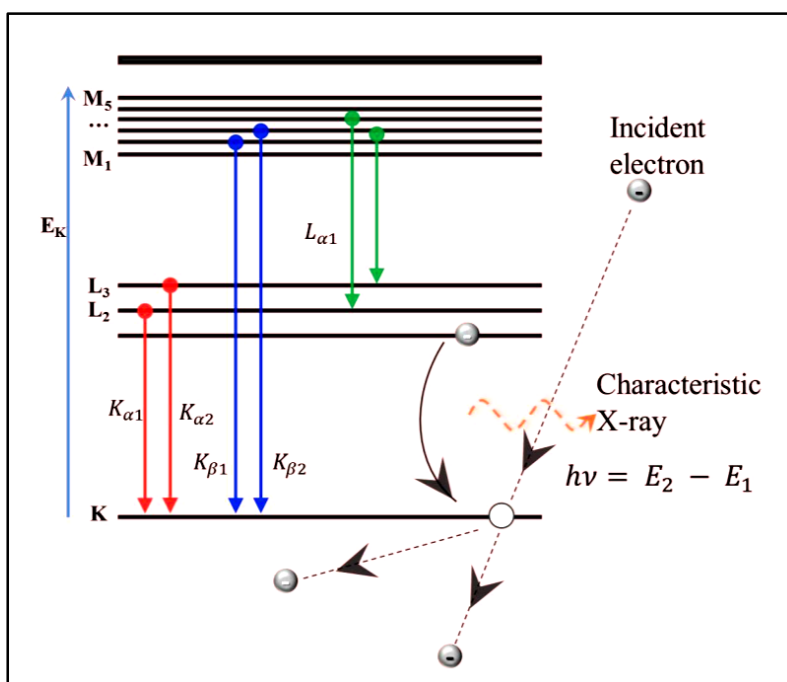

Figure 3.8 Production of characteristic X-ray photon

of energy to an inner shell electron such that the atom becomes able to ionize i.e. that inner shell electron may kick out into vacuum or transfer to lower unoccupied level leaving a vacancy there (considering K shell here). After that, a higher state electron, may be from L3 level, drops down to fill that vacancy. Then the excess energy is emitted in the form of X-ray quanta. It is well-known that a particular element has a characteristic number of electrons

confined in distinct energy states. As a consequence, the difference in energies between those states i.e. the energies of emitted characteristic X-ray photons are typical for that element. Also it is evident that more number of electrons produces more transitions.

The EDS X-ray detector is basically a solid state device which can be a lithium-drifted silicon. It counts the relative adequacy of the X-rays emitted vs. their energy. While the emitted X-ray hits the detector, a charge pulse is generated which is proportional to the energy of X-ray. Then, a charge sensitive pre-amplifier is used to transform the charge pulse into the voltage pulse that is still proportional to the energy of X-ray photon. After that, the signal is received by a multi-channel analyzer which sorts the pulses by voltage. For individual incident X-ray, the energy obtained from voltage measurement is forwarded to a computer to evaluate data and display them. Now, to detect the elemental composition of the samples, the X-ray energy spectrum versus counts is examined. EDX is an attachment of FESEM instrument and the digital image is shown in (**Figure 3.7**).

3.2.3.3. High resolution transmission electron microscope (HRTEM)

Transmission electron microscope (TEM) is the characterization equipment which is use to investigate crystal structure and the microstructure of any material simultaneously by diffraction and imaging technique. High resolution transmission electron microscopy (HRTEM) is another imaging mode of the transmission electron microscope (TEM) that gives more precise and resolute images of the crystallographic structure of the sample at an atomic scale. The earliest model of electron microscope was designed by Ruska and Knoll, in 1931. Then, in 1938, Eli Franklin Burton constructed the first empirical electron microscope. After that finally in 1939, Siemens and team built the first commercial TEM[12-14].

In this section, we will elaborate the basic mechanism of high resolution transmission electron microscopy (HRTEM) and selected area electron diffraction (SAED). The information about the microstructures, lattice spacing as well as electron diffraction patterns of the samples can be obtained following this investigation. In case of the imaging mode, presented in **Figure 3.9b,** firstly the intermediate lens is utilized to form the image which is at the first focal plane behave as the object of projector lens and further gets magnified. In this mode SAED aperture is not required, but occasionally insertion of the objective aperture becomes useful which is placed behind the focal plane of the objective lens (**Figure 3.9b**) and assists to choose a suitable area of the diffraction pattern. Also by altering the position of this aperture two different imaging modes can be obtained. **Figure 3.9a** represents the diffraction

mode where the intermediate lens is selected so that it considers the back focal plane (of the objective lens) as its object, whereas in the imaging mode, **Figure 3.9b,** the image plane (of the objective lens) acts as an object for the intermediate lens. **Figure 3.9c** shows a picture of TEM (JEOL- JEM-2100), which is used to examine the growth and microstructure of the powder samples. The JEM-2100 exhibits three individual condenser lenses and generates the maximum probe current for a particular probe size, which allows for improved analytical and diffraction capabilities. It has three pumping options including rotary, diffusion and sputtering ionization pump (SIP). The resolution of the instrument is 1.7 Å.

The resolution achieved at the time of routine measurements was 8 – 10 Å. Magnification in this instrument can be regulated from 50 X to 1,500,000 X with accelerating voltage 160 - 200 kV. TEM samples were prepared by dropping the suspension of the sample onto a carbon coated copper grid (with different mesh size) and allowing the solvent to evaporate.
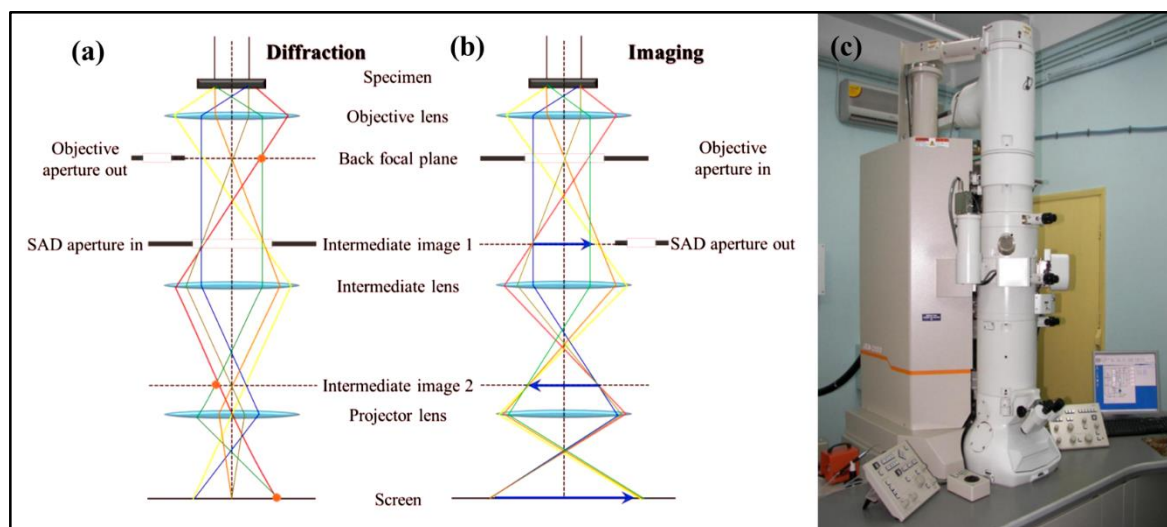

Figure 3.9 Diagrammatic presentation of the lenses and apertures in diffraction mode (a) and imaging mode (b), respectively. (c) Photograph of HRTEM instruments (JEOL-JEM-2100)

3.2.4. BET surface analyser

The Brunauer-Emmett-Teller (BET) theory forms the basis of one of the most significant analyses to investigate the surface features of nanostructured materials involving the process of adsorption of gases on solid surfaces. This theory basically focuses on the physical adsorption or physisorption of the gas molecules on sample surface to determine the specific surface area and pore size distribution of the materials. In 1938, BET theory was presented in the Journal of the American Chemical Society[15] by three scientists: Stephen Brunauer, Paul Hugh Emmett, and Edward Teller. For BET measurement a probing gas is required, usually known as adsorbate that should be chemically inert with the material (called adsorptive) upon

which the multilayer adsorption is employed. Generally nitrogen gas is used as adsorbate to probe the experimental surface. Due to this, the standard BET analysis is commonly performed at 77K which is the boiling point of nitrogen. The specific surface area of any sample can also be determined at different temperature and measurement scale by varying the probing adsorbate which may be water, argon, carbon dioxide etc. So, the specific surface area is a scale dependent property rely upon the utilized adsorbate molecule and its adsorption cross-section and it can be concluded that no single true value of it can be detectable. The schematic diagram and digital photograph of BET surface analyzer are shown in **Figure 3.10**.
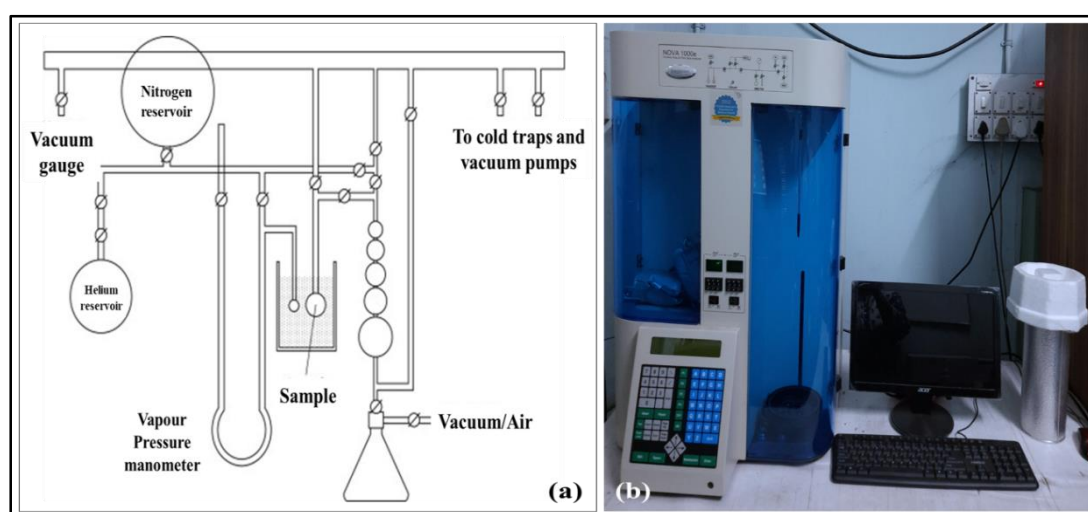

Figure 3.10 (a) Schematic representation of the apparatus (b) digital photograph of BET surface analyser.

BET theory is an addendum of Langmuir model only surveying the adsorption of multi-layered gas molecules where the formation of the upper layer can be initiated before the completion of a particular layer. Few assumptions are listed below[16]:

a. Adsorption happens on only the distinct sample-surface sites (one per molecule)

b. Only the interaction of a molecule in single adsorption site with the other of the upper layer is permissible

c. The adsorption and desorption rate is equal i.e. the topmost molecular layer maintains equilibrium with the vapour phase

d. A heat of adsorption must be supplied, as desorption is a kinetically limited procedure: this process is homogeneous i.e. a given molecule layer exhibits the same heat of adsorption; the heat of adsorption at the solid surface (for first layer) of the sample can be considered as E_1; the other layers can also be regarded as liquid or condensed species. And the adsorption heat equals liquefaction heat, thus $E_1 = E_L$.

e. The number of molecule layers tends to infinity at saturation pressure (i.e. analogous to the sample were encompassed by a liquid phase).

In a controlled atmosphere, a particular volume of solid sample is considered. Also consider i number of successive molecule layers may provide a fractional coverage θ_i of the sample surface. Assume the adsorption rate of $(i-1)^{th}$ molecular layer, $R_{ads,i-1}$, is proportional to the pressure P and fractional surface θ_i and also the desorption rate $R_{des,i}$ on a layer i is also proportional to θ_i

$$R_{ads,i-1} = k_i P \Theta_{i-1} \qquad (3.2.6)$$

$$R_{des,i} = k_{-i} \Theta_i \qquad (3.2.7)$$

For adsorption on layer (i-1), k_i is the kinetic constant and for desorption on layer i, k_{-i} is the kinetic constant and both of them are temperature dependent. The constants may be expressed following the Arrhenius law is given below:

$$k_i = \exp(-E_i/RT) \qquad (3.2.8)$$

Where E_i represents heat of adsorption which becomes E_l at the sample surface and E_L otherwise.

Adsorption capacity and catalytic activity of any samples are highly interconnected with the surface property of the same. Applying the BET method, the specific surface area and pore diameter of gallium oxide samples were calculated which results ~30 m^2/g surface area with mesoporous nature. Those materials can be employed as efficient catalyst materials.

3.2.5. Optical Spectroscopy

3.2.5.1. Ultraviolet-visible-near infrared (UV-Vis-NIR) spectrophotometer

The band gap of any semiconducting material can be easily determined following the characteristics of absorption or transmission of incident photon by that material. Now, if the incident photon energy is greater than band gap then it becomes absorbed otherwise gets transmitted. Hence this experiment results the precise measurement of the material's band gap[17]. A Shimadzu UV-Vis-NIR (UV-3101-PC) spectrophotometer is used to measure absorption or reflectance spectra of the gallium oxide and its hybrids nanostructures.

In case of parabolic band structure, the absorption coefficient (α) and the energy band gap (E_g) of the material can be related by following equation as proposed by Bardeen, [18]

$$\alpha h\nu = A(h\nu - E_g)^\gamma \qquad (3.2.9)$$

Where, $\gamma = 1/2$ for allowed direct transition, $\gamma = 2$ for allowed indirect transition, $\gamma = 3$ for forbidden indirect transition and $\gamma = 3/2$ for forbidden direct transitions.

A is defined by, $A = {}^I/_{I_0}$

Where, I_0 and I are the respective incident beam intensity and transmitted beams intensity, and E_g, the optical band gap of the material, which is basically the difference between valence band and conduction band energy and $h\nu$ is the incident photon energy. In case of direct transition, the relationship between $(\alpha h\nu)^2$ and the photon energy $h\nu$ reflects linear dependency. A plot of $(\alpha h\nu)^2$ vs. $h\nu$ gives a straight line and the intercepts on the energy axis at $(\alpha h\nu)^2 = 0$, will give the optical gap of the materials. A schematic presentation of working principle and the photograph of UV-Vis-NIR spectrophotometer is given in the **Figure 3.11**.
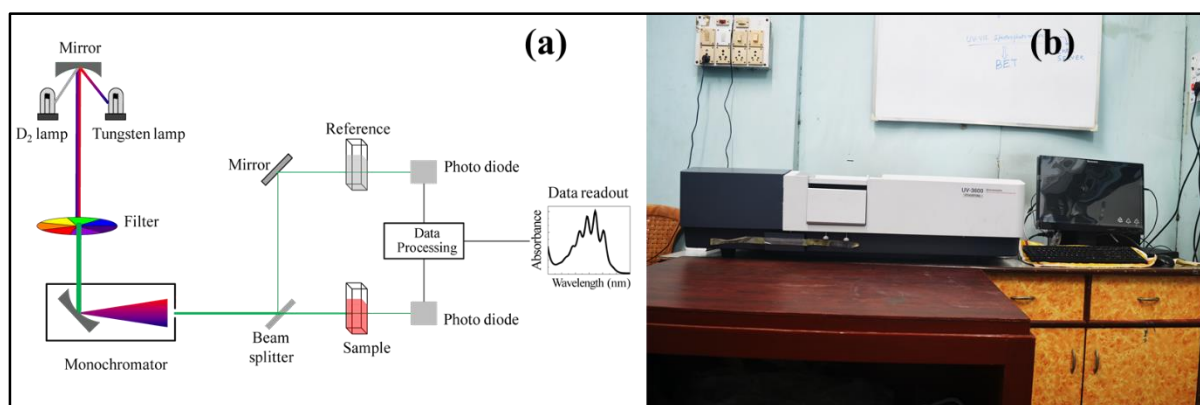

Figure 3.11 Digital photograph of UV-Vis-NIR spectrophotometer

3.2.5.2. Fourier Transform Infrared (FTIR) Spectrometer

Infrared radiation is that region of the electromagnetic spectrum which starts from the nominal red edge of the visible light to the microwave range. The infrared radiation becomes invisible to the naked human eye and it can be identified as warmth sensation on the skin. The IR region can be subdivided into three smaller sections known as far IR (400-20 cm^{-1}), mid IR (4000-400 cm^{-1}) and near IR (14000-4000 cm^{-1}). The fundamental vibrational levels of various molecules may alter in the mid IR region and for this reason; an infrared spectrometer operating in mid IR region uses a technique to obtain the infrared spectra by

collecting the sample signal's interferogram with the help of an interferometer. After that, to acquire the spectrum, a Fourier transform is executed on the interferogram. An Infrared (IR) spectrometer observes the interaction between the samples and infrared radiation and detects the frequencies at which the sample absorbs the radiation and the intensities of radiation.

In all types of IR-spectrometers, the intensity of absorption depends on the number of sample molecules under observation. According to Beer-Lambert's law, the relation between the transmitted intensity (I) and incident intensity (I_0) is written below:

$$I = I_0 e^{-\varepsilon cl} \qquad (3.2.10)$$

Or, in logarithmic form:

$$\log\left(\frac{I}{I_0}\right) = \varepsilon cl \qquad (3.2.11)$$

Where, ε is the extinction coefficient which depends on frequency, c is the concentration and l is the cell thickness. The Beer-Lambert law is the foundation for all quantitative infrared spectroscopy. Determination of the frequencies of the absorbed energy, allows the identification of the sample's chemical bonding present in a chemical structure. Most of the modern FTIR instruments is established on a Michelson Interferometer, consisting of two mirrors and a beam splitter. The basic principle of this instrument is to produce the interference between two light waves, traveling through two different optical path lengths. And that light waves should have same frequency and constant phase relation. A schematic of the spectrometer is shown in the **Figure 3.12a**.
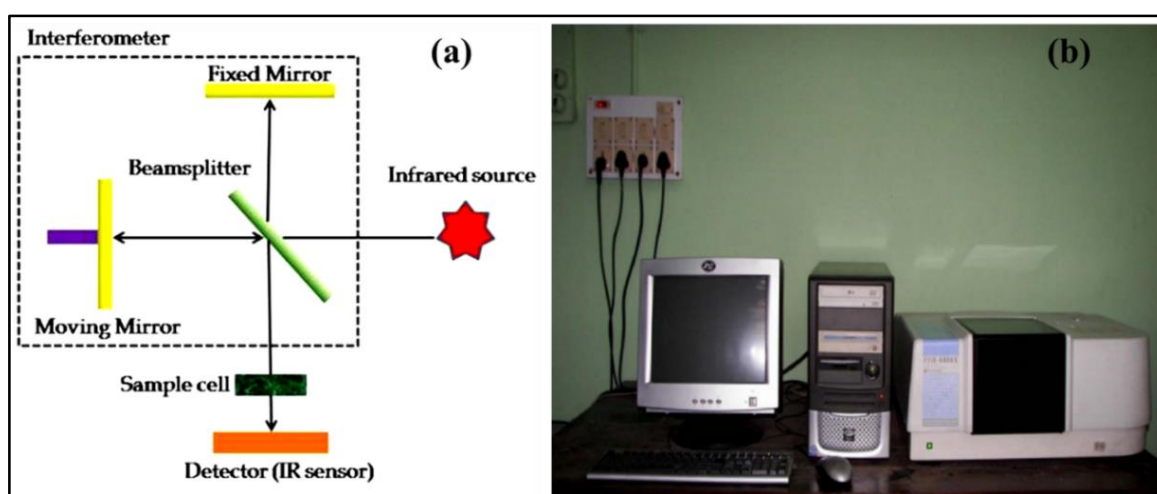

Figure 3.12 Schematic representation of the working principle (a) and photograph (b) of the FTIR spectrometer

Here the light source of the Michelson interferometer is the infrared radiation source presented in figure. After entering the interferometer, the beam of light hits the beam splitter. Then after reflection by the beam splitter, half of the light is propagated towards the fixed mirror. The rest of light is transmitted through the beam splitter and propagated towards the moving mirror. After that, two light beams may recombine to produce constructive or destructive interference which solely depends on the relative position of both the mirrors, moving and fixed ones. If the distance of both the mirrors and the beam splitter is same, then two reflected beams are totally in phase i.e. in zero path difference (ZPD) and the resulted signal intensity becomes maximum. The modulated beam is reflected from mirrors to the sample, where selective absorption takes place. Then from the sample the beam is directed towards the detector, which transforms the beam into an electrical signal. The source produced the cosine waves and that waves were modulated by the interferometer and finally reached to the detector in the form of an interferogram, which can be considered as a signature of intensity versus mirror position. It is basically a summation of all the IR light frequencies that cannot be practically interpreted in its original form. At last the signal from the detector is transferred to a computer which can convert it into an IR spectrum using Fourier transform (FT), a mathematical formula. The amplitude of each of the component signals can be calculated using that formula and the former also gives the intensity at the corresponding wavelength of light. In this study Shimadzu FTIR-8400S spectrometers were used for IR spectroscopic analysis of the films. A photograph of the instrument is shown in the **Figure 3.12b**.

3.2.5.3. Raman Spectrometer

In 1928, great Indian physicist C.V. Raman discovered that the interaction between photons and molecules occurs in inelastic manner, resulting spectral transition; which is known as Raman Effect. Raman scattering includes an alteration in rotational, vibrational, or electronic energy levels of a molecule. The vibrational energy of any scattered molecule can be accounted as the energy difference amidst the incident and Raman scattered photon[19]. Consequently, plotting the scattered light intensity versus energy difference we can get the Raman spectra of any sample.

Raman spectroscopy is a useful tool for the investigation of vibrational properties of nanostructured material. Raman analysis help to determine the chemical as well as structural informations, grain size, phase and also the knowledge of phonon confinement. The inelastic

nature of Raman scattering results an ample frequency difference between the scattered radiation and the incident one; when the scattering of any monochromatic radiation by a molecules takes place. Based on the vibrational state of the observed molecule, Raman scattered photon may possess higher or lower energy. If the energy of the scattering photon is lower than that of incident photons, Strokes shifted scattering occurs. Whereas higher energy of scattered radiation is denoted as Anti-strokes shift scattering. The intensity of Anti-strokes lines is weaker than that of the Strokes line, as a consequence Strokes lines are conventionally monitored for experimental purpose. In Raman Spectroscopy, a laser source, i.e. an intense monochromatic radiation is used as incident radiation on the sample. The weak scattered light is transited across the monochromator to exclude the Raleigh scattering and photodetectors detect only the Raman-shifted wavelength. The energy difference connecting the incident & scattered photons can be estimated as the difference in energy between initial and final vibrational levels ($\bar{v}$), or Raman shift in wavenumbers (cm^{-1}) that is determined by the following equation:

$$\bar{v} = \frac{1}{\lambda_{incident}} + \frac{1}{\lambda_{scattered}}$$

(3.2.12)

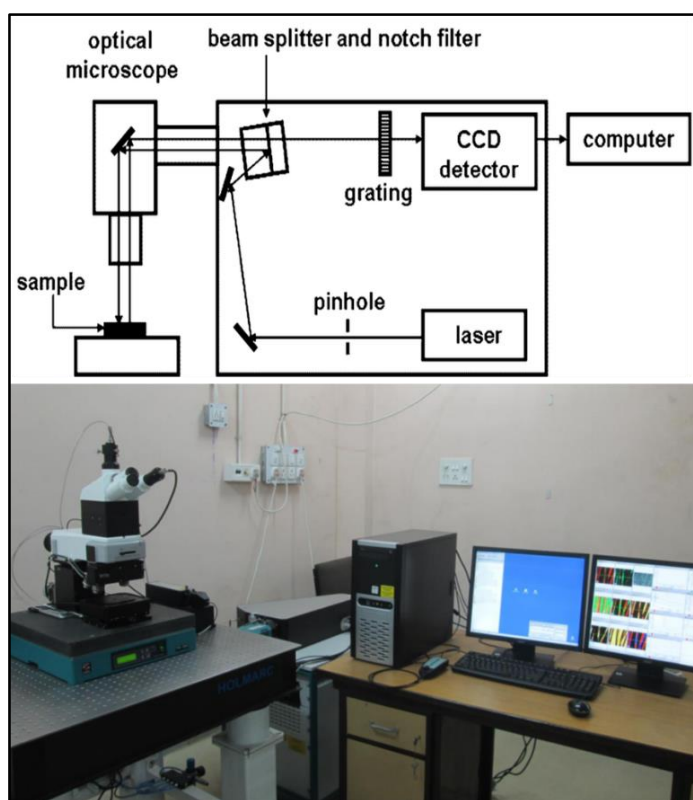*Figure 3.13 Working principle and digital photograph of the RAMAN spectrometer*

Where, $\lambda_{incident}$, and $\lambda_{scattered}$ represents the incident photon's wavelength and scattered photon's wavelength respectively, expressed in cm. The phonon confinement in a material can be observed as the shift in the Raman line frequencies from the bulk material. Acoustic modes of bulk materials are not observable due to their lower frequencies, however in case of nanomaterials it appears in the quantifiable range. The acoustic mode of frequency becomes inversely proportional to the particle size of the nanostructured materials. Optical phonon confinement ensures the shift in frequencies and asymmetrical broadening of longitudinal (LO) and transverse optical (TO) mode occures[20]. In the present work, Raman spectra were procured using a laser source (WITECH) with excitation wavelength (λ_{exc}) ~532 nm. The picture of the instrument is shown in **Figure 3.13**.

3.2.6. Mott-Schottky analysis set-up

The electrochemical measurements for Mott-Schottky analysis were carried out on a CHI760E in PGSTAT302 N AUTOLAB work station in a three-electrode system, where the samples were uniformly applied on a Ni foam as a working electrode, a Pt plate served as the counter electrode and an Ag/AgCl (saturated KCl) was as reference electrode. Whereas the electrolyte used was 0.1M Na_2SO_4 solutions. The working electrode was prepared as follows: 40 mg pristine sample, 5 mg acetylene black and 5 mg PVDF were used to prepare a uniform mixture. Then a requisite amount of NMP solution was added drop wise to the mixture to form black-colored slurry. After that the final mixture was vigorously and continuously stirred for 2 h. Then it was uniformly coated on properly cleaned Ni foam of area 1 cm^2. Finally the working electrode was dried overnight in an oven at 60 °C to improve adhesion. A schematic view of three-electrode configuration is represented in **Figure 3.14**.
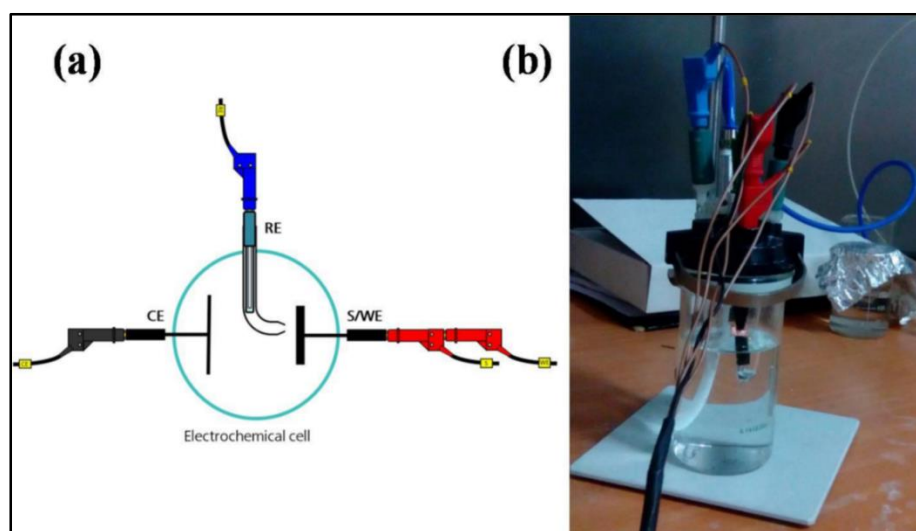

Figure 3.14 (a) Schematic view of the three-electrode configuration and (b) three-electrode cell attached in Autolab PGSTAT

To obtain clear vision about the positions of the conduction band and valance band edges of the pristine samples, Mott-Schottky studies were employed. For this, electrochemical impedance measurements for the samples were performed in dark and the analogous flat band potentials (V_{fb}) were determined using well-known Mott-Schottky equation[21]

$$\frac{1}{C^2} = \left(\frac{2}{\varepsilon_0 \varepsilon_r N_d e}\right) \times \left(V - V_{fb} - \frac{k_B T}{e}\right) \qquad (3.2.13)$$

Here, C= depletion layer capacitance, ε_0= vacuum permittivity (=8.85×10^{-12} $N^{-1}C^2m^{-2}$), ε_r= dielectric constant of semiconductor, N_d=carrier donor density, $k_B T/e$= temperature dependent correction term.

For open circuit condition, a n-type semiconductor normally has its Fermi level at a relatively higher position than the redox potential of the active electrolyte. It enables easy transmit of electrons from the semiconductor to the electrolyte triggering the accumulation of a positive charge in the space charge region. This is obvious from the upward bending of the band edges[21]. The reverse phenomenon can be expected in case of p-type semiconductors. In this experiment, the measurements of the samples can be taken at different frequencies such as 1.5 kHz, 2 kHz and 2.5 kHz etc. to find out the corresponding slopes of the $1/C^2$ *vs*. V plots. Positive and negative slopes indicate the n-type and p-type nature of the samples respectively. The flat band potential V_{fb} corresponds to conduction band for n-type and valance band for p-type materials[22]. Hence from the intercepts of the plots in potential (V)-axis, the positions of the conduction band and valance bands of the active samples can be easily determined.

3.3. Apparatus for photocatalysis measurement

The photocatalytic activity of as-synthesized gallium oxide nanostructures as well as their hybrid and also the degradation kinetics of different kinds of organic and inorganic contaminents in presence of catalyst materials were thoroughly investigated employing a photoreactor. It is also expected that the design of novel photoreactor, as in the case of waste-water treatment, could be engineered to obtain the greatest reaction yield, while expending the least amount of energy. To achieve these goals, photocatalytic reactors for waste-water treatment require careful design and the selection of a number of reactor parameters such as.

a) Catalyst type

b) Photoreactor

c) Illumination type

d) Place of the source of irradiation

The schematic illustration of the experimental setup of photocatalysis is presented in **Figure 3.15**.

Light source

Gallium oxide is a large band gap UV-transparent semiconducting material. It absorbs radiation below the visible range of light spectrum. Hence, photoactivation of as-synthesized material requires radiation with light of wave-length less than 384 nm. The irradiation type may be the crucial design issue for photocatalytic reactors. Our environmental reactor chamber was equipped with UV-C (200-280 nm) lamps (PHILIPS, emission maximum cantered at 254.6 nm). Light was provided by these UV tube inside the photoreactor.
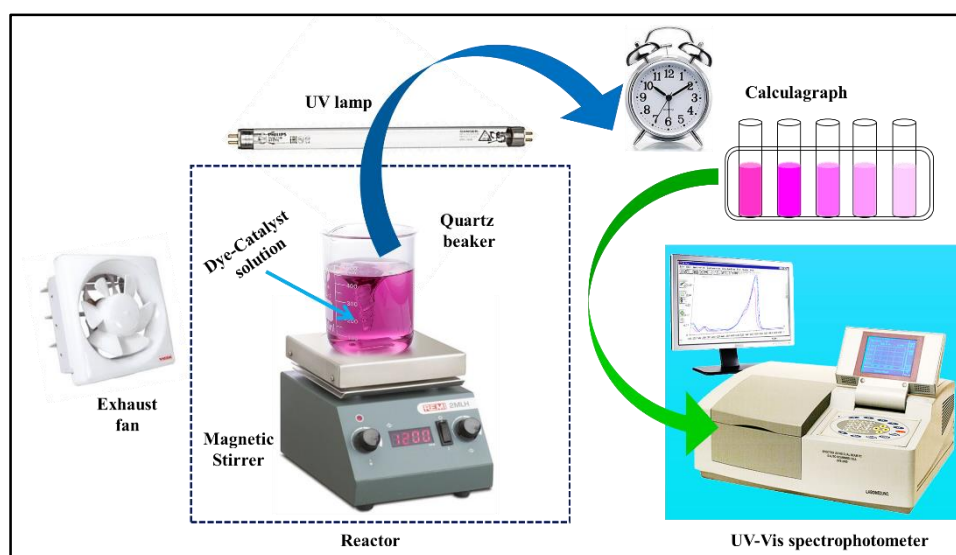

Figure 3.15 Schematic illustration of photocatalysis set up

Photoreactor

The optical path of the light within the reactor governs the choice of photoreactor geometries, which further determines how much radiation is absorbed by the reacting suspension and therefore determines the efficiency of the photocatalytic process. The most usual reactor geometries used for heterogeneous photocatalysis in the literature are (i) Immersion well photoreactor, (ii) Annular photoreactor, (iii) Elliptical photoreactor, (iv) Film type photoreactor, (v) Open up flow reactor etc.

All photocatalytic investigations were executed in a simple rectangular photoreactor presented in **Figure 3.15**. In order to prevent large temperature fluctuations during the

experimental procedure, an air-circulated exhaust was hooked with the backside of the reactor has fixed with siding door for collecting the reaction solutions. All four sides here made of black colored wood to protect the UV irradiation outside of the reactor. The sample cubic reactor to remove the hot air inside the reactor. The upper portion of the reactor was dispersed within dye solution in a 100 mL quartz beaker. Inside the photoreactor, the distance between 100 ml quartz beaker and the UV-lamp was maintained approximately 15 cm. The water in the reactor was stirred magnetically to increase the mass transfer between the headspace and the liquid as well as to provide a homogeneous system.

Light source location

For a photocatalytic reactor, the position of the irradiating source i.e. the UV or visible lamp plays an important role. This lamp position offers various configurations; such as (a) Reactors exhibiting an immersed light source, (b) Reactors possessing an external source of irradiation, (c) Reactors having distributed light sources. Our reactor chamber is an external source photocatalytic reactor where lamps are placed outside the solution. The lamps (three 40 W UV-C tube) are placed inside the chamber. Two tubes are on the chamber walls and one is on top of the chamber.

3.4.   Field electron emission measurement set-up

Field emission properties of gallium oxide and its hybrid samples were investigated using an ultra-high vacuum emission measurement setup. Equal amounts of different samples were pasted on conducting carbon tape, which was a cathode. Stainless steel made the conical tip of diameter 1.5 mm was considered as the collector (anode). The diode configuration was set up with a rotary-diffusion vacuum chamber which is trapped in liquid nitrogen and also an appropriate chamber baking arrangement exists there. Experiments were executed at base-pressure of $\sim10^{-7}$ mbar. Besides, before the field emission experiment, the ohmic nature of the contact was properly checked. Inter electrode separation was kept at 200 μm using a micrometer screw having screw-pitch of 10 micron. The field emission current-voltage analysis were done with the help of a multimeter (model 3440-1A). Strict monitoring was performed via a transparent viewport during the entire measurement to ensure no sparking near the sample or inter-electrode space. Emission characteristics were registered and

analyzed with the help of a personal computer. The schematic diagram of the field-emission apparatus is shown in **Figure 3.16.**

High voltage D.C. power supply

For field emission measurement, a D.C voltage is applied between the cathode which is the sample under investigation and the anode. For this purpose a 3 kV–500 mA DC regulated power supply unit (Model NTPL/ 91/03-04), manufactured by Neo Tele-Tronix Pvt. Ltd., Calcutta was used. The input to the unit is 230 V, 50 Hz, 1 Phase AC and output can continuously vary from 100 V to 3 kV DC. The power supply was housed within a powder coated steel enclosure movable with wheels.
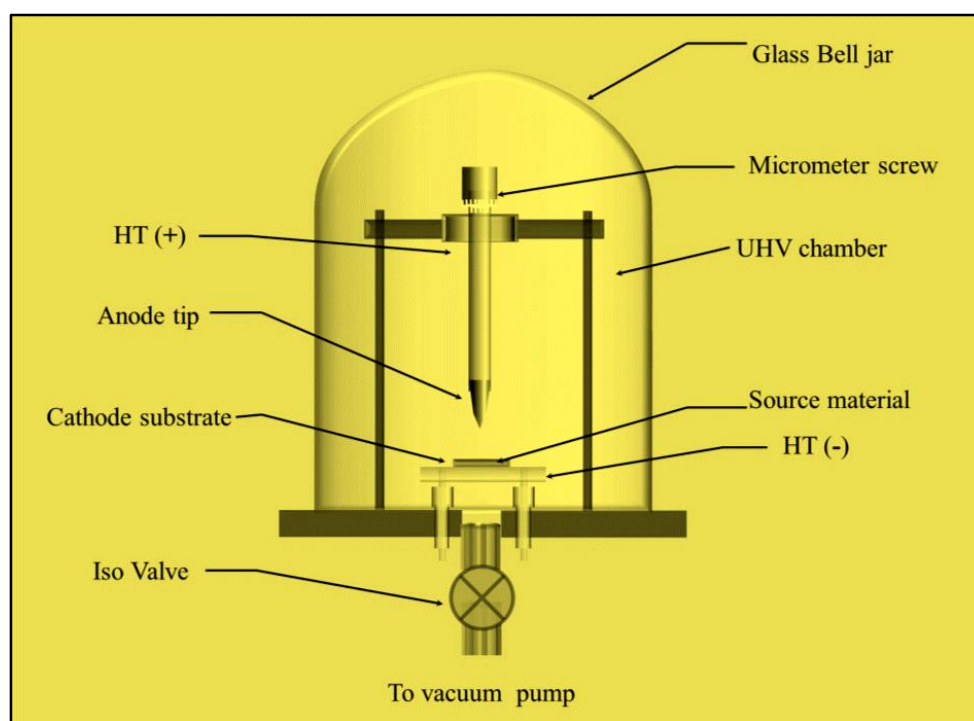

Figure 3.16 Schematic diagram of the field-emission measurement set-up

Electrometer, Multi-meter

Keithley electrometer (Model 671 and 6517A) was used to record current voltage characteristics and resistance of the samples. The voltage and current ranges are ± 1000 V and ±1 pA to ± 20 mA respectively. Another Keithley electrometer (Model 6514) was used to measure the field emission current having a current range of 100 nA to 21 mA. Also several multi-meters (RISH MULTI 15 S, Agilent (model 3440-1A)) were used during the experiment.

3.5. References

1. R. Prasad, and M. Pandey, Bulletin of Chemical Reaction Engineering and Catalysis, 7(1) (2012) 1-25.

2. L. W. Sumner, Z. Lei, B. J. Nikolau, and K. Saito, Natural product reports, 32(2) (2015) 212-229.

3. Y. Li, D. Zhao, and J. Liu, Scientific reports, 6(1) (2016) 1-11.

4. X. Xu, F. T. Huang, Y. Qi, S. Singh, K.M. Rabe, D. Obeysekera, J. Yang, M. W. Chu, and S. W. Cheong, Nature materials, 20(6) (2021) 826-832.

5. P. A. Hiltner, and I. M. Krieger, The Journal of Physical Chemistry, 73(7) (1969) 2386-2389.

6. A. L. Patterson, Physical review, 56(10), (1939) 978.

7. L. De Broglie, Recherches sur la Theorie des Quanta (Researches on the Quantum Theory). Ann. Phys., 3 (1925) 22-128.

8. C. Davisson, and L.H. Germer, Diffraction of Electrons by a Crystal of Nickel. Physical Review, 30(6) (1927) 705-740.

9. B. D. Culity and S. R. Stock. Elements of X-ray diffraction. Prentice Hall, New Jersey, 3edition, (2001).

10. D. C. Cox, Introduction to Focused Ion Beam Nanometrology, Morgan & Claypool, Publishers (2015).

11. C. R. Brundle, C. A. Evans and S. Wilson. Encyclopedia of materials characterization, Reed Publishing, USA, (1992).

12. P. E. J. Flewitt and R. K. Wild. Physical methods for material characterization. IOP Publishing Ltd, D. K. Schroder. Semiconductor materials and device characterization. Wiley Interscience, (2003).

13. D. B. Williams and C. B. Carter, Transmission Electron Microscopy, A Textbook for Materials Science, Springer, e-ISBN 978-0-387-76501-3 (2009).

14. M. DeGraef, Introduction to Conventional Transmission Microscopy Cambridge University Press New York (2003).

15. William D. Harkins, and J. George, Journal of the American Chemical Society 66(8) (1944) 1366-1373.

16. W. G. McMillan, and E. Teller, 1951. The Assumptions of the BET Theory. The Journal of Physical Chemistry, 55(1) (1951) 17-20.

17. B.G Streetman, Solid state electronics devices. Prentice Hall of India Pvt. Ltd, New York, (1995).

18. J. R. Dixon, and J. M. Ellis, 1961. Optical properties of n-type indium arsenide in the fundamental absorption edge region. Physical Review, 123(5) (1961) 1560.

19. B.N.J. Persson, On the theory of surface-enhanced Raman scattering. Chemical Physics Letters, 82(3) (1981) 561-565.

20. M. Rajalakshmi, A. K. Arora, B. S. Bendre, and S. Mahamuni, Journal of Applied Physics, 87(5) (2000) 2445-2448.

21. B. Das, B. Das, N. S. Das, S. Pal, B. K. Das, S. Sarkar, and K. K. Chattopadhyay, Applied Surface Science, 515 (2020) 145958.

Chapter 4

Tailored Mesoporous Nanocrystalline Ga$_2$O$_3$ for Dye-Selective Photocatalytic Degradation

Abstract

Porous brick-like low dimensional Ga_2O_3 nanostructures were fabricated through a low-cost chemical route having different phases synthesized at different temperatures. The pore-density was varied by varying synthesis temperatures and the materials exhibited a transformation from α-hexagonal to β-monoclinic phase. With traditional structural and morphological characterization, detailed contaminant removal properties were investigated for the as-prepared samples. The green cleaning efficiency was recognized to be influenced by crystal structure, surface morphology and surface charge type of the catalyst. All of the synthesized material showed promising performance in degradation of traditional organic hazardous dyes like rhodamine B (RhB), methyl orange (MO) and apparently invisible harmful water soluble chemical like phenol. An interesting feature, i.e., obtaining dye specific adsorbent out of the same materials and the mechanism for the ion selective photo-degradation process have been presented in this work. High degradation rate constants of 0.072 min^{-1}, 0.051 min^{-1} and 0.18 min^{-1} were obtained for RhB, MO and mixed dyes respectively with almost complete removal of the dyes. The role of intermediate radicals •OH, •O_2^- and h^+ was correlated with catalytic performances depending upon modification of band positions of the dyes. The mesoporous Ga_2O_3 structures are hence inferred as potential candidates for future water safety issues.
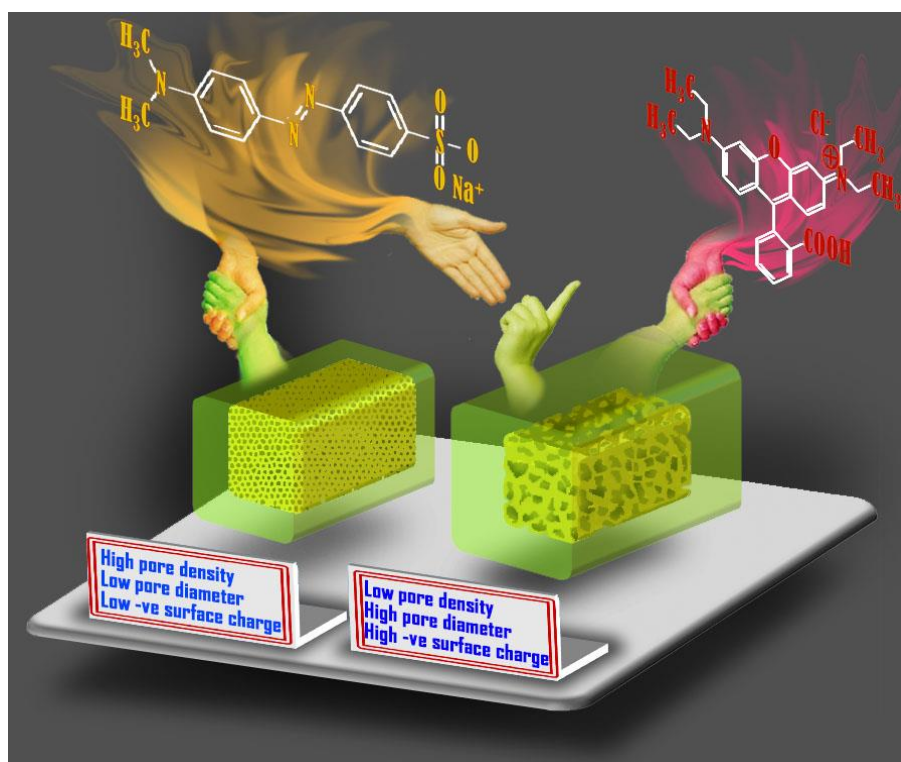
4.1. Introduction

With rapid progress in polymer based industrial products, easy contamination of consumable water via multicarbonic compounds has emerged as inevitable health threats[1]. Especially textile dye and apparently harmless disinfection agent, phenol can cause severe health hazards in both water dissolved, solid and vapour form[2-3]. Removal of such wastes from water was long ago recognized as alarming challenge as the drawbacks of some conventional methods like activated carbon adsorption, solvent extraction and common chemical oxidation was revealed in form of high cost or generation of hazardous by-products[4]. For example, more toxic chlorinated compounds may form during water purification by chlorination method[5].

Search for cleaner, safer and environment friendly water purification technologies is continuing although significant advancement has been achieved with the development of metal oxide nanoparticles photocatalysts such as TiO_2, ZnO, WO_3 under UV irradiation[6-8]. Moreover, fabrication of some transparent conducting oxides (TCO) nanostructures for even higher degradation efficiency was also reported and commercialized rapidly[9]. However, due to high production cost and comparatively low material yield, those new generation photocatalysts are still not widely used. Search for newer strategies to enhance the Photocatalytic activity of metal oxide[10] and improving its surface-to-volume ratio, porosity, structural uniformity, stability[11-12] etc. is hence of utmost importance.

Ga_2O_3 nanostructures have been a well-known photocatalyst[13] due to their flexible morphological shapes and dimension[14] and tunability of its multidirectional optoelectronic properties[15]. Five different polymorphisms exist in Ga_2O_3 like α, β, γ, δ, ε-gallia[16]. Among these crystalline phases, β-Ga_2O_3 having monoclinic crystal structure possesses excellent thermal and chemical stability. Most of those phases are easily achieved in cost effective synthesis routes. Being a wide band gap semiconductor β-Ga_2O_3 (E_g = 4.9 eV) is UV responsive[17] and a promising material in the field of photocatalysis, including the degradation of organic pollutants[18], water splitting[19], CO_2 reduction[20] etc. β-Ga_2O_3 exhibits several technological applications such as optoelectronic devices, high-temperature stable gas sensors, Schottky junction diode, activation and passivation coating, blue light emitter, luminescent phosphor, transparent conducting oxides, flat-panel display, thin film transistors, spin tunneling junctions[21-27] etc. Ga_2O_3 nanostructures have been considered as cost-effective materials[28] for water decontamination because of their superior charge separation[29], favourable mobility of the photo-generated electrons[30] and capability for converting light

energy into chemical energy[31]. Synthesis process of Ga_2O_3 nanostructures have been modified as per requirement and routes like physical deposition via vapour-solid[32], vapour-liquid-solid[33], laser ablation[34], chemical vapour deposition[35], arc-discharge[36], hydrothermal method[37], Microwave-assisted synthesis[38] are employed. However, synthesis route which could lead to tailored phase and morphological features with good reproducibility is still needed for Ga_2O_3 nanocatalysts.

In this work two types of Ga_2O_3 micro/nanobricks (α- and β-crystal structures) have been prepared where, with the variation of the calcination temperature porosity as well as crystalline phase of gallium oxide were found to vary considerably. Then their crystallinity, phase, morphology, composition, surface properties were investigated by conventional tools like X-ray diffraction (XRD), field emission scanning electron microscopy (FESEM), elemental mapping by energy dispersive X-ray analysis (EDX), BET surface analyzer respectively. The as-synthesized materials displayed a noticeable adsorption and exceptional photocatalytic performance under UV irradiation leading to decomposition of organic pollutants like Rhodamine B (RhB) and Methyl Orange (MO) under ambient condition. The entire photocatalysis performance was investigated keeping in mind several aspects of green cleaning technology. These are, the phase of Ga_2O_3 photocatalyst was selected for multiple dyes based on ion selectivity of the dyes; tuning of porosity of the particular phase of Ga_2O_3 for better degradation efficiency. Also, the photocatalyst loading was optimized for economic usage. Finally, reusability of the cleaning agent was ensured. Further aiming towards practical application for the proposed Ga_2O_3 nanocrystalline systems in catalytic degradation, some major real challenges of water contamination sector, like phenol and mixture of organic dyes were also subjected to photocatalysis test. The results showed a remarkable performance of the samples in prompt removal of those industrial pollutants. The mesopores with tunable densities have further potential to anchor noble metal and other external aids which might result visible nanophotocatalysts.

4.2. Experimental

4.2.1. Synthesis of Ga_2O_3 nano/micro bricks

All the reagents used in the synthesis procedure were analytical pure grade chemicals. Brick-like Ga_2O_3 were prepared by a simple chemical bath method followed by calcination following the method reported by Reddy et al. with some modifications[39] as shown in **scheme 1**. To prepare the growth solution initially hydrated Gallium nitrate $(Ga(NO_3)_3.nH_2O)$

(0.1 M) was dissolved into 100 ml of deionized (DI) water. Then the resulting solution was placed on a heater with magnetic stirring until the temperature reached to 105 ˚C. Maintaining that temperature ammonium hydroxide (NH₄OH) was added slowly into the solution until the pH was reached to 11. Afterwards white precipitates of gallium oxide hydroxide bricks were obtained and the final solution was heated for 4h under close atmosphere. After the solution was cooled to room temperature naturally, the precipitate was filtered and washed for several times with DI and ethanol. The collected samples were dried over night at 80 ˚C in an oven. Further, the as-synthesized GaOOH micro/nano bricks were calcined at three different temperatures of 500 ˚C, 700 ˚C, 1000 ˚C for 3h to obtain gallium oxide structures having α and β phases. The samples were labeled as G5, G7 and G10 respectively. One part of the sample was kept uncalcined and was branded as G0.
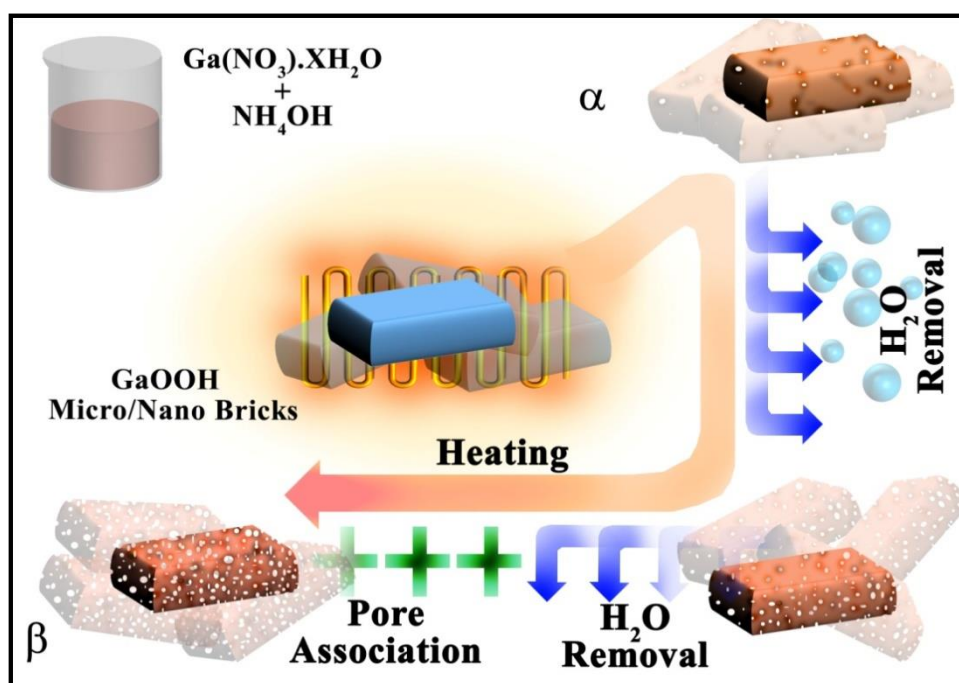
Scheme.1 Schematic of synthesis procedure of mesoporous α and β-Ga₂O₃

4.2.2. Characterization

All the samples including the hydroxide, G5, G7 and G10 were subjected to further characterization with various tools. The crystalline phases of the samples were confirmed using X-ray diffraction (XRD, BRUKER D8 Advance) analysis and elemental composition was studied using energy dispersive X-ray spectroscopy (EDX, equipped with electron microscope). Detail morphological features including the dimensions of the bricks along with pore dimension were studied using field emission scanning electron microscope (FESEM,

Hitachi, S-4800). Thermogravimetric analysis (TGA) of the sample G0 was performed using thermogravimetric analyzer (Mettler Toledo TGA/SDTA851e). The important parameter for catalysis - active surface area and porosity of the samples were analyzed using a BET surface analyzer (NOVA Quanta Chrome 1000e). The optical band gap of the sample was determined using reflectance studies via UV-Vis spectrophotometer (SHIMADZU-UV-3101-PC). The zeta potential of the samples was measured using Zetasizer Nano ZS (Malvern Instruments, UK).

4.2.3. Photocatalysis studies

To investigate the dye degradation properties, a standard photocatalytic set up was used for degradation of two dyes RhB, MO and their mixture (RhB+MO). Also an aromatic chemical, phenol, was investigated using the same set up. For a typical experiment, RhB stock solution of 0.01 g ml^{-1} was prepared. 10^{-5} M test solution was further prepared by addition of appropriate amount of de-ionized water to the stock solution. 0.03 g of the samples were added to this test solution separately and stirred in dark condition for 90 min. After dark stirring, the solutions containing each powder sample were exposed to UV irradiation within the photocatalysis experiment chamber. The photocatalysis experiment chamber contained a sample stirrer with stirring speed ranging up to 400 rpm and a special beaker made of quartz of 50 mm thickness contained the active medium for photocatalysis. The solution to radiation distance was maintained at a fixed 15 cm distance. Two 40 W UV tube (Phillips), capable of emitting 254.6 nm (UVC) wavelength UV-rays were attached above the stirring solution system to maintain a direct downward exposure. The entire system includes a rectangular covering encapsulation capable of stopping additional incident wavelengths from surrounding to ensure purity of the UV exposure. The catalysis process under UV exposure was carried out for different durations and parts of the solutions, sufficient for further spectroscopic analysis, were collected and filtered in different time intervals. The time evolved absorption spectra were recorded with the solutions collected in different time intervals.

A slightly different technique was employed for investigation of phenol degradation efficiency by Ga_2O_3 nanobricks. 0.01 g of raw phenol was added in 500 ml of de-ionized water to make the stock solution. The reaction was carried out by dissolving 22 mg of the samples in 40 ml of stock solution and initially stirred in dark condition for 1 h. The solution was then exposed under UV irradiation and degradation of phenol was observed with time interval of 30 min for 3 h. The collection of the filtrate was similar to that of RhB. However,

the detection of degradation via spectroscopy was carried out using photoluminescence spectrophotometer (PL,PLPC) JASCO FP-8300.

4.3. Result and discussion

4.3.1. Structural Studies

The XRD pattern of the prepared samples G0, G5, G7, G10 are shown in the **Figure 1.1**. The Observed diffraction peaks of as-synthesized GaOOH (G0) sample was well agreed with the crystalline orthorhombic (space group Pb_{nm}) structure (JCPDS 06-0180) with sharp distinct peaks found at $2\theta= 21.5$ °, 33.7 °, 35.3 °, 37.2 °, and 54.0 ° corresponding to the crystal planes (110); (130); (021); (111); (221) respectively. At calcination temperature 500 ℃, the as-prepared G0 microbars were transformed into α-Ga_2O_3 (G5) having hexagonal(space group $R\bar{3}c$) crystal structure with distinct and intense peaks, indicate good crystallinity (JCPDS 06-0503). A clear shift of phase from α to β-Ga_2O_3 with monoclinic crystal structure (JCPDS 76-0573, space group C2/m) was observed when the calcination temperature increased above 500 ℃. Such variation of crystal phase for Ga_2O_3 is well known[40] and often achieved by varying the synthesis temperature. The change in temperature was identified as the key factor for this change.

The grain size of the samples are calculated from XRD pattern using the Scherer's formula[41]

$$D = \frac{0.9\lambda}{\beta\,cos\theta} \tag{4.3.1}$$

Where, β is contributed by broadening of the diffraction peaks. Typically β is expressed as

$$\beta = \sqrt{\beta_{obs}^2 - \beta_{inst}^2} \tag{4.3.2}$$

Here, β_{obs} is the observed full width half maxima (FWHM), β_{inst} is the instrumental broadening. The instrumental broadening factor of BRUKER D8 Advance X-ray diffractometer was found to be 0.13226 °, θ is the diffraction angle, λ is the wavelength of the X-ray and 0.9 is the shape factor.

Now using equation (4.3.1) and (4.3.2) the corrected grain size for all the samples were calculated and it was found to be 54.2 nm for the sample G0. Among the oxide sample, the maximum grain size was estimated for sample G10 i.e. 31.5 nm whereas the grain size for G7 and G5 are 28.3 nm and 24.1 nm respectively. For oxide samples the increment of grain size

with higher synthesis temperature can be accounted for agglomeration of smaller grain into comparatively larger grain. Such association of grains is expected as higher synthesis temperature is liable to eliminate water and thus smaller grains shall move towards each other leading to the formation of larger grain. However, such widening of grain dimension via association of smaller grains is expected to leave behind large pore/holes. This was verified in FESEM studies (demonstrated later).
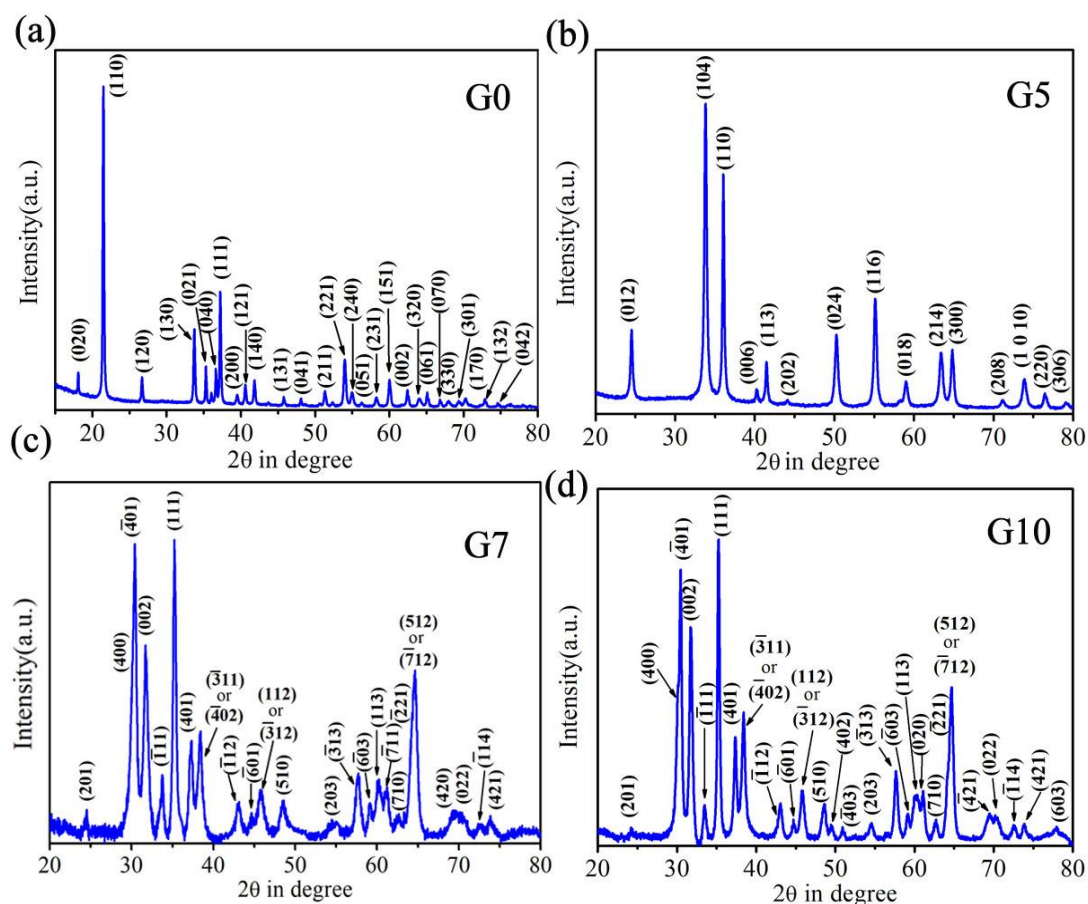

Figure 4.1 XRD patterns of the different samples (a) as-synthesized G0, (b) G5 calcined at 500 ˚C, (c) G7 calcined at 700 ˚C and (d) G10 calcined at 1000 ˚C

4.3.2. Compositional Studies

Though proper phase formation was inferred from XRD studies, the compositional analysis of the samples was carried out via EDX studies. Elemental mapping of constituent elements are often considered as an effective tool to confirm compositional purity and proper stoichiometry[8, 41]. The EDX elemental studies carried out for the samples showed uniform distribution of constituent elements within the samples presented in **Figure 4.2**. The EDX pattern of the samples did not show any trace of nitrogen in the Ga_2O_3 micro/nanobricks which rules out the possibility of the bricks to be composed of the Ga-precursor ($Ga(NO_3)_3$).

The atomic percentages of the constituent elements (presented in **Table 4.1**) were also recorded and the samples were found to exhibit almost proper stoichiometry.
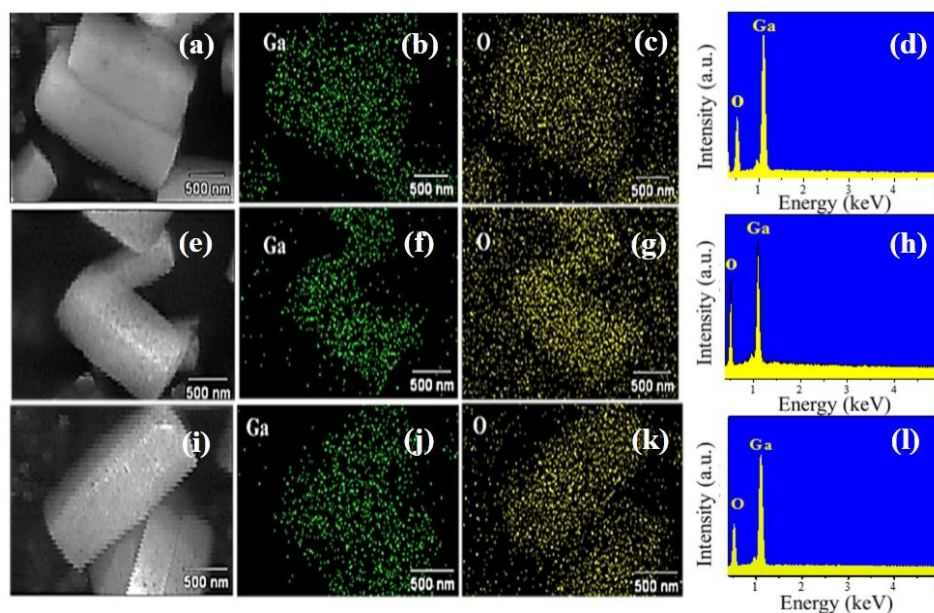

Figure 4.2 Elemental distribution and Energy dispersive X-ray spectroscopy (EDX) spectra of the sample G5 (a-d), G7 (e-h), G10 (i-l)

Table. 4.1 Comparison between the atomic percentages of the constituent elements for different samples

Sample	Atomic percentage of Ga (%)	Atomic percentage of O (%)
G5	42	58
G7	41.08	58.92
G10	39.6	60.4

4.3.3. Morphological Studies

The micrographic images of the Ga_2O_3 samples of different synthesis temperature are shown in **Figure 4.3**. The micrograph in **Figure 4.3a** show that in case of uncalcined sample, GaOOH micro/nanobricks are well formed but no specific porosity was found which is reflected in smooth surfaces of the nanobricks. As the hydroxide phase was calcined, some pores having small diameter are found to arise in the micro/nanobricks (**Figure 4.3b**). The dimension of pores increased as the synthesis temperature further increased as can be seen in **Figure 4.3(b-c)**. The Ga_2O_3 micro/nanobricks achieved pores with largest diameter (**Figure 4.3d**) when the calcination temperature was increased upto 1000 ℃ for sample G10.
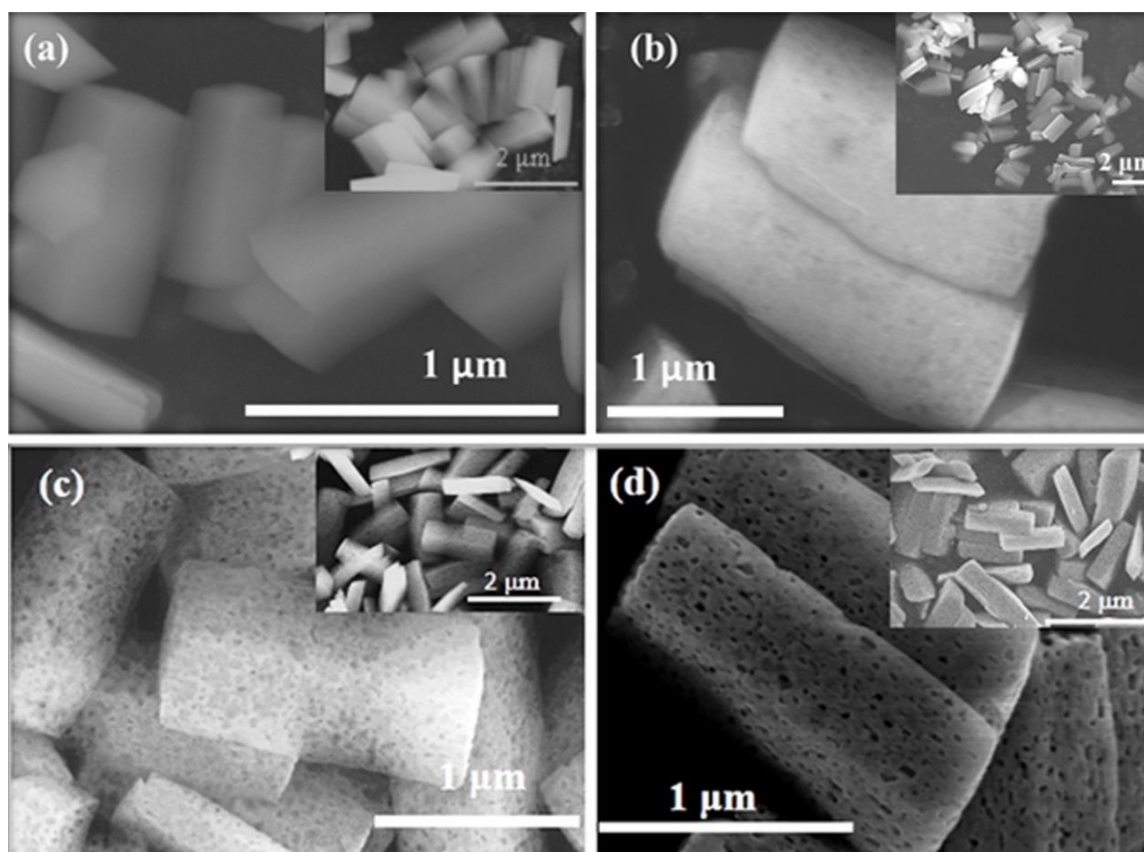
Figure 4.3 High magnification FESEM images of as-grown G0 (a), G5 (b), G7 (c), G10 (d). Inset shows their corresponding low magnification images

4.3.4. BET surface area studies

It is well known that the adsorption capability and photocatalytic performance of the sample depends on its larger surface area and abundant porous nature which appreciably enhance the contact opportunity of the dye molecules on the adsorbent surface and assists in diffusion or mass transfer of the dye molecules respectively. In view of the special morphological features observed in FESEM studies, the BET specific surface area and porous features of the bricklike nanostructured samples were quantified by using nitrogen adsorption desorption isotherms. The N_2- adsorption-desorption isotherm of the Sample G0 did exhibited type II pattern normally found for nearly non porous or macroporous materials represented in **Figure 4.4**. The specific surface area for sample G0 was found to be as small as 2 m^2/g. This shows the inferiority of sample G0 in view of surface related applications.
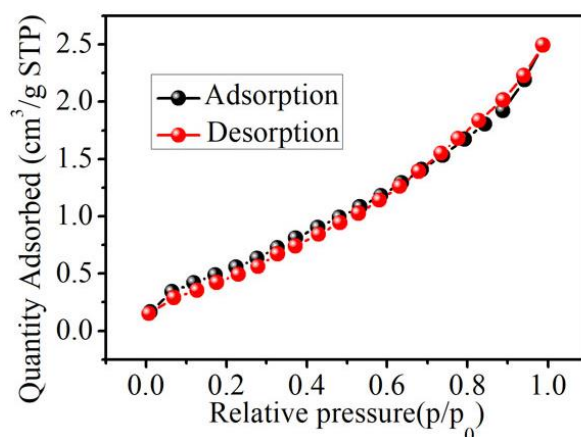
Figure 4.4 Nitrogen adsorption-desorption isotherms for the sample G0

However, the obtained results for samples G5, G7 and G10 are presented in **Figure 4.5**. The representative isotherms could be classified nearly as type IV pattern with a recognizable H3 hysteresis loop nearly in the relative pressure range (p/p0) of 0.5 to 1.0 indicating the existence of mesopores having diameter in the range between 2 to 50 nm. By the Barret-Joyner-Halenda (BJH) method it was determined that the average pore diameter is lowest (6 nm) for sample G5 and the same gradually increased with increasing calcination temperature. The specific surface area and average pore diameter values of the samples are listed in **Table. 4.2**. This result was further correlated with the photocatalytic performances of the samples.
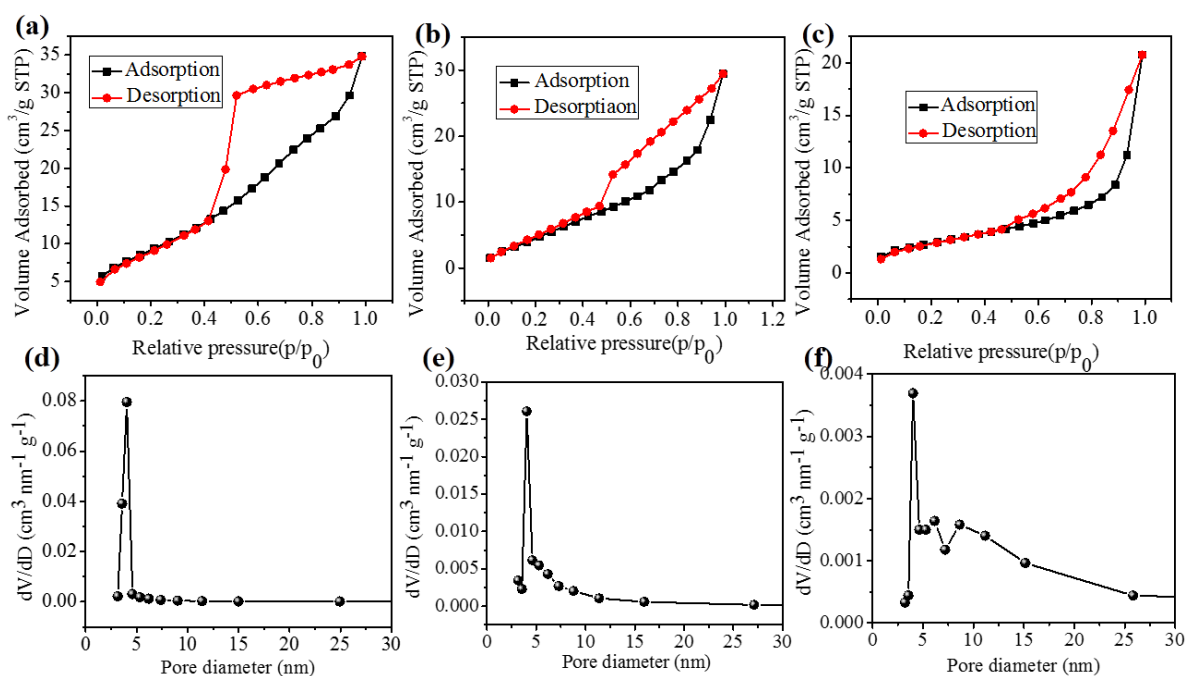

Figure 4.5 Nitrogen adsorption–desorption isotherms for the samples (a) G5, (b) G7, (c) G10 and the pore-size distribution plots for G5 (d), G7 (e), G10 (f)

Table 4.2 Comparison of grain size, surface area and pore diameter between the samples

Sample	Grain size from XRD (nm)	Surface area(m^2/g)	Average Pore diameter(nm)
G0	54.2	2	-
G5	24.1	34	6
G7	28.3	21	8
G10	31.5	10	12

> **Formation of mesopores:**

The regular variation of porous feature of the Ga_2O_3nano/microbricks with calcination temperature can be correlated to removal of water molecules from Ga_2O_3 crystal. As the synthesis temperature increases, the water molecules are removed from the GaOOH (G0 sample) crystal causing the formation of oxide phase of α-Ga_2O_3. In addition to converting the GaOOH into α-Ga_2O_3, removal of H_2O also leaves behind some holes/pores in the sample as observed in the FESEM image of sample G5. When the annealing temperature is further increased, formation of pores is not further contributed by H_2O removal as major portion of the sample was already converted into pure oxide phase of Ga_2O_3 there was hardly and H_2O molecules left behind.
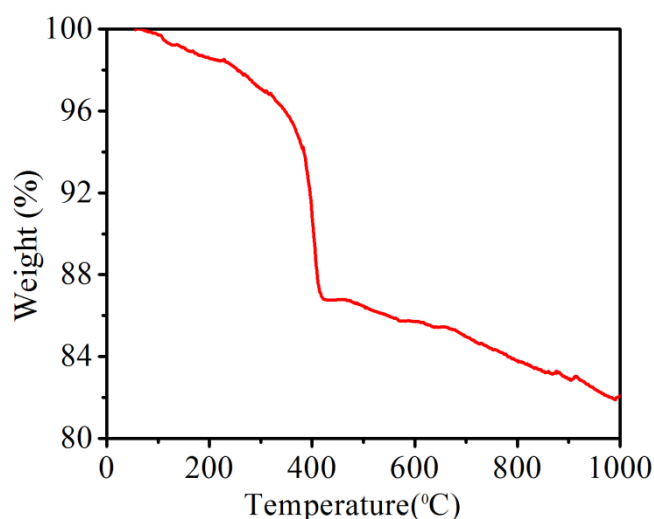

Figure 4.6 Thermogravimetric analysis (TGA) curve of sample G0

To judge the feasibility of this proposed mechanism, TGA analysis was carried out. The results (**Figure 4.6**) show that upto 400 ºC, water removal from the system is much faster. Beyond this, the outer surfaces of the bricks are already oxidized and hence are now having a heat insulating coat on them. This restricts fast heat penetration slowing down further oxidation as well as further removal of H_2O. However, in FESEM image of sample G7, the pores are found to further increase in dimension. This can be accounted for the association of smaller grains into large grain as reflected in XRD results. This same effect further caused increment in pore diameter in sample G10. Thus in this work, a simple process of tuning the porosity of Ga_2O_3 microbricks is established and the entire phenomenon was found to be simultaneously governed by water removal and grain association process.

4.3.5. Optical study

The optical band gaps of the as-prepared bricklike G5 and G10 nanocrystalline samples were determined from reflectance spectra and the same was presented in **Figure 4.7**. It was observed that the band gaps of the samples lie within UV range as reported in several other works[19]. So it is possible for UV activation of the valance electrons which may occur for Ga_2O_3.
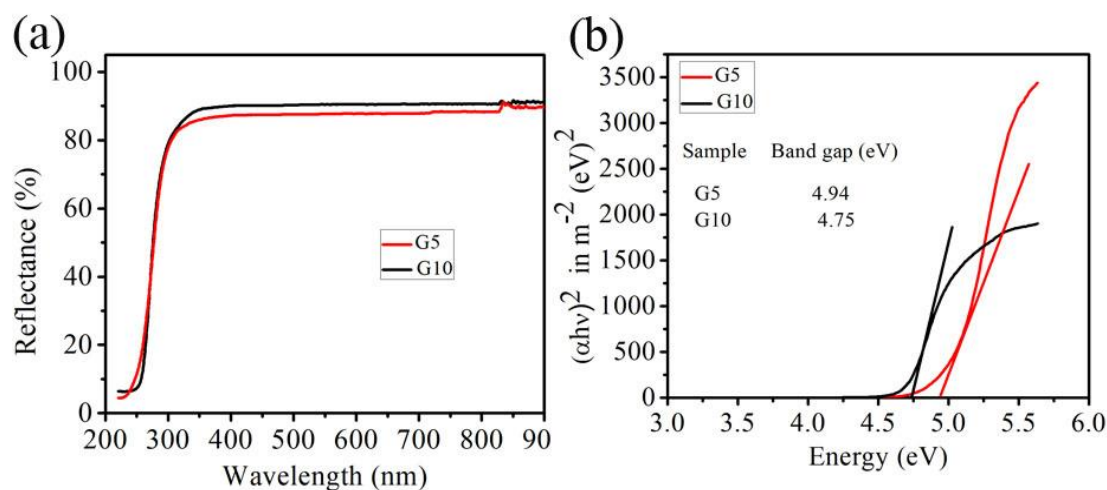

Figure 4.7 UV–Vis reflectance spectra of G5 and G10 (a), and their corresponding plot of $(\alpha E_{photon})^2$ versus E_{photon} (b) to evaluate the band gap

4.4. Ion selectivity of the dyes

All the samples G0, G5 and G10 were studied in detail to assess their performance in adsorption and degradation of the well-known hazardous anionic dye MO and cationic dye

RhB. According to the Beer-Lambert Law, absorbance is directly proportional to the concentration and reduction of absorption spectra means a decrease of concentration. **Figure 4.8** shows the time evolved UV absorbance spectra of adsorption and degradation of the dyes (MO and RhB) in presence of different catalysts. It can be clearly seen from the figure that after dark stirring the characteristic absorption peaks in the UV-Visible spectra of RhB (λ_{max}= 554 nm) and MO (λ_{max}= 464 nm) were reduced without any appreciable shift or appearance of new peaks with contact time, which indicates that the dyes were adsorbed only at the catalyst surfaces without any degradation.
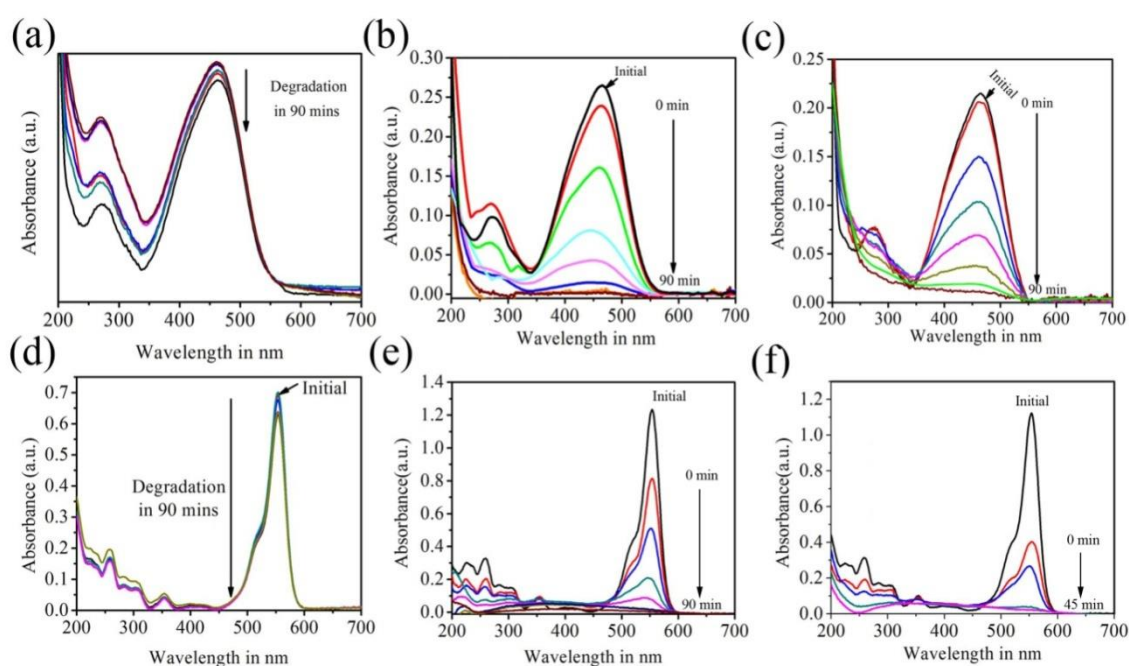

Figure 4.8 Time evolved UV-Vis absorbance Spectra of MO with sample G0 (a), G5 (b), G10 (c), and RhB with G0 (d), G5 (e), G10 (f)

Figure 4.9a demonstrates that the removal percentage of MO on sample G5 became 10% within first 60 minutes and an equilibrium condition was almost achieved within 90 minutes whereas G10 performed in a little inferior fashion (removal percentage 5%). Entirely reverse results were obtained for RhB which was significantly adsorbed by G10 (65%) and adsorption by G5 was comparatively lesser (35%). However, G0 showed negligible adsorption activity as no considerable change occurred in dye concentration during dark stirring in equivalent time range for any of the dyes. The morphological features, further supported with BET studies may be recognized as the reason behind this difference in the adsorption performance for different dyes. Sample G5 and G10 having high pore volume and effective surface area, offers maximum contact with dye solutions. This in turn results in

faster adsorption of dyes. Sample G0 having no morphological features favorable for photocatalysis and hence hardly shows any adsorption performance comparable to G5 and G10. However, the morphological features cannot solely explain the better adsorption of RhB on the sample G10 having comparatively less surface area. Some more crucial factor might be responsible for the same. In addition to morphology related porous features, surface electrostatic properties of the material often plays important role in selective adsorption. To investigate whether surface charge of the sample is responsible for such anomaly, zeta potential study in deionized water solvent was carried out. The result obtained from this study is presented in **Figure 4.9b.** It was observed that all samples show negative zeta potential values, whereas sample G5 (-10.9 mV) is less negative than sample G10 (-29 mV).
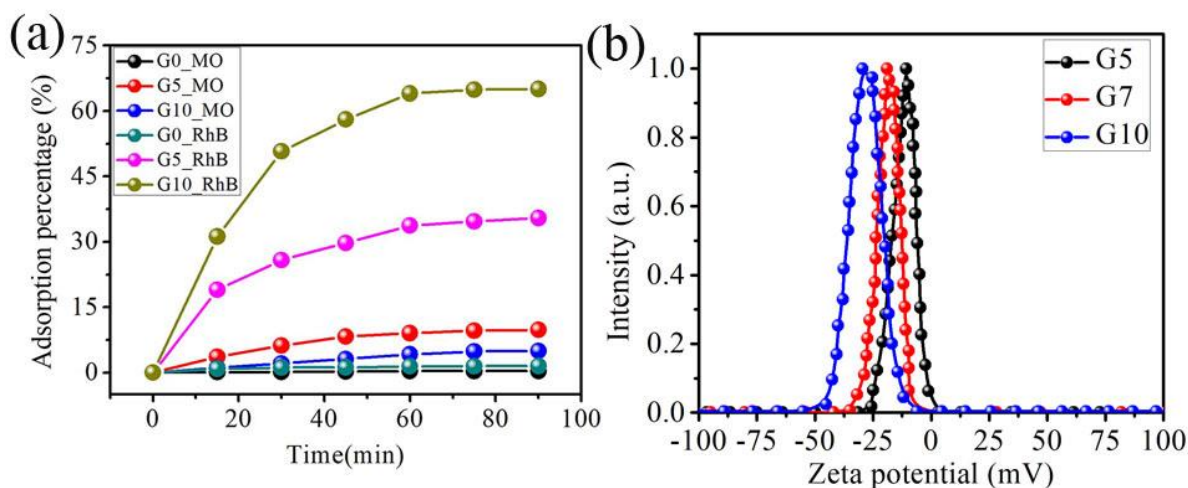

Figure 4.9 (a) Time resolved Removal percentage of cationic and anionic dyes over the samples G0, G5, G10,(b) Zeta potential of the sample G5, G7 and G10

An important factor, i.e. ionic identity of the dye may be correlated with the zeta results to explain that apparent anomaly[42-43]. It is well known that methyl orange is an anionic dye whereas RhB is a cationic dye[44]. On the other hand, inherent thermal tuning of crystalline phase i.e., α and β phases of Ga_2O_3 was employed in sample G5 and G10 respectively. A major change of surface charge can be associated with such a phase change which was reflected in zeta potential studies of the sample (**Figure 4.9b**). As both of the samples are negatively charged, they show a stronger electrostatic attraction towards the positively charged cationic dye (RhB) in the aqueous solution than that of the anionic ones (MO). Therefore RhB is more easily captured by the samples (adsorption capability follows a sequence of G10> G5) and faces faster adsorption. However, G5 exhibit comparatively less negative surface charge than that of G10 and hence its response towards anionic dye is comparatively better than that of G10.

4.5. Photocatalysis

4.5.1. Photocatalytic activity

Further, adsorption of dyes on catalyst surface may lead to maximum removal of contaminants by 65%. Consumable water must have higher degree of purity and that cannot be achieved solely by adsorption. As the most popular process, catalytic degradation of the dyes under UV irradiation was further attempted. The removal of the hazardous dyes investigated via time evolved UV-Vis study and the results are presented in **Figure 4.8**.
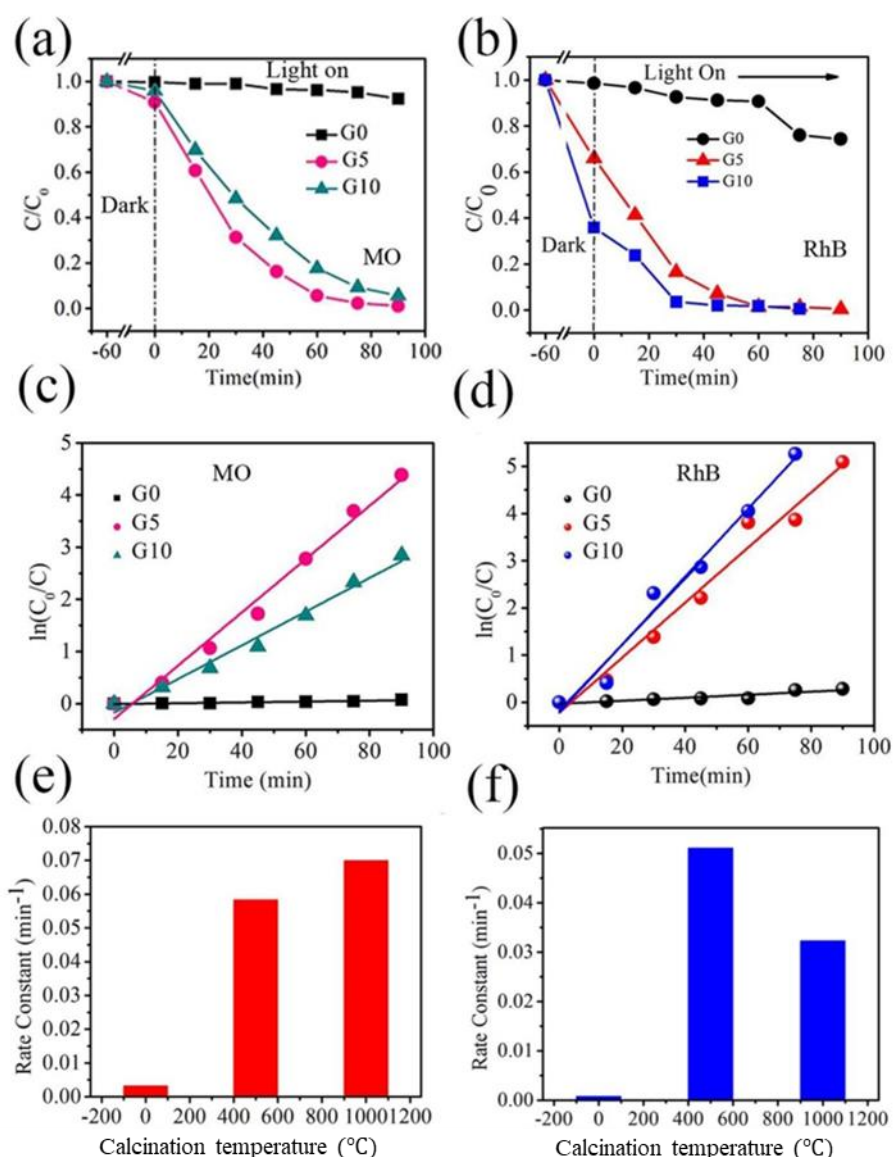

Figure 4.10 Photocatalytic degradation activities of the photocatalysts for MO (a) and RhB (b) corresponding kinetic plots of photocatalytic degradation (c) and (d) with various time under UV light irradiation, (e) and (f) the plot of rate constant with different calcination temperature respectively

The degradation performance of both dyes by samples G0, G5 and G10 with respect to time variation of concentration ratio is presented in **Figure 4.10(a-b)**. It can be clearly observed

that MO was almost completely degraded within 90 min by both the samples whereas sample G10 degraded RhB within 30 min, comparatively faster than that of sample G5 (~ 60 min). A more direct result was obtained from determination of degradation rate constants by fitting corresponding $\ln(C_0/C)$ *vs.* t plots (**Fig. 10(c-d)**) which follow the Langmuir- Hinshelwood pseudo first order kinetic reaction,

$$\ln\left(C_0/C_t\right) = kt \qquad (4.5.1)$$

Where C_0 is the initial concentration of the dye and C_t is concentration after time t. t is the irradiation time and k is the degradation rate constant. The results are represented in **Fig. 10 (e-f)** where sample G5 shows a higher rate constant (0.051 min^{-1}) in degrading MO than sample G10 (rate constant 0.032 min^{-1}). Similarly the value of degradation rate constant for RhB is higher for sample G10 (0.072 min^{-1}) than sample G5 (0.058 min^{-1}).

A comparative representation between the photocatalytic performances of this work with already reported gallium oxide are shown in **Table 4.2** which confirms that the micro/nanobrick systems are either more efficient or comparable to the already published identical systems.

4.5.2. Photocatalytic mechanism

The difference (and reverse nature) in degradation efficiencies for RhB and MO by G5 and G10 can be accounted for two factors. Firstly, ion selective adsorption of the dyes as explained in the earlier section and secondly, carriers transfer across the electronic bands of the dye molecule and the catalyst molecule. Considering the very basic mechanism behind photocatalysis, separation of photo-generated e^-/h^+ pair may be identified as one of the most important factors. Additionally, intermediate radicals $^\bullet$OH and $^\bullet$O$_2^-$, formed during photocatalysis process actually cause the physical degradation of the dyes[45]. To investigate the possible roles of these radicals in degradation process, scavenger test was carried out involving IPA, P-Benzoquinone and KI as scavengers for active species $^\bullet$OH, $^\bullet$O$_2^-$ and h$^+$ respectively. The specific contribution of active species in degradation of RhB and MO was investigated in radical trapping test, i.e. scavenger test. IPA, P-Benzoquinone and KI were introduced in the catalysis medium as quenching reagents for active species $^\bullet$OH, $^\bullet$O$_2^-$ and h$^+$ respectively. 1mM solution of BZQ, KI and IPA were separately used for this purpose. The solutions were added in the active medium prior to the commencement of catalysis process and then catalysis experiment was carried out following standard procedure. The filtrates

were collected at particular time interval and time evolved UV absorption spectra of the filtrates were recorded. The degradation percentages were calculated on the basis of concentration ratio of the dyes present in the solution shown in **Figure 4.11.** From the results, it was observed that removal of RhB was hindered significantly after addition of BZQ for all samples, which showed that superoxide radicals, *i.e.* $^{\bullet}O_2^-$ play major role in RhB degradation. Again, MO degradation was hardly affected by BZQ but it decreased appreciably after addition of IPA in case of both samples. This indicates that hydroxyl radicals, *i.e.* $^{\bullet}OH$ are the most important degradation agent for MO (**Figure 4.11**).
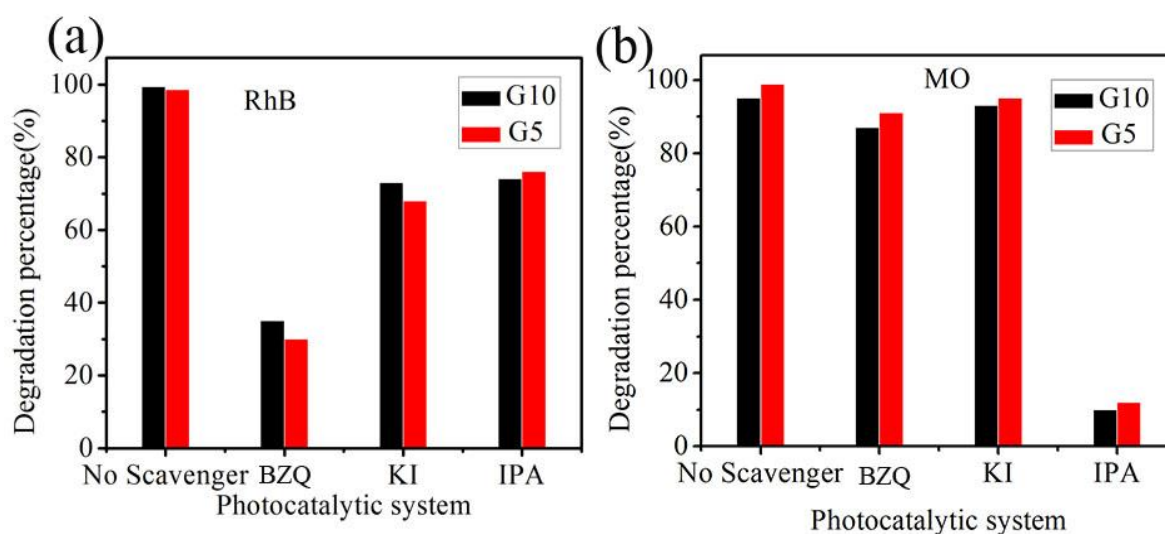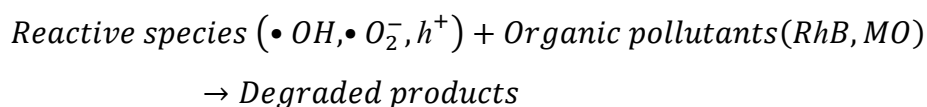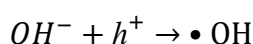

Figure 4.11 Photocatalytic degradation percentages of RhB (a) and MO (b) with addition of Scavengers to the catalyst dye solution

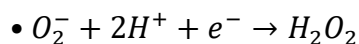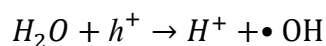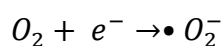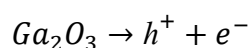The degradation process by these charged agents is dependent on the positions of electronic bands of the participating systems[56]. A schematic of the relative band positions are presented in **Scheme. 4.2**. The standard redox potential of $O_2/^{\bullet}O_2^-$ (-4.45 V *vs.* Vacuum[56]) is more negative than conduction band position of G5 (-2.6 eV *vs.* vacuum[49]) and the CB position of G10 (-2.95 eV *vs.* vacuum[57]) is even more negative than that of G5. So, the photogenerated electrons from the conduction band of G10 can easily reduce nearby O_2 molecules into $^{\bullet}O_2^-$ radical species. This may result into better degradation of RhB by G10 compared to G5. On the other hand VB position (-7.54 eV *vs.* vacuum) of G5 is more positive than that of G10 (-7.7 eV *vs.* vacuum).Now the position of $OH/^{\bullet}OH$ redox potential is at -6.46 V *vs.* vacuum[58] which is closer to G5 VB position. Hence formation of $^{\bullet}OH$ *via* the oxidation of water (i.e., OH^- or H_2O) by photogenerated holes should be enhanced in case of G5. This might result into better degradation of MO by sample G5 compared to G10.
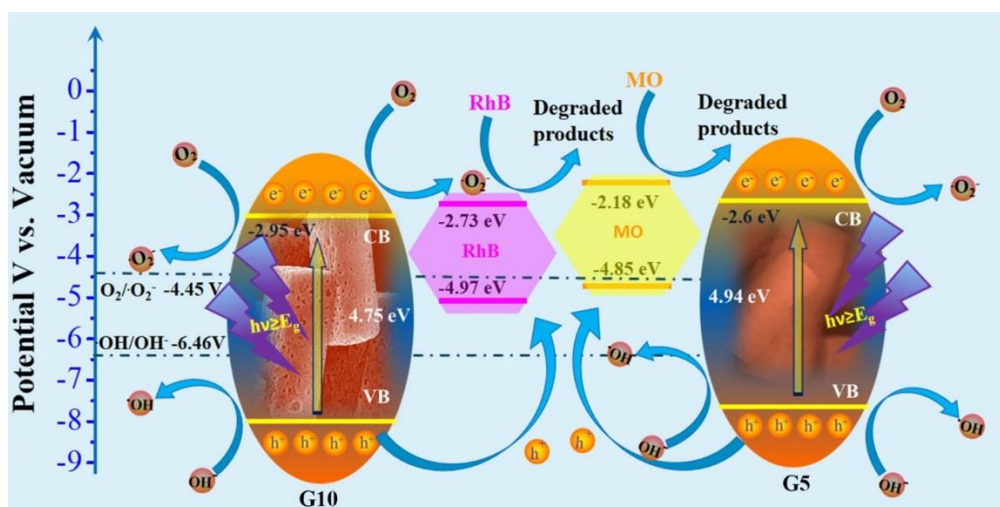
Scheme. 4.2 Proposed mechanism of photocatalytic degradation of Rhodamine B and Methyl Orange

The probable reaction steps behind the degradation of RhB and MO are demonstrated below leading to complete removal of the contaminants

$$Ga_2O_3 \rightarrow h^+ + e^-$$

$$O_2 + e^- \rightarrow \bullet O_2^-$$

$$H_2O + h^+ \rightarrow H^+ + \bullet OH$$

$$\bullet O_2^- + 2H^+ + e^- \rightarrow H_2O_2$$

$$H_2O_2 + e^- \rightarrow \bullet OH + OH^-$$

$$OH^- + h^+ \rightarrow \bullet OH$$

$$Reactive\ species\ \left(\bullet OH, \bullet O_2^-, h^+\right) + Organic\ pollutants(RhB, MO)$$
$$\rightarrow Degraded\ products$$
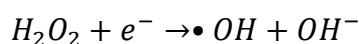
This as a whole explains the better degradation of RhB by sample G10 and higher rate constant of G5 for MO degradation. This mechanism is another proper example of ion selective photodegradation process[44, 46]. This proposed mechanism can also be extended to identical oxide systems as an additional tuning factor of wastewater treatment techniques.
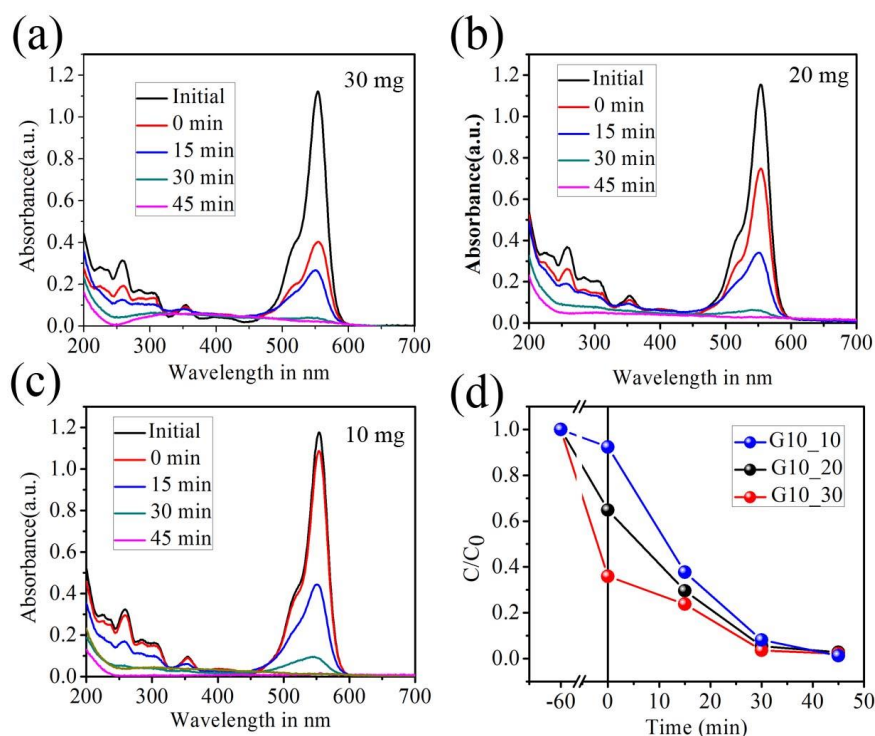
4.5.3. Effect of catalyst load variation

Figure 4.12 Time-dependent UV absorbance spectra of the RhB solution along with G10 having load 30 mg (a), 20 mg (b), 10 mg (c) taken at different times, corresponding (d) photocatalytic degradation activities of the photocatalysts

The effect of sample loading on the photocatalytic activity was also tested with G10, as this one emerged as the most efficient catalyst in general. The loading of the sample was varied from 10 mg to 30 mg and the entire process of photocatalysis test was repeated for each case. The results of time evolution of photocatalytic activity in varying load of catalyst are presented in **Figure 4.12(a-c).** The obtained results can be explained in two sections. In first step, i.e. physical adsorption is affected due to sample load variation. The removal of RhB by physical adsorption on catalyst surface is eventually a function of amount of sample in the solution and hence removal by adsorption is naturally decreased due to decrement of sample amount shown in **Figure 4.12d**. However, it can be clearly seen that the sample load does not affect the 'photocatalysis' performance appreciably. Even lower amount of catalyst showed almost same degradation performance while all other parameters were kept constant.

Table 4.2: Analysis of the photocatalytic performance with already reported gallium oxide and this work.

Material	Average Width/ diameter	Dye Concentration (mol/L)	Photocatalyst Concentration (mg/L)	Target dye	Illumination Source	Dye degradation after 60 min	Kinetic rate constant K(min⁻¹)	Ref.
α-Ga$_2$O$_3$ nano bricks	700 nm			RhB		98.3%	0.058	
				MO		94.4%	0.051	This
β-Ga$_2$O$_3$ nano bricks	500 nm	10⁻⁵ M	750	RhB	40 W UV lamp	98.6%	0.072	Work
				MO		82.4%	0.032	
α-Ga$_2$O$_3$ nanorods	300-400 nm	2x10⁻⁴ M	1000	RhB	100 W UV lamp	35%	--	[39]
β-Ga$_2$O$_3$ nanorods	300-400 nm	2x10⁻⁴ M	1000	RhB	100 W UV lamp	40%	--	[39]
Ga$_2$O$_3$ nano particles	400-900 nm	6mg/L	500	RhB	8 W UV lamp	90%	--	[47]
(β-Ga$_2$O$_3$ NWs)- (rGO) hybrids	80-90 nm	10⁻⁵M	200	MB	mercury lamp 500W	74%	0.0164	[48]
α-Ga$_2$O$_3$ nano plates	(25–250) nm	0.45 x10⁻⁵ M	90	Congo red	AM1.5 1000 W m⁻² solar simulator	70%	0.016	[49]
α-Ga$_2$O$_3$ nano plates	(25–250) nm	0.45 × 10⁻⁵ M	90	RhB	AM1.5 1000 W m⁻² solar simulator	53%	0.014	[49]
Floral β-Ga$_2$O$_3$ nanorods	1 μm	2x 10⁻⁵ M	1000	RhB	150 W xenon lamp	39%	--	[50]
β-Ga$_2$O$_3$ micro spheres	1-3 μm	2x10⁻⁵ M	1000	RhB	150 W Xenon lamp	60%	--	[51]
β-Ga$_2$O$_3$ nanorods	50 nm	2x10⁻⁵ M	1000	RhB	150 W Xenon lamp	34%	0.015	[52]
β-Ga$_2$O$_3$ nanobelts	50-90 nm	10⁻⁵ M	--	RhB	UV lamp	41%	0.0087	[53]
β-Ga$_2$O$_3$ sheet	--	2.15x10⁻⁵ M	500	CR	30 W UV lamp	33%	0.005	[54]
α-Ga$_2$O$_3$ nanorods	50-100 nm	0.84x 10⁻⁵ M	1000	RhB	UV lamp	62%	--	[55]

4.5.4. Recyclability test

The efficiency of G10 in photocatalysis under multiple use condition was also tested. The result of degradation efficiency of dyes RhB and MO for multiple cycles is presented in

Figure 4.13a. It can be clearly observed that the Ga_2O_3 microbar photocatalyst retain their photocatalytic performance even after 3rd cycle with infinitesimal variation of degradation rate constant (0.01%). The highly stable crystalline phase and the compositional invariance of Ga_2O_3 nanocatalyst were identified as the major reason behind this strong durability. The XRD pattern (**Figure 4.13b)** of G10 obtained after 3rd cycle also supported this inference. Compositional stability of the sample after photocatalysis was also confirmed from EDX study and the post-catalysis uniformity of constituent elements is presented in **Figure 13(c)**.
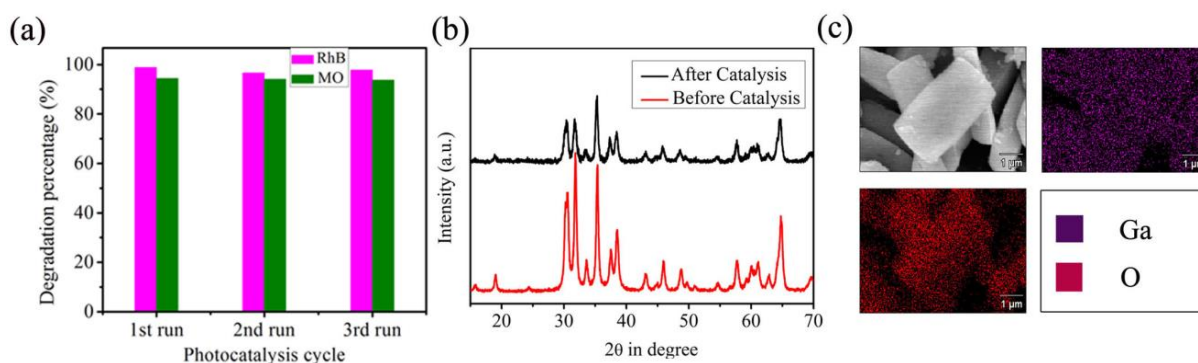

Figure 4.13 (a) Recyclability test for the degradation of RhB and MO by the sample G10 with load 10 mg, (b) XRD of the sample after and before catalysis, and (c) EDX of the sample G10 after 3rd run

4.5.5. Mixed Dye degradation

To investigate the photocatalytic performance of the samples in nearly real system, a mixed dye solution was treated under UV irradiation using sample G10. For this, RhB and MO solutions were mixed in 1:3 ratio and G10 was used in appropriate amount. Thereafter, dark stirring followed by standard photocatalysis experiment was carried out and time evolved UV-Vis absorption was investigated. In addition to normal photocatalysis test, the scavenger test was also carried out for mixed dyes to study the contribution of different reactive species (such as $^{\bullet}OH$, $^{\bullet}O_2^-$, h^+). The results are depicted in **Figure 4.14d**. It can be clearly observed from the time evolved UV-Vis absorbance spectra of mixture solution that the combined dye almost completely degraded within 30 min (**Figure 4.14a**). Like in the load variation test, these results can also be explained in two sections. Initially, during dark stirring, where physical adsorption of the (mixed) dye is the major phenomenon, we can see an appreciable decrement in removal percentage compared to the results obtained for same sample for the individual dyes (**Figure 4.8c, 4.8f** and **4.14a**). It is obvious that the dye to sample ratio significantly increased in case of mixed dye experiment and hence the adsorption of dye molecule on sample surface decreased significantly. However, appreciable change in

degradation performance was also observed for 'actual' photocatalysis part, i.e., after physical adsorption. The degradation rate enhanced almost 1.5 times for RhB by G10 in presence of MO in the solution. Again, significant enhancement of rate constant (4.5 times) was observed for MO by G10 in presence of RhB represented in **Figure 4.14c**.
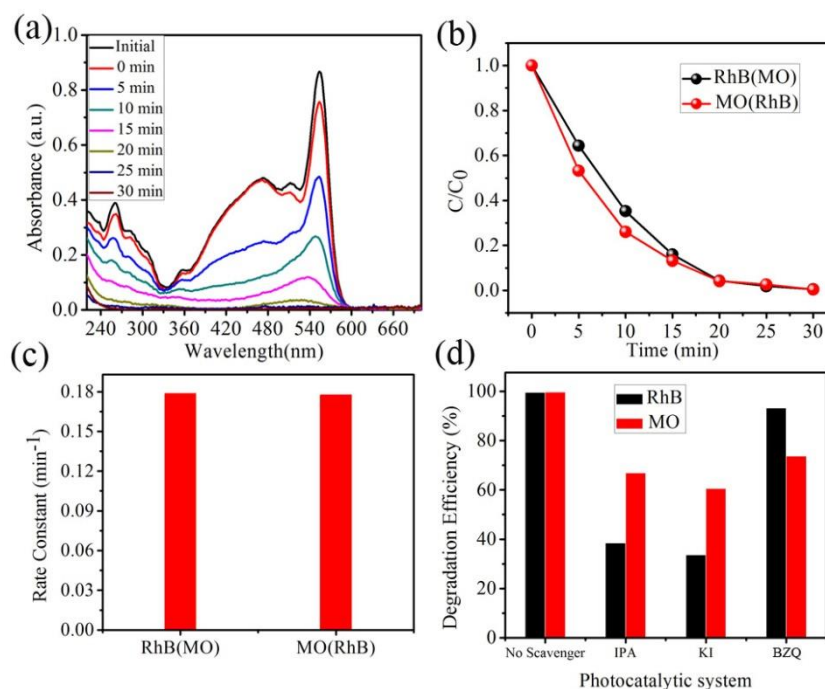

Figure 4.14 (a)Time-evolved UV-Vis absorption spectra of mixed dye (RhB and MO) solution along with G10 microcrystals taken at different times, corresponding (b) photocatalytic degradation activities of the photocatalysts, (c) degradation rate constant of different dyes in mixture, (d) Degradation percentage of RhB and MO with addition of scavengers

This remarkable enhancement of degradation performance of G10 for both dyes can be explained considering the electronic band positions and the effective surface charges of the catalyst. When the catalyst particle independently takes part in the degradation process, $^{\bullet}OH$ and $^{\bullet}O_2^-$ act as the major degrading radicals, a significant energy difference between valance band positions of RhB, MO and the sample can prevent considerable contribution from h^+. But the situation is quite favorable when the catalyst acts in presence of mixed dyes. Due to direct contact of the sample and both dyes, their electronic band positions are expected to influence mutually leading to their rearrangement energetically closer to each other. This should enable easier transfer of h^+ from sample to the dyes increasing its contribution in degradation process in addition to $^{\bullet}OH$ and $^{\bullet}O_2^-$ unlike the situation occurred in case of individual dyes. This explanation can be supported from the scavenger test result (**Figure 4.14d**). It can be seen that degradation efficiency of RhB and MO was now affected more after addition of KI and IPA compared to the effect of addition of BZQ. This is a clear

signature of significant contribution from h^+ which was not prominent in case of individual dyes (**Figure 4.11**).

4.5.6. Phenol degradation

Encouraged by the results obtained for different dye degradation, the efficiency of Ga_2O_3 nanocrystalline photocatalysts for degradation of hazardous chemical reagent 'phenol' was investigated. The process followed here was same as general photocatalysis experiment with only exception of recording of time evolved PL spectra for determination of phenol removal. The results are presented in **Figure 4.15**. It is found that the of $\ln(C_0/C)$ vs. t graphs could not be fitted with a single straight line, rather they can be fitted with two stage linear plots which indicate two-stage pseudo-first order degradation kinetics. Such type of behavior is often observed in literature related to photocatalysis[59-60]. The reason is hidden in the existence of two sub-steps in the catalysis process. In the first stage, contaminant molecules already attached on catalysis surfaces during dark stirring suffers degradation and dissociates into smaller organic compounds spending appreciable time. During this interval, comparatively smaller number of new long chained organic contaminant molecules can come to the contact of catalyst surface. This results in a lower rate of degradation. Once the previously attached contaminant molecules are broken and degraded into byproducts, probability of attachment of remaining few target molecules increases and thus the degradation rate also increases.

This proposed two step degradation process may be fitted using the following equation

$$C_t = C_0 e^{-k_1 t} \text{ for the range } 0 \le t \le t_1 \tag{4.5.1}$$

$$C'_t = C_{t_1} e^{-k_2(t-t_1)} = C_0 e^{-k_1 t_1} e^{-k_2(t-t_1)} \text{ for } t > t_1 \tag{4.5.2}$$

Where, C_0 is the concentration of the contaminant before UV illumination. C_t and C_t' are the concentrations of the same after degradation time t in stages 1 and 2, respectively under UV irradiation. k_1 and k_2 are the corresponding degradation rate constants. Considering this, the $\ln C_0/C$ vs. t graphs were separately presented these two sub-steps and fitted accordingly in two different pseudo first order degradation kinetics as can be observed in **Figure 4.15e.**

The results showed that like in the case of RhB, G10 sample emerged as the most efficient one to degrade phenol. The superiority of G10 in all kind of degradation was directly correlated to the most porous feature of the same. As the synthesis time increased, the porosity also increased from sample G5 to G10. Thus the effective surface area coming to

direct contact of the aqueous media containing the contaminant increases. Thus the probability of dye degradation increases multifold leading to more efficient catalysis rate constant.
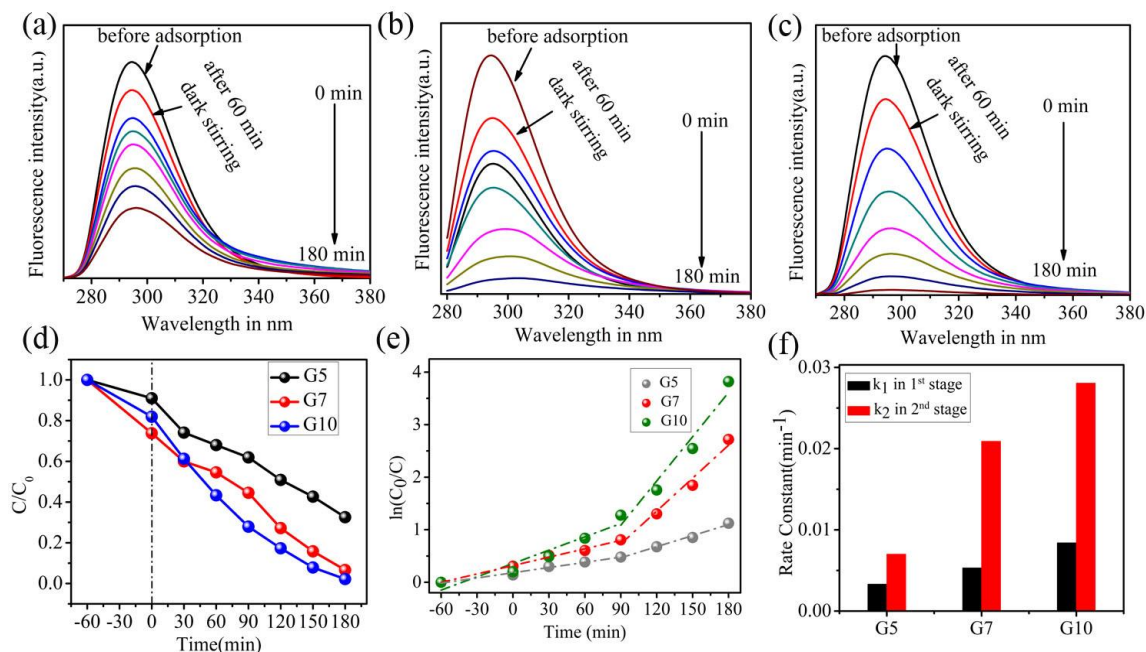

Figure 4.15 Time-dependent photoluminescence spectra of the phenol solution along with G5 (a), G7 (b), G10(c) microcrystals taken at different times, corresponding (d) photocatalytic degradation activities of the photocatalysts, (e) the kinetic plot of photocatalytic degradation with various time under UV light irradiation, and (f) the plot of rate constant with different calcination temperature

4.6. Conclusion

Ga_2O_3 nano/microbrick samples were prepared from direct calcination of hydroxide phase of the same. Variation of calcination temperature resulted in tuning of porosity of the synthesized samples. The photocatalytic activity of porous Ga_2O_3 microbricks was tested for water disinfection. It was observed that the phase, surface charge type and morphology together control the dye degradation performance. Surface electrostatic property was found to be the strongest factor among them and the same is proposed as ion selective adsorption process. It was also found that trace amount of Ga_2O_3 photocatalyst can remove hazardous dyes efficiently with appreciable recyclability. The degradation rate constants were found to be as high as 0.072 min^{-1}, 0.051 min^{-1} and 0.18 min^{-1} for RhB, MO and mixed dyes respectively ending with almost complete removal of the dyes. The samples were also found capable to remove chemical contaminant like phenol from water. A strong correlation of the intermediate radicals •OH, •O_2^- and h^+ with catalytic performances was established depending upon modification of band position of the dyes. This work is therefore conferred as a facile

technique to fabricate morphology tuned advanced Ga_2O_3 photocatalysts for multidirectional catalysis activity.

4.7. References

1. Y. Lu, X. Zhang, Y. Chu, H. Yu, M. Huo, J. Qu, J. C. Crittenden, H. Huo, X. Yuan, Appl. Catal. B: Environ. 224 (2018) 239-248.

2. M.-h Wu, L. Lia, Y.-c Xue, G. Xu, L. Tang, N. Liu, W.-y Huang, Appl. Catal. B: Environ. 228 (2018) 103-112.

3. K. M. Zhang, Z. G. Wen, J. Environ. Manage. 88 (2008) 1249–1261.

4. A. Bhatnagar, A. K. Minocha, Indian. J. Chem. Technol. 13 (2006) 203-217.

5. P. Xu, G. Zeng, D. Huang, L. Liu, C. Lai, M. Chen, C. Zhang, X. He, M. Lai and Y. He, RSC Adv. 4 (2014) 40828-40836.

6. S. Girish Kumar and L. Gomathi Devi, J. Phys. Chem. A 115 (2011) 13211–13241.

7. K. Intarasuwan, P. Amornpitoksuk, S. Suwanboon, P. Graidist, Sep. Purif. Technol., 177 (2017) 304–312.

8. V. Iliev, D. Tomova, L. Bilyarska, J. Photochem. Photobiol. A: Chem., 351 (2018) 69–77.

9. K. Nakata, A. Fujishima, J. Photochem. Photobiol. A: Chem.Reviews, 13 (2012) 169-189.

10. A. K. Arora, V. S. Jaswal, K. Singh and R. Singh, Orient. J. Chem. 32 (2016) 2035-2042.

11. B. Guo , H. Shen, K. Shu, Y. Zeng, and W. Ning, J. Chem. Sci, 121 (2009) 317–321.

12. A. B. Djurisic, Y. H. Leunga, A.M. ChingNga, Mater. Horiz. 1 (2014) 400–410.

13. Y. Kawaguchia , M. Akatsukab , M. Yamamotob , K. Yoshiokaa , A. Ozawaa, Y. Katoa , T. Yoshida, J. Photochem. Photobiol. A: Chem., 358 (2018) 459–464.

14. V. B. Kumar, R. K. Mishra, I. N. Pulidindi, Z. Porat, J. H. T. Luong, A. Gedanken, Energ. Fuel. 30 (2016) 7419−7427.

15. M. Passlack, E. F. Schubert, W. S. Hobson, M. Hong, N. Moriya, S. N. G. Chu, K. Konstadinidis, J. P. Mannaerts, M. L. Schnoes, and G. J. Zydzik, J. Appl. Phys., 77 (1995) 686-693.

16. M. Zinkevich, F. Aldinger, J. Am. Ceram. Soc. 87 (2004) 683-691.

17. A. Arias, N. Nedev, S. Ghose, J. Salvador, D. Mateos, M. C. Alvarez, O. Pe´rez, M. Sua´rez, B. Valdez-Salas, R. Droopad, (2018) 1-6.

18. M. Bagheri, A. R. Mahjoub, A. Ali Khodadadi and Y. Mortazavi, RSC Adv., 4 (2014) 33262–33268.

19. L. Li, B. Ma, H. Xie, M. Yue, R. Cong, W. Gao and T. Yang, RSC Adv., 6 (2016) 59450–59456.

20. Y. X. Pan, Z. Q. Sun, H. P. Cong, Y. L. Men, S. Xin, J. Song, and S. Hong Yu, Nano Research, 9(6) (2016) 1689–1700.

21. M. Bartic, C. I. Baban, H. Suzuki, M. Ogita, M. Isai, J. Am. Ceram. Soc., 90 (9) (2007) 2879–2884.

22. S. Nakagomi, K. Hiratsuka, Y. Kakuda, and K. Yoshihiro, ECS J. Solid State Sci. Technol, 6(2) (2017) 3030-3035.

23. T. Miyata, T. Nakatani, T. Minami, J. Lumin., 87-89 (2000) 1183-1185.

24. S. Kumar and R. Singh, Phys. Status. Solidi RRL 7, No. 10, (2013) 781–792.

25. N. Watanabe, J. Kim, K. Ide, H. Hiramatsu, H. Kumigashira, S. Ueda, H. Hosono, and T. Kamiya, ECS J. Solid State Sci. Technol, 6(7) (2017) 410-414.

26. S. L. Wang, J. W. Yu, P. C. Yeh, H.W. Kuo, L. H. Peng, A. A. Fedyanin, E. D. Mishina, and A. S. Sigov, Appl. Phys. Lett. 100 (2012) 063506.

27. Z. Li, C. de Groot, and J. H. Moodera, Appl. Phys. Lett. 77 (2000)3630.

28. R. Kumar, P. K. Dubey, R. K. Singh, A. R. Vaza, S. A. Moshkalev, RSC Adv. 6 (2016) 17669–17677.

29. Y. Hou, X. Wang, L. Wu, Z. Ding, X. Fu, Environ. Sci. Technol. 40 (2006) 5799-5803.

30. M.-G. Ju, X. Wang, W. Liang, Y. Zhao, C. Li , J. Mater. Chem. A, 2 (2014)17005-17014.

31. M. A. Nguyen, E. M. Zahran, A. S. Wilbon, A. V. Besmer, V. J. Cendan, W. A. Ranson, R. L. Lawrence, J. L. Cohn, L. G. Bachas, M. R. Knecht, ACS Omega 1(1) (2016) 41–51.

32. S. Sharma and M. K. Sunkara, J. Am. Chem. Soc. 124 (2002) 12288-12293.

33. M. C. Johnson, S. Aloni, D. E. McCready, and E. D. Bourret-Courchesne, Cryst. Growth. Des., 6(8)(2006) 1936-1941.

34. G. Wang, J. Park, X. Kong, P. R. Wilson, Z. Chen, and J. Ahn, Cryst. Growth. Des. 8(6) (2008) 1940-1944.

35. Kh. M. Al-khamis, R. M. Mahfouz, Abdulrahman A. Al-warthan, M. Rafiq, H. Siddiqui, Arab. J. Chem., 2 (2009) 73–77.

36. J. Q. Hu, Q. Li, X. M. Meng, C. S. Lee, and S. T. Lee, J. Phys. Chem. B 106 (2002) 9536-9539.

37. Yu Quan, Dong Fang, Xueying Zhang, Suqin Liu, Kelong Huang, Mater. Chem. Phys, 121 (2010) 142–146.

38. C. A. Deshmane, J. B. Jasinski, M. A. Carreon, Micro. Meso. Mater., 130 (2010) 97–102.

39. L. S. Reddy, Y. H. Ko, J. S. Yu, Nanoscale Res. Lett. 10 (2015) 364.

40. K. Girija, S. Thirumalairajan, Valmor R. Mastelarob and D. Mangalaraja, Anal. Methods, 8 (2016) 3224–3235.

41. B. Das, D. Sarkar, S. Maity, and K. K. Chattopadhyay, J. Mater. Chem. C, 3 (2015)1766–1775.

42. A. Chaudharya, A. Mohammada, S. M. Mobina, Mater. Sci. Eng. B 227 (2018) 136–144.

43. I. S. Grover, S. Singh, B. Pal, Appl Surf. Sci. 280 (2013) 366–372.

44. Q. Wang, B. Zhang, X. Lu, X. Zhang, H. Zhu, B. Li, Catal. Sci. Technol. 8 (2018) 6180-6195.

45. A. K. Adepu, R. Anumula, V. Narayanan, Micro. Meso. Mater. 247 (2017) 86-94.

46. J. Romão and G. Mul, ACS Catal. 6 (2) (2016) 1254–1262.

47. A. Dulda, Adv. Funct. Mater. Volume 2016, Article ID 3905625, 1-9.

48. X. Xu, M. Lei, K. Huang , C. Liang, J.C. Xu, Z. C. Shangguan, Q. X. Yuan, L. H. Mab, Y. X. Du, D. Y. Fan , H. J. Yang , Y. G. Wang, W. H. Tang, J. Alloy. Compd. 623 (2015) 24–28.

49. N. Syed, A. Zavabeti, Md. Mohiuddin, B. Zhang, Y. Wang, R. S. Datta, P. Atkin, B.J. Carey, C. Tan, J. v.Embden, A. S. R. Chesman, Jian Zhen Ou, T. Daeneke, and K. Kalantar-zadeh, Adv. Funct. Mater. 27 (2017) 1702295.

50. K. Girija, S. Thirumalairajan, A. K. Patra, D. Mangalaraj, N. Ponpandian, C. Viswanathan, Curr. Appl. Phys. 13 (2013) 652-658.

51. K. Girija, S. Thirumalairajan, V. R. Mastelaro, D. Mangalaraj, J. Mater. Chem. A, 3 (2015) 2617-2627.

52. K. Girija, S. Thirumalairajan, A. K. Patra, D. Mangalaraj, N. Ponpandian, C. Viswanathan, Semicond. Sci. Technol. 28 (2013) 035015.

53. L. C. Tien, W. T. Chen, C. H. Ho, J. Am. Ceram. Soc. 94 (2011) 3117.

54. M. Bagheri, A. R. Mahjoub, RSC Adv. 6 (2016) 87555-87563.

55. D. Li, X. Duan, H. Fan, W. Zheng, J. Mater. Chem. A 1 (2013)12417-12421.

56. H. Zhao, Y. Zhang, G. Li, F. Tian, H. Tang, R. Chen, RSC Adv., 10 (2016) 1-9.

57. Y. Xu, M. A.A. Schoonen, Am. Mineral., 85 (2000) 543–556.

58. H. Sameie, A. A. Sabbagh Alvani, N. Naseri, F. Rosei, G. Mul, B. T. Mei, J. Electrochem. Soc., 165 (7) (2018) 353-359.

59. D. Sarkarand K. K. Chattopadhyay, ACS Appl. Mater. Interfaces 6 (2014) 10044−10059.

60. K. K. Paul and P. K. Giri, J. Phys. Chem. C, 121 (2017) 20016−20030.

Chapter 5

Novel Ag$_2$O-Ga$_2$O$_3$ Type II p-n Heterojunction as an Efficient Water Cleanser for Green Cleaning Technology

Abstract

Ag$_2$O-Ga$_2$O$_3$ based type II p-n nanoheterojunctions were fabricated using ex-situ chemical reduction technique with different densities of Ag$_2$O attachment onGa$_2$O$_3$ surface. A systematic optimization was carried out to establish best performing junction aiming for photodegradation of the noxious organic dye methyl orange (MO). Thorough theoretical and experimental studies were performed to determine relative band positions and ensure charge transfer between the counterparts. Favorable alignment of the electronic bands of Ag$_2$O and Ga$_2$O$_3$ was identified as a key factor for prompt separation of photogenerated e$^-$/h$^+$ pair leading to faster decomposition of water contaminant dyes. The optimized nanoheterojunction sample also performed remarkably fast in degrading carcinogenic hazardous phenol and other dyes like rhodamine B (RhB), aniline blue (AB), eosin B (EB) and mixtures of dyes with different ionic identities. Additional advantages of these junction-based catalysts were also reflected in retainment of catalytic efficiency over multiple water disinfection cycles and its appreciable performance in active media of different pH values. With high degradation rate constants of 0.4158, 0.3306, 0.2436 and 0.207 min^{-1} for RhB, AB, MO, EB respectively, and multidimensional performance as green cleaning agent, this newly explored Ag$_2$O$_3$-gallia nanoheterojunctions are identified as a strong candidate for future water cleaning technology.
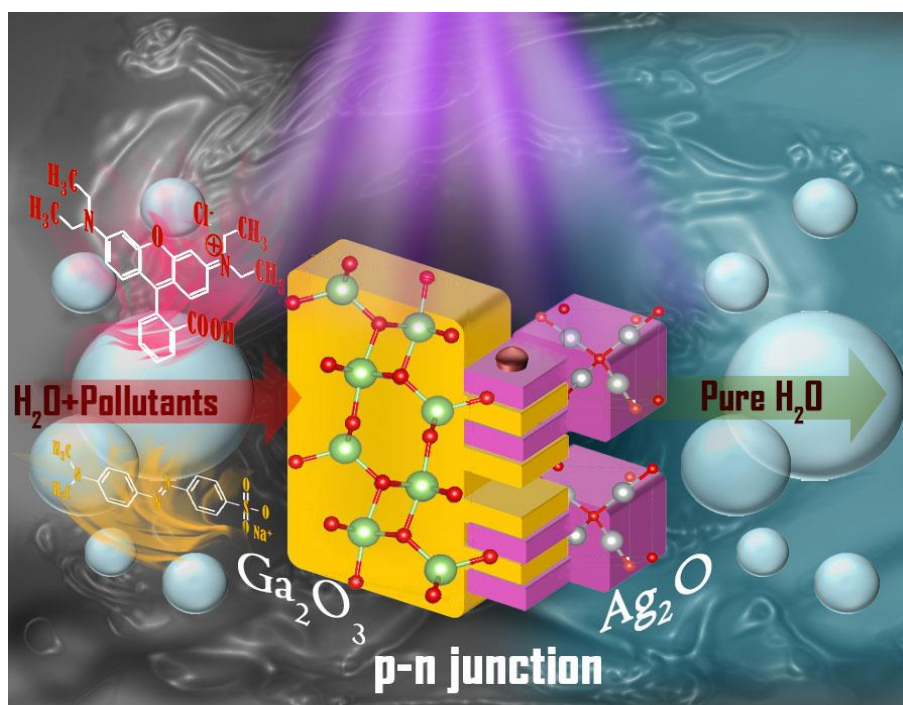
5.1.   Introduction

With the rapid development of device based industries, human urban life is under severe threat of pollution-triggered diseases and health issues. Especially, after the large scale use of polymers and related compounds in different varieties of modern products, organic wastes have emerged as a challenging factor against pure consumable water. Using wide range of semiconductor materials and their derivatives to address this issue has been attempted by materials scientists since few decades[1]. As a result, investigations of photocatalysis activities of semiconductors in pure[2] and composite[3] form have been reported in large numbers. As per those reports, efficiency in contaminant removal registered by semiconducting materials enhances multifold in nano regime[4]. However, with some exceptions, most of the semiconductor nanosystems claiming to be efficient water disinfectant are not free from limitations.

Primarily synthesis procedures of such nano catalysts often include complex techniques like vapor liquid solid (VLS)[5] or may result in very small yield like obtained via hydrothermal[6] method. Synthesizing such catalyst may also result in some hazardous by-products[7] which could add up newer challenge in pollution issues. Moreover, synthesis cost in some sophisticated routes[8] may not be suitable in industrial aspect and thus may be abandoned in areas where financial development is more alarming issue than environmental pollution. Additionally, any new catalyst systems beyond titania must be chosen carefully by considering factors like optical band gap, nanostructure dimension and dispersion capability in aqueous medium etc. Optical band gap is a key factor determining the excitation of the catalyst. Most of the classic photocatalysts exhibit wide band gap and thus are excited by UV illumination[9]. Nanostructure shape and dimension are other important parameters governing the catalytic activity of the water disinfectant agents. It is well known that low dimension of the catalysts helps easy separation of photogenerated e^-/h^+ pair leading to higher catalytic efficiency[10, 11]. A large number of techniques have also been developed to trigger prompt separation of e^-/h^+ pair by impurity doping[12], composite fabrication[13] and structural modification[14] but formation of heterojunction within the catalyst system has been accepted as the most efficient way in this regard. Keeping this in mind, several groups have attempted photocatalysis performance of junction based nanosystems so far[15, 37-48]. Choosing the p-n type counterpart requires similarity of band gaps, conductivity and dimension with the host catalyst structure. Among the large number of popular catalyst systems,

few fulfill the criteria of low cost high yield synthesis, tunable optical features and structural flexibility of junction formation in order to achieve better photocatalytic performance. Ga_2O_3 has already been recognized as a highly efficient photocatalyst[16] with tunable optical and electrical properties[17]. There are wide variety of synthesis techniques for fabricating low dimensional Ga_2O_3 with different crystalline phases[18]. In our earlier work we demonstrated a unique feature of ion selective photocatalytic ability of Ga_2O_3[19]. Being a traditional and well-functioning photocatalyst, comparable in all aspect with material like TiO_2, Ga_2O_3 has been studied for its catalytic behavior in different shapes[20], dimensions[21] and composites[22]. However, none of those studies have ever employed the facility of junction formation in catalytic activity of gallium oxide. Few studies with hybrid catalyst system involving gallium oxide have used carbon/graphene as the boosting agent[23]. The introduction of these carbon derivatives may be effective in view of catalysis aspect, but their individual synthesis and attachment with Ga_2O_3 may not be trivial.

This work has attempted easy ex-situ hybridization of Ga_2O_3 with Ag_2O is aiming facile fabrication of type II p-n nanoheterojunction based photocatalyst. Choosing Ag_2O as the p-type counterpart was inspired by compatible band alignment[24] and easy synthesis route[25] observed for similar junction based composites. Factors like finite difference of work function and electron affinities were employed to trigger easy separation of e^-/h^+ pair. In addition to that, from our previous study, synthesis of porous Ga_2O_3 via solid state method was optimized. Structural facility of the samples to be with dye molecules was predicted and thus synthesis of the hybrid system in simple wet chemical route was employed[19]. Different ratio of the junction components was optimized to fabricate most efficient photocatalysts. Thorough investigation via X-ray diffraction (XRD), field emission scanning electron microscopy (FESEM), high resolution transmission electron microscopy (HRTEM), energy dispersive X-ray analysis (EDX), X-ray photoelectrons spectroscopy (XPS) were performed to obtain phase, morphology and composition related information respectively. The type of the semiconductors and the positions of the electronic bands were studied using Mott-Schottky analysis in order to understand the mechanism behind the improved photocatalytic property. The possibility of charge transfer across the nanoheterojunction was simulated via first principle study using VASP software. The optimized most efficient gallia-Ag_2O sample showed extraordinary dye degradation capability to disintegrate hazardous dye like MO with high degradation rate constant of 0.2436 min^{-1}. In

addition to thorough photocatalysis study for MO, the optimized hybrid sample was tested for its capability in degrading a variety of dyes of different ionic identities, their mixtures and harmful colorless water pollutant like phenol to mimic realistic removal of water pollutants. Very encouraging outcome of these studies with degradation rate constant greater than 0.05 min^{-1} was obtained. This report of gallium oxide-Ag_2O nanoheterojunction establish this hybrid system as one of the most available future green cleaning agent and the facile fabrication can further be extended to cultivate other important applications of this novel nanojunction.

5.2. Experimental

$Ga(NO_3)_3.xH_2O$, absolute ethanol, NH_4OH, p-Benzoquinone, isopropanol, Na_2-EDTA, methyl orange, rhodamine B, eosin B and aniline blue were supplied by Sigma Aldrich. $AgNO_3$ and phenol were purchased from Merck. All purchased reagents were of analytical grade and used without further purification.

5.2.1. Preparation of Photocatalysts: 3D Ga_2O_3 microbricks

Ga_2O_3 were synthesized via simple chemical route followed by calcination. Typically 0.1 M of $Ga(NO_3)_3.xH_2O$ was dissolved into 100 mL water with continuous stirring. The temperature of the solution gradually increased from room temperature to 95 °C. After reaching the final temperature NH_4OH was added drop by drop to the solution until the pH of the solution reached 9. Then the solution was kept for 4 hours at that temperature. It was cooled down naturally to the room temperature. The collected white precipitate (GaOOH) was dried overnight at 60 °C and then calcined at 1000 °C for 3 hours to obtain β-Ga_2O_3.

5.2.2. Ag_2O attachment on to the Ga_2O_3 microbricks

All the samples were prepared via simple chemical reduction process. Firstly 0.6 g of the as prepared gallium oxide was dispersed via sonication into 100 mL of deionized water. Then NH_4OH was dropped to the suspension to adjust the pH of about 12. Measured amount of $AgNO_3$ was then added to the suspension controlling the molar ratio of Ga_2O_3 and $AgNO_3$ 6:1, 4:1, 2:1, 1:1, 1:2. After magnetically stirring the mixture for 2 hours, the obtained dark brownish Ag_2O/Ga_2O_3 p-n heterojunction photocatalyst were washed several times by deionized water and dried over night at room temperature. To synthesize pure Ag_2O same procedure was followed except the addition of the as prepared gallium oxide. Pure β-Ga_2O_3 and Ag_2O were named as

G1A0 and G0A1 and all the composite samples were labeled as G6A1, G4A1, G2A1, G1A1, and G1A2 respectively.

5.2.3. Characterization

Crystal structure of as-synthesized G1A0, G0A1 and p-n heterojunctions were investigated by using x-ray diffraction (XRD, BRUKER D8 Advance) analysis. The detailed morphological features including the microstructure, lattice image and the decoration of Ag_2O on Ga_2O_3 microbricks were examined by using high resolution transmission electron microscopy (JEOL-TEM 2100 (200 kV)) and field emission scanning electron microscopy (FESEM, S-4800, Hitachi) and the compositional analysis and chemical status were studied by energy dispersive X-ray spectroscopy (EDX, equipped with electron microscope) and X-ray photoelectrons spectroscopy (XPS, HSA-3500, SPECS, Germany). Zeta potential measurement for surface charge analysis at different pH was studied by Malvern Zeta sizer Nano-ZS 90 instrument with deionized water as the dispersion medium. UV–Vis diffuse reflectance spectra (DRS) of the powder samples were obtained by UV–Vis analysis (Shimadzu UV 3600 UV–Vis-NIR Spectrophotometer) using $BaSO_4$ as a reflectance standard. The electrochemical measurements for Mott-Schottky analysis were carried out on a CHI760E in PGSTAT302 N AUTOLAB work station in a three-electrode system, where the samples were uniformly applied on a Ni foam as a working electrode, a Pt plate served as the counter electrode and an Ag/AgCl (saturated KCl) was as reference electrode. Whereas the electrolyte used was 0.1M Na_2SO_4 solutions. The working electrode was prepared as follows: 40 mg pristine sample, 5 mg acetylene black and 5 mg PVDF were used to prepare a uniform mixture. Then a requisite amount of NMP solution was added drop wise to the mixture to form black-colored slurry. After that the final mixture was vigorously and continuously stirred for 2 h. Then it was uniformly coated on properly cleaned Ni foam of area 1 cm^2. Finally the working electrode was dried overnight in an oven at 60 °C to improve adhesion.

The first principles calculations were carried out using Vienna ab-initio simulation package (VASP) [26, 27] with the projector-augmented-wave (PAW) [28] approach. Perdew–Burke–Ernzerhof (PBE) functional[29] within the generalized gradient approximation (GGA) was implemented to deal with the exchange-correlation terms of the Hamiltonian. Plane wave basis set up to an

energy cut off 500 eV was utilized throughout the calculations. Γ centred k point meshes of (4×4×4) and (2×2×3) were used during the geometrical optimization and electronic property calculation of the β-Ga$_2$O$_3$ and Ag$_2$O unit cells respectively and k point mesh of (3×1×1) was utilized for the composite system. The calculation for the composite system was carried out by applying a vacuum slab of length 24 Å along the normal direction to the surface to ward off any spurious interactions. The structural relaxation processes were allowed to continue until the total energies converged below 1×10^{-5} eV/ atom. As the band gap values are typically underestimated in GGA based calculations, the Heyd–Scuseria–Ernzerhof (HSE06) hybrid functional[30] was used during the density of states (DOS) and band structure calculations. The PBE + D2 force field (Grimme's) method[31] was implemented for dispersive force corrections.

5.2.4. Photocatalytic study

Investigation of the photocatalytic performance of the samples was performed by the degradation of Methyl Orange (MO) and a series of experiments were executed in a standard lab made photocatalytic setup under UV light irradiation. In the typical experiment, stock solution of MO (0.01 g/mL) was prepared. Then the test solution of concentration 10^{-5} M was prepared by mixing the appropriate amount of DI water to the stock solution. 8 mg of the different Ag$_2$O/Ga$_2$O$_3$ photocatalysts were added to the 40 mL of the aqueous solution of MO. The suspension was then placed in dark for 1 hour with magnetic stirring to attain the adsorption-desorption equilibrium between the organic dye molecules and the heterojunction photocatalyst. After that at a particular interval of time, 3 mL of the suspension were collected and centrifuged for further spectroscopic analysis while it was exposed to UV irradiation (λ= 254.6 nm, UVC) using two 40 W UV tube (Phillips). By using UV-Vis spectrophotometer (SHIMADZU-UV-3101-PC), the residual dye concentration was detected. Same procedure was followed for the degradation of RhB, EB, AB and phenol using G2A1 as photocatalyst.

5.3. Results and Discussion

5.3.1. Structural analysis

The crystallinity and phase of the as prepared pure and composite samples with different precursor molar ratio were studied by X-ray diffraction pattern as shown in **Figure 5.1**.

Diffraction peaks corresponding to cubic Ag_2O [JCPDS 75-1532] and monoclinic β-Ga_2O_3 [JCPDS 76-0573] can be identified at their respective characteristic peak positions. It can be clearly seen that with increasing amount of silver precursor during the synthesis, samples G6A1-G1A2 acquired XRD peaks of higher intensity corresponding to cubic Ag_2O. Whereas, no peak corresponding to Ag_2O was obtained in the pristine sample G1A0 as expected.
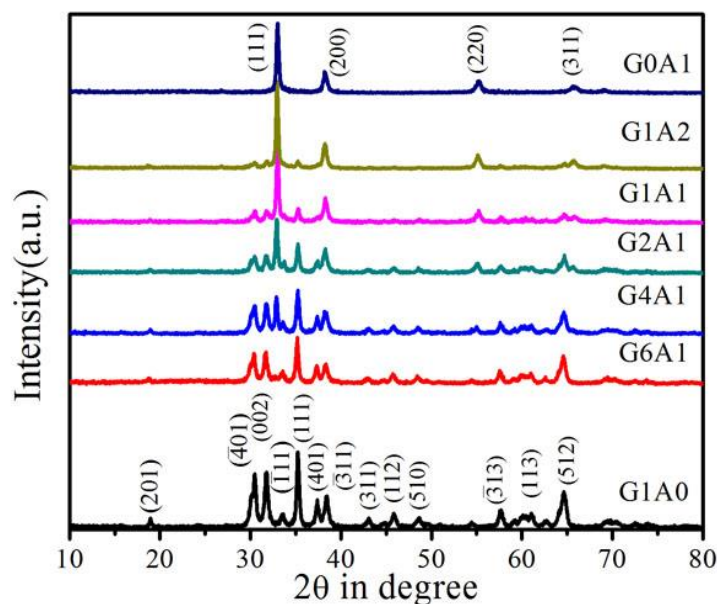

Figure 5.1 XRD patterns of the different samples

5.3.2. Morphological analysis

Morphological features of the samples were studied using FESEM and are presented in **Figure 5.2**. In general, the samples exhibit bricklike structure with approx. 500 nm width and breadth and ~few μm length. Increasing density of the attached Ag_2O NPs can be observed on the surfaces of the Ga_2O_3 bricks in case of samples G6A1, G4A1 and G2A1. The Ag_2O NPs with some occasional agglomeration of the same increased in number with gradual increment in input silver precursor. Sample G1A0 did not show any surface attachment as it was free from any ex-situ surface treatment. On the other hand, sample G1A1 and G1A2 showed dense Ag_2O agglomeration. It may be inferred that in these particular samples, due to high amount of Ag incorporation, the surface attached NPs agglomerated resulting in flake like structures which covered the host Ga_2O_3 bricks fully.
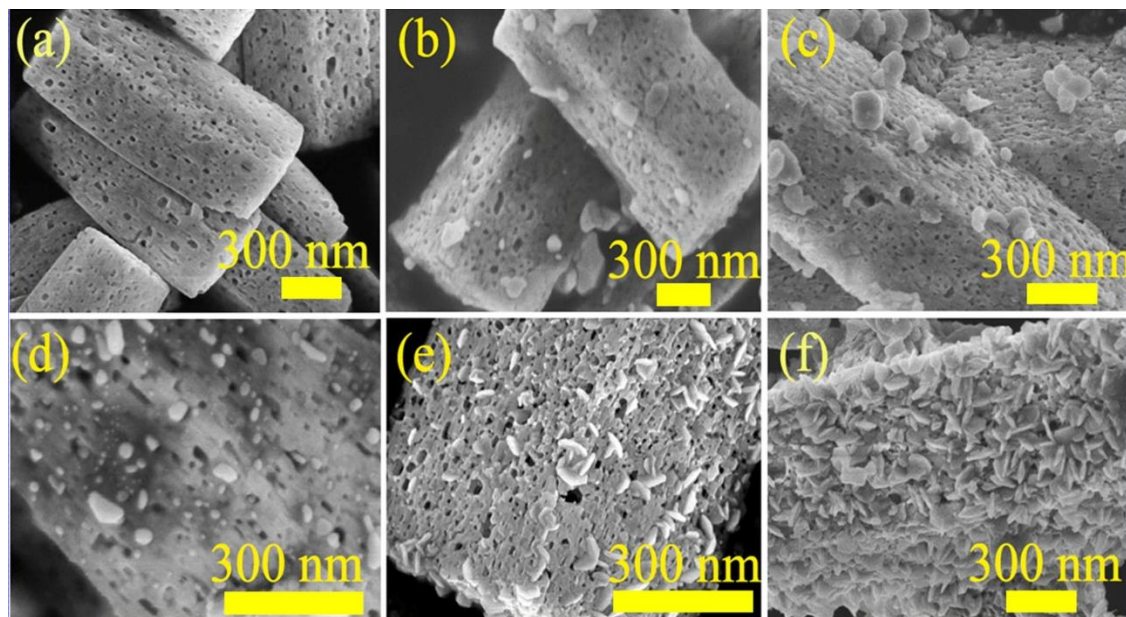
Figure 5.2 FESEM images of as-grown G1A0 (a), G6A1 (b), G4A1 (c), G2A1 (d), G1A1 (e), G1A2 (f)

For better understanding of the nature of attachment of Ag_2O NPs and their crystalline identity, HRTEM studies were carried out and the obtained micrographs are presented in **Figure 5.3**. As already mentioned in the above sub-section, there are discrete agglomerations of Ag_2O NPs on the Ga_2O_3 nanostructures. The TEM micrograph as shown in **Figure 5.3c**, revealed that the attachments have dimension ranging between $40 – 70$ nm. These NPs further agglomerated as the amount of silver precursor was increased for sample G1A1 and G1A2 resulting in flake like attachments covering the host Ga_2O_3 nanostructures. Clear and distinct lattice fringes were obtained for Ga_2O_3 and Ag_2O NPs for the samples indicating the proper crystallinity of both phases which is also in full agreement of our XRD studies. The lattice images of both phases are presented in **Figure 5.3** indicate the presence of (111) plane of gallium oxide and (111) plane of Ag_2O.
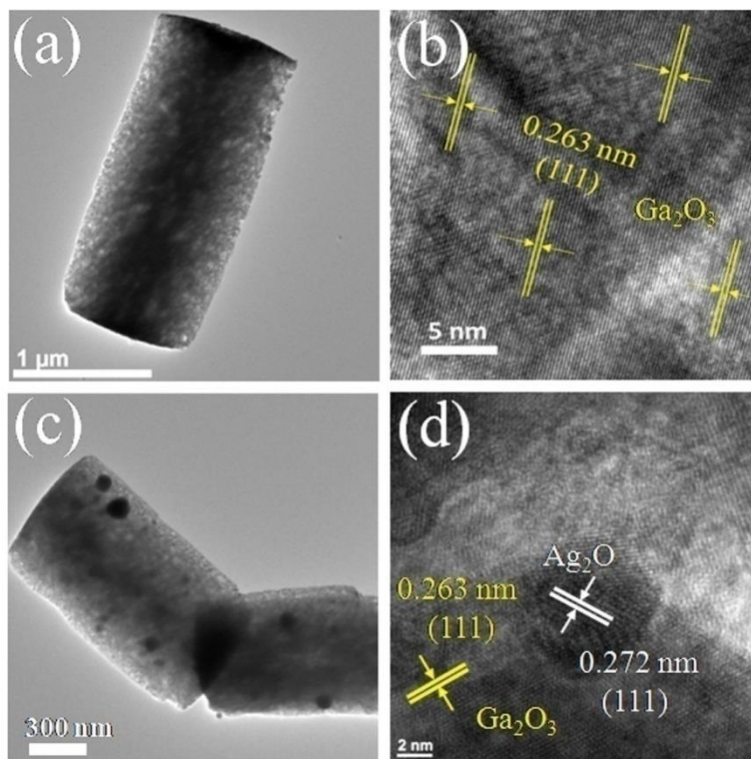
Figure 5.3 TEM images of pure G1A0 (a) and G2A1 (c), HRTEM lattice fringe image of G1A0 (b) and G2A1 (d) respectively
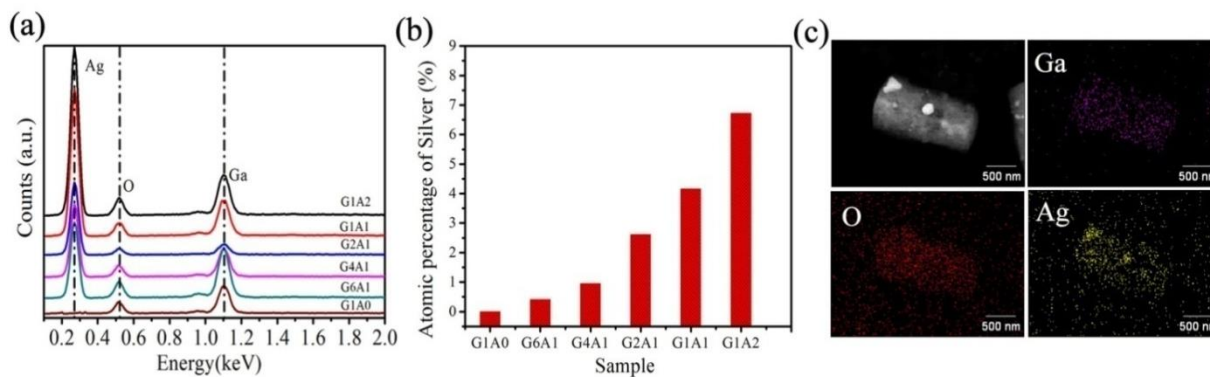
5.3.3. Compositional analysis

Figure 5.4 Energy dispersive X-ray spectroscopy (EDX) spectra (a), percentage of Atomic content of Ag (b) for different composite samples. Elemental distribution for the sample G2A1 (c)

All samples were analyzed by EDX (attached with FESEM) to obtain compositional information. As can be found in **Figure 5.4**, all samples contain expected constituent elements. For example,

the pristine sample (**Figure 5.4a**) G1A0 does not show any EDX peak for Ag whereas presence of EDX peak for Ag is observed for all other samples having Ag_2O NPs as surface attachments. Gradual increment of Ag atomic content can also be inferred from **Figure 5.4b**. Figure 5.4c depicts the elemental mapping of sample G2A1. It can be found that all constituent elements are distributed in adequate uniformity. Moreover, as mentioned in morphological analysis section, some occasional agglomerations of Ag_2O NPs are also visible in color indexed Ag mapping on Ga_2O_3 surface.

The XPS survey scan of sample G1A0 and G2A1are presented in **Figure 5.5**. Oxidation states of different elements in Ga_2O_3-Ag_2O hybrid system were studied and the results are presented in **Figure 5.6**. The full range spectrum of G2A1 composite shows the existence of all the characteristic peaks of both the pure materials (Ga, Ag and O).
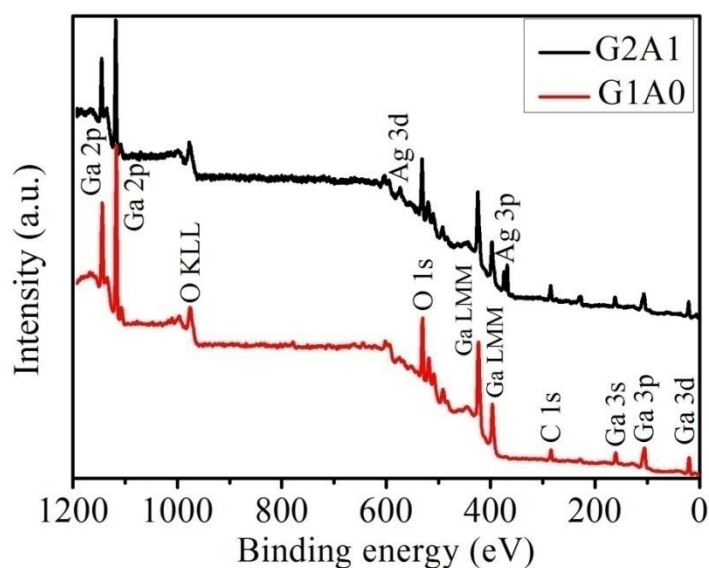

Figure 5.5 Full-range XPS spectra of the sample G1A0 and G2A1

The core level XPS spectra of G1A0 and G2A1 samples as presented in **Figure 5.6a** shows prominent peaks of Ga 2P states. For the pure sample G1A0 the energy peaks positioned at 1145.2 and 1118.5 eV in **Figure 5.6a** are arose from Ga $2p_{1/2}$ and Ga $2p_{3/2}$, representing the Ga-O bonding[32]. A minor blue shift of XPS peak was observed which can be accounted for the change in binding energy due to proper attachment of Ag_2O NPs. **Figure 5.6b** shows the Ag 3d core level spectra of the composite sample. The binding energy of Ag $3d_{5/2}$ and Ag $3d_{3/2}$ in Ag (I)

is always in the ranges of 367.6-367.8 eV and 373.6-373.8 eV, respectively[33]. For sample G2A1 the binding energies of Ag $3d_{5/2}$ and Ag $3d_{3/2}$ located at 367.6 and 373.6 eV (**Figure 5.6b**), which clearly demonstrated that silver mainly existed as Ag (I) in the composite sample. Acquired Core level XPS peaks of O 1S state for pure G1A0 (**Figure 5.6c**) and G2A1 samples (**Figure 5.6d**) were further deconvoluted to obtain constituent sub peaks. An additional peak occurring near 530.07 eV for G2A1 and absent in the pristine sample was assigned for the oxygen bound in attached Ag_2O NPs[38]. Characteristic XPS peaks of O 1S states occurring near 531.6 eV and 530.8 eV were assigned for the oxygen present in host Ga_2O_3 and for chemically adsorbed oxygen on the catalyst surface[34]. However, minor shifts of these two peaks were also observed and the same was identified to be occurring due to the presence of Ag_2O as surface attachment.
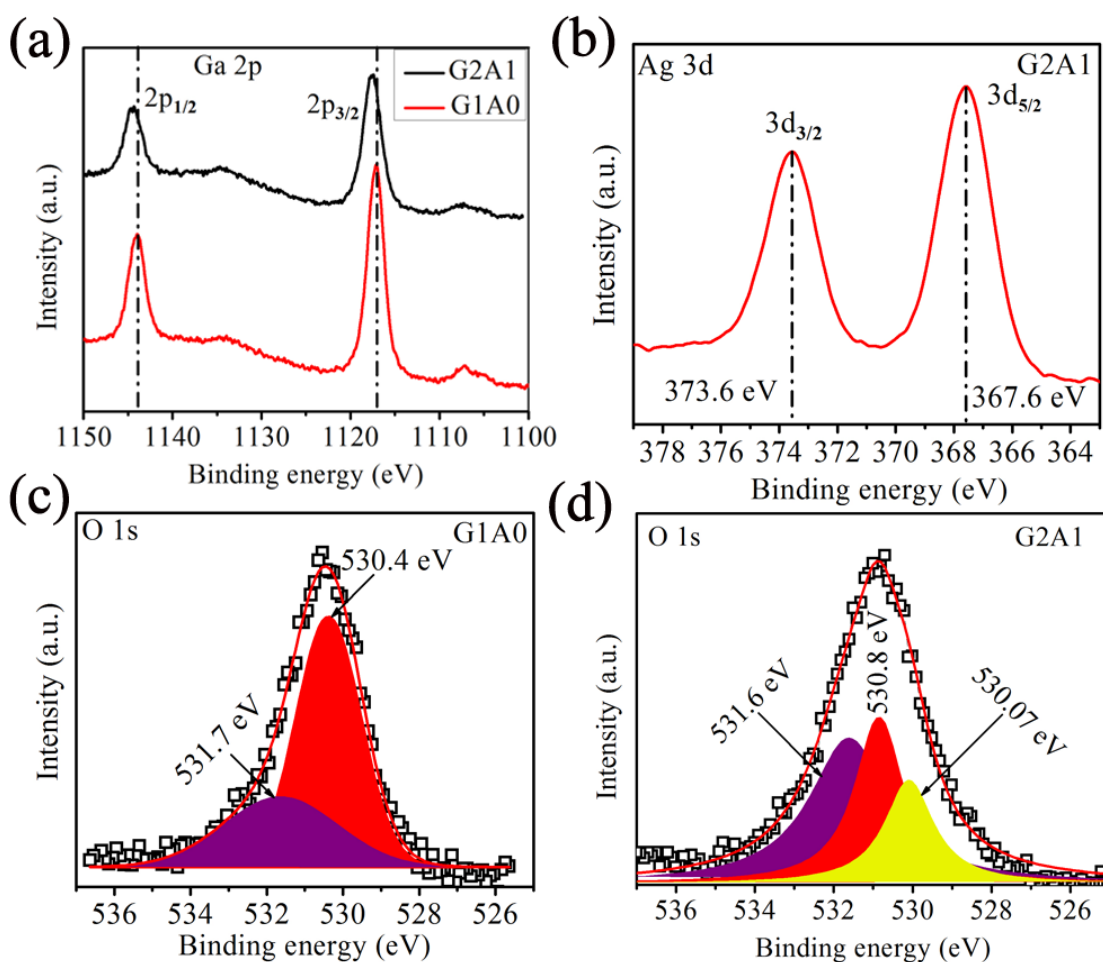

Figure 5.6 A comparison of the core level XPS Ga 2p spectra for pure G1A0 and G2A1 heterostructure (a) core level XPS Ag 3d spectra (b) for G2A1 heterostructure, and O 1s spectra for G1A0 (c) and G2A1 (d) respectively
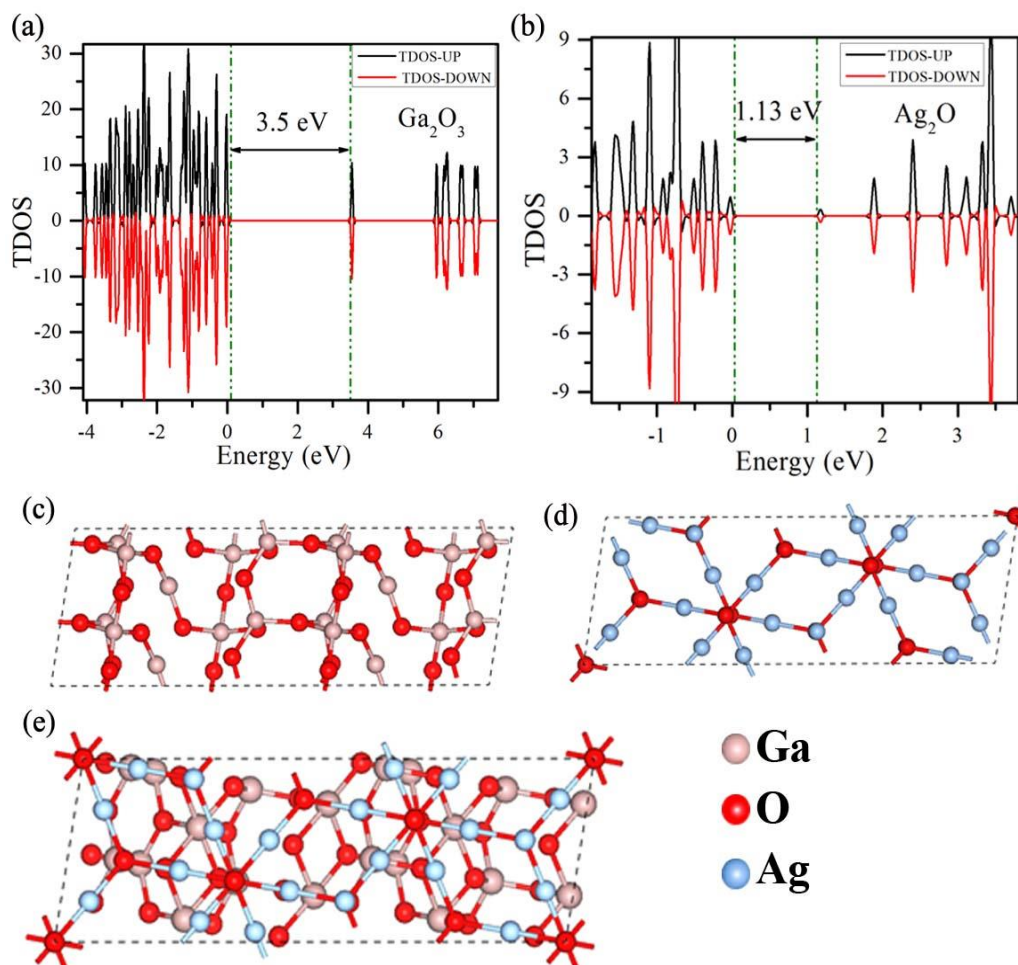
5.3.4. First principles study

We further carried out first principles calculations to determine the electronic properties of β-Ga_2O_3, Ag_2O and their composite system. Both β-Ga_2O_3 and Ag_2O were found to direct band gap semiconductor with both VBM and CBM situated at the Γ point and band gap values 3.5 eV and 1.13 eV respectively. The total density of states plots of pristine β-Ga_2O_3 and Ag_2O (as represented in **Figure 5.7(a, b)** revealed them to be non-magnetic in nature with zero spin polarization near the Fermi level. To study the composite system we selected the miller planes with most prominent peak in the XRD pattern which was found to be the (1 1 1) plane for both the system. The optimized structural model for the pristine and composite samples is presented

in **Figure 5.7(c-e).** To minimize the lattice mismatch between the β-Ga$_2$O$_3$ (1 1 1) and Ag$_2$O (1 1 1) planes the **b** lattice vector of the Ag$_2$O plane was rotated along [1 3 0] direction and a (2×2×1) super cell was considered for the β-Ga$_2$O$_3$ plane. After optimization the distance between the layers was observed to be ~ 2.1 Å with the Oxygen atom from the edge of each of the layers bonded with the Silver and Gallium atom from the edge of other layer. The band structure diagrams of the pristine materials are shown in **Figure 5.8(a-b)**. The planar average charge density along c-direction for the composite and each of the constituent layers individually were also investigated from the first principles calculations. The contribution from Ga$_2$O$_3$ and Ag$_2$O surface were added up and then it was subsequently subtracted from the average charge density of the composite system. It can be clearly inferred from **Figure 5.8(c-d)** that small but finite amount of charge was transferred from Ag$_2$O to β-Ga$_2$O$_3$ reinforcing the experimental observations.
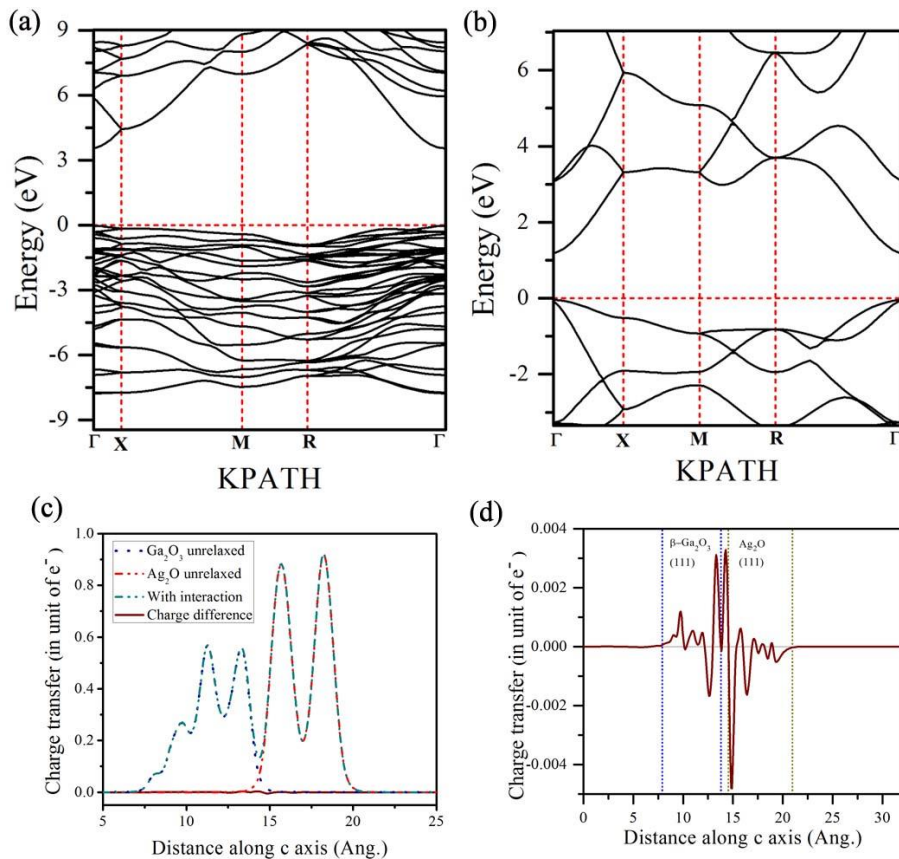

Figure 5.8 Band structure diagram of Ga$_2$O$_3$ (a) Charge transfer plot of the heterojunction (c) with respect to distance along the 'c' axis, (d) shows the zoomed view

5.3.5. Mott- Schottky studies

To obtain clear vision about the positions of the CB and VB edges of the pristine samples, Mott-Schottky studies were carried out. For this, electrochemical impedance measurements for the samples were performed under dark condition and the corresponding flat band potentials (V_{fb}) were determined using the well-known Mott-Schottky equation[35]:

$$\frac{1}{C^2} = \left(\frac{2}{\varepsilon_0 \varepsilon_r N_d e}\right) \times (V - V_{fb} - \frac{k_B T}{e}) \tag{5.1}$$

Here, C= depletion layer capacitance, ε_0=vacuum permittivity (=8.85×10^{-12} $N^{-1}C^2m^{-2}$), ε_r= dielectric constant of semiconductor, N_d=carrier donor density, $k_B T/e$= temperature dependent correction term.
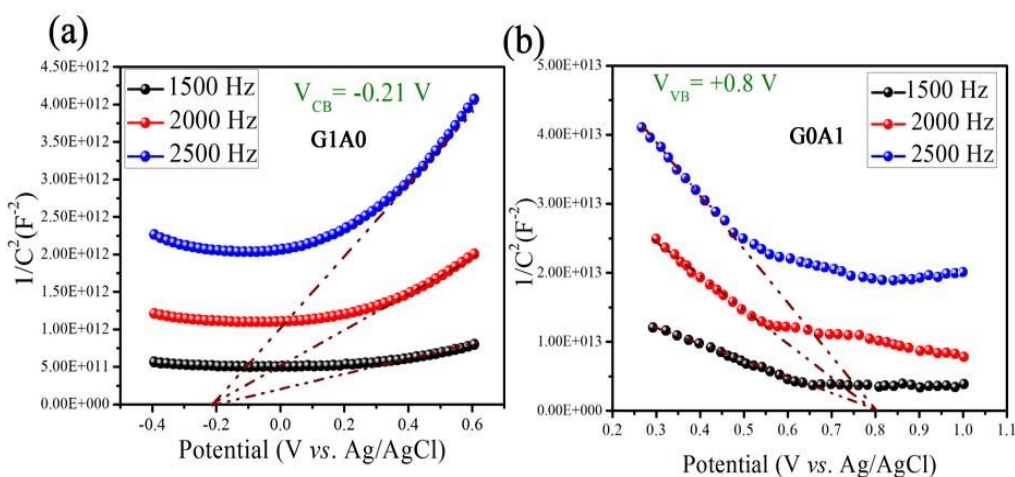

Figure 5.9 Mott-Schottky plots of (a) G1A0 and (b) G0A1 at three frequencies of 1.5 kHz, 2 kHz and 2.5 kHz

For open circuit condition, an n-type semiconductor normally has its Fermi level at a comparatively higher position than the redox potential of the active electrolyte. It enables easy transfer of electrons from the semiconductor to the electrolyte triggering the accumulation of a positive charge in the space charge region. This is obvious from the upward bending of the band edges[35]. The reverse phenomenon can be expected in case of p-type semiconductors. In this experiment, the measurements of both the samples were taken at three different frequencies of 1.5 kHz, 2 kHz and 2.5 kHz and the corresponding slopes of the $1/C^2$ *vs*. V plots (**Figure 5.9**) were found to be positive for G1A0 and negative for G0A1 indicating the n-type and p-type nature of the samples respectively. The flat band potential V_{fb} corresponds to conduction band

for n-type and valance band for p-type materials[36]. Hence from the intercepts of the plots in x-axis, the positions of the conduction band and valance bands of the active samples can be determined. Those values were determined to be -0.21 V and 0.8 V volts for G1A0 (CB edge) and G0A1 (VB edge) respectively considering Ag/AgCl as reference electrode which were further converted to saturated calomel electrode. After conversion, the position of conduction band of G1A0 was found to be -0.25 V and the valance band of G0A1 was found to be 0.76 V. Further the respective valence band edge potential and conduction band edge potential of the samples can also be obtained from the band gaps as assessed from DRS.

5.3.6. Diffuse reflectance spectra analysis

UV-Vis spectroscopic measurements (DRS study) were carried out for the pristine powder samples to figure out their energy band gaps. Sharp falls of Reflectance (%) are observed for the sample G1A0 near 264 nm and for G0A1 near 880 nm as shown in **Figure 5.10a**. The corresponding optical band gap of the samples can be obtained by employing Kubelka-Munk method as presented in **Figure 5.10(b-c)**. The direct optical band gaps are found to be 4.7 eV and 1.41 eV respectively for the samples G1A0 and G0A1.
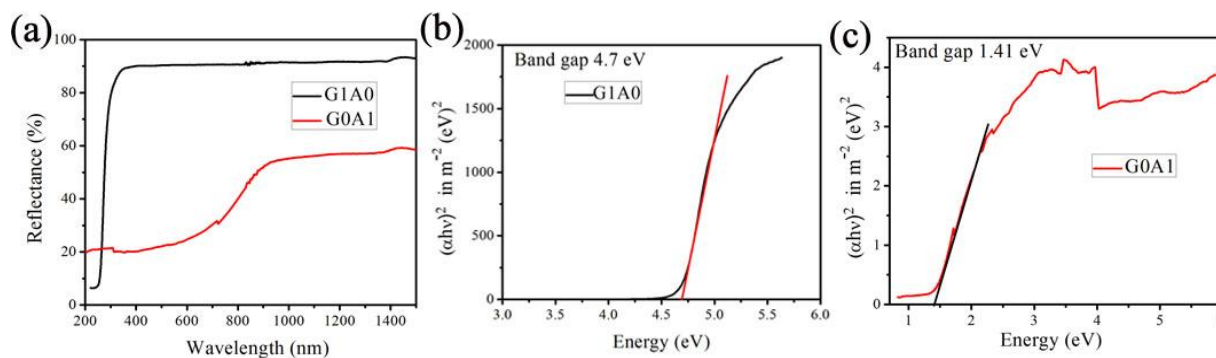

Figure 5.10 (a) Reflectance Spectra of the pristine samples G1A0 and G0A1, (b) Direct band gaps measured for G1A0 (b) and G0A1 (c) employing Kubelka-Munk method

5.4. Photocatalysis

5.4.1. Photocatalytic studies

Performance of the samples for hazardous dye removal was investigated using standard photocatalytic experiment method. Prior to that, absorption studies in UV-Vis range were performed (**Figure 5.10**) for the pristine and one of the composite samples to identify the

excitation range of the target photocatalyst. UV excitation for catalysis experiment was inferred from this study. Thereafter, a well-known AZO dye and a harmful anionic textile pollutant methyl orange were taken as target contaminant. The degradation profiles of MO with application of different samples are presented in **Figure 5.11**. It can be clearly seen that sample G1A0 and G0A1 degraded 82.2% and 33.5% of the initial MO solution respectively within 60 minutes (**Figure 5.11e)** whereas the degradation efficiency enhanced multifold for composite samples **(Figure 5.11a)** and MO was almost completely removed within just 9 minutes when G2A1 was used as catalyst. The faster degradation of MO by G2A1 is also reflected in the time evolved UV-Vis spectra of filtrated solutions as presented in **Figure 5.11b**. However, degradation of MO took longer durations for further increment of Ag_2O density on the host catalyst surface (sample G1A1 and G1A2). The photocatalytic reactions follow the Langmuir-Hinshelwood pseudo first order kinetics:

$$\ln \left({C_0}/{C_t} \right) = kt \tag{5.2}$$

Where C_0 denotes the initial concentration of the dye solution and C_t indicates concentrations at different time interval t, t is the irradiation time and 'k' denotes the first order degradation rate constant. The reaction kinetics plots for the samples are shown in **Figure 5.11c** respectively. The 'k' values for Pure G1A0 and G0A1 were found to be 0.0161 min^{-1} and 0.0072 min^{-1} respectively whereas G2A1 has a 'k' value of 0.2436 min^{-1} which is about 8 times greater than G1A0 and 33 times higher than G0A1. The other composite samples G6A1, G4A1, G1A1, G1A2 exhibited the 'k' value of 0.1271, 0.1991, 0.0605, and 0.03588 min^{-1} respectively presented in **Figure 5.11d.** Also the degradation efficiency (η) of the as-synthesized samples can be calculated using the equation,

$$\eta = \frac{C_0 - C_t}{C_0} \times 100 \tag{5.3}$$

Comparative performance of sample G2A1, G1A0, G0A1 and a special sample fabricated by simple physical mixture of Ga_2O_3 and Ag_2O was tested for MO degradation to identify the exact effect of junction fabrication between the two counterparts. Additionally, photolysis or self-degradation of MO under UV irradiation during equivalent time was also carried out. The results are depicted in **Figure 5.11e**. The blank test showed that degradation percentage of methyl

orange was negligible ranging under 3.5% by direct UV photolysis for 60 min in the absence of photocatalyst.
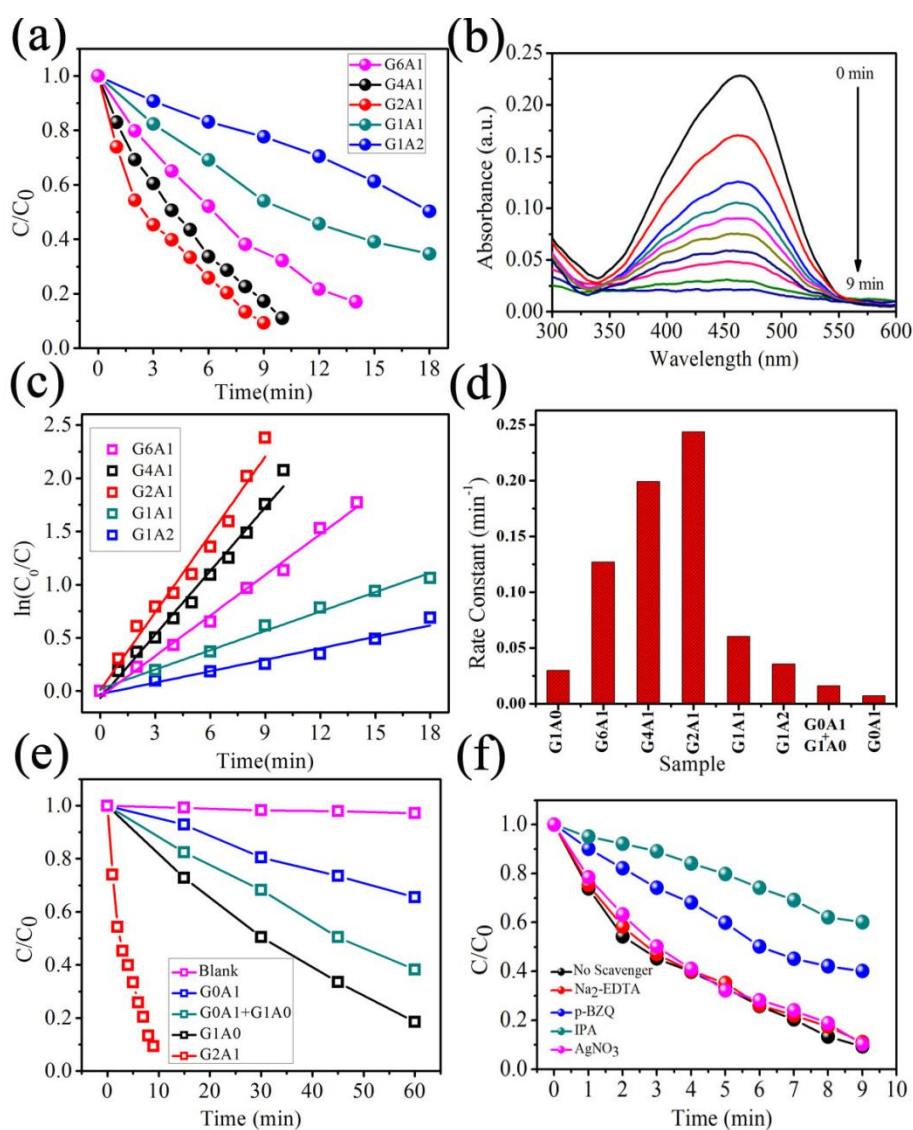

Figure 5.11 Photocatalytic degradation profiles of MO by different photocatalysts (a), time evolved UV-Vis absorbance spectra of methyl orange for photocatalyst G2A1 (b), the kinetic plot of photocatalytic degradation with various time under UV light irradiation (c), the plot of rate constant of different samples (d),Photocatalytic degradation profiles of MO with different pure, composite and physical mixture of pure samples (e),degradation profiles of MO in presence of different scavengers (f)

The physical mixture of Ga_2O_3 and Ag_2O (G1A0 + G0A1) also registered much inferior degradation performance compared to sample G2A1. Even the pure Ga_2O_3 sample appeared to be more efficient catalyst compared to the physically mixed sample. This is quite expected as equivalent loading of catalyst for these tests eventually included less amount of actual catalyst

(i.e. Ga$_2$O$_3$) in case of the physical mixture resulting in comparatively inferior degradation performance than pure gallium oxide. The composite evolved to be the best catalyst among these selective agents as carrier transport between the counterparts (discussed in next section) across the proper junction could occur only in case of the composite sample.

To identify the role of active species in photocatalysis process, scavenger test was carried out. The effect of radical scavengers in active photocatalysis media was investigated using 0.01 mol/L 1,4-benzoquinone, 0.01 mol/L IPA, 0.01 mol/L Na$_2$-EDTA and 0.01 mol/L AgNO$_3$ as scavengers for superoxide radicals ($\bullet O_2^-$), hydroxide radicals ($\bullet OH$), holes (h_{VB}^+) and electrons (e_{CB}^-) respectively. The C/C$_0$ plot presenting the effect of scavenger addition on the reaction rate of G2A1 composite sample is given in **Figure 5.11f.** Also corresponding degradation efficiency of the sample in presence of different scavengers with UV irradiation can be calculated**.** It can be seen that without any scavengers G2A1 can degrade 92% of Methyl Orange in 9 minutes. Whereas in presence of electron capturing agent AgNO$_3$ and hole capturing agent Na$_2$-EDTA it can degrade 89.2% and 87.8% of the dye within the same time. On the other hand degradation percentage decreased to a high extent after addition of 1, 4-benzoquinone (59.8%) and IPA (39.5%).This indicates that the superoxide and hydroxide radicals have major contribution in catalysis process.
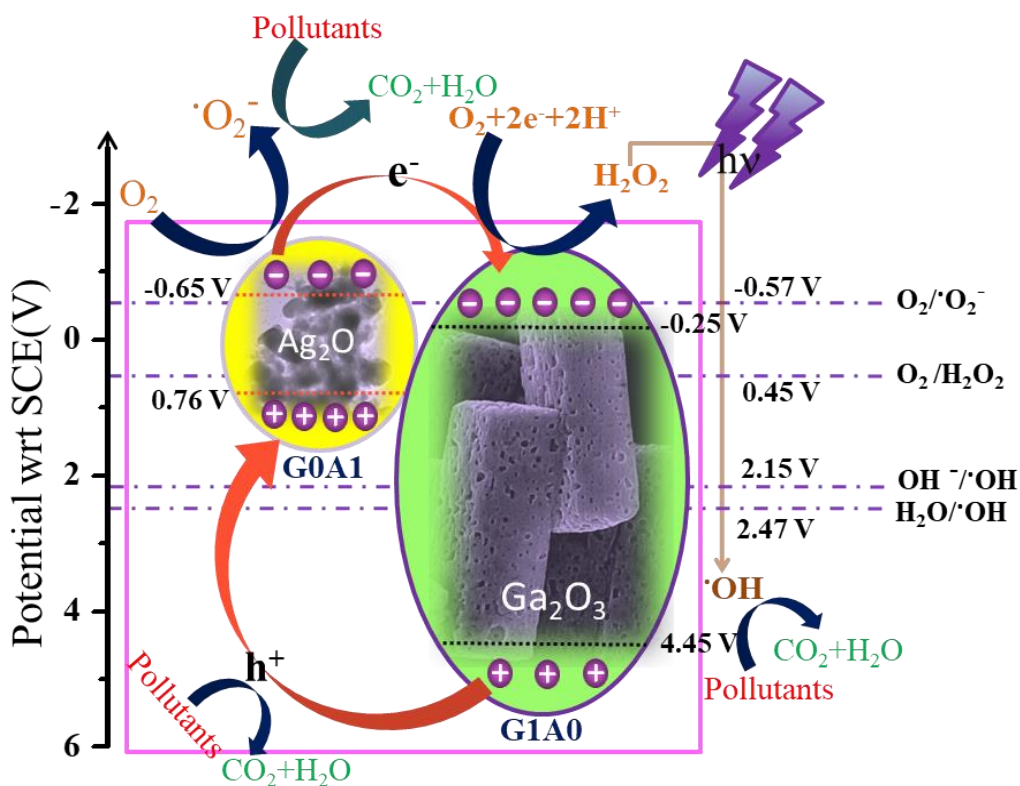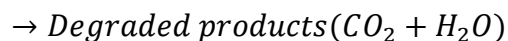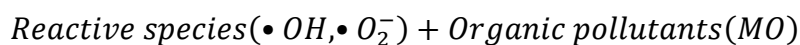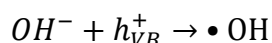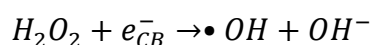
5.4.2. Plausible photocatalytic mechanism

The distinct enhancement of photocatalytic performance for the hybrid samples, compared to the pristine systems can be accounted for the unique feature of nanoheterojunction. To understand the origin of junction fabrication, the band positions of the counterparts were analyzed. The band gaps of the pristine samples were determined fromdiffuse reflectance spectra (DRS) analysis and it was found to be 4.7 eV and 1.41 eV for G1A0 and G0A1 respectively. Also, the n-type nature of G1A0 and p-type nature of G0A1 were predicted from the Mott-Schottky analysis. Formation of heterojunction between the counterparts due to close proximity is hereby possible leading to local band alignment at the interfaces (as depicted in **Scheme. 1**). The valance band edge potential of G1A0 (+4.45 V w.r.t SCE) is more positive than that of G0A1 (+0.76 V w.r.t SCE) whereas the conduction band edge potential of G0A1 (−0.65 w.r.t SCE) is more negative than that of G1A0 (−0.25 V w.r.t to SCE). During the photoctatalytic reaction the hybrid system is

excited by UV irradiation, a huge number of photo induced electron–hole pairs are generatedand transferred from one semiconductor to another depending upon the respective band edge potentials. In ideal independent situation, as in case of G1A0 or G0A1, in absence of separation channel like heterojunction, most of those photogenerated e^-/h^+ pairs instantly recombine and cannot be used for inducing degradation radicals. Thus the samples showed comparatively inferior photodegradation performance. This type of premature recombination is restricted in presence of proper junction within the active catalyst as fabricated in samples G6A1-G1A2. Due to active barrier potential and properly aligned Fermi level, the photogenerated e^-/h^+ pairs are easily separated and their recombination is suspended for a longer duration. These independent electronic charges can easily move towards the semiconductor surface due to low dimension of the counterparts and come into contact with the dye molecules adsorbed there. Thereafter, those charges may react with the media and the dissolved oxygen leading to formation of superoxide and hydroxyl radicals. Alternatively, those charges are also capable to directly interact with the dye molecules leading to their degradation into non-toxic products. It is found that the redox potential for $O_2/\bullet O_2^-$ (-0.57 V) is more negative than the conduction band edge of G1A0 (-0.25 V) which hinders the reduction from O_2 to $\bullet O_2^-$ at the CB edge of G1A0 by contributing a photogenerated electron. Also, it is to be noted that the redox potential of $OH^-/\bullet OH$ ($+2.15$ V) and $H_2O/\bullet OH$ ($+2.47$ V) are at a higher positive potential than the valance band edge of G0A1. Hence the VB of G0A1 cannot promote the oxidation reaction of H_2O/ OH^- to $\bullet OH$ by supplying a photogenerated hole. However, scavenger tests confirm the involvement of these active radical species in Photocatalytic performances. So the formation of type II heterojunction can eliminate such limitations against oxidation and reduction reactions by facilitating inter-component charge transfer.

It is observed that the redox potential of O_2/H_2O_2 ($+0.45$ V) is more positive than the CB edge potential of G1A0. Hence the electron rich CB of G1A0 can trigger the reduction of O_2 to H_2O_2 by supplying photogenerated electrons in its CB and also H^+ ions from the solution. The active radical $\bullet OH$ can be easily formed with the reaction of H_2O_2 and an electron from the system. On the other hand, as the position of VB edge of G1A0 ($+4.45$ V) is more positive than the oxidation potential of H_2O and OH, photogenerated holes are trapped by H_2O/OH leading to formation of $\bullet OH$ radicals. There is also transfer of holes from the VB edge of G1A0 to the VB edge of G0A1 which results in the h^+ rich VB of the same. These holes can directly take part into the dye

degradation performance. The presence of the superoxide radical $\bullet O_2^-$ can be attributed to the occurrence of reduction reaction at the more negative CB edge of G0A1. All of these radicals further participate into actual photocatalytic degradation of the organic MO molecules which can be demonstrated in the following set of reactions,

$$[Ga_2O_3/Ag_2O] + hv \ (photon \ energy) \rightarrow h_{VB}^+ + e_{CB}^-$$

$$O_2 + \ e_{CB}^- \rightarrow \bullet O_2^-$$

$$H_2O + h_{VB}^+ \rightarrow H^+ + \bullet OH$$

$$\bullet O_2^- + 2H^+ + 2e_{CB}^- \rightarrow H_2O_2$$

$$H_2O_2 + e_{CB}^- \rightarrow \bullet OH + OH^-$$

$$OH^- + h_{VB}^+ \rightarrow \bullet OH$$

$$Reactive \ species(\bullet OH, \bullet O_2^-) + Organic \ pollutants(MO)$$

$$\rightarrow Degraded \ products(CO_2 + H_2O)$$
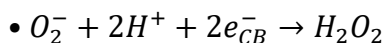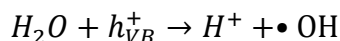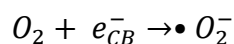
Scheme.1 Probable photocatalytic mechanism of p-Ag₂O/n-Ga₂O₃ nanoheterjunction

The entire degradation process is completed within lesser time due to continuous supply of huge number of photo induced superoxide and hydroxide radicals in case of the junction based samples which is much quicker than independent pure systems. The number of nanoheterojunctions were increased from sample G6A1 to G1A2 by simply varying the molar ratio of the Ag-precursor. As observed from FESEM image, coverage of Ga_2O_3 surface by Ag_2O NPs reaches a maximum for sample G1A2. Too high density of surface attachment actually hinders the incidence of sufficient UV photons to excite the system properly which leads to comparatively inferior catalysis performance.

5.4.3. Recyclability test

The multiuse capabilities of the samples were tested under identical conditions to establish the effectiveness of nanoheterojunctions. The result of the recyclability test up to 5 cycles is presented in **Figure 5.12a**. After completion of each cycle, the catalyst material was centrifuged, collected and dried to be used for the next cycle. It was observed that the degradation efficiency remained more than 75% after 5 cycles. The catalyst was subjected to XRD study (**Figure 5.12b)** after 5 cycles of catalysis process and it was observed that sample G2A1 could retain its phase purity even after prolonged UV irradiation and catalysis performance. This includes even better applicability of the new proposed gallium oxide based heterojunctions as green cleaning agents.
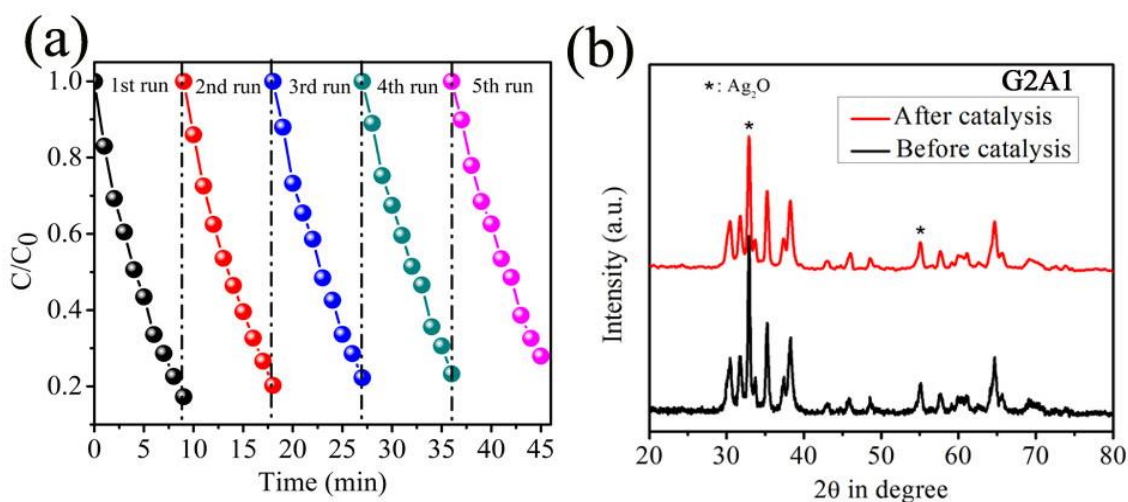

Figure 5.12 (a) Recyclability test for the degradation of MO by the sample G2A1 up to 5th run and (b) XRD of the sample after and before catalysis after 5th run

5.4.4. Effect of pH

In order to mimic actual contaminant removal, the best sample G2A1 was applied as a catalyst in different pH values of active photodegradation media (**Figure 5.13a).** The pH values were varied by adding 1M HCl and 1M NaOH solutions in the active media and other photocatalysis conditions were kept same for all cases. It was found that the catalyst could perform even better in acidic media by degrading MO within 5 min. However, the degradation performance slightly retarded in alkaline medium. To investigate the actual reason behind this, zeta potential study in deionized water solvent was carried out to evaluate the surface electrostatic properties of the catalyst (**Figure 5.13b).** Zeta potential of the sample G2A1 in different pH value *i.e.* at 2, 7 and 12 was found to be +7.0, −9.0 and −30.2 mV respectively. It was observed that positive surface charges increased at lower pH value causing better interaction of the catalyst with anionic dye like MO, whereas more negative surface charges at higher pH caused comparative hindrance in dye attachment causing respective inferior degradation.
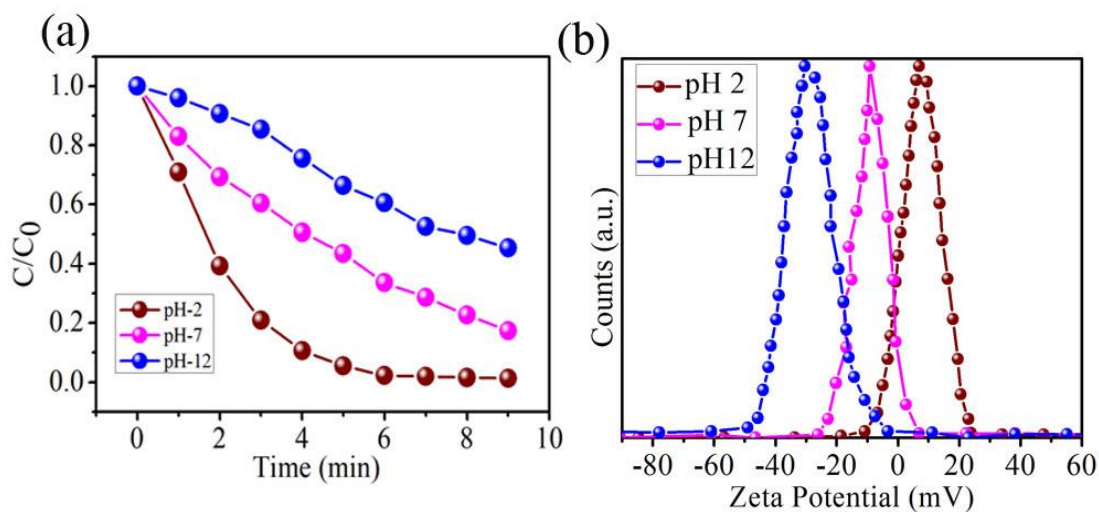
Figure 5.13 Photocatalysis degradation profiles of MO (a) and Zeta potential with catalyst sample G2A1 at different pH

5.4.5. Degradation of different dyes, phenol and dye mixtures

A thorough study on possible realization of the green cleaning performance by sample G2A1 and its pristine counterparts was carried out dealing with some other dyes with different ionic identities, their mixtures and colorless hazardous chemicals. For this purpose, cationic dyes Rhodamine B and anionic dye Aniline blue and Eosin B were used. Additionally, a common chemical reagent -phenol, known for its corrosiveness and toxicity was subjected to degradation

by the samples. Standard photocatalysis experiment was followed for the dyes and time evolved photoluminescence study was performed for phenol which does not exhibit any prominent absorbance position in UV-Vis range. The results are summarized in **Figure 5.14**. It can be seen that all the dyes were degraded within 20 min whereas degradation of phenol was completed within 50 min. The performance of G2A1 sample in degrading phenol was observed to be much more efficient than obtained for pristine samples like G1A0 and G0A1. In view of the degradation rate constant, all the dyes showed appreciably high degradation constant (> 0.2 min^{-1}). Even phenol was degraded moderately fast which is distinctly higher than that of reported for similar catalyst systems[19].
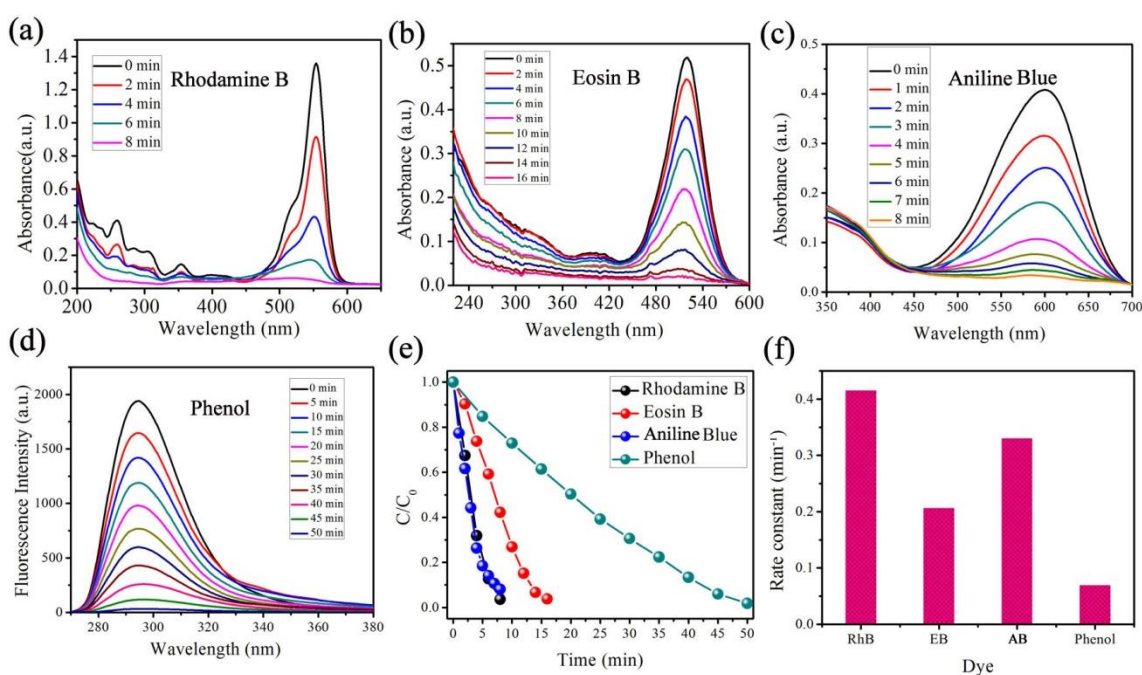
Figure 5.14 Time evolved UV-Vis absorbance spectra of Rhodamine B (a), Eosin B (b), Aniline Blue(c) and time evolved photoluminescence spectra of phenol (d) with photocatalyst G2A1,the kinetic plot of photocatalytic degradation with various time under UV light irradiation (e)and the plot of rate constant of different dyes (f)

Efficiency of degradation exhibited by sample G2A1 was further studied comparatively with that of G1A0 and G0A1 for more realistic dye solution, i.e. mixtures of multiple dyes. For this, standard cationic-anionic and anionic-anionic dye mixtures were prepared by mixing RhB-EB and EB-MO respectively in 1:1 molar ratio. Those mixtures were subjected to photocatalytic experiment using those three samples. The results are presented in **Figure 5.15**. It can be clearly seen that sample G2A1 performed the best in degrading both the mixtures and exhibited a rate constant ~ 0.1 min^{-1}. This study, involving phenol and realistic dye mixture, up to our best

knowledge is unique for any Ag_2O based heterojunction catalyst and hence no comparative analogy regarding the rate constant could be made. However, with remarkable degradation performance exhibited by the optimized Ag_2O-Ga_2O_3 nanoheterojunction catalyst system in removal of dyes of different ionic identity, realistic mixture of multiple dyes, performance stability in different pH, satisfactory multiple usability and removal of hazardous apparently invisible chemical reagent like phenol, all possible issues related to modern water disinfection can be addressed. Hence this work features the Ag_2O-Ga_2O_3 nanoheterojunction catalyst system absolutely prepared for proper commercialization.
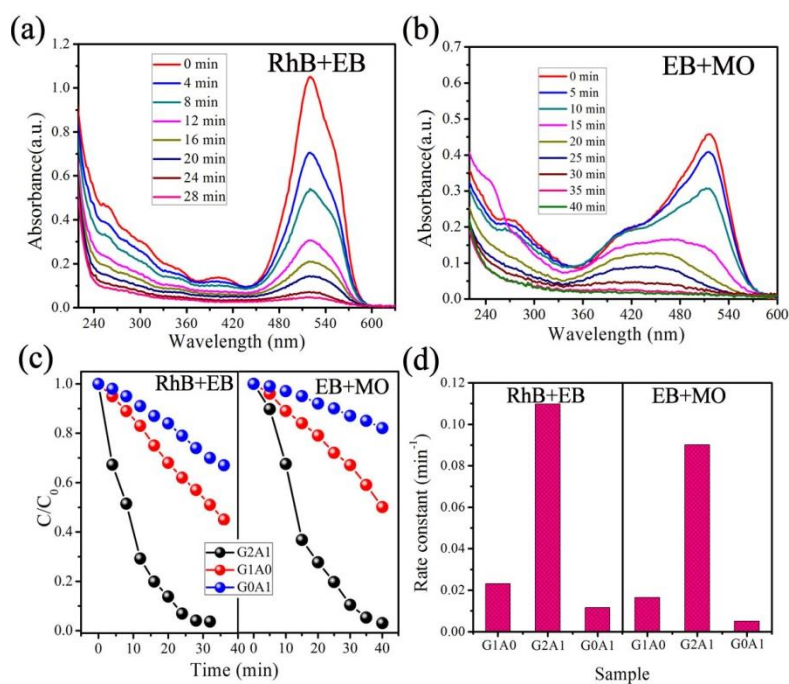
Figure 5.15 Time evolved UV-Vis absorbance spectra different mixed dyes, Rhodamine B with Eosin B (a) and Eosin B with Methyl Orange (b); degradation kinetics of the mixed dyes (c)in presence of different samples G2A1, G1A0 and G0A1 and the plot of their corresponding rate constants (d)

A comparative study of catalytic performances of Ag_2O based nanoheterojunctions is presented in **Table 5.1**. It can be clearly inferred from the table that gallia-Ag_2O nanoheterojunction samples can exhibit comparable or better photocatalytic degradation performance than most of the reported nanoheterojunction systems.

Table. 5.1 Comparative photocatalytic performance of other materials having p-n junction with Ag_2O:

catalyst used and amounts	conc. and volume of dye	light source	Degradation time (min)	degradation%	reference
Ag_2O/TiO_2 **(9 mg)**	10 mg/L 30 ml **(MO)**	300 W high pressure Hg lamp 500 W Xe lamp	60 min 240 min	93.7% for pure TiO_2& 98.2% for Ag_2O/TiO_2 20% by TiO_2& 94.1% (mass ratio of Ag_2O and $TiO_2$was 50%)	[38]
$Ag_2O/graphene$ oxide (50 mg)	50 mg/L **(MB)**	500-W Xenon mercury lamp	60 min	97% (for P25 30% degradation of MB dye in 100 min)	[39]
$Ag_2O/Sodium$ alginate-rGO aerogel beads (30 mg)	5 mg/L **(RhB)** 30 ml 10 mg/l **(OII)**	500 W Xelamp	150 min 60 min	96% 93%	[40]
Ag_2O/TiO_2 **(40 mg)**	10^{-5} M, 40 ml **(MO)**	40 W UV tube	30 min	100% (67% with pure TiO_2)	[37]
Ag_2O/Bi_2MoO_6 **(30 mg)**	5.75 mg/L **(MO)** (50 mL)	300 W Xe lamp	180 min	90% (31% with pure Bi_2MoO_6)	[41]
Ag_2O/CeO_2	50 mL, 10 mg/L **(EFA)**	300 W Xe lamp	120 min	87% (no degradation with CeO_2)	[42]
$Ag_2O/g-C_3N_4$	10^{-5} mol/L **(RhB)**	350 W xenon lamp	60 min	100% (80% with g-C_3N_4, 50% with Ag_2O)	[43]
AgO/TiO_2 nanobelts (20 mg)	20 ml/L, 20 ml **(MO)**	20 W UV lamp	25 min	100% (20% with TiO_2)	[44]
Ag_2O- TiO_2 (20 mg)	10 mg/L (100 mL) **(MO)**	250W lamp (visible)	90 min	88% (~ 40% with TiO_2)	[45]
$Ag_2O/Bi_2O_2CO_3$ heterojunctions (50 mg)	10^{-5} M, 50 ml **(MO)**	300 W Xe lamp	15 min	100% (20% with pure $Bi_2O_2CO_3$%)	[46]
Ag/Ga_2O_3 Composite (90 mg)	20 mg/L (180 ml) **(RhB)**	25 W mercury lamp	120 min	99%	[47]
Ag_2O/ZnO (30 mg)	20 mg/L (100 ml) **(MB)**	UV light with power of 40 W	120 min	88% (70% with pure ZnO)	[48]
Ag_2O/Ga_2O_3 Heterojunction (8 mg)	10^{-5} M, 40 ml **(MO)** **(RhB)** **(Eosin B)** **(AB)**	40 W UV lamp	9 min 8 min 16 min 8 min	92% 98% 99% 96%	This Work

5.5. Conclusion

Ag$_2$O/Ga$_2$O$_3$ nanoheterojunctions were fabricated using facile photochemical reduction technique with varying densities of surface attached Ag$_2$O by simple variation of precursor molar ratios. After thorough characterization with XRD, FESEM, TEM, XPS and EDX for structural, morphological and compositional studies respectively, the samples were tested for photocatalytic performance to degrade hazardous organic dye MO. As predicted from VASP simulations, band alignment and charge transfer between Ag$_2$O and gallia with successive retardation of e$^-$/h$^+$ pair recombination was identified as the key factor behind enhancement of photocatalytic activity of gallia nanostructures. Also the approximate band edge potentials were calculated from Mott-Schottky studies which assisted to provide an insight into the probable transfer route of the photogenerated electrons and holes. It was observed that an optimized density of surface attached Ag$_2$O NPs could boost the photocatalytic performance of gallia in degrading a variety of dyes of different ionic identities, their mixtures and harmful colorless water pollutant like phenol to mimic realistic removal of water pollutants with high degradation rate. Additional studies of reusability test, multiple dye disintegration performance and capability of dye degradation in varying pH media established the optimized Ag$_2$O-gallia type II p-n nanoheterojunction sample as one of the most promising representative of smart water disinfection technology.

5.6. References

1. A. Mills and S. L. Hunte, A Chem. 108(11) (997) 1-35.
2. N. Tripathy, R. Ahmad, H. Kuk, Y. B. Hahn, and G. Khang, Ceram. Int. 42(8) (2016) 9519-9526.
3. Z. Liu, Q. Wang, X. Tan, Y. Wang, R. Jin, and S. Gao, Sep. Purif. Technol. 215 (2019) 565-572.
4. J. C. Wang, H. H. Lou, Z. H. Xu, C. X. Cui, Z. J. Li, K. Jiang, Y. P. Zhang, L. B. Qu, and W. Shi, J. Hazard. Mater. 360(2018) 356-363.
5. Y. S. Sue, K. Y. Pan, and D. H. Wei, Appl. Surf. Sci. 471 (2019) 435-444.
6. A. Hamdi, L. Boussekey, P. Roussel, A. Addad, H. Ezzaouia, R. Boukherroub, and Y. Coffinier, Mater.Des. 109 (2016) 634-643.

7. A. Khataee, S. Arefi-Oskoui, M. Fathinia, A. Fazli, A. S. Hojaghan, Y. Hanifehpour, and S. W. Joo, J. Ind. Eng. Chem. 30(2015) 134-146.

8. A. M. Ilyas, M. A. Gondal, U. Baig, S. Akhtar and Z. H. Yamani, Sol. Energy. 137 (2016) 246-255

9. M. Ebadi, O. Amiri, and M. Sabet, Sep. Purif. Technol. 190 (2018) 117-122.

10. E. P. Da Silva, M. E. Winkler, W. M. Giufrida, L. Cardozo-Filho, C. G. Alonso, J. B. Lopes, A. F. Rubira, and R. Silva, J. Colloid Interface Sci. 535(2019) 245-254.

11. C. Zhou, D. Huang, P. Xu, G. Zeng, J. Huang, T. Shi, C. Lai, C. Zhang, M. Cheng, Y. Lu and A. Duan, Chem. Eng. J. 370 (2019) 1077-1086.

12. S. A. Ansari, M. M. Khan, M.O. Ansari, and M. H. Cho, New J Chem. 40(4) (2016) 3000-3009.

13. S. F. Yang, C. G. Niu, D. W. Huang, H. Zhang, C. Liang, and G. M. Zeng, Environ. Sci.: Nano, 4(3) (2017) 585-595.

14. B. Bethi, S. H. Sonawane, B. A. Bhanvase, and S. P. Gumfekar, Chem. Eng. Process: Process Intensif. 109(2016) 178-189.

15. C. Ray, and T. Pal, J. Mater. Chem. A, 5(20) (2017) 9465-9487.

16. V. Ghodsi, S. Jin, J. C. Byers, Y. Panand P. V. Radovanovic, J. Phys. Chem. C. 121(17) (2017) 9433-9441.

17. E. Chikoidze, H. J. Von Bardeleben, K. Akaiwa, E. Shigematsu, K. Kaneko, S. Fujita, and Y. Dumont, J. Appl. Phys. 120(2) (2016) 025109.

18. Y. Oshima, E. G. Víllora, and K. Shimamura, Appl. Phys. Express, 8(5) (2015) 055501.

19. B. Das, B. Das, N.S. Das, S. Sarkar, and K. K. Chattopadhyay, Micropor.Mesopor.Mater.288 (2019) 109600.

20. C. Han, W. Mao, K. Bao, H. Xie, Z. Jia, and L. Ye, Int. J. Hydrogen Energy, 42(31) (2017) 19913-19919.

21. Y. Wang, N. Li, P. Duan, X. Sun, B. Chu and Q. He, J. Nanomater. 16(1) (2015) 126.

22. W. Zhang, B. S. Naidu, J. Z. Ou, A. P. O'Mullane, A. F. Chrimes, B. J. Carey, Y. Wang, S. Y. Tang, V. Sivan, A. Mitchell, and S. K. Bhargava, ACS Appl. Mater.& inter. 7(3)(2015) 1943-1948.

23. J. Wei, J. Yang, Z. Wen, J. Dai, Y. Li, and B. Yao, RSC Adv. 7(60) (2017) 37508-37521.

24. S. Li, K. Xu, S. Hu, W. Jiang, J. Zhang, J. Liu and L. Zhang, Appl. Surf. Sci. 397(2017) 95-103.

25. S. Fu, Y. He, Q. Wu, Y. Wu, and T. Wu, J. Mater. Res. 31(15) (2016) 2252-2260.

26. G. Kresse and J. Hafner, Phys. Rev. B. 47 (1993) 558.

27. G. Kresse and J. Hafner, Phys. Rev. B. 49 (1994) 14251.

28. P. E. Blöchl, Phys. Rev. B. 50(1994) 17953.

29. J. P. Perdew, K. Burke and M. Ernzerhof, Phys. Rev. Lett. 77 (1996) 3865.

30. A. V. Krukau, O. A. Vydrov, A. F. Izmaylov and G. E. Scuseria, J. Chem. Phys. 125 (2006) 224106.

31. S. Grimme, J. Comput. Chem. 27 (2006) 1787-1799.

32. C. X. Xu, X.W. Sun, and B. J. Chen, Appl. Phys. Lett. 84(9) (2004) 1540-1542.

33. H. T. Ren, and Q. Yang, Appl. Surf. Sci. 396(2017) 530-538.

34. L. Xu, B. Wei, W. Liu, H. Zhang, C. Su and J. Che, Nanoscale Res. Lett. 8 (2013) 536.

35. D. Huang, X. Yan, M. Yan, G. Zeng, C. Zhou, J. Wan, M. Cheng, and W. Xue, ACS Appl. Mater. Interfaces 10 (25) (2018) 21035–21055.

36. C. Zhou, Z. Zeng, G. Zeng, D. Huang, R. Xiao, M. Cheng, C. Zhang, W. Xiong, C. Lai, Y. Yang and W. Wang, J. Hazard. Mater. 380 (2019) 120815.

37. D. Sarkar, C. K. Ghosh, S. Mukherjee and K. K. Chattopadhyay, ACS Appl. Mater. Interfaces. 5(2) (2012) 331-337.

38. H. T. Ren, Q. Yang, Appl. Surf. Sci. 396 (2017) 530-538.

39. J. Ahmad and K. Majid, Adv. Compos. Hybrid. Mater. 1(2) (2018) 374-388.

40. Y. Ma, J. Wang, S.Xu, S. Feng, J. Wang, Appl. Surf. Sci. 430 (2018) 155-164.

41. J. Zhang, H. Liu, and Z. Ma, J. Mol. Catal. A: Chem. 424(2016) 37-44.

42. X. J. Wen, C. G. Niu, L. Zhang, C. Liang, and G. M. Zeng, Appl. Catal. B: Environ. 221(2018) 701-714.

43. S. Liang, D. Zhang, X. Pu, X. Yao, R. Han, J. Yin, and X. Ren, Sep. Purif. Technol. 210 (2019) 786-797.

44. W. Zhou, H. Liu, J. Wang, D. Liu, G. Du, and J. Cui, ACS Appl. Mater. Interfaces. 2(8) (2010) 2385-2392.

45. K. K. Paul, R. Ghosh, and P. K. Giri, Nanotechnol. 27(31) (2016) 315703.

46. N. Liang, M. Wang, L. Jin, S. Huang, W. Chen, M. Xu, Q. He, J. Zai, N. Fang, and X. Qian, ACS Appl. Mater. Interfaces. 6(14) (2014) 11698-11705.

47. M. Li, Z. Yu, Y. Hou, Q. Liu, L. Qian, C. Lian, X. Rao and X. Yang, Chem. Eng. J. 370 (2019) 1119-1127.

48. S. P. Prakoso, V. Paramarta, H. Tju, A. Taufik and R. Saleh, Journal of Physics: Conference Series 776 (2016) 012051.

Chapter 6

Morphology Tuned Ga₂O₃ Nanostructures for Visible Light Assisted Dye Sensitized Photocatalytic Water Remediation

Abstract

Low dimensional Ga_2O_3 was synthesized via a facile chemical route aiming at easy morphological tuning. Different Gallia-precursors as starting materials for hydrothermal synthesis eventually led to spherical nanoparticles and fractured nanobricks as the end product. In addition to the regular characterization of phase, morphology, chemical bond, and surface-related investigations; both the samples were subjected to visible-light-induced photocatalytic degradation of toxic organic pollutants. Despite its wide band gap, the samples showed an efficient dye degradation ability under visible excitation which was explained as originating due to sensitization of the dyes. In the thorough investigation of rhodamine B (RhB) dye-degradation, the nitrate-salt originated nanobricks appeared to be more efficient than the nanospheres fabricated using chloride-salt with degradation rate constants of 0.0394 min^{-1} and 0.0057 min^{-1} respectively. The performances of the samples differed due to their electronic band position. Also, morphological features like higher specific surface area, porosity, and aspect ratio enabled faster degradation of RhB for nanobricks. However, lower surface area, as reflected from BET studies and inherent agglomeration, caused comparatively weaker degradation performance of the nanospheres. This remediation technology can provide a lead for the optimization of similar future catalyst systems to be fabricated using the hydrothermal-synthesis route for the purpose of wastewater treatment.

6.1. Introduction

Hazardous components originating from industrial by-products have been identified as a major threat to human health. Most of these pollutants, often find their way through consumable water causing severe health issues. Popular electronic devices like RO machines are normally applied as a potential solution, however, is not desirable considering the wastage of water by these types of equipment during the purification process. On the other hand, water purification employing specially designed novel materials is a comparatively more acceptable technique. Photocatalytic treatment for wastewater purification of nanostructured materials is of utmost importance in this regard[1-2]. Starting from classic oxide systems involving TiO_2[3] to novel multipurpose chalcogenides[4] and numerous carbon nanostructures[5] - the list of efficient nanocatalysts is not a short one. Each of them has its own merits and drawbacks.

Beyond a doubt, titania and its derivatives are the leading candidates in this group[6-7]. Other oxides like ZnO, CuO can be synthesized easily, but they often lack degradation efficiency in comparison to titania[8-12]. Carbon compounds, on the other hand, can absorb pollutants[13] which may require further separation of the absorbed components. Complete degradation of inherent pollutants in cost-effective routes is therefore necessary. Photoassisted degradation procedures involving most of the advanced catalysts require UV irradiation[14]. Maintaining a constant UV irradiation in wastewater treatment infrastructure may not be cost-effective and space compatible. Moreover, the fabrication of a considerable number of popular nanocatalysts involves sophisticated instrumental setup like PLD[15], VLS[16], microwave[17], etc. Though the requirement of UV irradiation for photocatalysis may be eliminated using novel metal (Ag, Au) incorporation over the catalyst surface[18-19], it may add up newer difficulties in the fabrication route[20]. In search of potential solutions to the above issues, a new class of materials like CeO_2, Ga_2O_3 were proposed[21-23] in recent studies. Especially, Ga_2O_3 and its derivatives have shown important outcomes in this regard[24]. We also have thoroughly studied the catalytic behaviour of gallium oxide nanostructures in our previous works[25-26]. Tuning the porosity of Ga_2O_3 micro/nanostructures in cost-effective routes and their implementation for wastewater treatment is widely studied in related communities[26]. Gallium oxide shows appreciable efficiency in hazardous dye degradation almost up to the level of titania. Additionally, there are plenty of low-cost synthesis techniques like solid-state reaction[27], hydrothermal route[28], etc. for obtaining low dimensional Ga_2O_3 photocatalysts. Different techniques like morphological modification[29], incorporation of impurity[30], and combining

into binary composites[31] have been identified as possible routes of enhancement of the degradation ability of gallium oxide based systems. However, Ga_2O_3 normally exhibits a wide band gap[32] and excitation of this material requires UV wavelength. Narrowing down its band gap to the visible range may not be that straightforward. So, photocatalytic degradation via visible excitation for Ga_2O_3 should be planned in alternative ways. Exciting the catalyst as well as the pollutant via the same visible irradiation may be a remarkable idea in this regard. An entire new field of dye-sensitized photocatalysis has flourished based on this idea. Several oxide and chalcogenide materials have shown faster degradation of hazardous dyes when assisted with dye sensitization[33-37]. However, the fabrication of novel catalyst systems which can operate either by direct excitation in its wide band gap region or participating in dye-sensitized catalysis via easy career transport is necessary for future green cleaning technology. Such a system would be perfectly able to utilize the entire range of available excitation spectra in the catalysis process.

In this view, this work demonstrates an easy fabrication technique to synthesize different morphologies of Ga_2O_3 with a minor variation of synthesis parameters. The obtained samples were characterized thoroughly for phase purity, morphology, bonding information, and effective surface area with appropriate techniques. In view of the importance of surface charge type in attracting dye molecules, the zeta potential values of the samples were also determined. Finally, the photodegradation capabilities of the samples were investigated using the standard method degrading rhodamine B. It was observed that the samples which exhibit brick-like structures could degrade hazardous dyes more efficiently compared to the gallia samples having spherical features. The dye degradation mechanism was also found to be governed by dye sensitization via visible irradiation. Moreover, the electronic band position of the samples, determined from the Mott-Shottky study, was found to be compatible with that of the dye molecules. This was also identified to be encouraging the photo-assisted charge transfer across them. The scavenger test, catalyst dose variation, and the reproducibility of degradation behaviour were also tested properly for the best performing sample. This work, therefore, opens up newer possibilities to use morphology tuned Ga_2O_3 system for visible photocatalysis technology.

6.2. Experimental

Gallium trichloride (GaCl$_3$, purity >99.99%), Gallium (III) nitrate hydrate (Ga(NO$_3$)$_3$.xH$_2$O), absolute ethanol, Sodium hydroxide (NaOH), p-Benzoquinone, Isopropanol (IPA), Na$_2$-EDTA, Rhodamine B were supplied by Sigma Aldrich. Silver nitrate (AgNO$_3$) was purchased

from Merck. The commercially available reagents were purchased and used without further purification. Deionized (DI) water was used to prepare the required aqueous solutions.

6.2.1. Synthesis of Ga$_2$O$_3$ powders

All precursors were acquired commercially and used without further purification. In a typical synthesis procedure, 80 ml 0.1 M GaCl$_3$ (purity >99.99%) was prepared in DI water and the same was subjected to the addition of an appropriate amount of aqueous NaOH to maintain the pH value of the reaction media at 10. The mixed solution was further subjected to hydrothermal treatment at 120 ℃ for 18 hours within a Teflon-lined autoclave. The hydrothermal setup was allowed to cool down naturally and the precipitate was collected. The same was washed repeatedly with ethanol and DI to obtain the GaOOH form of the sample. The hydroxide phase was allowed to be heated overnight heating at 80 ℃, and then it was calcined at 800 ℃ for 5 hours to produce gallium oxide named as GOS. The sample GOB was prepared following the above-mentioned procedure only the precursor GaCl$_3$ was replaced by Ga(NO$_3$)$_3$.xH$_2$O.

6.2.2. Characterization

The as-prepared sample was characterized using an X-Ray diffractometer (XRD, Bruker D8 Advanced) to ensure proper phase formation. Further, the bonding information of the sample was investigated using Fourier transform infrared spectrophotometer (Shimadzu FTIR-8400S) in transmittance mode. The average dimensions and shape of the nanostructures were investigated using field emission scanning electron microscopy (FESEM, Hitachi S-4800). Specific surface area and porosity of the as-prepared samples were analysed using a BET surface analyser (NOVA Quanta Chrome 1000e).The optical band gap of the samples was calculated using reflectance studies via UV–Vis spectrophotometer (SHIMADZU-UV-3101-PC). Despite the reported band gap of the sample in the UV range, the photocatalytic activity was investigated under visible irradiation keeping in mind the ease of application, possible dye sensitization, and occasional agglomeration of the sample. Also, the zeta potential of the samples was measured using Zetasizer Nano ZS (Malvern Instruments, UK).

6.2.3. Photocatalytic studies

In a typical photocatalytic experiment, a test solution of rhodamine B with 10^{-5} M strength was prepared. 0.03 g of the synthesized powder sample was added to the 40 ml of the prepared solution. Prior to the application of exciting irradiation, the suspension was subjected to dark stirring for 1 hour to ensure the adsorption-desorption equilibrium between the catalyst and dye molecules. Furthermore, the catalyst-dye solutions were placed under

visible light irradiation using a 400 W high-pressure mercury lamp (Philips-HPL-N G/74/2, MBF-400 W, 200-250V) covering the wavelength range 365 nm to 679 nm. A UV cut-off filter was employed to the source. The irradiation source to sample suspension surface separation was maintained at 15 cm. Following the traditional method, 3 ml of the suspension were collected after certain time intervals and centrifuged (5000 rpm for 2 min) to separate the photocatalyst. The time evolved absorption spectra (peak at 554 nm) of the filtrate were recorded with the solutions collected at different time intervals.

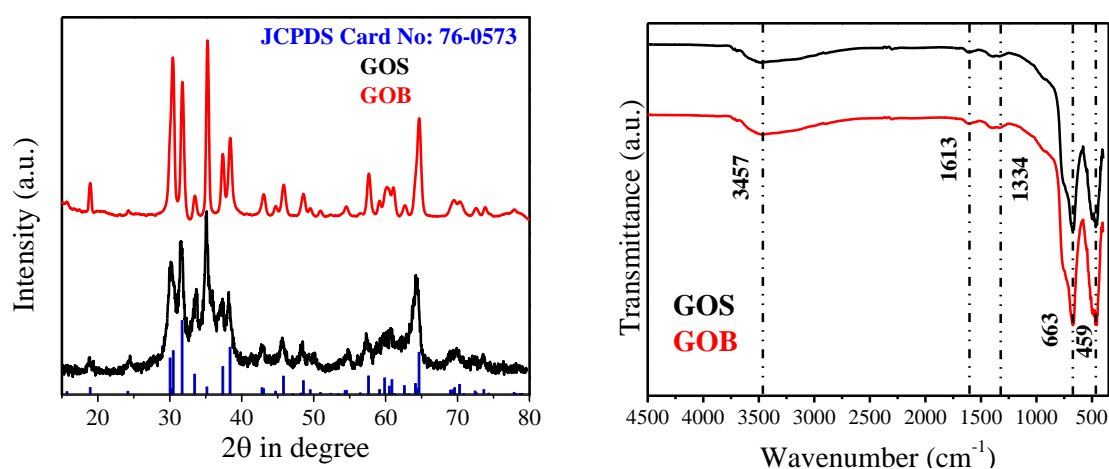## 6.3. Results and discussion

6.3.1. Structural studies

Figure 6.1 (a) XRD patterns and (b) FTIR spectra of the samples

The XRD patterns of the samples are depicted in **Figure 6.1a**. The presence of diffraction peaks in different 2θ values was correlated with the standard JCPDF card [76-0573] and thus proper phase formation was inferred. A distinct difference in the sharpness of the diffraction peaks could be observed between GOS and GOB. The broadening of the diffraction peaks was correlated with its probable smaller range of ordering. The crystallites sizes were determined from the XRD pattern using well known Scherrer equation mentioned below.

$$d = \frac{0.9\,\lambda}{\beta\cos\theta} \tag{6.1}$$

Where, d represents the crystallite size, λ is the wavelength of the X-ray, 0.9 is the shape factor, β is the broadening of the diffraction peaks and θ is the diffraction angle. The grain sizes were found to be 13.5 nm and 19.5 nm for the samples GOS and GOB respectively.

The functional groups that exist within the sample in the range 400 to 4000 cm^{-1} can be easily identified by the FTIR spectrum represented in **Figure 6.1b**. The peak is around 3457 cm^{-1} and can be assigned to the stretching vibration of the H-O-H groups[38]. Also, the week band

near 1613 cm^{-1} and 1334 cm^{-1} represent the bending vibration of adsorbed molecular water and stretching vibrations of O-H bonds[28]. The two sharp peaks near 649 cm^{-1} and 470 cm^{-1} were also observed for both the samples, indicating the presence of Ga-O bending vibration and Ga-O stretching vibration respectively[28].
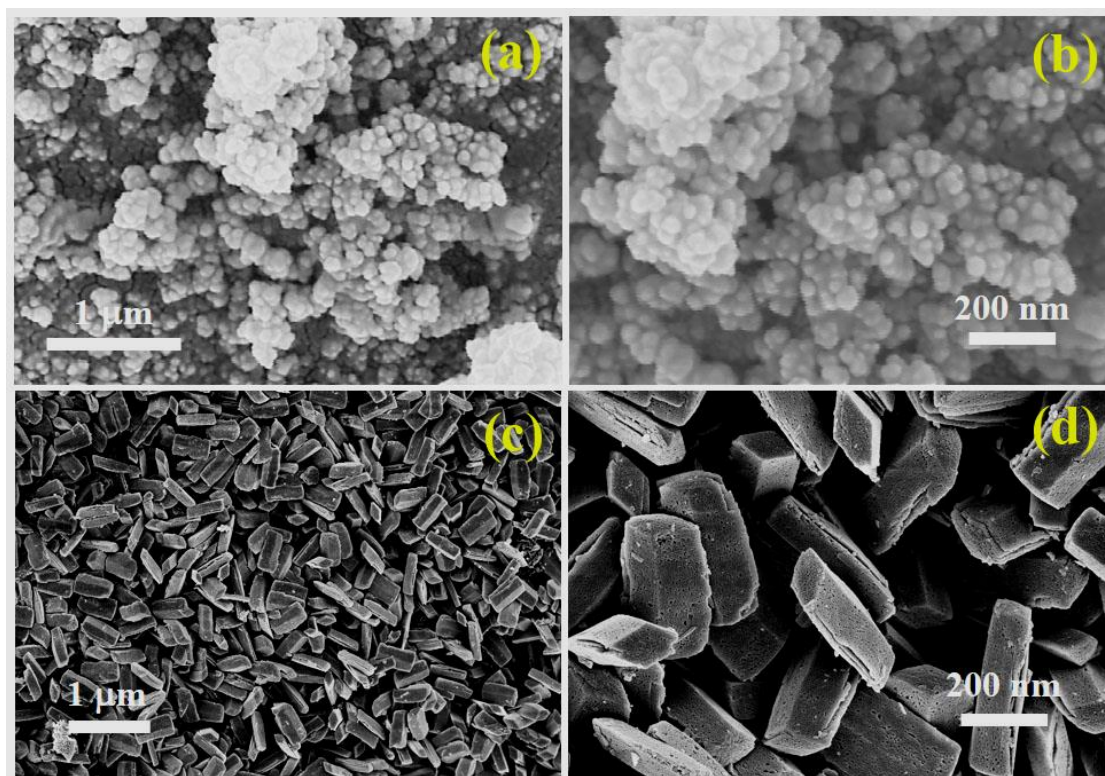
6.3.2. Morphological analysis

Figure 6.2 Low and high magnification FESEM images of the samples GOS (a, b) and GOB (c, d)

The morphology of the samples was characterized using FESEM and the obtained micrographs are presented in **Figure 6.2**. It can be seen that sample GOS consists of agglomerated Ga_2O_3 particles of average dimension ~30 nm. However, a considerable distribution of dimension was also observed for these nearly spherical Ga_2O_3 particles.

On the other hand, GOB samples were found to be ~ 500 nm long and 50×50 nm^2 cross-sections, though the distribution of dimension was observed in this case also. In addition to its definite brick-like structure, the samples were found to be comprised of a huge number of tiny pores. Also, the shapes of that sample were found to be uniform. The creation of the pores within the GOB samples can be associated with the gradual removal of water molecules from their hydroxide phase, which is demonstrated in many of our other works[24-26].

6.3.3. BET surface area studies

Observing the presence of numerous pores in the sample GOB, BET surface area investigation was carried out for the sample and the respective results are presented in **Figure 6.3**. The presence of type IV (according to IUPAC classification) N_2 adsorption-desorption isotherm (**Figure 6.3a)** with H3 type hysteresis loop within the relative pressure range 0.5 to 1 confirms the existence of mesoporous structure in the case of the GOB sample. The respective BJH pore size distribution is shown in **Figure 6.3b** which indicates a narrow pore distribution ranging from 5 nm to 15 nm. Whereas, GOS sample exhibits type V isotherm, which represents the weak gas-solid interaction characteristics (the N_2 adsorption is very small at low relative pressure, but after nominal adsorption, the force between gas molecules initiates further adsorption). The specific surface areas were found to be 6 m^2/g and 35 m^2/g respectively for GOS and GOB samples. The presence of numerous pores in GOB is the prime factor causing such a high surface area of the same. Again, high surface area, in turn, triggers higher contact with pollutant dye molecules which may lead to a higher probability of degradation of the dye.
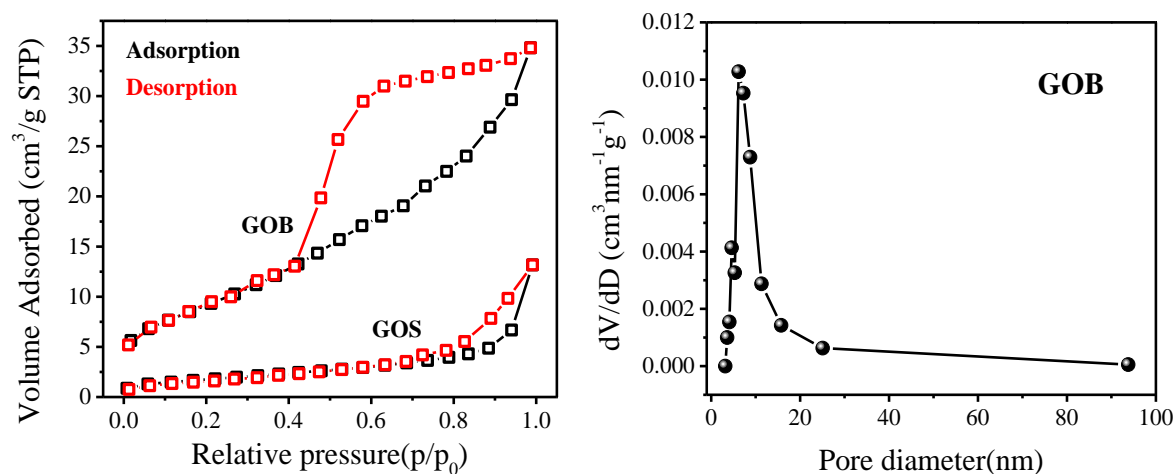

Figure 6.3 (a) N₂ adsorption-desorption isotherm of the samples, (b) porosity distribution profile of GOB sample

6.3.4. Optical property study

Appropriate excitation wavelength in a photocatalytic experiment is a crucial factor for the successful degradation performance of any catalyst. The samples GOS and GOB were also tested for their optical band gap via diffuse reflectance spectroscopy study and the outcome is presented in **Figure 6.4**. The optical band gaps were determined using the Tauc relation,

$$\alpha h\nu = A(h\nu - E_g)^n \tag{6.2}$$

Where, E_g is the optical band gap, h represents the Planck's constant and ν is the frequency of incident photons, A is a constant called the band tailing parameter, and n is the index, which can have different values (2, 3, 1/2 and 1/3) corresponding to indirect allowed, indirect forbidden, direct allowed and direct forbidden transitions, respectively[39]. The band gaps of GOS and GOB were found to be 4.48 eV and 4.13 eV respectively. These results are in full agreement with the earlier reports[24-26] involving wide band gap Ga_2O_3. Though wide band gap photocatalysts are normally excited via UV irradiation, here in this work, we attempted an investigation of the dye degradation capability of gallium oxide under visible irradiation. This optical study was employed to ensure that no defect-induced secondary band gap exists in the samples and the degradation phenomenon is primarily influenced by dye sensitization.
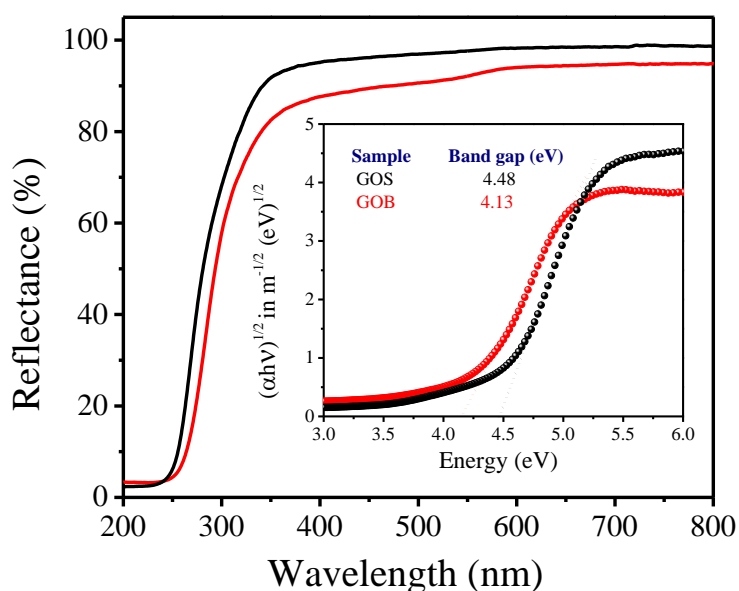

Figure 6.4 Diffuse reflectance spectra of the samples, inset show the corresponding Tauc plot.

6.3.5. Mott-Schottky study

In order to achieve proper information about the possible positions of energy bands for the catalyst samples, Mott-Shottky studies were carried out by performing electrochemical impedance measurements under dark condition. The flat band potential (V_{fb}) was determined using the Mott-Schottky equation,

$$\frac{1}{C^2} = \left(\frac{2}{\varepsilon_0 \varepsilon_r N_d e}\right) \times \left(V - V_{fb} - \frac{k_B T}{e}\right) \qquad (6.3)$$

Where, C represents the depletion layer capacitance, k_B= Boltzmann constant, T= temperature, e= electronic charge, ε_0 = vacuum permittivity (= $8.85 \times 10^{-12} N^{-1} C^2 m^{-2}$), ε_r =

dielectric constant of semiconductor, N_d = carrier donor density. The obtained results are depicted in **Figure 6.5**. Here, the electrochemical measurements of both the samples were carried out at three different frequencies of 1500 Hz, 2000 Hz, and 2500 Hz. It can be observed that the corresponding plots show positive slopes indicating the n-type nature of the samples. Hence the flat band potential can be correlated to conduction band positions. The values of conduction band potential, measured from the intercepts of the $1/C^2$ *vs.* V plots in the V-axis, were found to be -0.20 V and -0.47 V for GOS and GOB respectively using Ag/AgCl as a reference electrode. Those values were further converted with respect to a normal hydrogen electrode (NHE) and thus the positions of the conduction bands were calculated to be -0.001 V and -0.27 V respectively for the samples GOS and GOB. Further, the positions of the valance bands were obtained using the calculated values of band gaps (from the DRS study) of the respective samples.
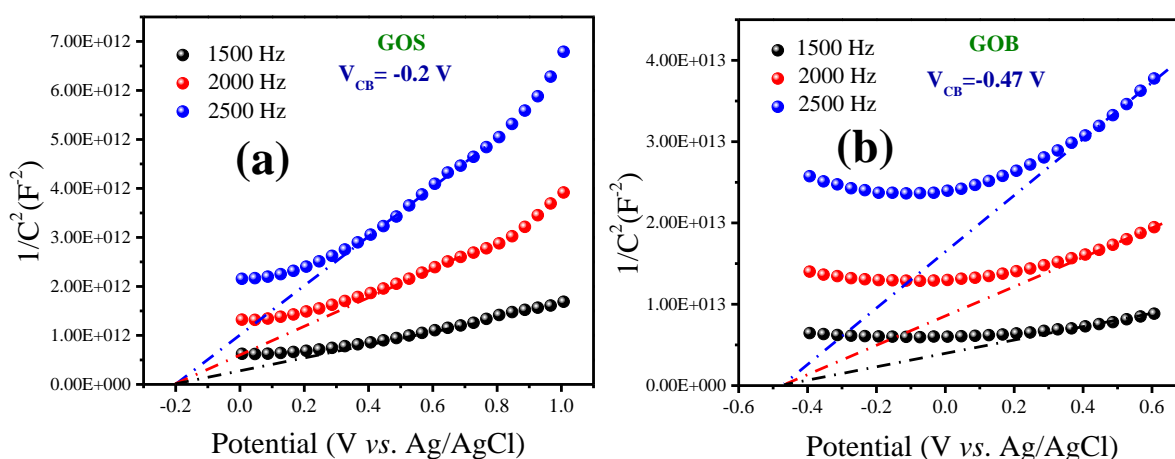

Figure 6.5 Mott-Schottky plots for the samples (a) GOS and (b) GOB at three different frequencies of 1500 Hz, 2000 Hz and 2500 Hz

6.4. Adsorption study

To achieve the adsorption-desorption equilibrium between the catalysts to dye molecule, 1 hour dark stirring was performed before the illumination. The initial removal of the dye via adsorption process was estimated by performing co-dispersion of the samples with the dye under dark condition. The obtained data depicted in **Figure 6.6a** shows that within 1 hour GOS and GOB samples can adsorb ~ 5% and 45% of initial RhB concentration respectively and equilibrium occurs. Comparatively higher adsorption by GOB sample was correlated with two important factors – higher porosity and surface electrostatic property.

Evidently, GOB samples exhibit much higher porosity as well as specific surface area compared to the GOS samples as observed from FESEM micrographs and BET studies and thus attach a higher amount of RhB molecules.

To analyse the effect of surface charge state in adsorption performance, zeta potentials of the samples, in a de-ionized water solvent, were determined from DLS studies. **Figure 6.6b** represents the zeta potential values for the samples GOS and GOB were -3.7 mV and -15.3 mV respectively. It was observed that GOB exhibit more negative zeta potential compared to GOS, this enables a higher probability of cationic dye adsorption by GOB than GOS.
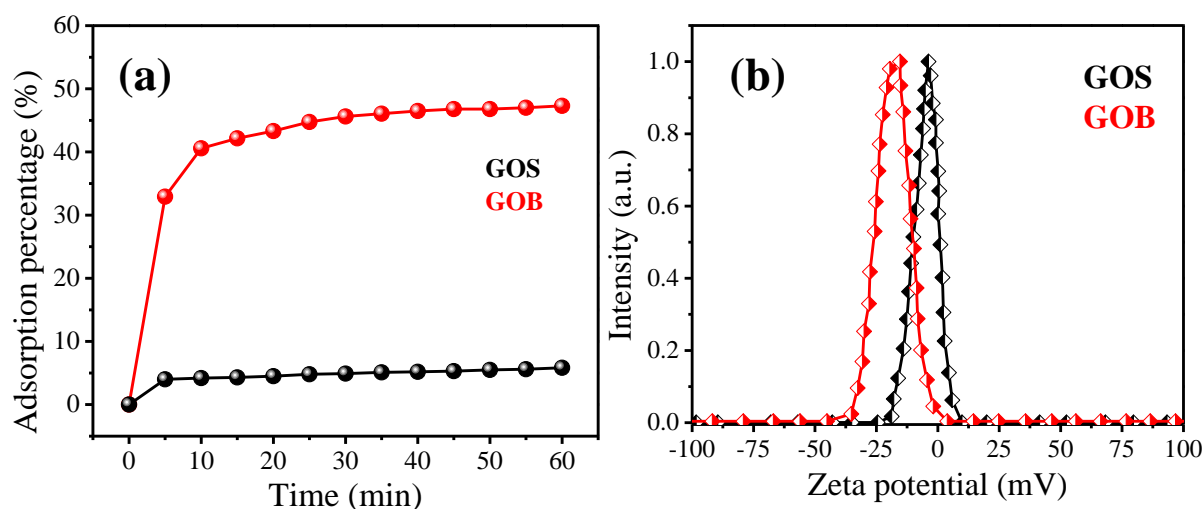

Figure 6.6 (a) Time evolved adsorption percentage of dye RhB in presence of the samples GOS and GOB (b) Zeta potential of the samples

6.5. Photocatalytic activity of Ga$_2$O$_3$ samples

The photocatalytic performance of the samples, both spheres and bricks were analyzed in detail and the results are summarized in figure 6.7. **Figure 6.7(a, b)** represent the time evolved UV-Vis absorbance spectra of RhB in the presence of the catalyst Sample GOS and GOB respectively. It can be clearly observed that the sample GOS took 180 minutes to degrade 69% of the initial concentration of RhB whereas distinctly faster degradation of RhB was registered by the GOB samples and it was almost 98% within only 80 minutes of irradiation. In agreement with the results depicted in figure 6.7a and 6.7b, the dye removal efficiency of GOB was found to be much higher and the same is reflected in figure 6.7c. The degradation rate constants were determined from ln (C_0/C) *vs.* time graph (figure 6.7d) which follows Langmuir-Hinshelwood pseudo 1st order kinetics and can be fitted with a straight line

following the equation (6.4). It was observed that GOB could degrade RhB much faster than GOS with a degradation rate constant of 0.03942 min^{-1}.
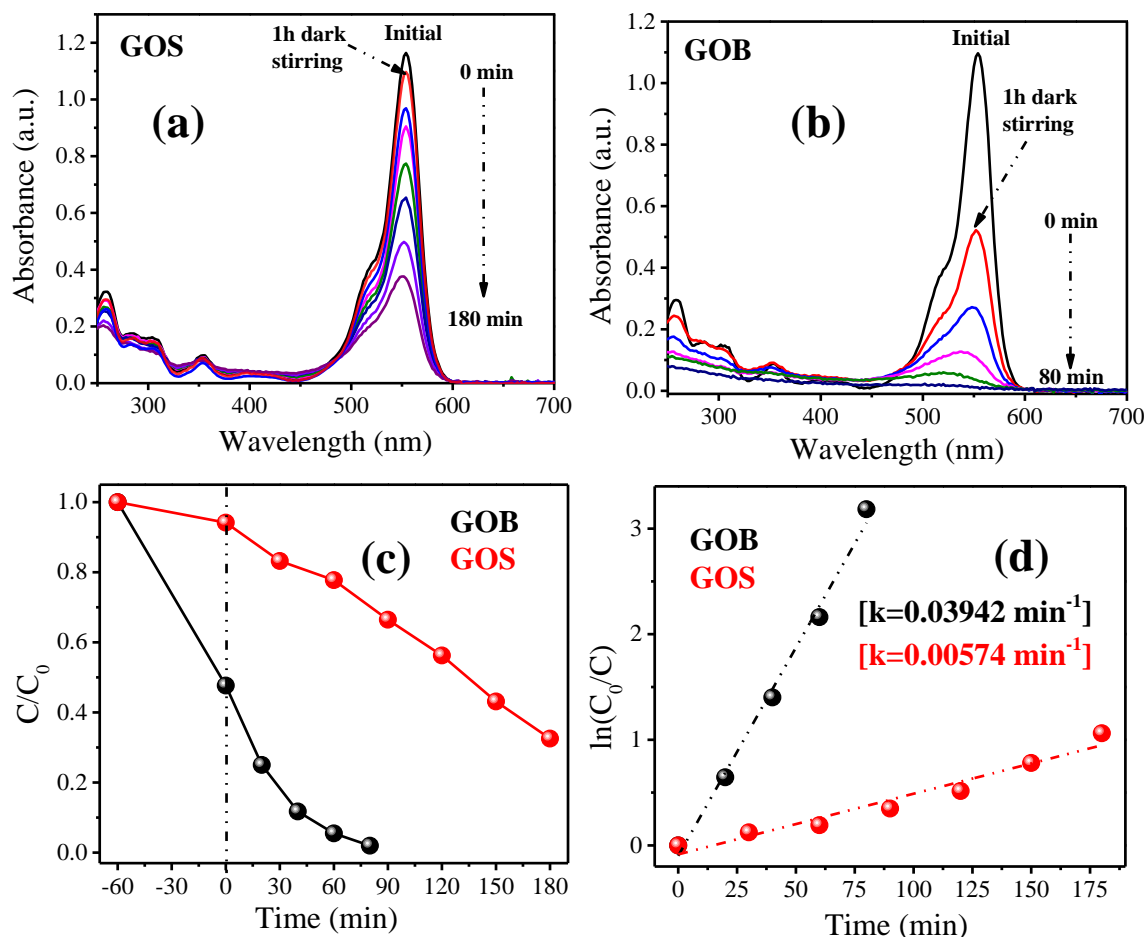
$$ln\left(\frac{C_0}{c}\right) = kt \qquad (6.4)$$

Figure 6.7 Time evolved UV-Vis absorbance spectra of the RhB dye in presence of catalyst GOS (a) and GOB (b), C/C$_0$ vs. time plot (c), ln (C$_0$/C) vs. time plot (d)

To predict the actual radicals active in photocatalytic degradation, a scavenger test was carried out following the standard method. p-Benzoquinone, AgNO$_3$, IPA, and Na$_2$-EDTA have commonly used scavengers for superoxide radicals, electron, hydroxide radicals, and holes respectively. Those reagents were used here to detect the contributions of the active radicals. The results are summarized in **Figure 6.8(a-b)**. It can be clearly seen that degradation efficiency evidently diminished in the presence of p-BQ and AgNO$_3$. This indicates the key contribution of superoxide radicals and electrons in the degradation process. Variation of catalysis performance with varying catalyst amounts was studied under the same conditions and the obtained results are presented in figure 6.8c. It can be clearly observed that

the overall catalytic performance of the GOB sample did not vary much with alteration of catalyst amount. However, minor enhancement in adsorption performance was observed from the study, which can be accounted for an enhanced number of adsorption sites with increment in catalyst amount.
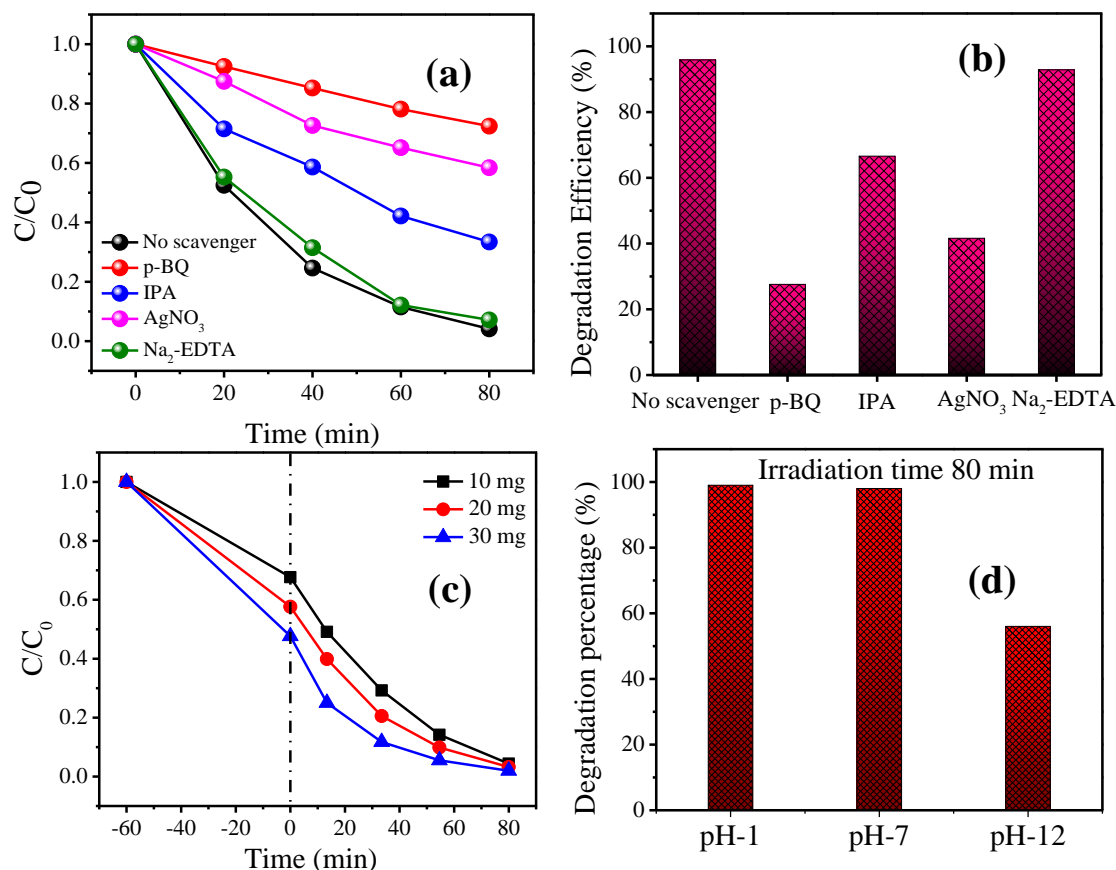

Figure 6.8 (a) C/C_0 vs. time plot, (b) degradation efficiency plot of the dye solution with catalyst GOB in presence of different scavengers, (c) C/C_0 vs. time plot with different catalyst (GOB) dosage, (d) degradation performance in different pH

In order to simulate evident pollutant removal, the catalyst GOB was employed in different pH values of active photodegradation media (**Figure 6. 8d**). The pH values were varied by adding 1M HCl and 1M NaOH in the active media and other photocatalysis conditions were kept same for all cases. It was found that the degradation performance of the catalyst was not differed much in acidic media (~98.5%), whereas it was slightly retarded in alkaline medium (~58.6%) with 80 min visible light irradiation.

A major parameter for the identification of good catalytic material is its reusability under similar conditions. The GOB sample, which showed the most efficient catalytic activity, was subjected to multiuse investigation. The results, as depicted in figure 6.9 clearly indicate that GOB samples could degrade RhB almost with similar efficiency even after 3 consecutive

cycles. To ensure that the sample could retain its phase purity, XRD studies were carried out for the sample after the catalytic performance. It can be observed that no major alteration occurred in the diffraction pattern which indicates the strong multiuse ability of the sample.
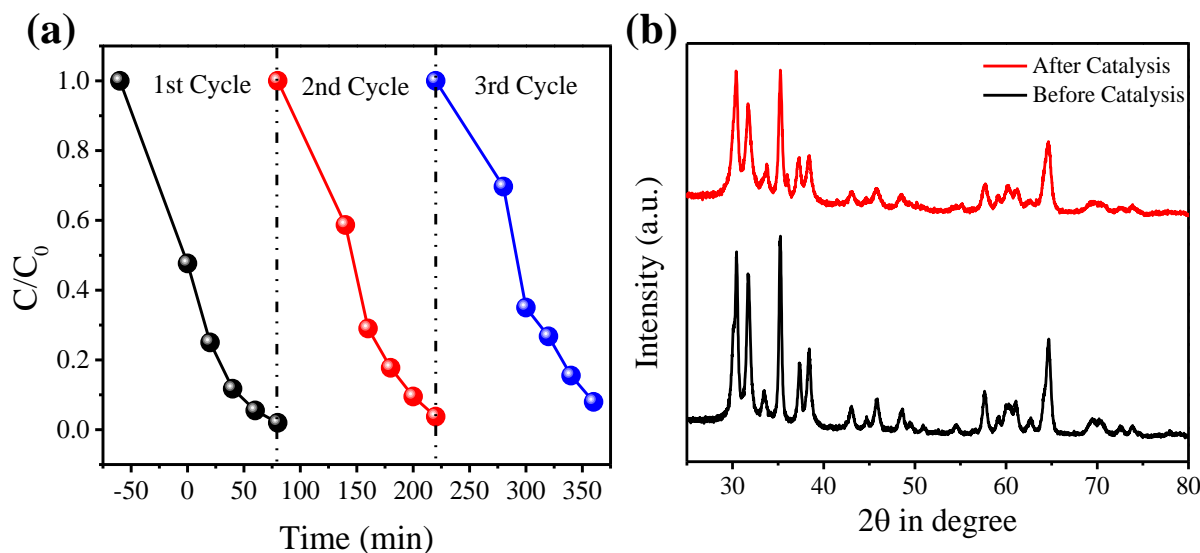

Figure 6.9 (a) Reusability test for the degradation of RhB in presence of the catalyst GOB (b) XRD pattern of the sample after and before catalysis

6.6. Photocatalysis mechanism

First of all, degradation of RhB under visible light is normally expected from low band gap materials. On the contrary, Ga_2O_3 generally exhibit a wide band gap in the UV range. Aiming to use visible light for hazardous dye degradation employing wide band gap material like gallium oxide, the facility of dye sensitization was redeemed. Attachment of dye molecules on the catalyst surface was also ensured employing the zeta potential measurement to analyse the surface electrostatic features of the material. The dye RhB is a well-known cationic dye. On the other hand, the zeta potential studies for both the samples showed negative surface charges (**Figure 6. 6b**) when deionized water was used as a solvent. This opposite charge type was identified as an important factor favouring dye adsorption on the gallia catalyst surfaces. In the detailed mechanism of degradation, the dye along with the sample is excited by the incident visible irradiation. Considering the probable transfer of photogenerated carriers across the dye-catalyst systems, the electronic energy levels of the participating components were determined. Mott-Schottky analysis confirms the conduction band edge potentials for the samples GOS and GOB were -0.001 V and -0.27 V (*vs.* NHE) respectively[41]. Also, the valance band edge potential of the samples can be easily determined simply by adding the band gap values with their corresponding CB potentials. Whereas, the
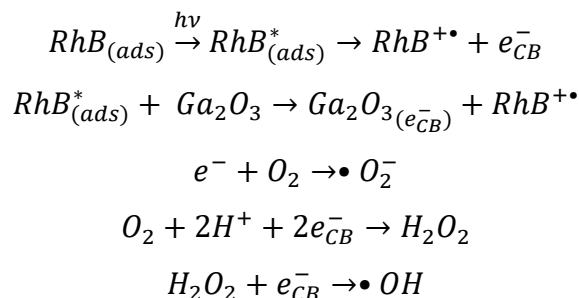
178

HOMO and LUMO positions of the rhodamine B dye are found to be $+1.14$ V and -1.10 V respectively[40] with respect to NHE and considered accordingly. The obtained values were plotted comparatively and are presented in **scheme 6.1** on the basis of which, the photocatalytic mechanism was further analysed.
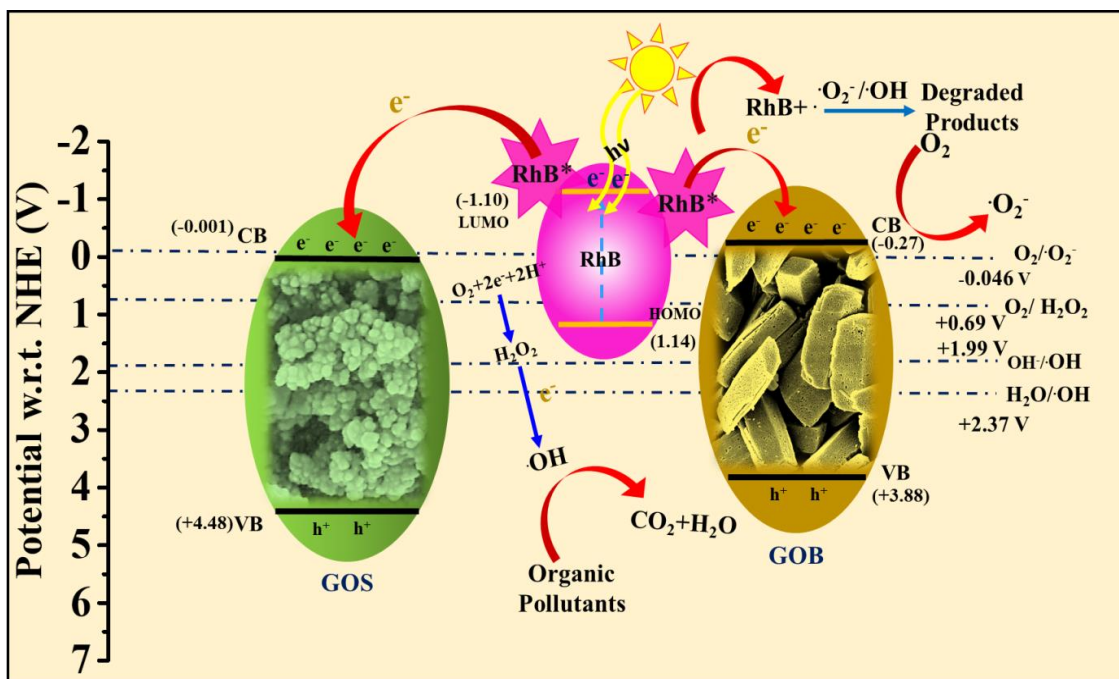

Scheme. 6.1 Schematic representation of dye degradation mechanism

Being excited by the visible illumination, the RhB releases electron which further participates in the degradation process. The electrons supplied by photoexcited RhB molecules are eventually transferred to the conduction band of the samples. The CB potential of GOB is energetically in close proximity to the RhB LUMO level. Also, the CB potential of GOB is lower compared to the reduction potential of $O_2/\bullet O_2^-$ and O_2/H_2O_2. Hence the surface absorbed oxygen molecules of the sample GOB may trap these additional CB electrons and are converted into $\bullet O_2^-$ radicals along with H_2O_2 followed by $\bullet OH$ radicals. On the other hand, the CB position of GOS is beneficial only for the reduction of O_2/H_2O_2 which also confirms the better degradation performance of the sample GOB. Also in the presence of the superoxide and hydroxide radicals, the active RhB^+ radicals may take part in its self-degradation. $\bullet O_2^-$ plays a major role in catalytic degradation of RhB here. In addition to conversion of surface absorbed oxygen into $\bullet O_2^-$ radicals, photogenerated electrons can also

directly take part in the degradation and also create hydroxide radicals via these following steps.

$$RhB_{(ads)} \xrightarrow{h\nu} RhB^{*}_{(ads)} \rightarrow RhB^{+\bullet} + e^{-}_{CB}$$

$$RhB^{*}_{(ads)} + Ga_2O_3 \rightarrow Ga_2O_{3(e^{-}_{CB})} + RhB^{+\bullet}$$

$$e^{-} + O_2 \rightarrow \bullet O^{-}_2$$

$$O_2 + 2H^{+} + 2e^{-}_{CB} \rightarrow H_2O_2$$

$$H_2O_2 + e^{-}_{CB} \rightarrow \bullet OH$$

These available radicals actively disintegrate RhB molecules, resulting in the formation of CO_2 and H_2O as final products.

$$RhB_{(ads)} + \bullet OH \rightarrow CO_2 + H_2O$$

$$\bullet OH / \bullet O^{-}_2 + RhB^{+\bullet} \rightarrow CO_2 + H_2O$$
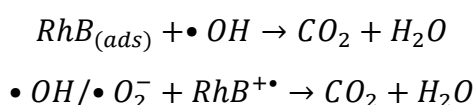
In addition to the good photocatalytic performance by the samples GOB and GOS, a notable difference in their degradation efficiency was also observed. In almost every aspect, GOB samples exhibited better performance than the GOS. Normally, dimensional shrinkage is associated with the better catalytic activity of any system. Though the GOS samples exhibit smaller dimensions than the GOB samples, they showed comparatively inferior catalytic performance. This fact can be taken into account for the morphology of the catalytic sample synthesized here.This fact may be accounted for the morphology of the catalysts sample synthesized here. Though the GOS samples apparently exhibit lower dimensions, GOB samples are facilitated higher specific surface area with numerous poreswhich are actually responsible for better degradation performance. Moreover, minor agglomeration of the spherical structures can also be observed in the GOS sample, which may be responsible for less amount of open sample surface leading to inferior degradation performance. The apparently larger brick-like sample consists of a large number of pores which effectively enhances better contact of dye molecules to gallium oxide compared to the GOS samples. Additionally, GOB was found to exhibit more negative zeta potential compared to GOS. This is an important factor in favour of higher dye adsorption by GOB than GOS. As a consequence of this enhanced contact with dye molecules, degradation of the same became favourable in the case of GOB.

6.7. Conclusion

Different low dimensional structures of Ga_2O_3 were synthesized via a chemical route. Proper phase formation and chemical bond information of the samples were confirmed by X-ray

diffraction studies and FTIR analysis. The formation of spherical and brick-like shapes of the sample was observed in morphological studies, whereas BET surface area investigation revealed a higher effective surface area and porosity for the brick-like samples. This enhanced surface area of the comparatively larger sample was correlated with the numerous pores present in the brick-like sample. Investigation of photocatalytic degradation of rhodamine B via the samples was performed under visible light irradiation where both the samples showed considerable degradation of the dye with a degradation rate constant of 0.0394 min^{-1} and 0.0057 min^{-1}. Being a wide band gap material, the degradation capability of gallium oxide under visible exposure has been taken into account by the dye sensitization mechanism. Better performance of brick-like structure was correlated with larger surface area, porous structure, and the suitable band position of the sample. This particular sample also showed remarkable reusability inferring possible application of the same as a future leading cleaning agent.

6.8. References

1. C. S. Uyguner-Demirel, N. C. Birben and M. Bekbolet, Catal. Today. 284 (2017)202-214.

2. R. Zhang, Y. Liu, M. He, Y. Su, X. Zhao, M. Elimelech and Z. Jiang, Chem. Soc. Rev. 45(21)(2016) 5888-5924.

3. Z. Fan, F. Meng, M. Zhang, Z. Wu, Z. Sun and A. Li, Appl. Surf. Sci. 360 (2016) 298-305.

4. M. D. Regulacio and M. Y. Han, Chem. Res. 49(3) (2016)511-519.

5. Y. H. Ng, S. Ikeda, M. Matsumura and R. Amal, Energy Environ. Sci. 5(11) (2012) 9307-9318.

6. Z. Liu and Z. Ma, 2019. Mater. Res. Bull. 118 (2019)110492.

7. S. Khanchandani, S. Kumar and A. K. Ganguli, Chem. Eng. 4(3) (2016)1487-1499.

8. M. T. Man, J. H. Kim, M. S. Jeong, A. T. T. Do and H. S. Lee, J. lumin. 185 (2017) 17-22.

9. J. Liu, J. Jin, Z. Deng, S. Z. Huang, Z. Y. Hu, L. Wang, C. Wang, L. H. Chen, Y. Li, G. Van Tendeloo and B. L. Su, J. Colloid Interface Sci. 384(1) (2012) 1-9.

10. K. Sahu, S. Kuriakose, J. Singh, B. Satpati and S. Mohapatra, J. Phys. Chem. Solids. 121(2018) 186-195.

11. M. Verma, M. Mitan, H. Kim and D. Vaya, J. Phys. Chem. Solids, 155 (2021) 110125.

12. A. J. Antony, S. M. J. Kala, C. Joel, R. B. Bennie and S. Praveendaniel, J. Phys. Chem. Solids, (2021) 110169.

13. Y. Yan, M. Zhang, K. Gong, L. Su, Z. Guo and L. Mao, Chem. Mater. 17(13) (2005)3457-3463.

14. S. Franz, D. Perego, O. Marchese and M. Bestetti, J. Water Chem. Technol. 37(3) (2015) 108-115.

15. T. Warang, N. Patel, A. Santini, N. Bazzanella, A. Kale and A. Miotello, Appl. Catal. A-Gen. 423 (2012)21-27.

16. Y. S. Sue, K. Y. Pan and D. H. Wei, Appl. Surf. Sci. 471 (2019) 435-444.

17. K. Pingmuang, A. Nattestad, W. Kangwansupamonkon, G. G. Wallace, S. Phanichphant and J. Chen, Appl. Mater. Today. 1(2) (2015) 67-73.

18. R. Beura, R. Pachaiappan and T. Paramasivam, J. Phys. Chem. Solids. 148 (2021) 109689.

19. C. Machut, N. Kania, B. Léger, F. Wyrwalski, S. Noël, A. Addad, E. Monflier and A. Ponchel, Catalysts. 10(7) (2020) 801.

20. H. Liu, H. Liu, J. Yang, H. Zhai, X. Liu and H. Jia, Ceram. Int. 45(16) (2019) 20133-20140.

21. Y. Zhai, S. Zhang and H. Pang, Preparation, Mater. Lett. 61(8-9) (2007)1863-1866.

22. A. D. Liyanage, S.D., Perera, K. Tan, Y. Chabal and K. J. Balkus Jr, ACS Catal. 4(2) (2014) 577-584.

23. K. Girija, S. Thirumalairajan, A. K.Patra, D. Mangalaraj, N. Ponpandian and C. Viswanathan, Semicond. Sci. Technol. 28(3) (2013)035015.

24. B. Das, B. Das, N. S. Das, S. Pal, B. K. Das, S. Sarkar and K. K. Chattopadhyay, Appl. Surf. Sci. 515 (2020)145958.

25. B. Das, B. Das, S. Pal, R. Sarkar, N. S. Das, S. Sarkar and K. K. Chattopadhyay, AIP Conference Proceedings 2220(1) (2020) 020013.

26. B. Das, B. Das, N. S. Das, S. Sarkar and K. K. Chattopadhyay, Micro. Meso. Mater. 288 (2019) 109600.

27. H. Sudrajat and T. K. Nguyen, Optik. 223 (2020)165370.

28. L. S. Reddy, Y. H. Ko and J. S. Yu, Nanoscale Res. Lett. 10(1) (2015)1-7.

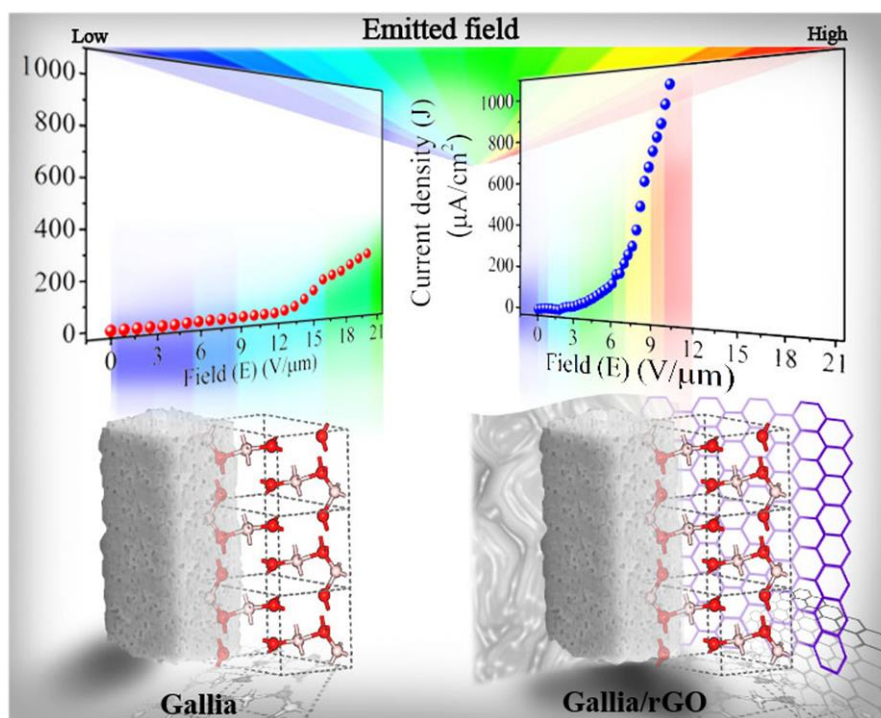29. Y. Sakata, T. Nakagawa, Y. Nagamatsu, Y. Matsuda, R. Yasunaga, E. Nakao and H. Imamura, J. Catal. 310 (2014)45-50.

30. C. Han, W. Mao, K. Bao, H. Xie, Z. Jia and L. Ye, Int. J. Hydrog. Energy. 42(31) (2017)19913-19919.

31. A. S. Deshpande, D. G. Shchukin, E. Ustinovich, M. Antonietti and R. A. Caruso, Adv. Func. Mater. 15(2) (2005) 239-245.

32. B. Zhao and P. Zhang, Catal. Commun. 10(8) (2009)1184-1187.

33. P. Chowdhury, J. Moreira, H. Gomaa and A. K. Ray, Ind. Eng. Chem. Res. 51(12) (2012)4523-4532.

34. H. Zhao, Y. Zhang, G. Li, F. Tian, H. Tang and R. Chen, RSC Adv. 6(10) (2016)7772-7779.

35. J. J. Samuel and F. K. Yam, Mater. Res. Exp. 7(1) (2020) 015051.

36. M. Molla, A. Islam, I. Tateishi, M. Furukawa, H. Katsumata, T. Suzuki and S. Kaneco, Chem. Eng. 1(2) (2017) 8.

37. S. Chakrabarti, B. Chaudhuri, S. Bhattacharjee, P. Das and B. K. Dutta, J. Hazard. Mater. 154(1-3)(2008)230-236.

38. Y. Quan, D. Fang, X. Zhang, S. Liu and K. Huang, Mater. Chem. Phys. 121(1-2) (2010) 142-146.

39. F. A. Mir, Results Phys. 4 (2014)103-104.

40. H. Zhao, Y. Zhang, G. Li, F. Tian, H. Tang and R. Chen, RSC Adv. 6(10) (2016)7772-7779.

41. Y. Xu and M. A. A. Schoonen, Am. Mineral. 85 (2000) 543-556.

Chapter 7

Enhanced field emission properties of rGO wrapped Ga$_2$O$_3$ micro/nanobricks: Experimental investigation with theoretical validation

Abstract

Aiming for efficient cold cathode applications in low dimension, pure and rGO wrapped gallium oxide micro/nanobricks were synthesized via cost-effective solid-state and hydrothermal routes. The synthesized samples were characterized using X-ray diffractometry, field emission scanning electron microscopy, high-resolution transmission electron microscopy, and Raman spectroscopy for phase, morphology, composition, and structure-related investigations. In addition, all samples were thoroughly investigated, and as a result, experimental modifications were adapted accordingly for improving the field emission properties. Remarkable enhancement of field-emission performances with a high emission current-density of 1.08 mA/cm^2 and enhancement factor of 7400 has been observed as an effect of rGO wrapping. The results have been correlated with the increase in the availability of emission sites and proper charge carrier transport between the components in the hybrid structure. Furthermore, the probability of charge carrier transport across Ga$_2$O$_3$ /rGO junction was validated using theoretical analysis via DFT calculations. Moreover, the improvement of field emission properties due to rGO wrapping was also predicted from ANSYS simulations. Hence, 3.5 times increment of current density and 2.5 times lowering of turn-on field, the Ga$_2$O$_3$/rGO hybrid system emerged as one of the most functional future cold cathodes. This work opens up new applications for Ga$_2$O$_3$-based composites beyond the sensing and catalysis sectors.

7.1. Introduction

Emission-based devices and their application in multicomponent equipment have been the prime focus of materials scientists for many decades. Several well-performing cold cathode emitters have been developed with numerous and continuous efforts by various research groups. Carbon and carbon-based composites are the leading candidates in this regard[1, 2]. A large number of carbon-based systems in 0D, 1D, 2D, and 3D forms are widely studied for their electron emission[3-6] and other optoelectronic properties[7, 8]. However, different metal nanostructures have also emerged as potential electron emitters and are being used commercially on a large scale[9, 10]. A major problem of such metallic nanostructured systems like tungsten nanowire emitters is its production cost, inadequate transparency, and limitation of fabrication routes that disable their use in low-cost household systems[11]. On the other hand, the availability of pure carbon-based systems with different dimensions is very high, but at the same time, a large number of efforts have been devoted to optimizing the cost of production, yield, and varieties of emission parameters[12, 13]. Though carbon-based emitters are used in many devices, there is ample scope for further studies on issues like enhancing their transmittance for a practical transparent conducting emitter device. Furthermore, carbon-based materials have an inherent hydrophobic nature. This can impose an additional barrier in applications of related compounds when used in an aquatic environment. Nanostructured semiconductor systems are often proposed as a possible way out of these types of restrictions. Mainly oxide semiconductor nanostructures have emerged as popular emitter systems. For example, a report by Chen et al. showed that the inclusion of structural hierarchy in simple ZnO nanowire could enhance its emission property multifold[14]. Similarly, aspect ratio enhancement in cobalt oxide nanostructures can tune up its cold emission behavior as proposed by Jadhav et al[15]. Chatterjee et al. experimentally and analytically showed that random meshes of Cu_2O nanorods are also capable of cold emitting electrons[16]. Such systems may also be associated with the additional benefit of versatile applications such as photocatalysis[17-19], solar energy harvesting[20, 21], novel supercapacitors[22, 23], etc.

Nevertheless, any oxide system, in pure form and even with the wide variety of morphologies, has hardly achieved a similar efficiency as classic carbon-based emitters. CNTs, as shown by Lahiri et al.[24] and Ahn et al.[25], could reach a current emission density as high as the mA range with simple assistance by some metals and metal alloys. On the other hand, Ahmed et al.[26] reported substantial lowering of the turn-on field of DLC by Cu incorporation. CNR also exhibited enhanced field emission after structural modification[27].

Oxide and other newer emitter systems are yet to achieve appreciable development in this regard. Moreover, after in-depth study with 2D carbon systems, i.e. graphene, emitter-based systems have achieved an exemplary efficiency and are already in a position to be commercialized. 2D carbon sheets are the most efficient emitters due to their electron-rich character, edge effects, and wrinkle-related facilities[28, 29]. Those novel features are often enhanced when those transparent carbon sheets are anchored in the column or other suitable nanostructures. For example, Chen et al.[30] showed that graphene sheets could be a smarter emitter when placed on Si tips rather than metal foil. Gou et al.[31] reported enhanced emission current stability from graphene sheets being anchored on ZnO QDs. Hence, boosting any other novel nanostructured system, with a trace amount of graphene or related carbon nanostructure may be helpful in many aspects. It can improve the emission properties of the composite system without any considerable change of inherent multifaceted applications of the host. Enhancement of different properties with one-time assistance of graphene is also reported[32]. Thus, the electron emission performance of graphene modulated oxide nanostructures draws attention. A large number of low dimensional oxide systems have already shown great multipurpose activities[33, 34], in addition to efficient field emission properties. Among such oxides, gallium oxide, a classic sensor and catalyst, has also shown effective hybridization with graphene resulting in enhanced photocatalytic activity[35] and charge storage ability[36]. In most cases, in situ hybridization with graphene is preferred to avoid external impurity and ensure proper molecular level contact between the oxide system and graphene[37]. However, dealing with Ga_2O_3 can be more accessible in this regard too. As reported in our earlier work, Ga_2O_3 nanostructures can be synthesized at high temperatures with tunable crystalline phases and morphology[38]. Due to the nanostructures' high stability, they can be easily employed to undergo hydrothermal treatment along with graphene oxide being transformed into reduced graphene oxide (rGO). This indeed can modify the technique in a quasi- in situ one resulting in a contaminant free Ga_2O_3/rGO hybrid system with regular proper molecular level contact. The final product, powder form, may be more applicable in new age flexible devices than rigid and opaque systems like tungsten nanowire-based emitters.

This work demonstrates the first attempt of investigation of field emission properties of gallium oxide in a graphene-based composite system. Initially, Ga_2O_3 nanostructures with various crystalline phases and morphology were fabricated. Secondly, their field emission properties were studied to identify the sample with better performance for hybridization with rGO. The modification of the electrical properties of Ga_2O_3 after hybridization with rGO was

ensured via DFT-based calculations. The amount of rGO incorporation was optimized to fabricate the best performing Ga_2O_3 based electron-emitter system. After that, the electrode separation was also optimized to get the best field emission performance of the composite sample. It was observed that the sample synthesized with Ga_2O_3/rGO weight ratio 5:1 exhibited ~ 1.08 mA/cm^2 emission current density with a turn-on field as low as 2.01 V/m^{-1} at 200 mm electrode separation. The enhancement of emission characteristics of Ga_2O_3 nanostructures via rGO wrap was also supported by ANSYS MAXWELL simulations. Some of the key features of this work may be summarized as, Firstly, this work first introduces rGO wrapped Ga_2O_3 as a potential candidate for future emission-based devices along with its other classic applications. Secondly, it includes an effortless synthesis procedure with no requirement of complicated devices, which may be commercially helpful for large-scale synthesis. Thirdly, the final product being non-toxic and powder in nature can be crucial in ex-situ coating on future emission-based devices. The idea explored here should directly combine the facilities of graphene with an environmentally stable compound like gallium oxide and may open up newer applications of this hybrid system.

7.2. Experimental section

Commercially available reagents were purchased and used without further purification. Deionized (DI) water was used to prepare the required aqueous solutions.

7.2.1. Synthesis of Ga_2O_3 micro/nanobricks

Ga_2O_3 were synthesized via chemical route followed by solid-state calcination. Typically 0.1 M of $Ga(NO_3)_3.xH_2O$ (Sigma-Aldrich, 99.99%) was dissolved into 100 ml deionized water with continuous stirring. The temperature of the solution gradually increased from room temperature to 90 ℃. After reaching the final temperature, ammonium hydroxide (NH$_4$OH, 30-32%) was added drop by drop to the solution until the pH of the solution reached 9. Then the solution was kept for 4 hours at that temperature. It was cooled down naturally to room temperature. The collected white precipitate (Gallium oxide hydroxide, GaOOH) was dried overnight at 60 ℃ and then calcined at 500 ℃ and 1000 ℃ for 3 hours to obtain α-Ga_2O_3 and β-Ga_2O_3 respectively. Two more samples of β-Ga_2O_3 were synthesized via calcination at 800 ℃ and 1200 ℃ as part of the optimization process.

7.2.2. Synthesis of Graphene Oxide (GO) by modified Hummer's method

Graphene oxide (GO) was prepared via modified Hummer's method. Commercially available graphite powder (Sigma-Aldrich, 99.99%), sodium nitrate (99.99%) & potassium permanganate (99.99%) were used as starting materials. The proper amount of pure graphite & sodium nitrate was mixed with concentrated sulfuric acid (98 %) keeping the temperature below 2 ℃ and stirred for up to 6 hours. Then Potassium permanganate ($KMnO_4$) was slowly added to the pre-treated solution under vigorous stirring for 120 min in an ice bath keeping the temperature below 0 ℃. Further, it was kept as it is for another 2 hours. Then the solution was taken out from the ice bath and heated at 50 ℃ -60 ℃ for approximately 1 hour without stirring. The mixture was again stirred for 1h and further diluted with 200 ml of DI water. After that, H_2O_2 (30%) was added. Upon addition, the mixture turned bright yellow from the dark brown. The mixture was then filtered and washed several times with DI water until the pH of the solution became 7. Then final GO is dispersed in DI water with 1:1 loading (1 mg/ml). The solution was centrifuged at 5000-6000 rpm for proper exfoliation of GO & supernatant was collected.
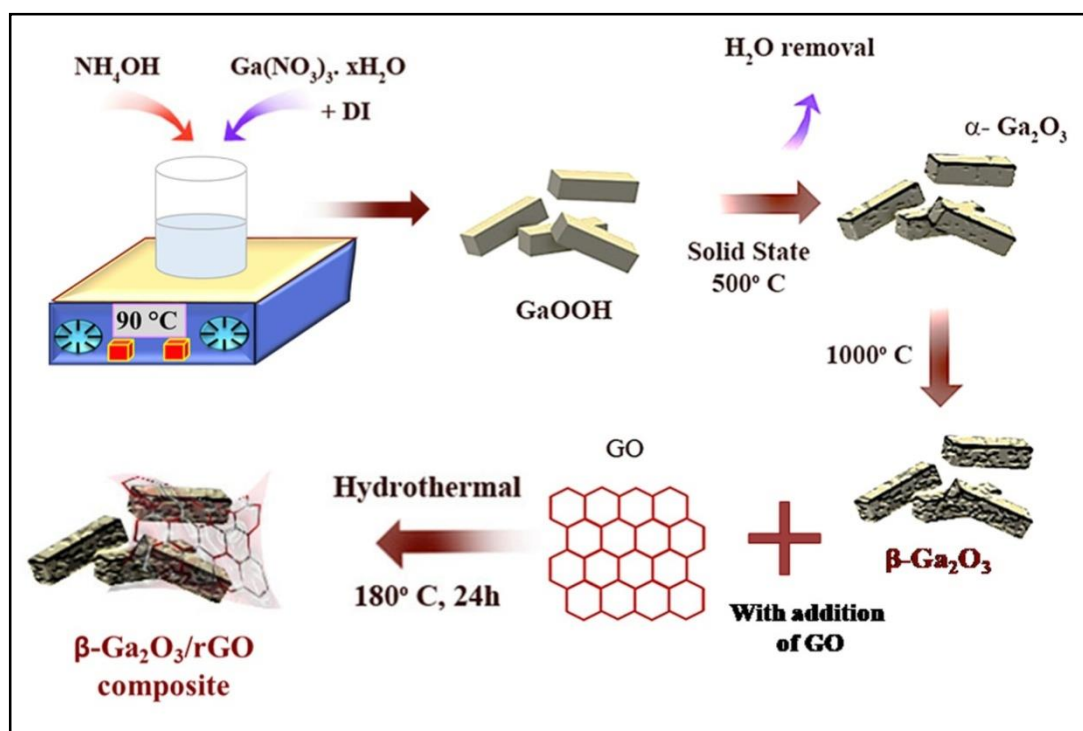
Scheme 7.1 Synthesis schematic of the β-Ga₂O₃/rGO composite

7.2.3.   Synthesis of Ga_2O_3/rGO composite:

Ga_2O_3/rGO composite was synthesized via a simple hydrothermal method. First, 60 mg of as-synthesized Ga_2O_3 micro/nanobricks was mixed into the 40 ml of as-prepared homogeneous GO solution and magnetically stirred for 3 hours to form a uniform suspension. Then the solution was poured into a Teflon-lined stainless-steel autoclave (capacity 60 ml) maintaining 180 °C for 24 hours under auto-generated pressure to produce Ga_2O_3/rGO composite system. This process confirmed the GO-reduction. Finally, the collected residue from the hydrothermal was washed with DI water and dried at room temperature to obtain the final product. The different composite samples were synthesized with varying amounts of GO (3 mg, 6 mg, 12 mg) and the as-prepared samples were marked as GR3, GR6, and GR12, respectively. **Scheme 7.1** represents the schematics of the synthesis process.

7.2.4.   Characterization

The synthesised samples' crystal structure and phase purity were studied by an X-Ray diffractometer (XRD, BRUKER D8 Advance). Morphology of the samples represented the microstructure, lattice image, and the wrapping of the pristine sample with rGO. The analyses were confirmed using high-resolution transmission electron microscopy (TEM; JEOL-TEM 2100) (operating voltage 200 kV), and field emission scanning electron microscopy (FESEM, S-4800, Hitachi) with accelerating voltage 5.0 kV. Room temperature Raman spectra were recorded using a Raman spectrometer (alpha 300, Witec, Germany, laser source of λ= 532 nm). The first-principles calculation executed theoretical investigation with density function theory (DFT). The cold-cathode emission properties of the pristine and composite samples were studied in a laboratory-made ultra-high vacuum field emission measurement set-up. The probable emission characteristics of the samples with a degree of rGO-wrapping were further confirmed by theoretical simulations using ANSYS MAXWELL software. The outcome of this simulation-based study was correlated with the experimental results.

7.2.5.   Theoretical methods

The first-principles calculations were accomplished using the Vienna ab-initio simulation package (VASP)[40, 41]. During structural optimizations and energy calculations, the ion cores were described using Projector Augmented wave (PAW)[42] method. Also, the Perdew-Burke-Ernzerhof (PBE)[43] functional was utilized to describe the exchange-correlation contributions. The calculations were performed using the generalized gradient approximation (GGA) framework. During all the calculations, the energy cut-off value of the plane wave basis was set equal to the highest energy cut-off value described in the pseudo potential profile of the

constituent elements. All the systems were set to relax until the total energies and forces converged below 1×10^{-5} eV/ atom and 1×10^{-3} eV/ Å respectively. A $(3 \times 2 \times 1)$ Γ-centred k-point mesh was utilized during the pure and composite systems' relaxation and work function calculation. A vacuum slab of length 20 Å was placed perpendicular to the surface of the pure and hybrid systems to eliminate any spurious interaction between their periodic images. Charge transfer within the hybrid system was calculated using Bader charge analysis[44]. The contribution from the Van Der Waals forces was taken into account via the PBE +D2 (Grimme's) method[45], as implemented in VASP. The planar average charge density difference ($\Delta\rho_{avg}$) along the direction perpendicular to the plane of the composite system (along the z-direction) was calculated using the following formula:

$$\Delta\rho_{Avg}(z) = \rho_{Avg}^{Ga_2O_3+Graphene}(z) - \rho_{Avg}^{Ga_2O_3}(z) - \rho_{Avg}^{Graphene} \tag{7.2.1}$$

Where, $\rho_{Avg}^{Ga_2O_3+Graphene}(z)$, $\rho_{Avg}^{Ga_2O_3}(z)$ and $\rho_{Avg}^{Graphene}$ are the planar average charge density along z-direction of the composite, bare β-Ga$_2$O$_3$-(1 1 1) surface slab, and bare graphene systems respectively. The positive value of $\Delta\rho_{Avg}(z)$ indicates accumulation of charge, whereas negative values indicate charge depletion.

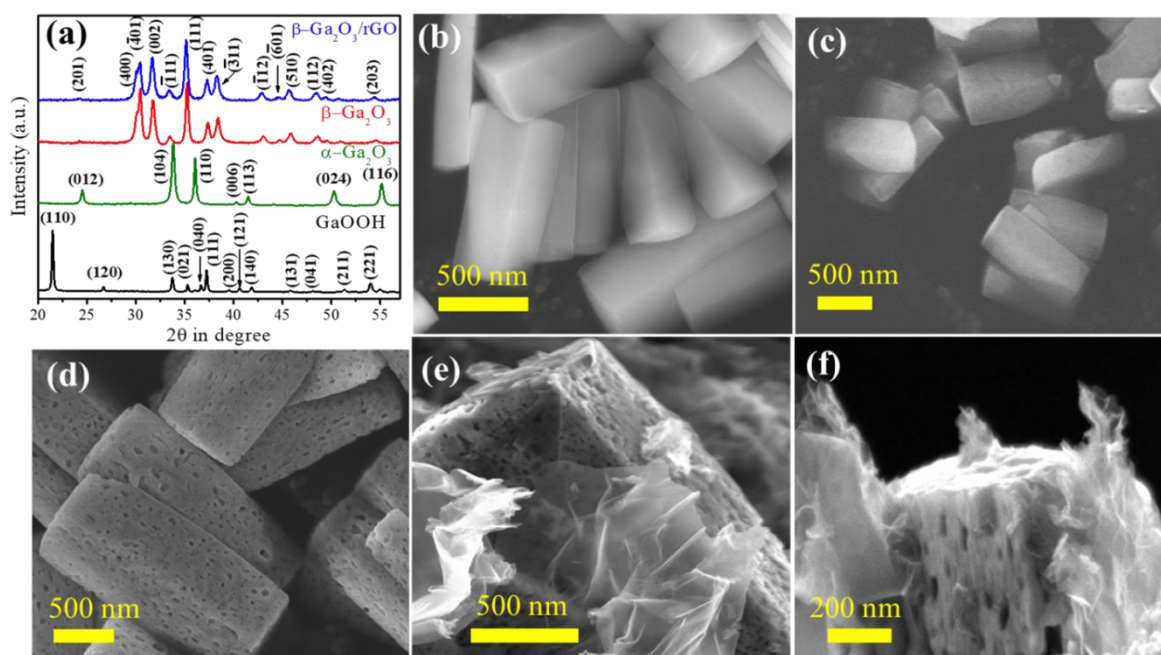## 7.3. Results and discussion

7.3.1. Structural Studies

Figure 7.1 X-ray diffraction patterns of the samples (a), FESEM images of as-synthesized GaOOH (b), α-Ga$_2$O$_3$ (c), β-Ga$_2$O$_3$ (d), and β-Ga$_2$O$_3$/rGO (GR12) (e-f)

194

The structural properties of the samples are summarized in **Figure 7.1a**. It can be seen that all the samples exhibit good crystallinity indicated by intense diffraction peaks for the hydroxide, α and β phases. The peaks appearing near 21.4º, 33.7º, 37.2º and 54.03º were assigned to (1 1 0), (1 3 0), (1 1 1), and (2 2 1) planes of orthorhombic GaOOH phase, respectively [JCPDS 06-0180]. Similarly, XRD peaks at diffraction angles 24.5º, 33.7º, 36.0º, 50.2º, and 55.1º were assigned to (0 1 2), (1 0 4), (1 1 0), (0 2 4), and (1 1 6) planes of hexagonal α-Ga_2O_3 phase (calcined at 500 ºC) respectively [JCPDS 06-0503]. For the sample calcined at 1000ºC, XRD peaks occurred at diffraction angles 30.4º, 31.7º, 35.1º, 37.3º, 38.3º and 45.8º were assigned to ($\bar{4}$ 0 1), (0 0 2), (1 1 1), (4 0 1), ($\bar{3}$ 1 1) and (1 1 2) planes of monoclinic β-Ga_2O_3 phase, respectively [JCPDS 76-0573]. Also, the XRD pattern of the rGO wrapped sample is presented in **Figure 7.1a.** The figure indicates no significant signature of crystalline peaks of rGO. So, the nature of graphene in the hybrid sample was further studied via a Raman spectrophotometer (discussed later).

7.3.2. Morphological Studies

The morphologies of the samples are depicted in **Figure 7.1,** where general bricklike shapes of the nanostructures are observed. On average, the bricks exhibit 2 μm length and 0.5×0.5 $μm^2$ cross-sectional area. Additionally, in **Figure 7.1(c-d),** the α-Ga_2O_3 and β-Ga_2O_3 samples showed uniform porosity on their surface, that was not observed in the case of the hydroxide system (**Figure 7.1b**). The porosity in the oxide system was correlated with the removal of water molecules with increasing calcination temperature. Sample α-Ga_2O_3 was synthesized at a comparatively lower temperature of 500 ºC, which was increased up to 1000 ºC to synthesize β-Ga_2O_3. Higher temperature ensured the gradual removal of residual moisture molecules of GaOOH samples leaving behind characteristic pores in the sample and transforming it into α-Ga_2O_3. However, further increment of synthesis temperature caused agglomeration of the particles adjoining the earlier pores forming larger pores of higher volume. **Figure 7.1(e-f)** represents the β-Ga_2O_3 samples wrapped with rGO. Due to a nominal increment of GO input during the synthesis process, a higher amount of rGO wrapping on β-Ga_2O_3 bricks was observed. So that the sample GR3 was found with the least amount of attached rGO sheets, and it was relatively increased in the case of the sample GR6. And finally, for the sample GR12, a proper rGO-sheet wrapping on β-Ga_2O_3 micro/nanobricks was obtained.

The nature of wrapping on Ga_2O_3 bricks for sample GR12 was further analyzed via transmission electron microscopy, and the obtained micrographs are presented in **Figure 7.2**. Transparency of the rGO sheets is detectable in the TEM micrograph 7.2a, whereas close proximity in the lattice level of the rGO sheets and Ga_2O_3 bricks can be confirmed from the HRTEM image depicted in **Figure 7.2b**. The lattice spacing was measured to be 0.263 nm which corresponds to the (111) plane of β-Ga_2O_3. The thickness of the individual layers of multilayer rGO sheets was roughly estimated to be 0.2 nm.
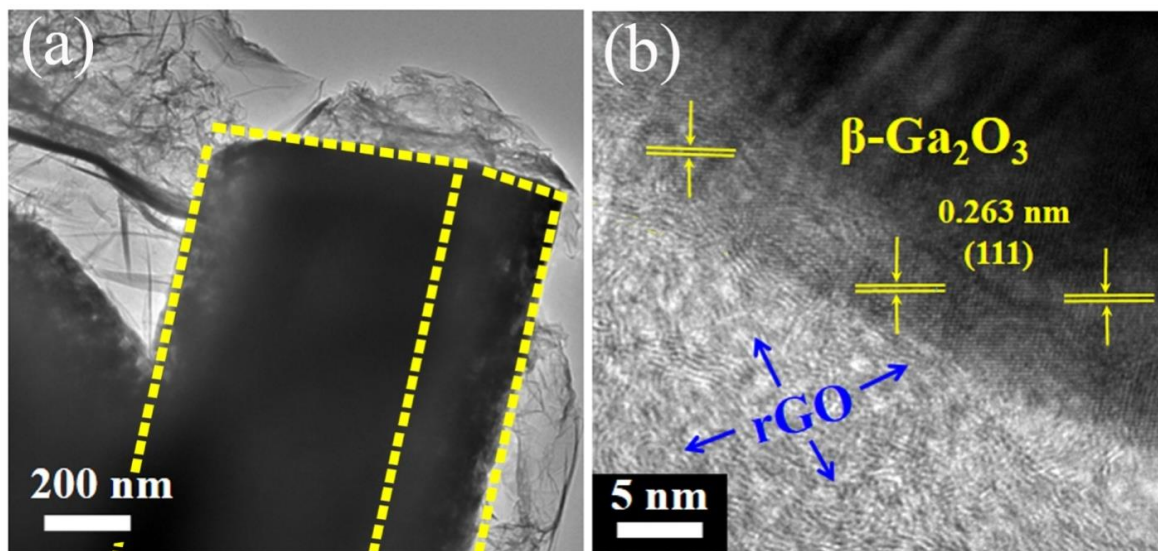

Figure 7.2 HRTEM microstructure (a) and crystal lattice fringes (b) of the composite sample GR12
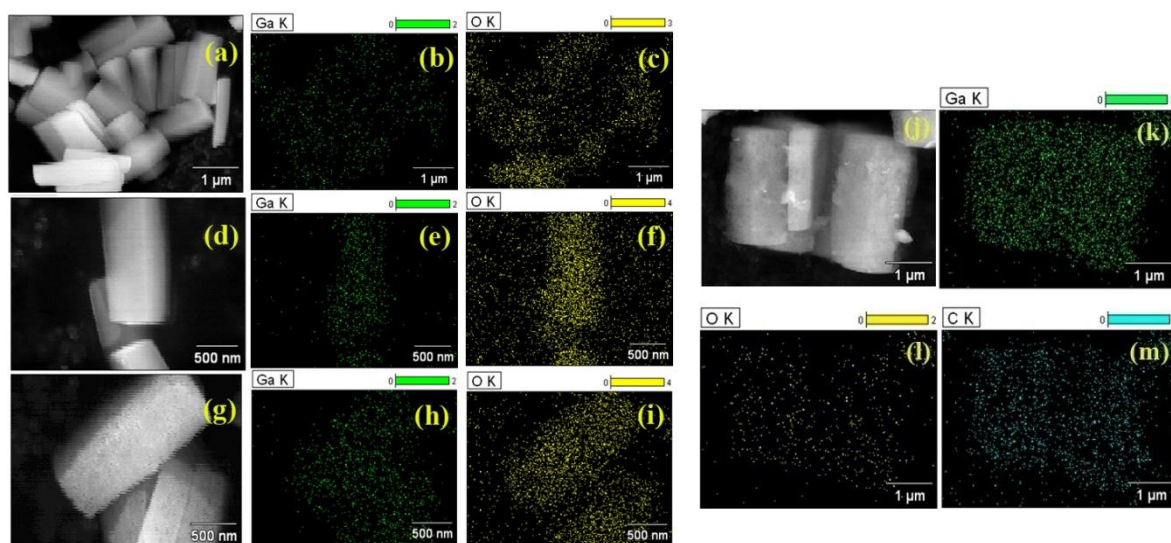
7.3.3. Compositional Studies

Figure 7.3 Elemental distribution (EDS mapping) of the samples- GaOOH (a–c), α-Ga_2O_3 (d-f), β-Ga_2O_3 (g-i) and β-Ga_2O_3/rGO composite (j-m)

The uniform distribution of the constituent elements was confirmed by the EDX study of the samples GaOOH, α-Ga$_2$O$_3$, β-Ga$_2$O$_3$, and β-Ga$_2$O$_3$/rGO composite presented in **Figure 7.3**. Also, the existence of graphene in β-Ga$_2$O$_3$/rGO sample can be ensured by the presence of elemental carbon in that hybrid system, as shown in their corresponding EDX mapping.

7.3.4. Raman studies

The Raman spectra of samples β-Ga$_2$O$_3$, GO and β-Ga$_2$O$_3$/rGO composite are presented in **Figure 7.4**. The vibrational modes detected for β-Ga$_2$O$_3$ nanostructures (**Figure 7.4a**) were further assigned as A$_g$ and B$_g$ modes (**Table T1**). A slight variation of the positions of Raman peaks was observed for pristine and rGO wrapped gallium oxide. This type of variation typically indicates proper carrier exchange between the counterparts in a composite. **Figure 7.4b** shows the characteristic peaks of graphene around 1356 cm^{-1} and 1600 cm^{-1}, which were accounted for the D and G band, respectively. The D band corresponds to sp^3 carbon atom vibration, indicating the structural defects and the disorder in the GO sheets. Also, the G band can be correlated with the vibrations of sp^2 carbon domains. The intensity ratio of the D band to G band (I$_D$/I$_G$) is associated with the ratio of the size of the sp^3 domains to sp^2 domains. The higher the intensity ratio of (I$_D$/I$_G$) specify the smaller the sp^2 domains. The I$_D$/I$_G$ ratio of the composite sample was found to be 1.04, which is higher than that of GO (0.92). The significant increment of I$_D$/I$_G$ ratio is because of the enhancement of structural defects and disorders after the hydrothermal treatment. Also, due to the restoration of sp^2 carbon in the graphene lattice, corresponding shrinkage of the sp^2 domain size occurred, indicating the inclusion of H atoms in the system. This phenomenon confirms the I$_G$ value decrement during the GO to rGO reduction process. Thus an enhanced I$_D$/I$_G$ ratio indicates that after the hydrothermal method, the GO in the composite system has been reduced to rGO.

Additionally, the D and G bands corresponding to rGO present in the composite were found to be at 1350 cm^{-1} and 1593 cm^{-1}, respectively (**Figure 7.4c**) which are at notably different positions as seen in pristine rGO, i.e., at 1353 cm^{-1} and 1592 cm^{-1}, respectively (**Figure 7.4d**). Such a shift in band position may be accounted for π-π interaction between the counterparts, β-Ga$_2$O$_3$ and rGO. π electrons being delocalized to rGO from the host β-Ga$_2$O$_3$ is the primary reason behind this shift.
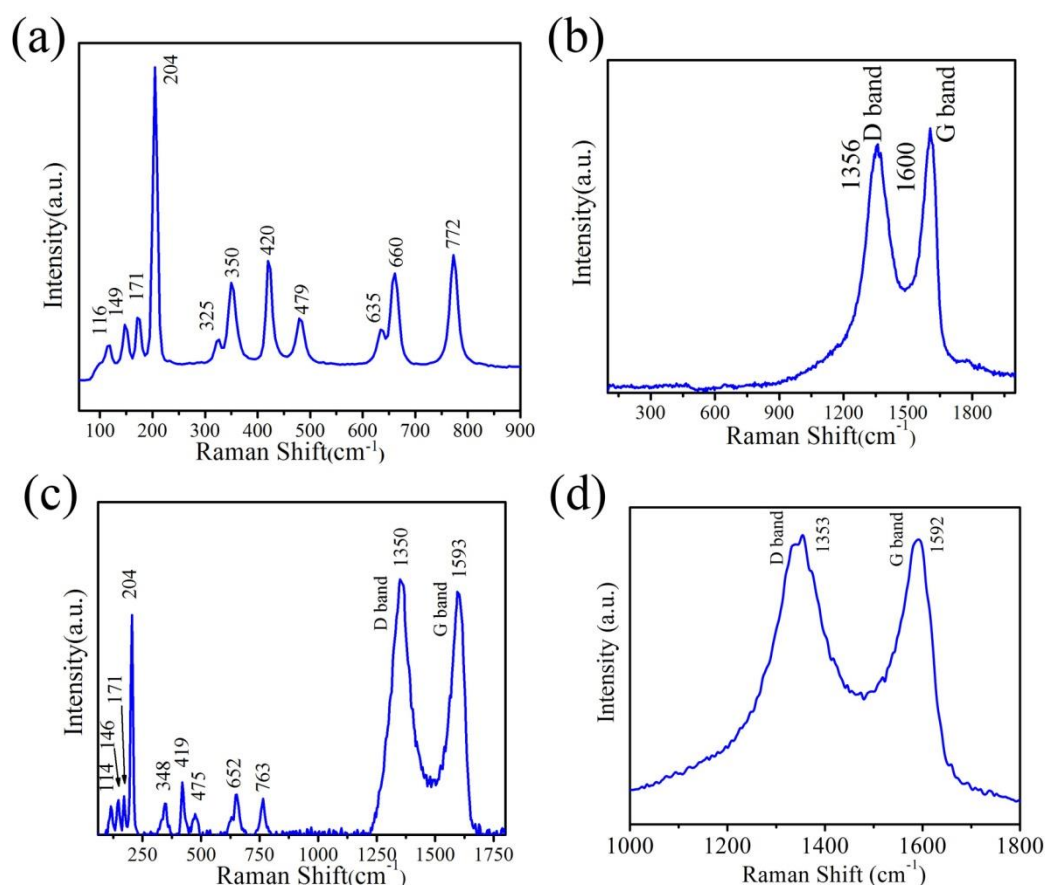
Figure 7.4 Raman spectra of β-Ga₂O₃ (a), GO (b), β-Ga₂O₃/ rGO composite (c), and rGO

Table 7.1: Spectral position of the Raman peaks of the phonon modes of β-Ga$_2$O$_3$, given in cm^{-1}

Spectral position of Raman peaks (cm^{-1})	116	149	171	204	325	350	420	479	635	660	772
Phonon mode	$B_g^{(1)}$	$B_g^{(2)}$	$A_g^{(2)}$	$A_g^{(3)}$	$A_g^{(4)}$	$A_g^{(5)}$	$A_g^{(6)}$	$A_g^{(7)}$	$A_g^{(8)}$	$B_g^{(5)}$	$A_g^{(10)}$

7.3.5. Density functional theory (DFT): Work function calculation

The work function of β-Ga$_2$O$_3$ and the modulation of the work function value as β-Ga$_2$O$_3$ is wrapped by rGO were further estimated using first-principles calculations.The (1 1 1) β-Ga$_2$O$_3$ surface slab, comprised of a few atomic layers, was fully relaxed until the convergence criteria described in the 'Theoretical methods' section are met. The work function of the optimized β-Ga$_2$O$_3$ surface slab was calculated subsequently using first-principle methodologies. To construct the β-Ga$_2$O$_3$/rGO composite system, the **a** lattice vector of the graphene unit cell was rotated towards [3 1 0] direction, so that the lattice

vectors of the β-Ga₂O₃ surface slab and rotated graphene unit cell are oriented almost identically to minimize the shear strain. We considered the ideal case of completely reduced graphene oxide (rGO) to reduce the computational cost. Upon minimizing the shear strain, the lattice mismatch between the two components of the composite system was further reduced by considering (2×1×1) and (1×4×1) supercells for β-Ga₂O₃ (unit cell lattice constants: **a** = 3.04 Å and **b** = 9.50 Å) and rotated graphene system (unit cell lattice constants: **a** = 6.49 Å and **b** = 2.46 Å) respectively. Thus within this model, the lattice mismatch was kept down to 6.32% and 3.45% respectively along **a** and **b** lattice vectors of the composite system.
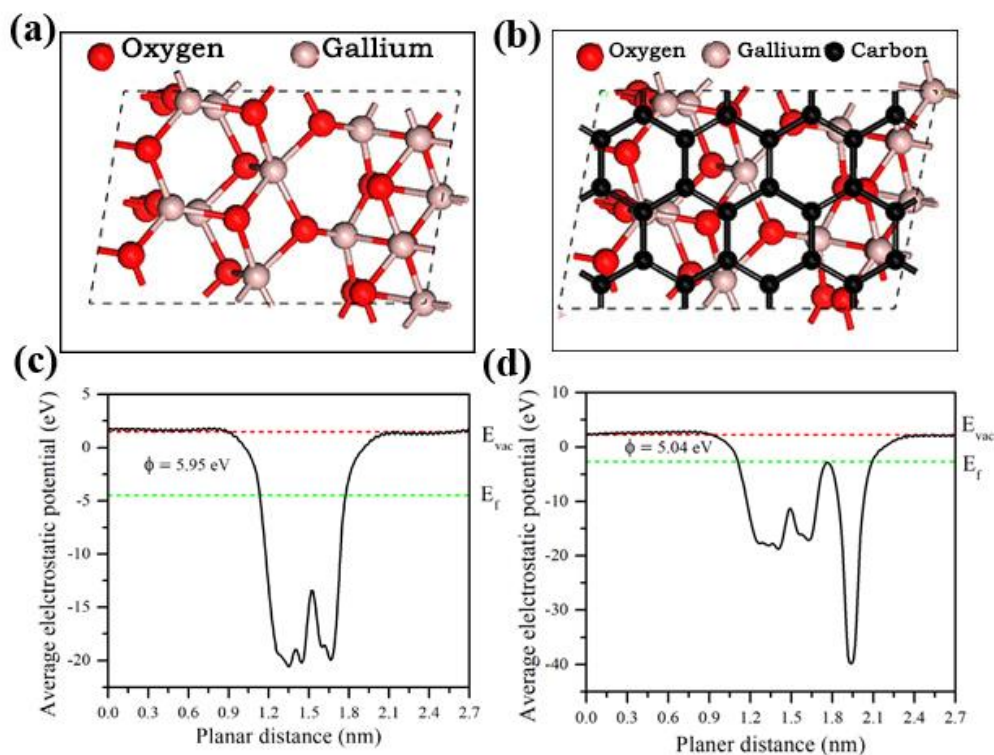

Figure 7.5 Optimized structural models of β-Ga₂O₃ (a), and β-Ga₂O₃/rGO composite (b); and corresponding average electrostatic potential vs. planar distance plot (c-d)

The obtained most stable structures of pure and composite Ga₂O₃ unit cells are provided in **Figure 7.5(a-b)**. **Figure 7.5(c-d)** represents the planar average electrostatic potential plot versus the planar distance obtained from the first-principles calculations. The vacuum energy (E_{vac}) was considered as the planar average electrostatic potential at a large distance from the surface. Also, the DFT calculations provided the Fermi energy (E_F) value of the samples. And thus, the required work function Φ was calculated using the following formula:

$$\Phi = E_{vac} - E_F \tag{7.3.1}$$

Finally, for the (111) surface of gallium oxide, the work function (ϕ) value was calculated as

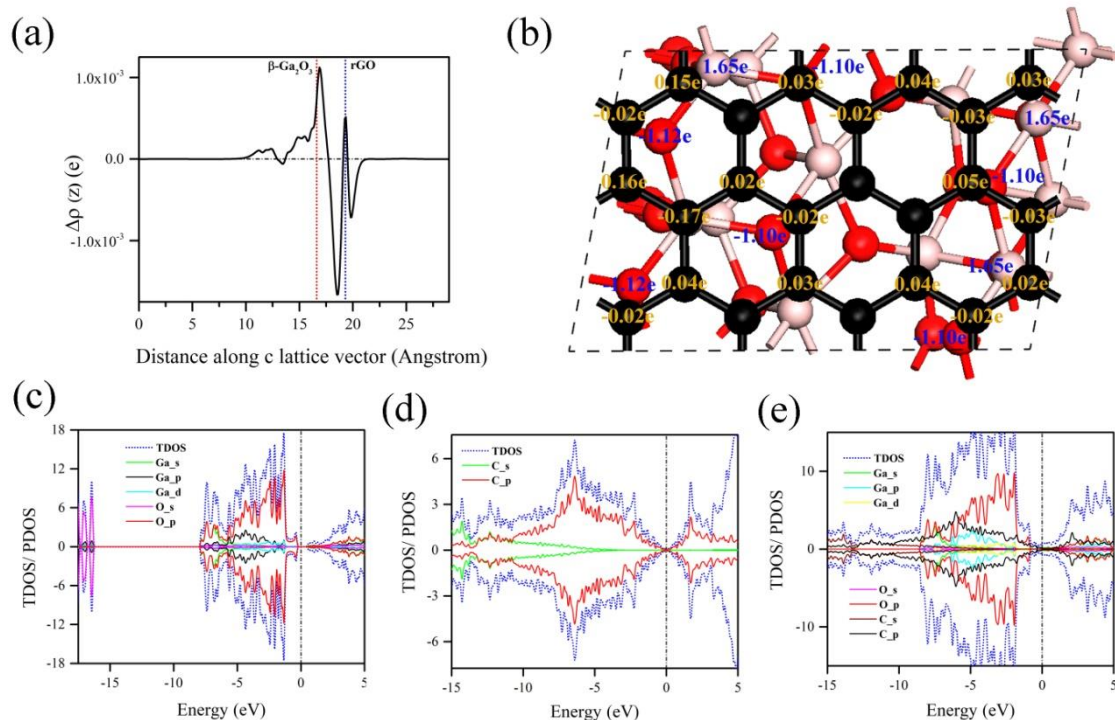5.95 eV, and the same for rGO wrapped gallium oxide was found to be 5.04 eV.

Figure 7.6 Planar average charge density difference for the β-Ga₂O₃/rGO composite system along c lattice vector (z direction) of the cell (a), Charge transfer between the atoms near the β-Ga₂O₃/rGO interface (b), Total and partial density of states for (c)β-Ga₂O3 (1 1 1) surface slab, (d) rGO (graphene) and (e) β-Ga₂O₃/rGO composite system

The planar average charge density difference ($\Delta\rho_{avg}$ (z)) of the composite system was calculated along the z-direction using equation (7.1) and is graphically represented in **Figure 7.6a**. Figure indicates that charge is transferred from rGO to β-Ga₂O₃, thus reducing the work function value. The obtained nature of variation of $\Delta\rho_{avg}$ (z) in the rGO wrapped β-Ga₂O₃ agrees well with prior theoretical work on the same system[46]. The Bader charge analysis of the rGO wrapped β-Ga₂O₃ system reveals that the oxygen atoms present in the surface of the β-Ga₂O₃-(1 1 1) slab receives electronic charges in the composite formation, whereas the gallium atoms lose electronic charge. High oxygen concentration on the surface of β-Ga₂O₃ acts as a receiver of electronic charge overall, supporting the results obtained from the plot of $\Delta\rho_{avg}$ (z). The carbon atoms present in rGO both receive and donate charges regionally. The charge transferred to or from the atoms within the interaction region between β-Ga₂O₃ and rGO is represented in **Figure 7.6b**. To gain further insights into the changes of electronic properties upon the formation of the β-Ga₂O₃/rGO composite system, the total and partial density of states (TDOS and PDOS) of the composite system, and both the components in their pure states were calculated. The calculated TDOS and PDOS of the β-Ga₂O₃ (1 1 1)

plane, rGO, and β-Ga$_2$O$_3$/rGO composite systems are represented in **Figure 7.6(c-e)**. As the rGO system was replicated as the completely reduced graphene monolayer, the TDOS of rGO shows a semi-metallic nature with zero density of states at the Fermi level. The β-Ga$_2$O$_3$ (1 1 1) surface slab was found to be semiconducting with a low band gap value, as evident from figure 7.6 (c). The highest occupied states are contributed mainly by the oxygen p-orbitals. Interestingly, rGO wrapping converts the composite system into a metallic one with a non-zero density of states (DOS) at the Fermi level (**Figure 7.6e**). The non-zero DOS at the Fermi level is contributed by the carbon p, oxygen p, and gallium s orbitals.

7.4.   Field emission studies

Field emission properties of the sampleswere investigated using an ultra-high vacuum emission measurement setup. Equal amounts of different samples were pasted on conducting carbon tape, which was a cathode. Stainless steel made the conical tip of diameter 1.5 mm was considered as the collector. Inter electrode separation was kept at 200 µm using a micrometer screw. Strict monitoring was performed via a transparent viewport during the entire measurement to ensure no sparking near the sample or inter-electrode space.
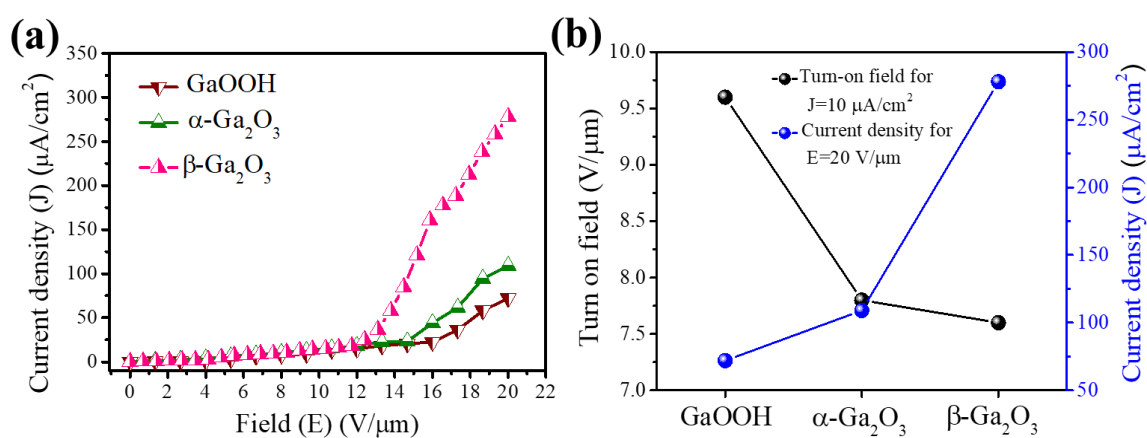

Figure 7.7 J-E characteristics (a) and plots of turn-on fields and current density values (b) of the as-synthesized GaOOH, β-Ga$_2$O$_3$, and β-Ga$_2$O$_3$ samples

The electron emission current density (J) was plotted as a function of the macroscopic input field (E), and the same is presented in **Figure 7.7**. Output current density verses electric field strength plot shows a maximum current density of 278 µA/cm^2 at 20 V/µm external fields corresponding to β-Ga$_2$O$_3$ nano-bricks. At the same applied field α-Ga$_2$O$_3$ and GaOOH samples achieved a current density of 110 and 72 µA/cm^2, respectively. It is confirmed from these graphs that there is a gradual decrement in turn-on fields (corresponding to an emission current density of 10 µA/cm^2) from GaOOH to α-Ga$_2$O$_3$ to β-Ga$_2$O$_3$ (**Figure 7.7b**). So, it can

be concluded that GaOOH shows the most inferior emission behaviour, which was slightly improved in the case of α-Ga$_2$O$_3$ and further enhanced for β-Ga$_2$O$_3$. However, poor emission activity executed by the hydroxide sample can be correlated with the presence of inherent moisture molecules which actively absorb emitted electrons causing additional potential barriers. Moreover, the comparative emission behaviour for α-Ga$_2$O$_3$ and β-Ga$_2$O$_3$ cannot be directly correlated with the crystalline phases of the emitters. The morphological changes due to synthesis conditions for α and β-Ga$_2$O$_3$ were identified as the key factors for enhanced emission properties in the case of β-Ga$_2$O$_3$. As mentioned in the morphological analysis, higher densities of larger pores were found in β-Ga$_2$O$_3$ compared to α-Ga$_2$O$_3$. Due to this, the β-Ga$_2$O$_3$ sample exhibit additional effective surface area and a higher number of active sites for carrier transfer. This effectively lowered the turn-on field and enhanced the emission current density for β-Ga$_2$O$_3$. Together, these factors established β-Ga$_2$O$_3$ samples to be the most effective emitter sample. Therefore, this sample was further used to study of FE properties of the related composite.

The cold emission activities of β-Ga$_2$O$_3$ wrapped with different amounts of rGO are presented in **Figure 7.8**. Among the composite samples, the emission current density was minimum for sample GR3 (~324 µA/cm^2 at 10.5 V/µm external fields), and it was enhanced remarkably for the sample GR12 (~1.08 mA/cm^2 at 10.5 V/µm external fields) presented in **Figure 7.8a**. Now, for a cold cathode, emission current (I) and applied electric field (E) are related by the equation[47]

$$I = \frac{Aa\beta^2 E^2}{\phi} exp^{\frac{-b\phi^{3/2}}{\beta E}} \qquad (7.4.1)$$

Where, β is the field enhancement factor,

φ is local work function (in eV),

A is the emission area, calculated considering the tip diameter, which is (π/4)×1.5 mm^2),

a =1.54 × 10^{-6}A eV V^{-2} and b = 6.83 × 10^3 eV$^{-3/2}$ V (µm)$^{-1}$ are Fowler-Nordheim (F-N) constants.

E is the externally applied field (in V/µm).

Eqn. (7.3) can be rewritten as

$$\ln\left(\frac{J}{E^2}\right) = \ln\left(\frac{a\beta^2}{\phi}\right) - \frac{b\phi^{\frac{3}{2}}}{\beta E} \qquad (7.4.2)$$

Where, J (= I/A) represents the emission current density.

Further, ln (J/E^2) vs $1/E$ was plotted, which was found to be linear, having slope (m) = $-b\phi^{3/2}/\beta$ and respective intercept = $\ln(a\beta^2/\phi)$.

So with the knowledge of this slope, one can figure out the field enhancement factor β using

$$\beta = -\frac{b\phi^{3/2}}{m} \qquad (7.4.3)$$

The turn-on field and threshold field (defined as the field required extracting emission current density of 10 μA/cm² and 100 μA/cm², respectively) were determined and compared for different samples. As depicted in **Figure 7.8c**, it can be seen that sample GR3 exhibits the highest turn-on and threshold field. However, those values gradually decreased with a higher amount of rGO incorporation and reached a minimum of 3.6 V/μm and 5.3 V/μm, respectively, for sample GR12.
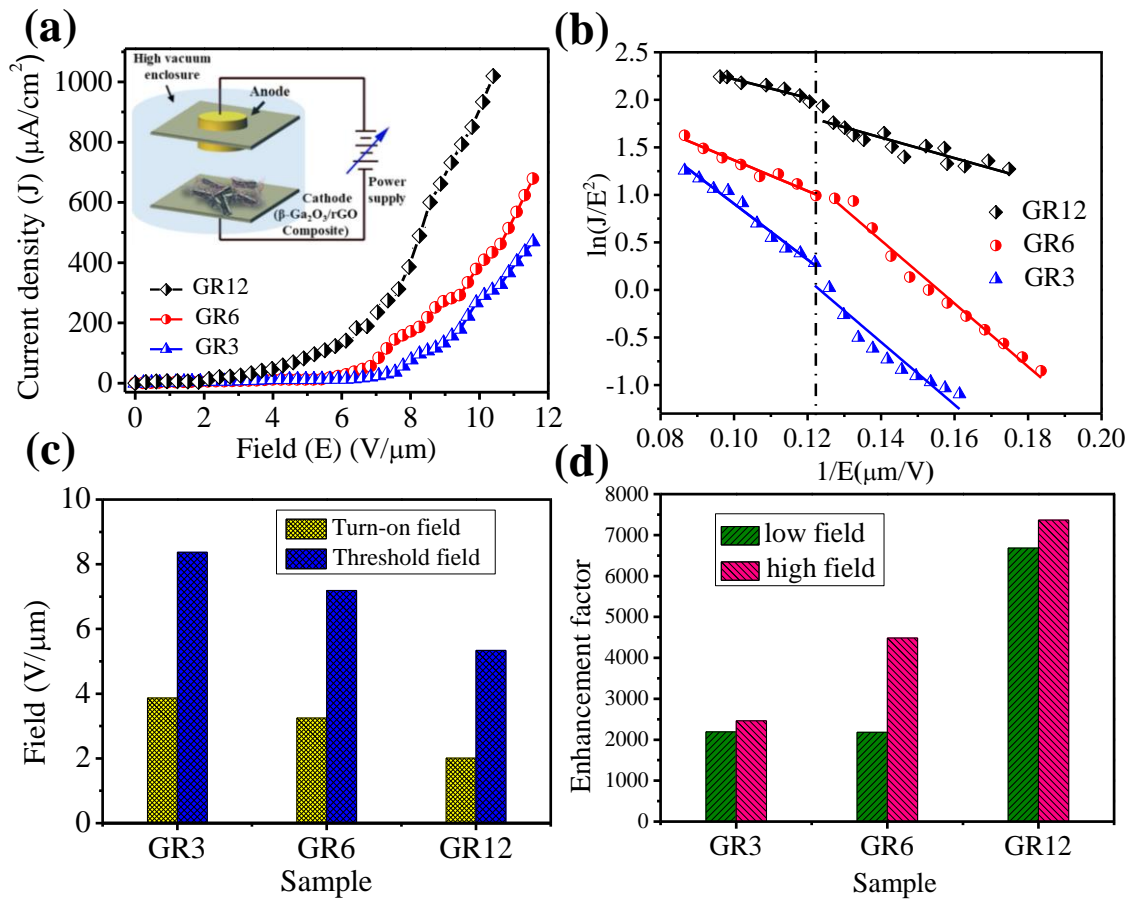

Figure 7.8 J–E characteristics (a), F-N plots (b) of the as-synthesized β-Ga₂O₃/rGO samples, the plot of the turn-on field and field enhancement factor vs. composite samples (c-d), inset of (a) shows the schematic diagram of the experimental cathode-anode set-up

In addition to emission current density, the field enhancement factor is also a key parameter for a good cold emission property. The theoretically calculated value of the work function for the Ga₂O₃/rGO composite system was used to determine the field enhancement factors of different rGO wrapped samples. In agreement with current density and turn-on properties, the

field enhancement factor was also highest for GR12 and inferior for GR3. The F-N plots were obtained from the $\ln(J/E^2)$ *vs* 1/E graph (**Figure 7.8b**).

The negative slopes of these Fowler-Nordheim plots ensure cold emission nature, but appreciable non-linearity can also be observed. Such apparent non-linearity in F-N slopes is common even in the case of traditional field emitters[48]. This non-linearity is expected when the FE experiment is carried out in a wide range of applied macroscopic fields. To analyze this apparent non-linear nature, the F-N slopes were divided into two subsections. Each subsection was correlated with high and low applied fields. Those subsections were fitted individually, and their slopes were utilized to determine field enhancement factors for high and low applied macroscopic fields. The obtained values of field enhancement factors are shown in **Figure 7.8(d)**. Enhancement factors in the lower field region exhibited a smaller value than that of the high field region. This may be accounted for the space-charge effect active near the emission sites. Those space charges commonly originate from the ionization of trace amounts of residual gases in the inter-electrode separation[48]. Their ionization depends upon the intensity of the applied field. Those ions or space charges contribute to the sample originated electrons in a high field, resulting in a higher enhancement factor. In both sections, the enhancement factors were found to increase for the rGO wrapped sample compared to the pristine one.

7.5.   Field emission mechanism

All the experimental evidence directly indicated superior field emission behavior of Ga_2O_3/rGO composite, and the same was found to enhance with an increasing amount of rGO wrapping. The first-principles study has been performed on a composite sample to determine the reason for this improvement. The computed work function value for pure β-Ga_2O_3 (1 1 1) is 5.95 eV, whereas, for rGO, it is comparatively lower (4.53 eV). Generally, a Schottky electric field is established at the interface of two materials due to their different work functions[49]. The reported values energy band gap (E_g) of β-Ga_2O_3 is 4.9 eV and electron affinity of β-Ga_2O_3 and rGO are 3.9 eV and 4.2 eV, respectively[38, 50]. Based on the above values, the energy band structure of the Ga_2O_3 and rGO before contact can be drawn. The work function difference enables the free electron transfer from thin rGO sheets to the host β-Ga_2O_3 at the junction between the counterparts and finally, the Fermi levels get aligned. Now due to alignment of Fermi level, Ga_2O_3 energy bands bend down towards the interface because of the Schottky electric field, which is schematically shown in **Figure 7.9.** On

application of an external electric field, the carriers from the Ga_2O_3 conduction band can be easily transferred through the potential barrier following the junction between Ga_2O_3 and rGO, and embellish the rGO sheets with a higher carrier density. Further, the carriers start tunnelling through the vacuum barrier when a stronger electric field is applied (presented in **Figure 7.9**). And finally, the anode collected them, ensuring a higher current density for composite samples.
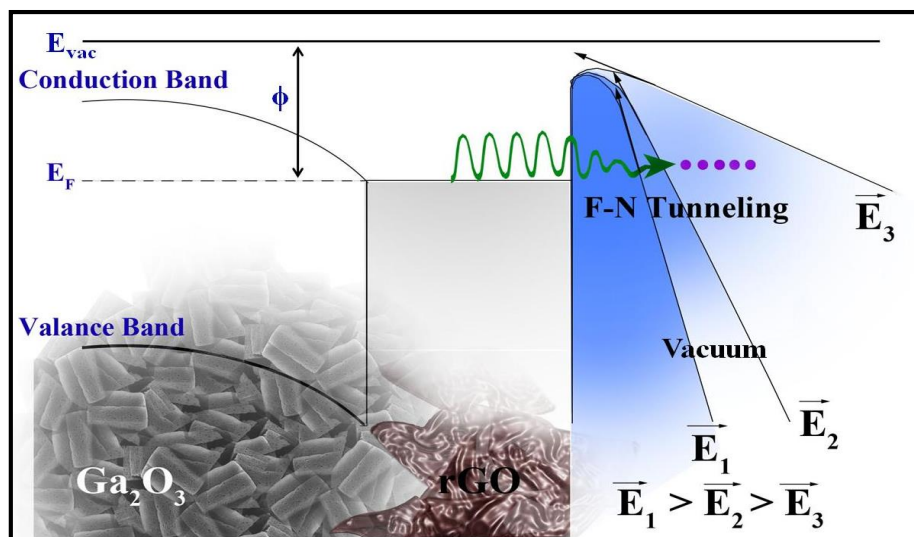

Figure 7.9 Band diagram schematics of Ga₂O₃/rGO composite representing the possible mechanism of field electron emission (E_vac: vacuum energy level, EF: Fermi level, ϕ: work function)

Also, the counterparts' electron affinity values accommodate easy electron transfer from Ga_2O_3 to rGO causing the latter to be more electron-rich when the composite system is excited with an external field. And finally, once the charge transfer towards the surface wrapped rGO is achieved, morphological features play an essential role. rGO is well-known for its wrinkles, and FESEM micrographs obtained in our study also confirm the same. Moreover, these wrinkled sheets of rGO become even sharper once they are wrapped on the host Ga_2O_3 micro/nano-bricks surface. Thus, being suitably groomed with favourable morphology and adequate carrier density, the surface wrapped rGO forms numerous efficient electron emission sites in the composite system. This enhances the output emission current density and a low turn-on field, as reflected in sample GR12. Also, a considerable increment of field enhancement factor can be found, which may be correlated with effective work function. For example, the density functional theory studies predicted the considerable lower work function for the Ga_2O_3/rGO composite system (5.09 eV) from the host Ga_2O_3 (5.95 eV). This shrinkage of local work function resulted in the higher field enhancement factor for the composite system with gradual increments of rGO boost. However, the incorporation of rGO

as the surface wrap was further increased to optimize the entire composite application features. It was observed that further increment of rGO incorporation caused inferior emission behavior of the composite (**Figure 7.10**).
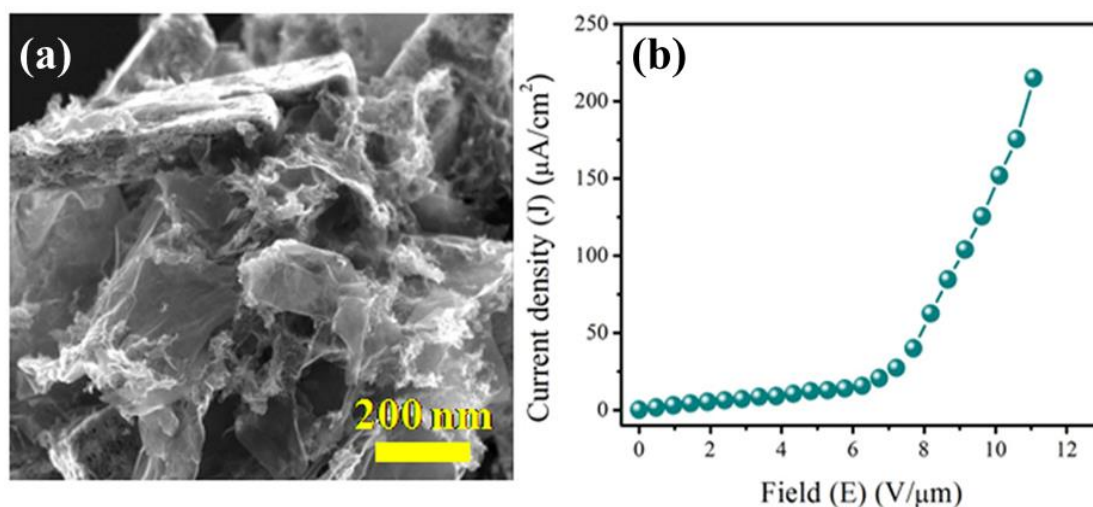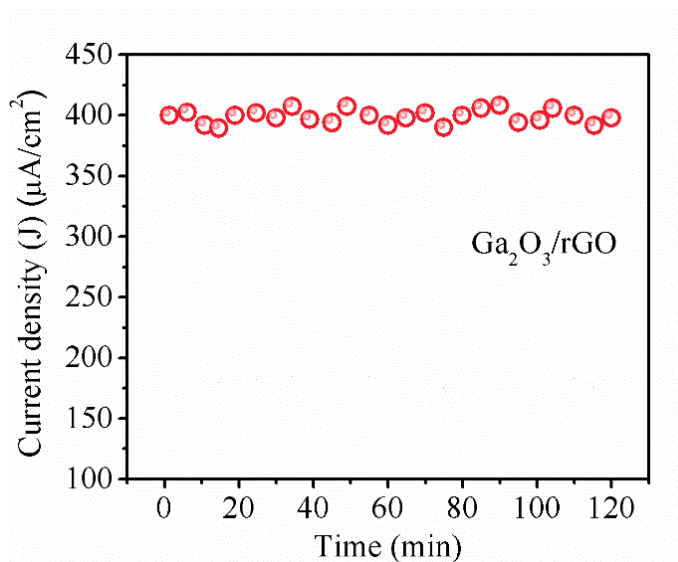

Figure 7.10 FESEM image (a) and corresponding field emission characteristics (J-E plot) (b) of the sample with higher amount of rGO with respect to Sample GR12

Furthermore, it can be mentioned that the higher rGO wrapped samples include too many effective emission sites. This in turn caused a screening effect and restricted the emission behavior of the neighboring sites. As a result, comparatively poor emission properties were observed. To visibly point out the impact of rGO incorporation, the field emission characteristics of rGO, β-Ga$_2$O$_3$, and β-Ga$_2$O$_3$/rGO composite may be sketched in a same graph. Here, **Table 7.2** represents the comparison of field emission characteristics of the GR12 composite sample with other rGO nanocomposites reported in the literature.

The stability of emission current is a key factor for device fabrication using any potential cold emitter sample. Here, the best performing composite sample was subjected to standard emission stability test under external macroscopic field 8 V/μm for 120 min. The obtained result is summarized in **Figure 7.11**. Sample GR12 exhibited an almost stable emission current presented in the figure. Usually, fluctuations in emission current originate from lattice defects and the non-uniform distribution of emission sites on the emitter surface. After wrapping by rGO sheets, emission electrons are released from the rGO surface rather than the host emitter, i.e., Ga$_2$O$_3$ micro/nano-bricks. RGO sheets, an appreciably conducting one, offer uniform distribution of emission sites. The hybrid system is free from the direct consequences of natural lattice defects of gallium oxide. These properties together may contribute to an almost stable emission current density.

Table 7.2: Comparison of field emission characteristics of GR12 composite sample with other rGO nano-composites reported in the literature

Sample	Turn-on field (E_{tu}) (Vμm^{-1}) (current density)	Threshold field (E_{th}) (Vμm^{-1}) (current density)	Field enhancement factor (β)	Ref.
Bi_2Se_3/rGO composite	2.38 (@10μA/cm^2)	4.61(@100 μA/cm^2)	4981	[51]
SnS_2/RGO composite	2.65 (@ 1 μA/cm^2)	--	3700	[52]
G–SnO_2 composite	5.39 (@ 1 μA/cm^2)	10.2 (@ 1 mA/cm^2)	901	[53]
rGO–Ag NWs	2.4 (@ 1 μA/cm^2)	--	1985	[54]
WS_2–RGO composite	2 (@ 1 μA/cm^2)	--	2994	[55]
RGO-TiO_2	1(@ 10μA/cm^2)	--	6000	[56]
Ga_2O_3/rGO	2.01 (@10μA/cm^2)	5.34 (@100μA/cm^2)	7366	This Work

Figure 7.11 Temporal current stability profile for β-Ga_2O_3/rGO (GR12) composite

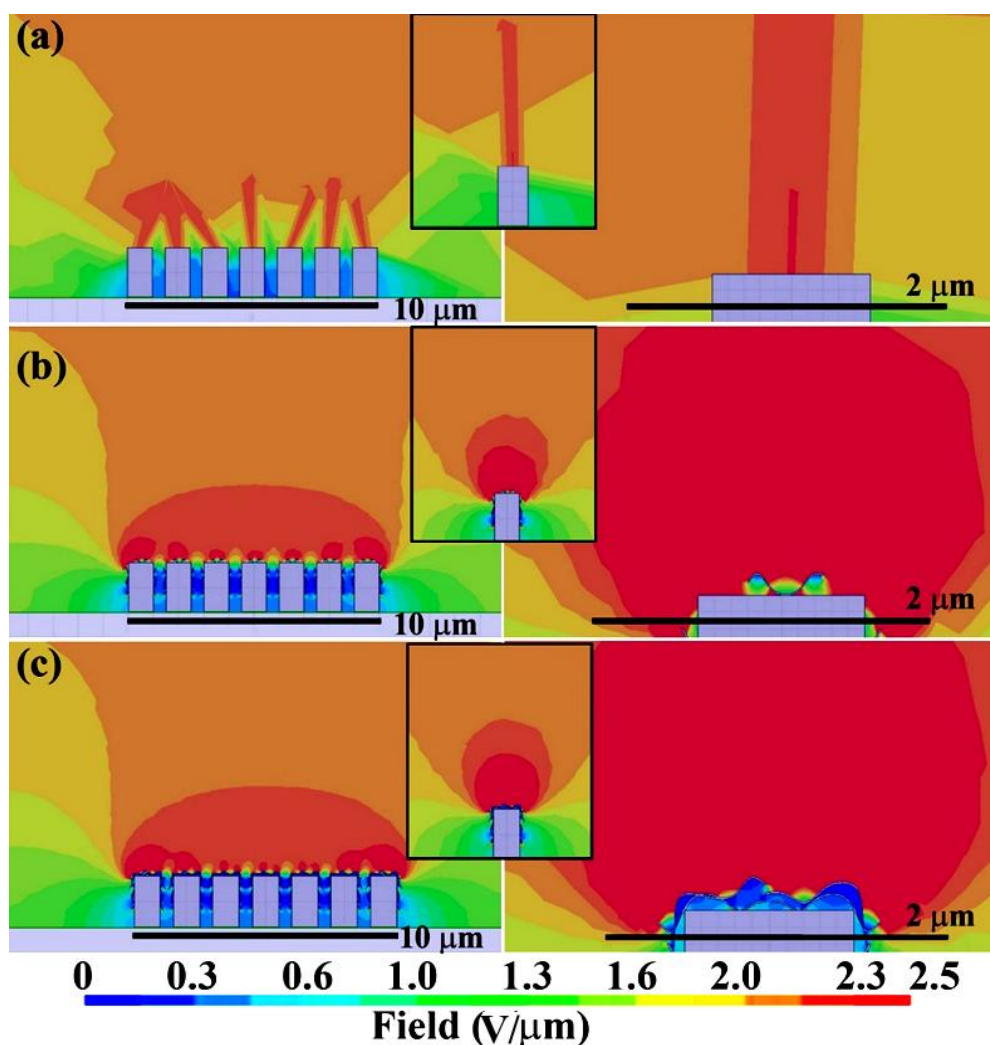## 7.6.   ANSYS simulation for field electron emission performance

Figure 7.12 ANSYS simulation of field emission distributions of β-Ga₂O₃ microbricks (a) and β-Ga₂O₃/rGO composite (b-c)

To cross-check the validity and the reproducibility of the field emission studies, theoretical simulations were executed using ANSYS Maxwell software with finite element analysis. For this, Ga_2O_3 micro/nanobricks were designed using appropriate software tools. In this regard, the actual dimensions of the nanostructures, as obtained from FESEM studies, were considered. Ga_2O_3/rGO hybrid systems were also modelled similarly with a random variation of the rGO wrapping amount. All the models were then subjected to virtual input electric field, and the inter-electrode separation was maintained as per actual basis. The output field distribution for each model was plotted using colour mapping near the vicinity of the emitter, and the results are depicted in **Figure 7.12**. It can be clearly observed that the output emission enhanced multifold after rGO wrapping. Also, the local enhancement of the fields wasensured at the rGO-Ga_2O_3 point of contact. The enhancement of the field is also predicted

208

via simulated results as obtained experimentally. The inter-component charge transfer and morphological modification were identified as the key factors of such enhancement.

7.7. Conclusion

Ga_2O_3/rGO composites were synthesized using gallium oxide micro/nanobricks as starting components via combined solid-state and hydrothermal processes. The samples were tested to investigate their field emission properties along with basic characterizations. A detailed theoretical investigation (DFT study) was carried to support the enhancement of emission current after rGO wrapping. Additionally, the feasibility of such enhancement was also predicted using ANSYS-based theoretical simulations. A remarkable enhancement of emission current density by 3.5 times and 2.5 times lowering of the turn-on field was observed due to rGO wrapping over gallium oxide. The composite system facilitated with huge emission current, low turn-on field, and higher stability, open up newer scopes for future emission-based technologies.

7.8. References

1. D. Ghosh, K. Sarkar, P. Devi, K. H. Kim, and P. Kumar, Renew. Sust. Energ. Rev.135 (2021) 110391.

2. N. Shimoi, and K. Tohji, Appl. Mater. Today. (2021) 101284.

3. P. Gabdullin, A. Zhurkin, V. Osipov, N. Besedina, O. Kvashenkina, and A. Arkhipov, Diam. Relat. Mater.105 (2020) 107805.

4. X. H. Yang, and F. G. Zeng, J. Alloy Compd. 817 (2020) 152767.

5. J. H. Deng, G. A. Cheng, R. T. Zheng, B. Yu, G. Z. Li, X. G. Hou, M. L. Zhao and D. J. Li, Carbon. 67 (2014) 525-533.

6. Y. Wu, J. Li, J. Ye, Y. Song, X. Chen, S. Huang, Z. Sun and W. Ou-Yang, J. Alloys Compd. 726 (2017) 675-679.

7. T. T. L Chau, T. P. Vu, H. T. Le, C. X. Nguyen, T. D. Luong, P. T. A. Le, N.T.T. Dang, L. V. Nguyen and N.D. Cuong, Opt. Mater. 116 (2021) 111100.

8. Y. Fu, G. Zeng, C. Lai, D. Huang, L. Qin, H. Yi, X. Liu, M. Zhang, B. Li, S. Liu, and L. Li, Chem. Eng. J. 399 (2020) 125743.

9. J. Xu, K. Yu and Z. Zhu, Physica E: Low Dimens. Syst. Nanostruct. 42(5) (2010) 1451-1455.

10. F. Liu, C. Shen, Z. Su, X. Ding, S. Deng, J. Chen, N. Xu and H. Gao, J. Mater. Chem. 20(11) (2010) 2197-2205.

11. J. Y. Chang, Y. Yang, and L. Wang, Int. J. Heat Mass Transf. 87 (2015) 237-247.

12. D.V. Gorodetskiy, A.G. Kurenya, A.V. Gusel'nikov, K.I. Baskakova, D.A. Smirnov, V.E. Arkhipov, L.G. Bulusheva, and A.V. Okotrub, Mater. Sci. Eng. B. 262 (2020) 114691.

13. N. Wu, Q. Hu, R. Wei, X. Mai, N. Naik, D. Pan, Z. Guo, and Z. Shi, Carbon. 176 (2021) 88-105.

14. Z. Zhang, X. Song, Y. Chen, J. She, S. Deng, N. Xu, and J. Chen, J. Alloy Compd. 690 (2017) 304-314.

15. H. Jadhav, S. Suryawanshi, M. A. More, and S. Sinha, J. Alloy Compd. 744 (2018) 281-288.

16. S. Chatterjee, A. Pal, I. Mukherjee, I. Chakraborty, and P. Ayyub, J. Alloy Compd. 789 (2020) 1-5.

17. K. Kannan, D. Radhika, K. K. Sadasivuni, K.R. Reddy, and A. V. Raghu, Adv. Colloid. Interface. Sci. 281 (2020) 102178.

18. V.H. Nguyen, H.H. Do, T. Van Nguyen, P. Singh, P. Raizada, A. Sharma, S. S. Sana, A. N. Grace, M. Shokouhimehr, S. H. Ahn, and C. Xia, Sol. Energy. 211 (2020) 584-599.

19. J. Zhang, E. Ding, S. Xu, Z. Li, A. Fakhri, and V. K. Gupta, Int. J. Biol. Macromol. 164, (2020) 1584-1591.

20. S. Noor, S. Sajjad, S.A.K. Leghari, and M. Long, J. Clean. Prod. 277 (2020) 123280.

21. S. John, and S. C. Roy, Appl. Surf. Sci. 509 (2020) 144703.

22. D. Majumdar, and S. Ghosh, J. Energy. Storage. 34 (2021) 101995.

23. P. N. K. Reddy, D. P. Shaik, V. Ganesh, D. Nagamalleswari, K. Thyagarajan, and P. V. Prasanth, Appl. Surf. Sci. 561 (2021) 150092.

24. G. Kaur, N. V. Pulagara, R. Kumar, and I. Lahiri, Diam. Relat. Mater. 106 (2020) 107847.

25. S. Park, A. P. Gupta, S. J. Yeo, J. Jung, S. H. Paik, M. Mativenga, S. H. Kim, J. H. Shin, J. S. Ahn, and J. Ryu, Nanomaterials. 8(6) (2018) 378.

26. S. F.Ahmed, M. S. Alam, and N. Mukherjee, Physica E: Low Dimens. Syst. Nanostruct. 97 (2018) 120-125.

27. M. Li, H. Luo, W. Qian, W. Huang, L. Wan, and C. Dong, J. Mater. Chem. C. 7(28) (2019) 8730-8736.

28. R. Kumar, R. K. Singh, A. K. Singh, A. R. Vaz, C. S. Rout and S. A. Moshkalev, Appl. Surf. Sci. 416 (2017) 259-265.

29. B. Ramezanzadeh, S. Niroumandrad, A. Ahmadi, M. Mahdavian and M. M. Moghadam, Corros. Sci. 103 (2016) 283-304.

30. L. Chen, H. Yu, J. Zhong, J. Wu, and W. Su, J. Alloy Compd. 749 (2018) 60-84.

31. L. Sun, X. Zhou, Y. Zhang, and T. Guo, J. Alloy Compd. 632 (2015) 604-608.

32. Y. Zhao, L. Liu, T. Cui, G. Tong and W. Wu, Appl. Surf. Sci. 412 (2017) 58-68.

33. G.K. Weldegebrieal, Inorg. Chem. Commun. 120 (2020) 108140.

34. Y. Feng, H.H. Rijnaarts, D. Yntema, Z. Gong, D.D. Dionysiou, Z. Cao, S. Miao, Y. Chen, Y. Ye, and Y. Wang, Water. Res. 186 (2020) 116327.

35. X. Xu, M. Lei, K. Huang, C. Liang, J. C. Xu, Z. C. Shangguan, Q. X. Yuan, L. H. Ma, Y. X. Du, D. Y. Fan and H. J. Yang, J. Alloy Compd. 623 (2015) 24-28.

36. S. B. Patil, I. Y. Kim, J. L. Gunjakar, S. M. Oh, T. Eom, H. Kim and S. J. Hwang, ACS Appl. Mater. Inter. 7(33) (2015) 18679-18688.

37. Z. S. Wu, G. Zhou, L. C. Yin, W. Ren, F. Li and H. M. Cheng, Nano Energy. 1(1) (2012) 107-131.

38. B. Das, B. Das, N. S. Das, S. Sarkar, and K. K. Chattopadhyay, Micro. Meso. Mater.288 (2020) 109600.

39. B. Das, B. Das, N. S. Das, S. Pal, B. K. Das, S. Sarkar, and K. K. Chattopadhyay, Appl. Surf. Sci. 515 (2020) 145958.

40. G. Kresse and J. Hafner, Phys. Rev. B. 48 (1993) 13115.

41. G. Kresse, J. Furthmüller, and J. Hafner, Phys. Rev. B. 50(18) (1994) 13181.

42. P. E. Blöchl, Phys. Rev. B. 50(24) (1994) 17953.

43. J. P. Perdew, K. Burke, and M. Ernzerhof, Phys. Rev. Lett. 77 (1996) 3865.

44. W. Tang, E. Sanville, and G. Henkelman, J. Phys.: Condens. Matter. 21(2009) 084204.

45. S. Grimme, J. Comput. Chem. 27 (2006) 1787-1799.

46. H. Yuan, J. Su, R. Guo, K. Tian, Z. Lin, J. Zhang, J. Chang, Y. Hao, Appl. Surf. Sci. 527 (2020) 146740.

47. S. Pal, N. S. Das, B. Das, B. K. Das, S. Mukhopadhyaya and K. K. Chattopadhyay, Appl. Surf. Sci. 530 (2020) 147102.

48. S. Santra, N. S. Das, D. Sen and K. K. Chattopadhyay, J. Phys. D: Appl. Phys. 47(50) (2014) 505301.

49. J. Qi, H. Zhang, D. Ji, X. Fan, L. Cheng, H. Liang, H. Li, C. Zeng and Z. Zhang, Adv. Mater. 26 (2014) 3735–3740.

50. P. A. Khomyakov, G. Giovannetti, P. C. Rusu, G. V. Brocks, J. Van den Brink and P. J. Kelly, Phys. Rev. B. 79(19) (2009) 195425.

51. B. Das, S. Sarkar, R. Khan, S. Santra, N. S. Das and K. K. Chattopadhyay, RSC Adv. 6(31) (2016) 25900-25912.

52. C.S. Rout, P.D. Joshi, R.V. Kashid, D.S. Joag, M.A. More, A. J. Simbeck, M. Washington, S. K. Nayakand, D.J. Late, Appl. Phys. Lett. 105 (2014) 043109.

53. J. Ding, X. Yan, J. Li, B. Shen, J. Yang, J. Chenand, Q. Xue, and ACS Appl. Mater. Inter. 3 (2011) 4299–4305.

54. A. K. Samantara, D.K. Mishra, S.R. Suryawanshi, M.A. More, R. Thapa, D. J. Late, B. K. Jena and C.S. Rou, RSC Adv. 5 (2015) 41887.

55. C.S. Rout, P.D. Joshi, R.V. Kashid, D.S. Joag, M.A. More, A.J. Simbeck, M. Washington, S.K. Nayak and D.J. Late, Sci. Rep. 3 (2013) 3282.

56. Y. Agrawal, G. Kedawat,P. Kumar, J.D. wivedi, V.N. Singh, R. K. Gupta and B. K. Gupta, Sci. Rep. 5 (2015) 11612.

Chapter **8**

Grand Conclusion and Future Prospects

In this chapter we summarize the main conclusions of the research presented in the chapters 4-7 of the thesis and outline future research directions.

8.1. Grand conclusion:

The work presented in this thesis discusses (i) the synthesis methods of different phases of Ga_2O_3 nanostructures with controlled porosity, surface area and morphology; (ii) the goal to gain a better understanding of the structural, electrical, optical and photocatalytic properties of pristine and composite gallium oxide nanomaterials; (iii) investigation of the visible light assisted photocatalytic performance of Ga_2O_3; (iv) to design efficient Ga_2O_3 based field-emitters.

The major conclusions of the works presented in this thesis in each individual work are:

Tailored mesoporous nanocrystalline Ga_2O_3 for dye-selective photocatalytic degradation

- Ga_2O_3 nano/microbrick samples were prepared from direct calcination of hydroxide sample synthesized by simple chemical bath method. Pore density and pore diameter were tuned with variation of calcination temperature.

- Trace amount of Ga_2O_3 photocatalyst can remove hazardous dyes efficiently with appreciable recyclability. The degradation rate constants were found to be as high as 0.072 min^{-1}, 0.051 min^{-1} and 0.18 min^{-1} for RhB, MO and mixed dyes respectively ending with almost complete removal of the dyes. The samples were also found capable to remove chemical contaminant like phenol from water.

- Phase, surface charge type and morphology together control the dye degradation performance. Also the surface electrostatic property of the samples was found to be the strongest factor in ion selective adsorption process.

- A strong correlation of the radicals $\bullet OH$, $\bullet O_2^-$ and h^+ with catalytic performances was established depending upon modification of band position of the dyes. This work is therefore conferred as a facile technique to fabricate morphology tuned advanced Ga_2O_3 photocatalysts for multidirectional catalysis activity.

Novel Ag_2O-Ga_2O_3 type II p-n heterojunction as an efficient water cleanser for green cleaning technology

- Ag_2O/Ga_2O_3 nanoheterojunctions were fabricated using facile photochemical reduction technique with varying densities of surface attached Ag_2O by simple variation of precursor molar ratios.

- After thorough characterization with XRD, FESEM, TEM, XPS and EDX for structural, morphological and compositional studies respectively, the samples were tested for photocatalytic performance to degrade hazardous organic dye MO.

- As predicted from VASP simulations, band alignment and charge transfer between Ag_2O and Ga_2O_3 with successive retardation of e^-/h^+ pair recombination was identified as the key factor behind enhancement of photocatalytic activity of Ga_2O_3 nanostructures. Also the approximate band edge potentials were calculated from Mott-Schottky studies which assisted to provide an insight into the probable transfer route of the photogenerated electrons and holes.

- It was observed that an optimized density of surface attached Ag_2O NPs could boost the photocatalytic performance of Ga_2O_3 in degrading a variety of dyes of different ionic identities, their mixtures and harmful colourless water pollutant like phenol to mimic realistic removal of water pollutants with high degradation rate.

- Additional studies of reusability test, multiple dye disintegration performance and capability of dye degradation in varying pH media established the optimized Ag_2O-Ga_2O_3 type II p-n nanoheterojunction sample as one of the most promising representative of smart water disinfection technology.

Morphology tuned Ga_2O_3 nanostructures for visible light assisted dye sensitized photocatalytic water remediation

- Different low dimensional structures of Ga_2O_3 were synthesized via a chemical route. Proper phase formation and chemical bond information of the samples were confirmed by X-ray diffraction studies and FTIR analysis.

- The formation of spherical and brick-like shapes of the sample was observed in morphological studies, whereas BET surface area investigation revealed a higher effective surface area and porosity for the brick-like samples. This enhanced surface area was correlated with numerous pores present in the brick-like sample.

- Investigation of photocatalytic degradation of rhodamine B via the samples was performed under visible light irradiation where both the samples showed considerable removal of the dye with a degradation rate constant of 0.0394 min^{-1} and 0.0057 min^{-1}.

- Being a wide band gap material, the degradation capability of gallium oxide under visible exposure has been taken into account by the dye sensitization mechanism. Better

+ performance of brick-like structure was correlated with larger surface area, porous structure, and the suitable band position of the sample.

+ This particular sample also showed remarkable reusability inferring possible application of the same as a future leading cleaning agent.

Enhanced field emission properties of rGO wrapped Ga_2O_3 micro/nanobricks: Experimental investigation with theoretical validation

+ Ga_2O_3/rGO composites were synthesized using gallium oxide micro/nanobricks as starting components via combined solid-state and hydrothermal processes.

+ The samples were tested to investigate their field emission properties along with basic characterizations.

+ A detailed theoretical investigation (DFT study) was carried to support the enhancement of emission current after rGO wrapping. Additionally, the feasibility of such enhancement was also predicted using ANSYS-based theoretical simulations.

+ A remarkable enhancement of emission current density by 3.5 times and 2.5 times lowering of the turn-on field was observed due to rGO wrapping over gallium oxide. The composite system facilitated with huge emission current, low turn-on field, and higher stability, open up newer scopes for future emission-based technologies.

8.2.   Scope of future work:

Although a number of significant results have been obtained and described in the thesis which I believe has enhanced our understanding about different aspects Ga_2O_3 nanostructures, but still I believe there are many areas where more work is necessary. If I get the scope to continue, I would like to pursue the following areas or research in near future:

❑ Development of new and easier synthetic strategies for different gallium oxide nanostructures.

❑ Tuning of size, morphology and properties of $Ga_2O_3.$

❑ Doping effect at anionic site in Ga_2O_3 nanostructure is an important area where practically no work exists in the literature.

❑ Fabrication of Ga_2O_3 composite with different polymer or any other oxide material.

❑ Modification of Ga_2O_3 nanostructure for smart visible light assisted photocatalysis.

❑ Fabrication of memory devices.

❑ Photodetector and photovoltaic application.